AD

A060053

LEVEL

AMMRC CTR 76-32   VOLUME IV

BRITTLE MATERIALS DESIGN, HIGH TEMPERATURE GAS TURBINE
MATERIAL TECHNOLOGY

Technical Report By:

Donald G. Miller, C.A. Andersson, S.C. Singhal, F.F. Lange,
E.S. Diaz and R. Kossowsky;   R.J. Bratton, Program Manager

WESTINGHOUSE ELECTRIC CORPORATION
Pittsburgh, PA. 15235
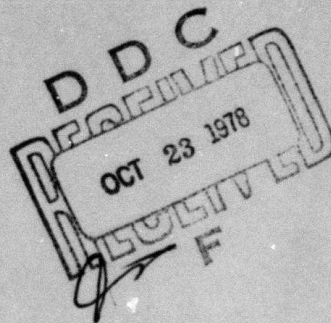December, 1976

Final Report

Contract Number DAAG 46-71-C-0162

Sponsored by the Advanced Research Projects Agency

ARPA Order Number 1849

Project Code Number 1D10

Agency Accession Number OD 4733

Prepared for

ARMY MATERIALS AND MECHANICS RESEARCH CENTER
Watertown, Massachusetts 02172

78 10 19 074

AMMRC CTR-76-32 — Vol. IV

BRITTLE MATERIALS DESIGN, HIGH TEMPERATURE GAS TURBINE MATERIAL TECHNOLOGY. Volume IV.

Technical Report By:

Donald G. Miller, Westinghouse Electric Corp., Pittsburgh, PA 15235
C. A. Andersson, Westinghouse Electric Corp., Pittsburgh, PA 15235
S. C. Singhal, Westinghouse Electric Corp., Pittsburgh, PA 15235
F. F. Lange, Westinghouse Electric Corp., Pittsburgh, PA 15235
E. S. Diaz, Westinghouse Electric Corp., Pittsburgh, PA 15235
R. Kossowsky, Westinghouse Electric Corp., Pittsburgh, PA 15235

265 p.

December 1976

Final Report. 1 Jul 71 - 30 Jun 76,

Contract Number DAAG 46-71-C-0162, ARPA Order-1849

D.D.C.

OCT 23 1978

Prepared for:

ARMY MATERIALS AND MECHANICS RESEARCH CENTER
Watertown, Massachusetts 02172

141 250

Abstract

In 1971 Norton obtained an exclusive license to produce Lucas hot pressed silicon nitride in the United States. That process made a high-density, high strength ceramic material with excellent potential for high temperature application, i.e., industrial gas turbine components, available commercially. Project funds were used to develop an engineering property data base to describe Norton HS130/Noralide NC132 silicon nitride and Noralide NC203 silicon carbide. The list includes tensile, flexure , shear, and compressive strengths from room temperature to 2550°F for appropriate directions in anisotropic materials along with elastic/shear moduli and Poisson's ratio. Creep resistance is defined in terms of creep strain and stress rupture life as a function of temperature, time, and environment. Thermal properties were also considered, i.e., thermal expansion, conductivity, and specific heat. Equipment and test procedures are discussed.

No material characterization study is complete without a thorough examination of microstructure. Morphology, grain boundaries, and the effects of compositional variations are considered with respect to silicon nitride and silicon carbide.

The microstructural characterization led to process and product improvements in the commercial materials and eventually revealed paths for the development of improved varieties of silicon nitride and silicon carbide. Westinghouse activity in the area of material development involving magnesia and/or yttria silicon nitride systems is reviewed to put the entire question of materials and their critical part in component design and development into proper perspective.

TABLE OF CONTENTS

78 iii 10 19 074

LIST OF FIGURES

xi

LIST OF TABLES

FOREWORD

<u>The Stationary Gas Turbine Project</u> represents the Westinghouse contribution to the Defense Advanced Research Project Agency (DARPA) sponsored "Brittle Material Design, High Temperature Turbine" program, Order Number 1849, Contract Number DAAG-46-71-C-0162.

The final report is presented in four volumes as follows:

Volume I - Program Summary

Volume II - Ceramic Stator Vane Development

Volume III - Rotor Blade Development and Turbine Modification

Volume IV - Materials Technology

Final results of static rig testing and analysis for the tenth semi-annual report period are included as part of this final report which represents a comprehensive project review summarizing the activities from July 1, 1971 to June 30, 1976.

Westinghouse performed this work under subcontract to the Ford Motor Company, prime contractor for the Defense Advanced Research Project Agency. The Army Material and Mechanics Research Center (AMMRC) at Watertown Arsenal, Watertown, Massachusetts, served as Program Monitor for DARPA.

The program's overall Principal Investigator was Mr. A. F. McLean, who also served as Program Manager for the Ford Vehicular Turbine Project.

Dr. R. J. Bratton was Principal Investigator and Program Manager for Westinghouse. Mr. D. G. Miller served as Project Engineer. Mr. A. N. Holden, now deceased, functioned as Project Manager at Westinghouse Generation Systems Division from July 1, 1971 to May 1, 1975. Mr. G. Levari succeeded Mr. Holden with Mr. C. R. Booher, Jr, accepting responsibility for design, analysis and rig testing for the Division at that time.

Westinghouse wishes to acknowledge the efforts of the following personnel who contributed to the program:

1. Dr. Maurice J. Sinnott who conceived and started the program when he was at DARPA in 1971.

SECTION 1

1.1 INTRODUCTION

The "Brittle Materials Design High Temperature Gas Turbine" program was formulated under the auspices of the Defense Advanced Research Projects Agency(DARPA) of the Dept. of Defense (DOD) to demonstrate and encourage the use of brittle material design concepts in the successful application of ceramics as structural components in high temperature gas turbines. The talents of the Ford Motor Company and Westinghouse, as prime and subcontractor, respectively, were directed toward the development of a vehicular ceramic turbine (Ford) and a ceramic stator vane for a large stationary gas turbine (Westinghouse). The Army Materials and Mechanics Research Center (AMMRC) served as technical monitor for DARPA.

The 5-year performance period of the Westinghouse Stationary Gas Turbine Project, July 1, 1971 through June 30, 1976, is summarized in Volume I, "The Program Summary" of this report. A comprehensive discussion of Ceramic Stator Vane Development is presented in Volume II which includes: Preliminary Design and Analysis, Three Generations of Ceramic Vane Assembly Design and Analysis, Static Rig Test Results at 2200 and 2500°F, a Ceramic Vane Performance Review and finally Ceramic Stator Vane Fabrication.

Volume III, "High Temperature Stationary Gas Turbine - Ceramic Rotor Blade Development and the Turbine Modification," reports the engineering Aspects of Three-Dimensional Heat Transfer and Stress Analysis, Ceramic Rotor Blade Design and Analysis, and the Advanced Turbine Design Modification.

Volume IV, "High Temperature Stationary Gas Turbine - Material Technology," presented here, will review the engineering properties of hot pressed silicon nitride and silicon carbide, the microstructural characterization of these materials and their environmental stability. A section on new material development is included to summarize the work performed in this important area during the last year of the contract (July 1975 through June 1976). The extensive material properties data base which accumulated over the 5-year period of program performance has been tabulated for future publication by the Army Materials and Mechanics Research Center (AMMRC).

Figure 1-1 is reproduced from Volume I to emphasize the iterative development of ceramic components for an industrial gas turbine as identified in Figure 1-2. The turbine itself is shown in Figure 1-3.

1

Component development and material technology follow parallel but inter-
acting paths to provide the coordination for fabrication, static-rig
testing and final demonstration in the overall project plan. Failure
analysis with design modification, further analysis and material improve-
ment form the iterative loop required for successful application.
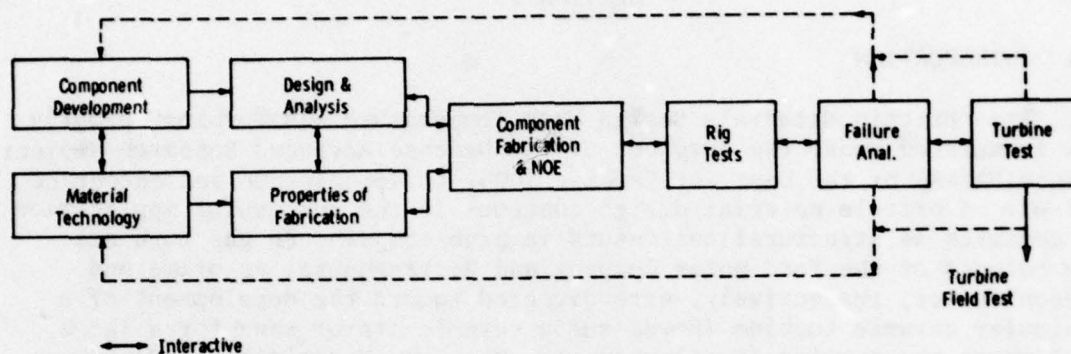
Figure 1-1. Iterative Development Procedure for Industrial
Gas Turbine Components

Overall program objectives, as originally proposed and finally
accomplished, are illustrated in Figure 1-4. Final rotor blade design
and computer simulation were delayed, then terminated in 1973 to permit
full concentration of effort on the formidable tasks of ceramic vane
development and static rig construction. The 30 megawatt turbine
demonstration was also delayed and then terminated when it became obvious
that the rapidly escalating costs of an advanced turbine rig conversion
and the need for additional verification of stator vane performance in
the static rig placed this task beyond a reasonable scope of funding
within the designated period of performance (5 years).

All of the essential elements of the ceramic stator vane development
appear in Figure 1-5. The design process with appropriate analysis
proceeded logically from the preliminary stages, through Vane Designs I
and II to the final third generation, three-piece stator vane assembly
with tapered-twisted airfoil. Component fabrication had to follow a
parallel rather than a subsequent or series route in many cases,
anticipating the design because of the long lead time required to meet
the static rig test specifications as scheduled. Fabrication processes
were developed as part of component manufacture, thus complicating the
procedure. The second generation airfoil, for example, was committed to
procurement before analysis disproved design viability. The static rig
test facility, planned as a simple modification of an existing rig,
became a dynamic development activity coincident with the design and
fabrication tasks. Indeed, the static rig requirement to test at 2500°F
became the critical element in the project plan. Only once, in the
final phases of the program when a supplier failed to deliver acceptable
third generation hardware on time, was a critical delay experienced for
a reason other than static rig availability.

2
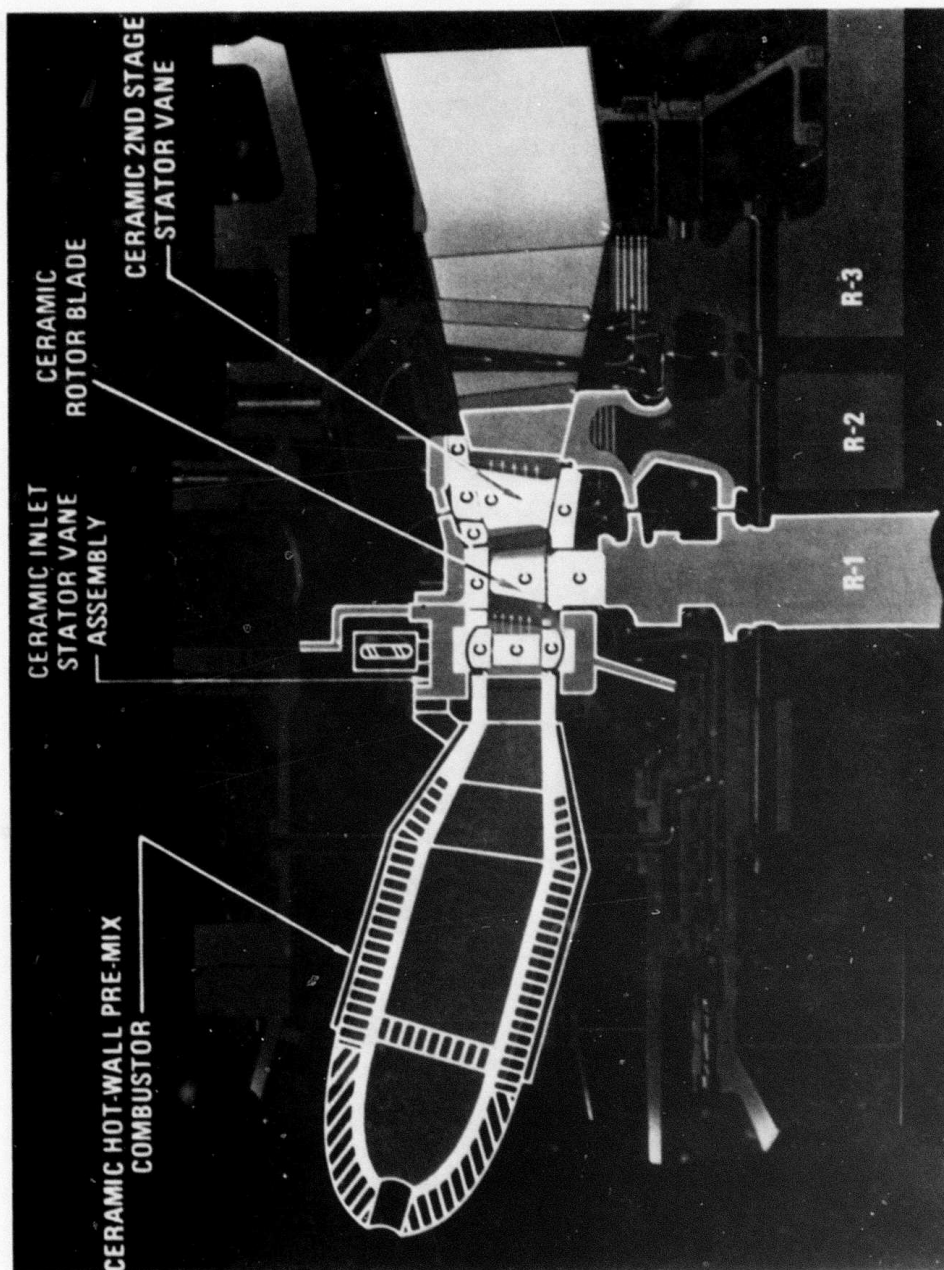
Figure 1-2. Conceptual Ceramic Turbine for Power Generation

Compressor — Combustor — Power Turbine — Exhaust

WESTINGHOUSE
W 251 GAS TURBINE
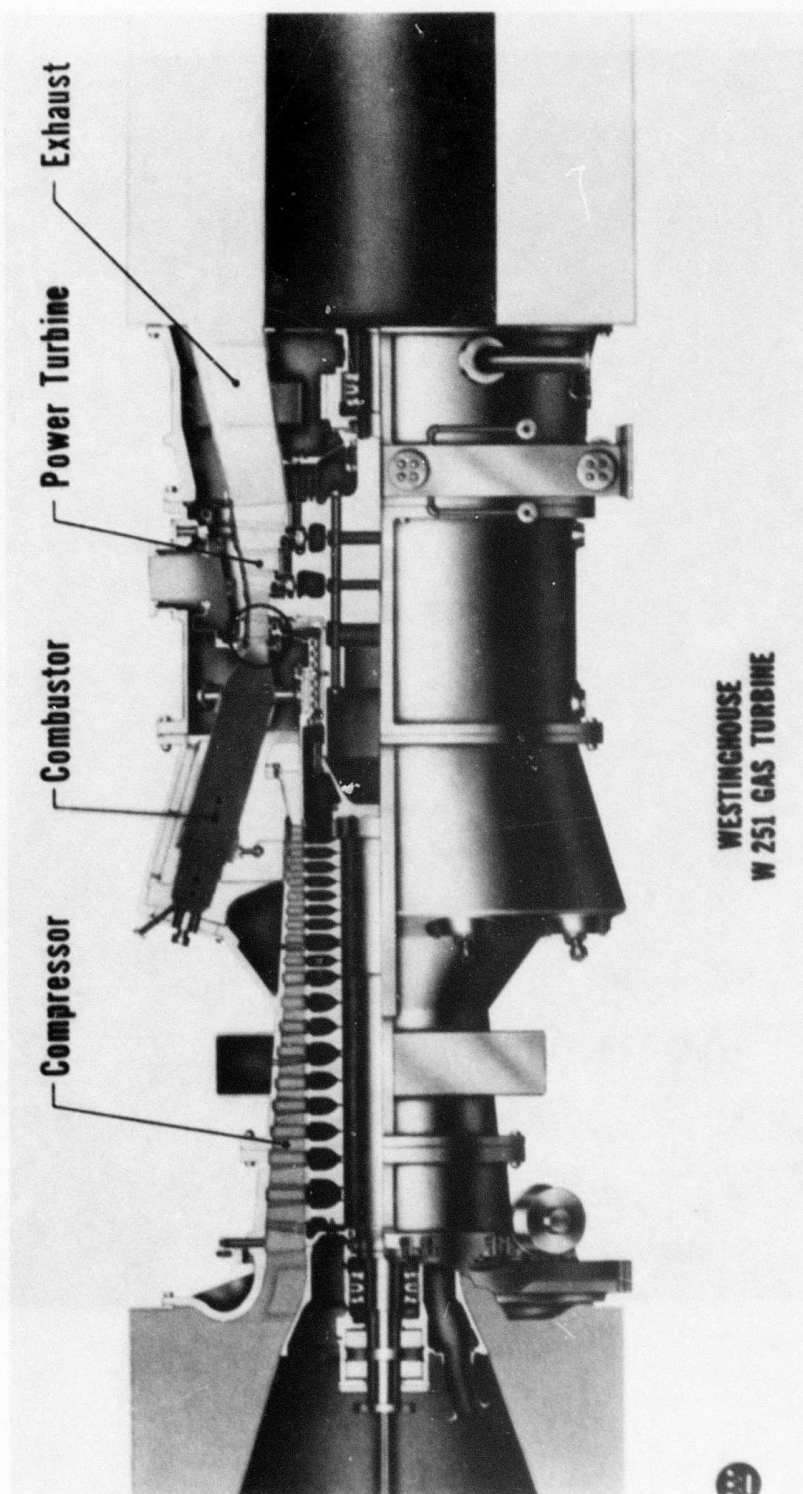
Figure 1-3. Westinghouse W251 Gas Turbine

4
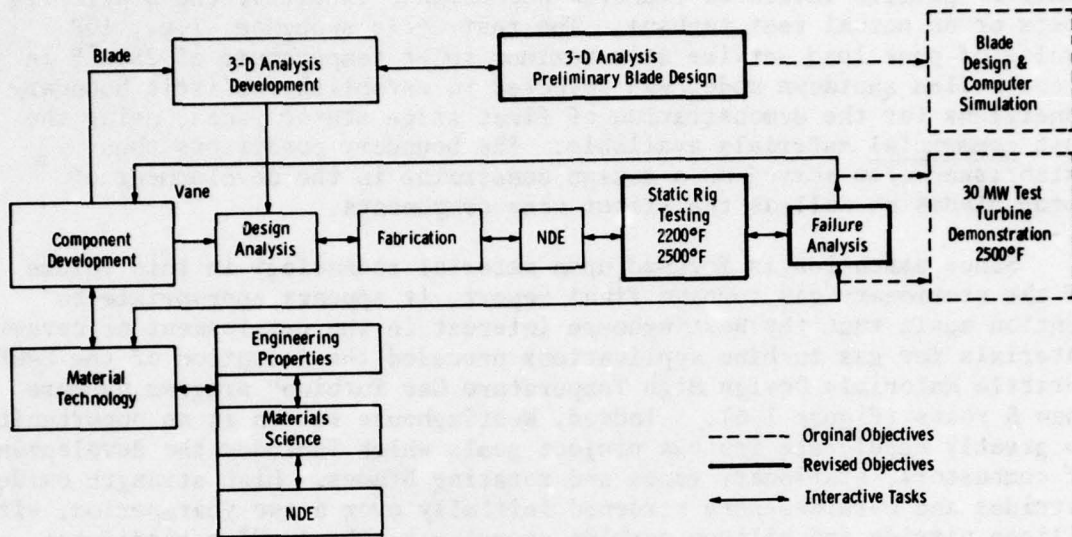
Figure 1-4.   DARPA Stationary Turbine Project - Iterative Development Plan
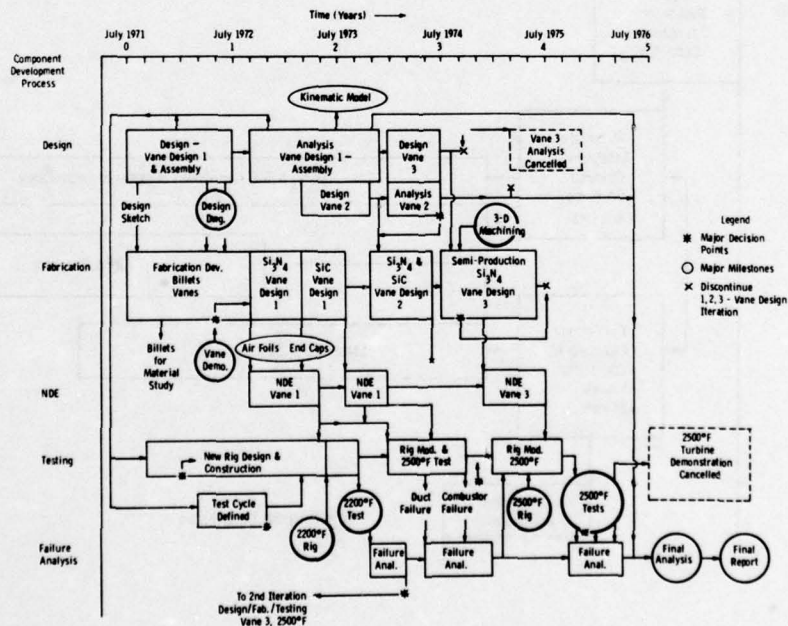
Figure 1-5.   Stator Vane Development on Stationary Turbine Project

5

Although the total effort was directed toward higher service temperatures to increase power and efficiency, no attempt was made to achieve specific levels of improved performance in either the static rig tests or an actual test turbine. The test cycle sequence, i.e., 100 cycles of peak load service at a maximum inlet temperature of 2500°F in a controlled shutdown mode, was selected to establish realistic boundary conditions for the demonstration of first stage stator vanes, using the best commercial materials available. The boundary conditions thus established also served as a design constraint in the development of rotor blades as well as the stator vane components.

Since attention is focused upon material technology in this volume of the stationary gas turbine final report, it appears appropriate to mention again that the Westinghouse interest in the development of ceramic materials for gas turbine applications preceded the inception of the DARPA "Brittle Materials Design High Temperature Gas Turbine" program by more than 5 years (Figure 1-6). Indeed, Westinghouse saw in it an opportunity to greatly accelerate its own project goals which included the development of combustors, stationary vanes and rotating blades. High strength oxides, nitrides and carbides were screened initially over a two year period, with silicon nitride and silicon carbide emerging as the leading candidates.
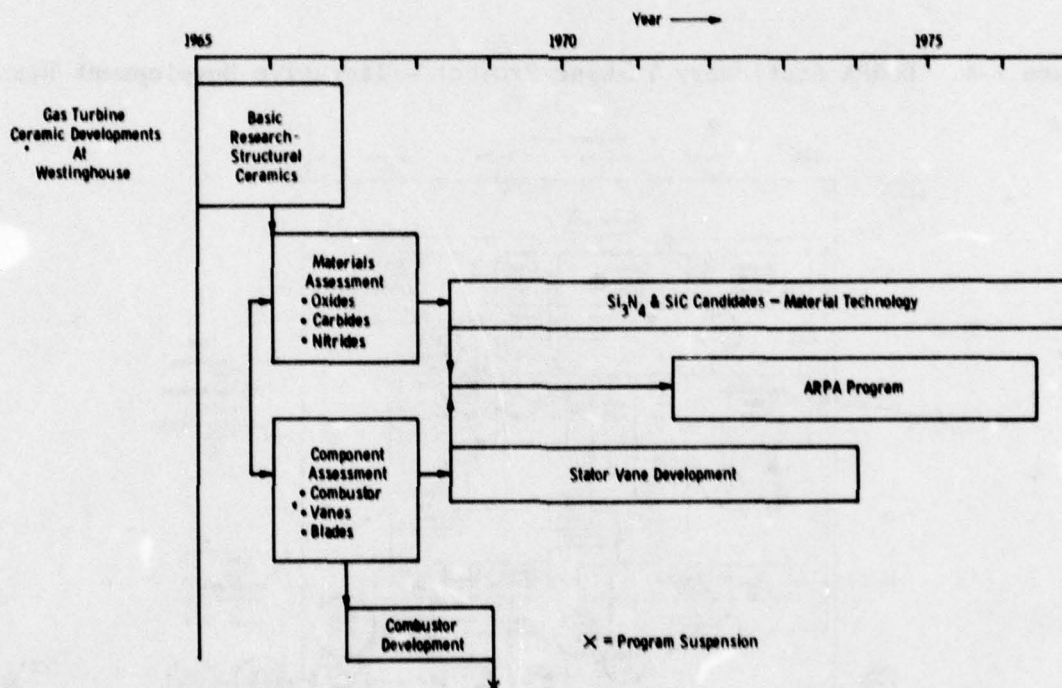
Fig. 1-6. Stationary Turbine Project Background Chart

Reinforced castable ceramic materials were proposed and tested as combustor linings. The concepts appeared feasible but further development was curtailed in favor of first row stator vanes because these were considered more critical to improved turbine performance. To this end:

1. Conceptual designs were developed.

2. A three-piece ceramic vane design was selected.

3. A preliminary 2-D finite element stress analysis of vane airfoils was conducted.

4. Fabrication methods for both silicon nitride and silicon carbide were investigated.

5. A development approach and procedures were structured.

The critical aspects of Materials Technology to this program cannot be overemphasized. While it was clearly DARPA's intent at the beginning of the program to stress design with brittle materials by turbine demonstration, the development of silicon nitride in viable hot-pressed and reaction-sintered forms provided incentive. Cursory property data were available to describe Lucas hot-pressed silicon nitride, and Norton had become a licensed source of that material in the United States by the time the Stationary Gas Turbine Project was formulated. However, Norton expected to achieve superior properties from their production, making mandatory a full-scale assessment of engineering properties and material characterization, which were considered fundamental input to a successful design activity.

The materials technology effort was extensive. A statistical test program was set up to determine the pertinent physical and thermal properties of the best commercial grade of hot-pressed silicon nitride, Norton HS130, which eventually evolved into Noralide NC132. Silicon carbide was included later after the development of Noralide NC203. Test facilities were upgraded to 2500°F capability for engineering property evaluation. The microstructural characterization of both silicon nitride and silicon carbide supplied information concerning the behavior of the respective materials to establish a basis for improvements. An exhaustive study of corrosion-erosion provided an insight into long-term performance and stability of Si_3N_4 and SiC in a turbine environment.

SECTION 2

THE ENGINEERING PROPERTIES OF Si_3N_4 AND SiC

2.1 INTRODUCTION

The comprehensive test program to define the engineering properties of Norton hot pressed silicon nitride (HS130 which became Noralide NC132) and silicon carbide (Noralide NC203) required a statistical minimum of eight to ten repetitions or tests (specimens) per condition for all primary properties over an incrementally divided range from room temperature to 2500°F. The temperature interval choosen was 500°F with spacing at 1800, 2100, 2300 and 2500°F provided to carefully identify the high temperature portions of the performance curves. Ten billets were randomly selected from the original forty, with random sampling of remnant material from component manufacture to occur subsequently in the case of silicon nitride. Three of eighteen silicon carbide billets were employed with random sampling of the remnant material. Size and rate effects were assessed but not necessarily with statistical inference except in the flexural mode where hundreds of specimens were involved.

Weibull statistical theory was used to analyze the flexural test results in terms of failure probability and volume/area effects. An attempt was made to ascribe the statistical characteristics derived from large population flexural testing to other primary properties described only by minimum populations in tensile, shear and fatigue. Estimates of tensile strength in the weak direction of silicon nitride (Figure 2-1) were made by statistical comparison in lieu of meaningful test data.

At the outset, a system was devised to relate specific material properties with loading conditions as they exist in an operating gas turbine. The intention to identify critical areas by coding, cross comparisons, and plotting in the fashion of Table 2-1 were not very successful. Plots of condition versus property produced a poorly developed maize of intersecting lines lacking objectivity or trends. In certain instances, the modeling of tests to reflect machine conditions proved meaningful, specifically low and high cycle fatigue.

9

Hot Pressing Direction

Perpendicular Specimen

Parallel Specimen
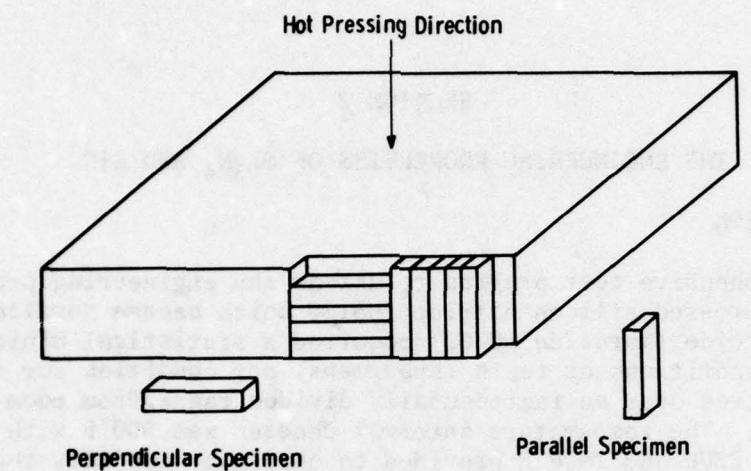
	Perpendicular Specimen	Parallel Specimen
Westinghouse	98,600 ± 6,000 psi	Westinghouse	73,000 ± 11,000 psi
Norton	125,000 ± 16,000 psi	Norton	107,000 ± 17,000 psi

Norton data - 3 pt Bend,   (W) - 4 pt Bend

Figure 2-1.   Definition of Anisotropic Property Directions
in Hot Pressed Silicon Nitride

TABLE 2-1

TURBINE CONDITIONS VERSUS PHYSICAL PROPERTY

		<u>INPUT CODING CORRELATIONS</u>	Code
I.	Loading	Tension	1
		Compression	2
		Shear	3
		Bending	4
II.	Ballistic Impact	Modulus of elasticity of impactor	5
		Change of momentum	6
III.	Chemical Environment		7
IV.	Temperature		8
V.	Time	Period of cycle	9
		Number of cycles	10
VI.	Geometry	Gross size	11
		Notch radii	12
		Orientation (to loads)	13
		Crack size, orientation	14
		Surface finish	15

MATERIAL CODING
(Experimental Observations)

I.	Strains	Elastic tension	a
		Elastic compression	b
		Elastic shear	c
		Viscous tension	d
		Viscous compression	e
		Viscous shear	f
II.	Cracks	Crack energy	g
		Crack length	h
		Crack geometry	i
		Crack orientation	j
		Crack nucleation	k
III.	Basic Material Properties		l
	(Thermodynamics, phase, grain size damage, thermal expansion, etc.)		
IV.	Corrosion		m
V.	Erosion		n
VI.	Solubility (or binary reactions)		o

11

2.2 TENSILE PROPERTIES

2.2.1 BACKGROUND

The strength of a ceramic under pure tension was considered the most desirable for reliable engineering design. However, tensile strength, particularly at high temperatures, was difficult and expensive to obtain. Complex high temperature grips, extremely precise machining accuracy, and difficulty with accurate alignment generally precluded a large number of tension tests.[1]

This dilemma was resolved initially by supplementing tension data with reliable flexural data through the use of Weibull[10] statistical characterization of brittle materials. Weibull theory attributes the failure of brittle materials to flaws randomly distributed throughout the material; thus, the larger the volume under high stress, the higher the probability of failure. A bend specimen with only the outer fibers under the maximum stress is expected to survive a higher load than a tensile specimen with the entire gage volume under maximum stress.[2] The risk of failure for a number of materials is proportional to

$$\int_V \left(\frac{\sigma}{\sigma_o}\right)^m dV$$

where stress and volume are represented by σ and v, respectively. The Weibull modulus, m, and normal stress, σ_o, are characteristics of the material tested. In some cases

$$\int_V \left(\frac{\sigma - \sigma_u}{\sigma_o}\right)^m dV$$

is found to be more appropriate where σ_u is the third material parameter.

Twenty-four values of RT fracture strength obtained in three-point bending by the Norton Company were used to calculate values of m = 9.1, σ_u = zero and σ_o = 57,800 psi for hot pressed silicon nitride (HS130). The average fracture strength in both four-point bending and tensile loading was predicted from these values and compared with test data obtained at Westinghouse (Figure 2-2).[2]

Weibull parameters were also determined for hot-pressed silicon nitride in the weak direction at 2350°F. In this case m = 8.7 and σ_o = 29,200.[2] By regressive curve fitting, these data were combined with

12

$$\sigma_1 = \sigma_2 \left(\frac{K_2 V_2}{K_1 V_1} \right)^{1/m}$$

	Experimental	Weibull Prediction
	125,000 psi	-----
	98,600 psi	100,000 psi
	54,000 psi	53,500 psi
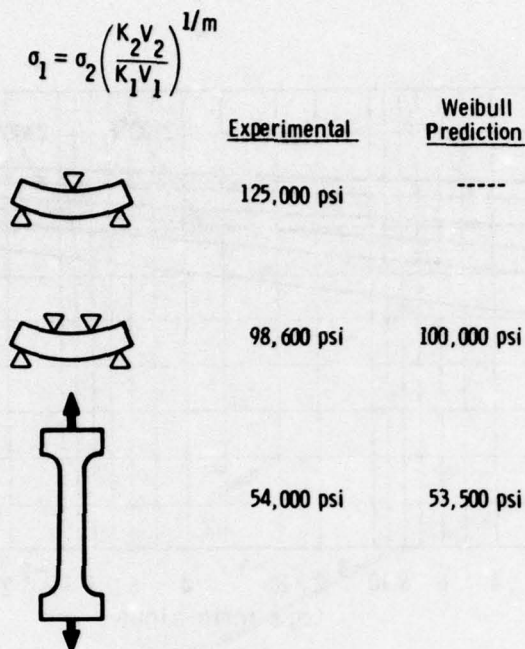
Figure 2-2. Effect of Test Mode on the Strength of Si_3N_4

flexural data that show a strain rate dependence at high temperature to produce the following expression relating temperature, strain rate and volume to tensile strength:

$$\sigma_T = \frac{28,600 \; \dot{\epsilon}^{\left(\frac{27.5}{2920-T}\right)}}{V^{.11}} \pm 12\%$$

where T is in degrees F, V is in cubic inches and $\dot{\epsilon}$ is in inch/inch-minute. Predicted tensile properties appear in Figures 2-3, 2-4 and 2-5 for increasingly larger volumes under stress.[2]

2.2.2 THE TEST PROGRAM

The statistical tensile test program was established to develop the engineering property data required for hot pressed silicon nitride and silicon carbide and also to confirm the Weibull results.[3] A minimum of eight repetitions per temperature condition at room temperature, 1000°F, 1800°F, 2100°F, 2300°F and 2500°F were performed at a strain rate of 0.001 inch/inch/minute. Three repetitions/condition were performed at 0.01 and 0.0001 inch/inch/minute to test strain rate effects within the limits of the universal tensile test machines employed. If the rate

13
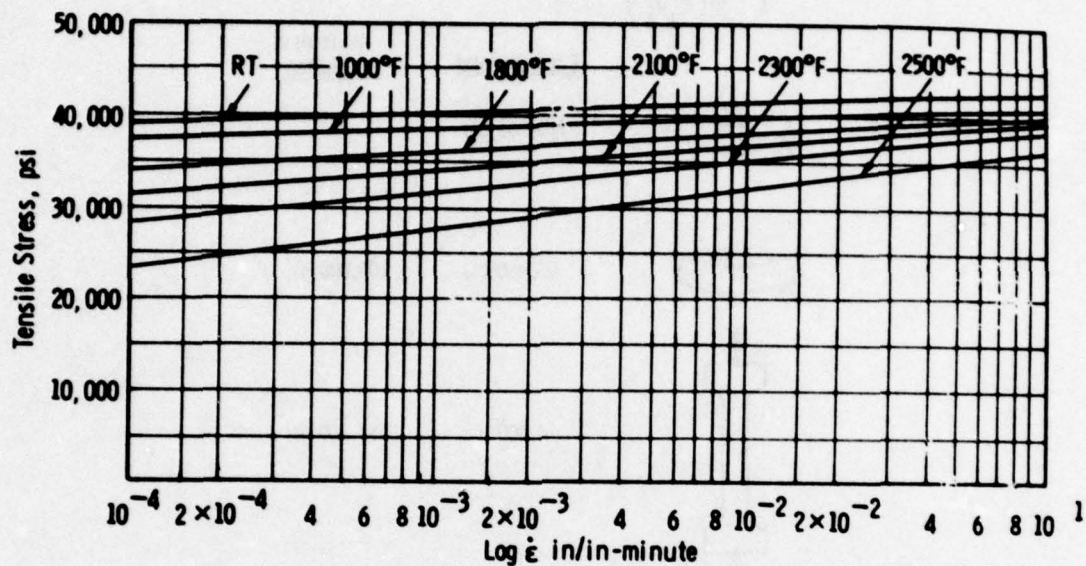
Figure 2-3. The Predicted Tensile Strength of Hot Pressed Si_3N_4 as a Function of Temperature and Strain Rate - Volume 0.1 in³
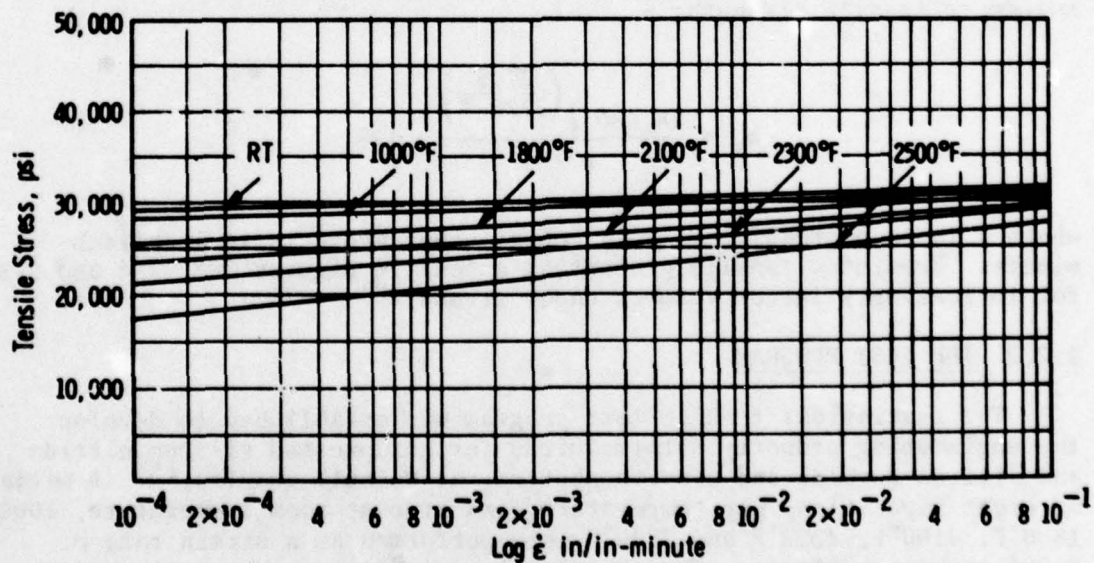
Figure 2-4. The predicted Tensile Strength for Hot Pressed Si_3N_4 as a Function of Temperature and Strain Rate - Volume 1.0 in³

14
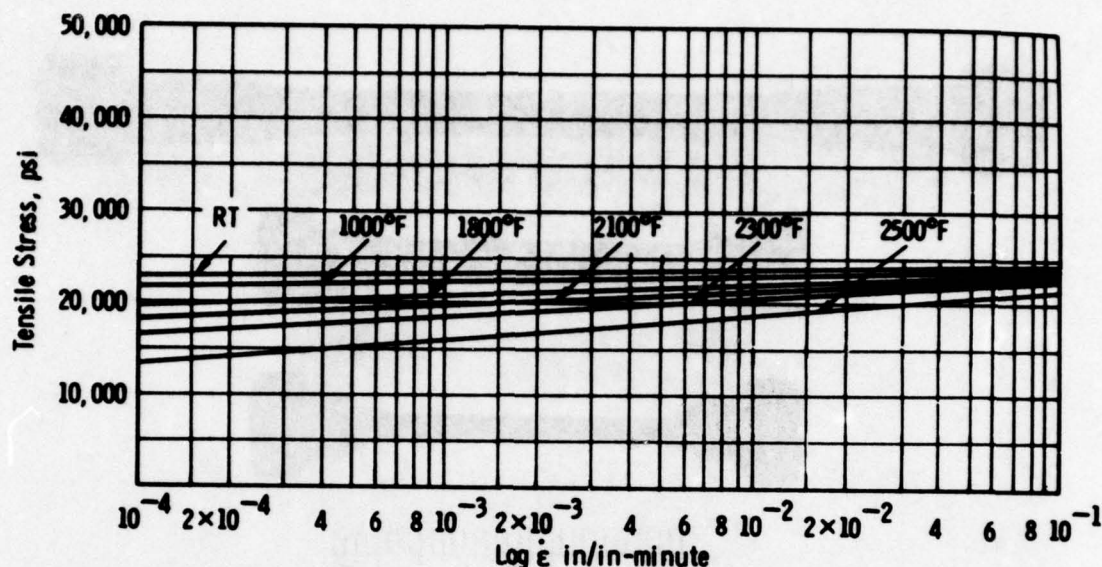
Figure 2-5. The Predicted Tensile Strength of Hot Pressed Si_3N_4 as a
Function of Temperature and Strain Rate - Volume 10.0 in^3

effects were positive, five additional specimens or tests were provided
to complete the statistical requirements. (Strain rate sensitivity was
not observed in either silicon nitride or silicon carbide. Results
could not be differentiated within the scatter of resultant data.) Data
were reduced with respect to ultimate strength, yield if applicable,
stress-strain, elastic modulus and Poisson's ratio. The range of
volumes under stress, in the three tensile specimens employed, was not
sufficiently different to assess size effect (random flaw distribution)
in the tensile mode.

The tensile specimens illustrated in Figure 2-6 are defined in
Figure 2-7. A button-head type was preferred because threaded specimens
are impractical to make from ceramic materials.[3] Grips were made small
to reduce side loading. The 2.25 inch gage length was specified for
modulus measurements to increase the total strain measured to resolvable
limits with high modulus materials. The 0.25 inch gage diameter was
the smallest practical for the direct measurement of Poisson's ratio.
The 0.145 inch gage diameter specimen was reserved specifically for
high temperature ultimate strength measurements where the load bearing
capacity of silicon carbide load train parts was questionable (750 lb
at 2500°F).[3]

Theoretical stress concentrations at the fillet radius were cal-
culated for the 5.50 inch and 3.00 inch specimens: 1.025 and 1.065,
respectively. An elliptical fillet would have reduced the stress con-
centration, but the specimen would have been much more difficult to
machine and finish with the grinding marks in the axial direction. No

15
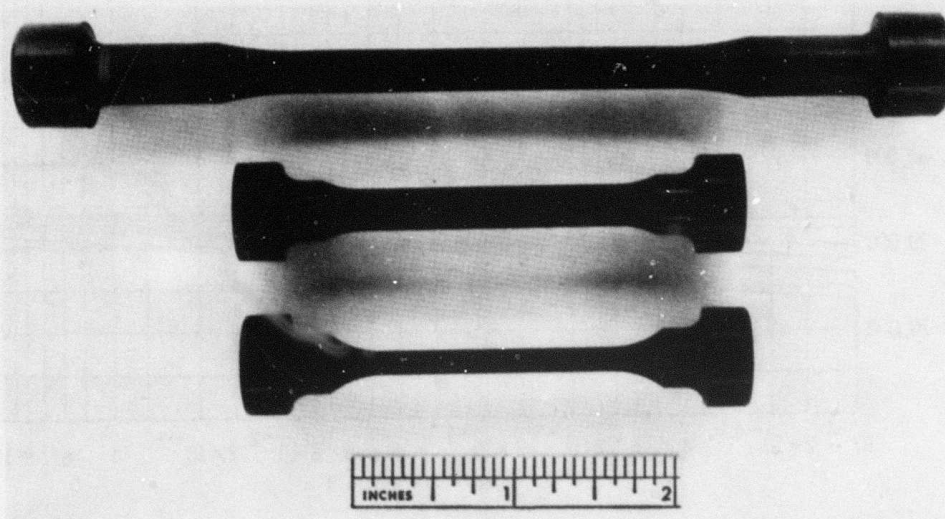
Figure 2-6. Tensile Specimens

All Specimens:
Concentric .0005
Final Finish Axial Grind
with 320 Diamond Wheel
No Undercut on Radii
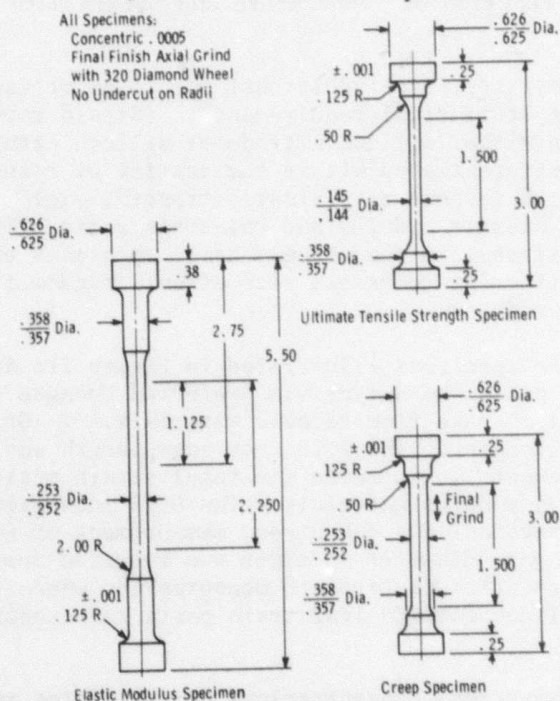
Figure 2-7. Tensile Test Specimen Specifications

16

indication of stress concentration was found at the gage length radius with 0.15-inch gage length strain gages. Stress concentration did not affect the performance of the specimens in any way.

The gripping arrangement for the tensile and tensile creep tests is diagrammed in Figure 2-8.[1] Metal grips, made from Inconel 713C, Mar-M200, or Nicrotung were used up to 2100°F. Above 2100°F, silicon nitride couplings were used with "KT" silicon carbide pull rods.
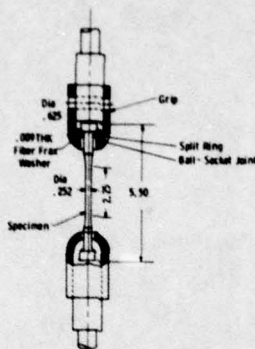
Figure 2-8. Gripping Arrangement for Tensile and Creep Tests

The ceramic couplings were split, two halves held together with a ring. The pull rods were attached to Inconel X750 extensions by a split ring and threaded colar.[4] Three coupling designs were evaluated: (1) an open buttonhead grip with split inserts under the specimen head, (2) a ball-and-socket type made of Nicrotung, and (3) the split ceramic with the ring retainer. Specimen alignment was achieved most quickly with the ceramic type. Superior specimen alignment was not achieved with the ball and socket. It proved difficult to use because friction at the contact surface of the large ball prevented the load train from straightening out under load. Oxidation of the ball surface complicated this problem. While Never-Seez anti-seize compound prevented seizing at surfaces and at threaded connections, it did not improve alignment significantly.

The actual tensile test setup is shown in Figure 2-9. A silicon carbide extensometer was designed to minimize damping and extraneous loads. Proper location was assured by fitting the knife edges of the extensometer into "V" blocks cemented to the specimen at both ends of the gage length (Figure 2-10).

The strain signal for elastic modulus measurement was produced by miniature LVDT's located in each pair of extensometer arms. A two-channel amplifier was used to permit simultaneous recording of the strain measurement with load response from the tensile machine on an x-y recorder. The extensometer met ASTM E83-67 Class B-1 requirements.

17
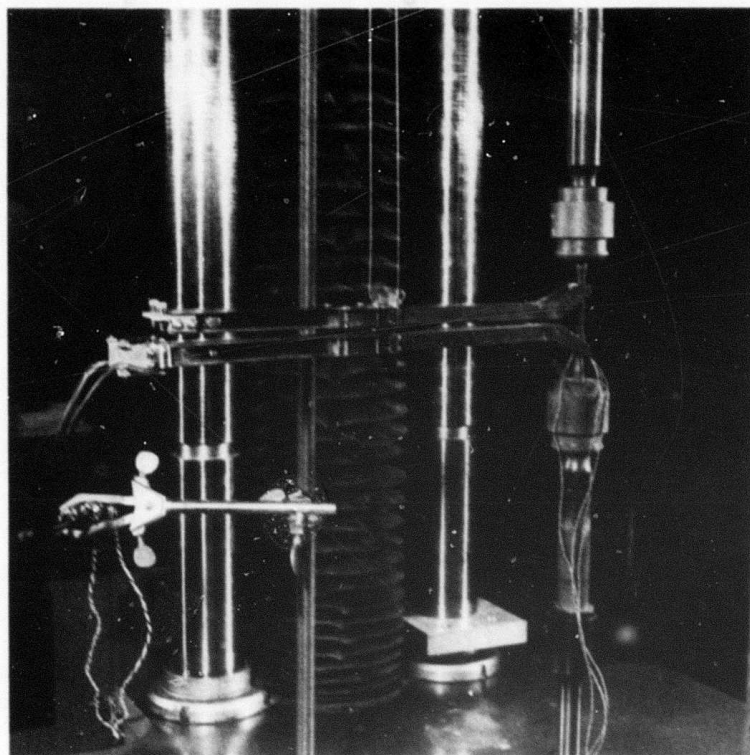
Figure 2-9. Extensometer and Ceramic Grips
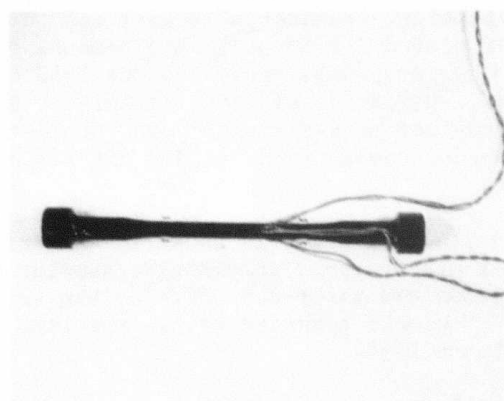
Figure 2-10. Tensile Specimen with Alignment Gages and
Extensometer Attachments

A hinged, platinum-wound, 2800°F resistance furnace was used.[4] This permitted easy attachment of the extensometer through a rectangular opening. Quick checkout of the strain-measuring system was accomplished readily before test.

Fiberfrax or zirconia washers were used to distribute the load uniformly over grip contact areas. Proper axial alignment of the specimen and load train was attained by means of three-point adjustable attachment fixtures at the frame and cross bar of the tensile machine. Adjustments to correct eccentric loading were made with reference to nine strain gages bonded to the specimen in sets of three at both ends and in the middle of the gage section (Figure 2-11). Strain gages within each circumferential array, 120° apart, were made to agree within 2 percent under 50 lb load before tests were started.[4] Once the load train was properly aligned for any series of tests, the six strain gages at the ends of the gage section were not required for accurate specimen alignment. The strain gages burned off at elevated temperatures.
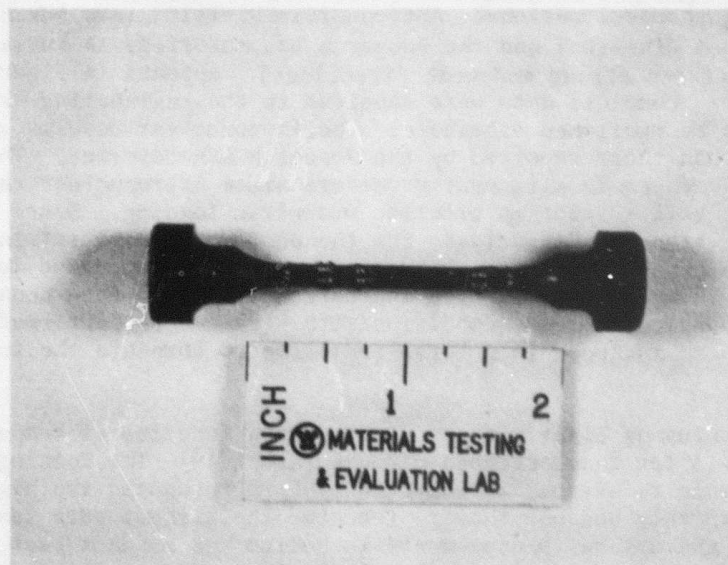
Figure 2-11. Strain Gaged Ultimate Strength Specimen

19

Two types of strain gages were used: Micro Measurements EA-03-500 GB-120 for the 5.50 inch specimens and Micro Measurements EA-06-062 AP-120 for the 3.00 inch specimens. The smaller gages were required on the 3.00 inch specimens because the longer ones could not be bonded to the 0.145 inch diameter section accurately. Considerable difficulty was experienced in attachment. Bond failures occurred with Eastman 910 adhesive. Micro Measurements 610 adhesive cured 2 hours at 300°F was used successfully.[4]

Removal of the specimens from the ceramic grips after testing at 2500°F presented a problem. Silicon dioxide formed on the surfaces of the couplings, bonding all parts together. At times, the retaining ring was heated while the split halves were pressed out to break the entire assembly apart. The ends of the "KT" silicon carbide pull rods released free silicon which collected inside the coupling. This bonded the coupling to the pull rod. The loss of free silicon also degraded the pull rod to the extent that fracture occurred after every fourth test. A load limit of 1250 lb was imposed at 2500°F to minimize pull rod failure.

2.2.3 TENSILE TEST RESULTS

The Tensile Testing of Norton HS130 Silicon Nitride was performed at two Westinghouse locations: Astronuclear Division (now Advanced Energy Systems Division) and the Research Laboratories. A summary of test results (both strong and weak directions) appears in Figure 2-12 and Table 2-2.[6] Complete data were compiled in the Engineering Property Data Base to be published elsewhere. The Astronuclear results generally were lower than those reported by the Research Laboratories. This may reflect differences in alignment procedure since Astronuclear relied solely on dial gage verification to preclude eccentric loading. Since the averages and standard deviations, for the most part, were retained within the envelope of the R&D data, coincident compilation appeared to be justified. There was no positive indication of strain rate sensitivity. Therefore, only three tests/condition/strain rate were performed, and these data were included in a total summation to complete the test requirement.

The modulus of elasticity is plotted as a function of temperature in Figure 2-13 for three methods of measurement.[3] The Corning Glass sonic resonance technique, as reported by Ford, produced the highest values, presumably because they represented the highest rate test. The accuracy of the optical measurements in helium was suspect because of contrast problems. Data obtained mechanically at 0.001 inch/inch/minute were considered most representative because that rate best reflects thermal loading in a stationary gas turbine vane operating in the cyclic mode of peaking-type service.
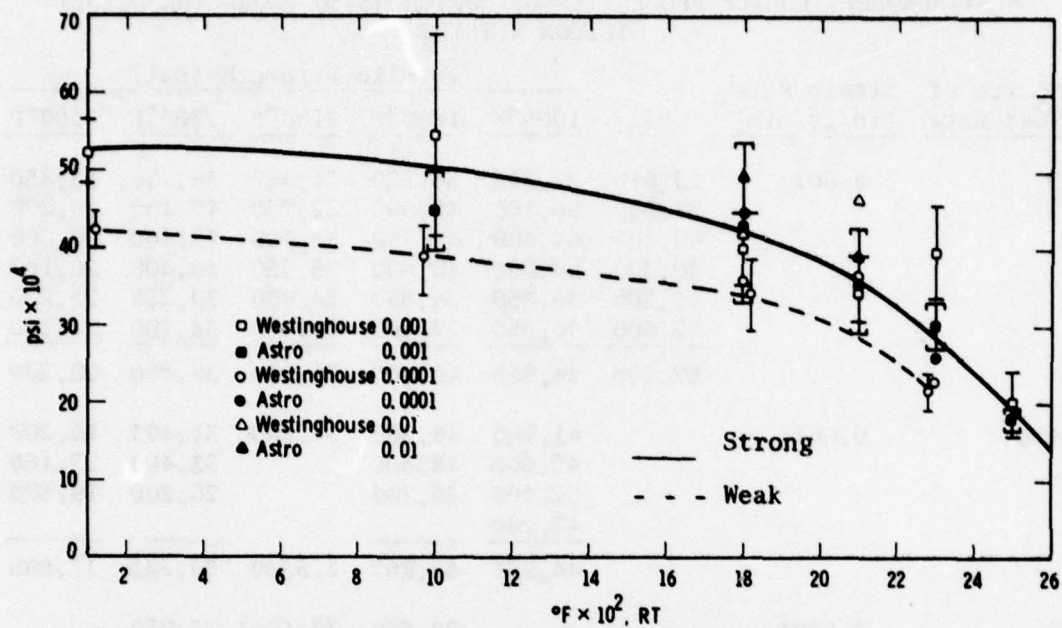
Figure 2-12. The Tensile Strength Properties of Norton HS130 (Noralide NC132) Silicon Nitride as a Function of Temperature
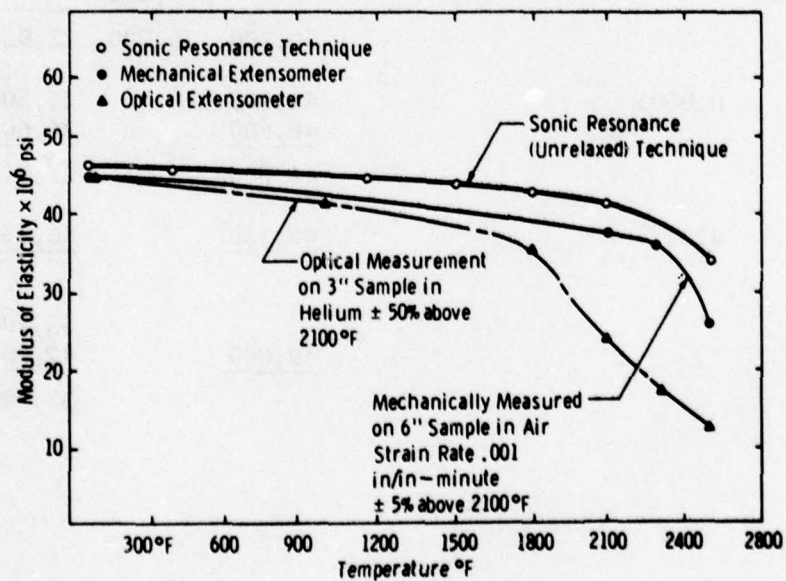
Figure 2-13. The Effect of Temperature on the Elastic Modulus of Norton HS130 (Noralide NC132) Silicon Nitride

21

TABLE 2-2

WESTINGHOUSE TENSILE PROPERTIES OF NORTON HS130 (NORALIDE NC132) SILICON NITRIDE

Source of Test Data	Strain Rate (in/in/min)	Tensile Strength (psi)					
		RT	1000°F	1800°F	2100°F	2300°F	2500°F
R&D	0.001	59,650	72,050	36,550	31,450	36,250	13,450
		54,650	56,100	48,000	32,750	42,100	20,200
		69,800	64,300	42,250	38,900	45,400	20,000
		40,300	60,000	40,800	35,350	46,400	20,100
		46,300	36,850	36,850	34,900	30,250	25,250
		42,600	40,450	37,400	36,000	38,200	22,300
		52,200	54,950	403,00	34,900	39,800	20,200
Astro	0.001		41,500	49,200	35,800	31,400	16,200
			42,600	48,800		33,400	17,400
			52,400	30,900		26,200	19,800
			43,200				
			44,925	42,967	3,5800	30,333	17,800
R&D	0.0001			29,800	39,100	22,950	
				42,600	24,950		
					41,800		
					37,350		
					37,800		
				36,200	36,200	22,950	
Astro	0.0001				41,000	25,500	
					48,600	26,600	
					44,800	27,550	
R&D	0.01				42,550	46,650	
Astro						35,700	
					49,000	42,900	
						39,300	

22

Two other specimens (HS110 material) were stressed to ultimate failure at room temperature.[1] Loading was accomplished incrementally in 10,000 psi sequentially higher steps, with load reduction to 1,000 psi between steps. These tensile data are reported in Table 2-3. While fracture occurred in Si_3N_4-TS-01 during the sixth loading cycle at 59,650 psi, this specimen sustained a total stress of 62,000 psi on the fifth application of load. Specimen Si_3N_4-TS-02 failed during the fifth loading, 2 seconds after maximum stress was reached. All other results were obtained by strain gage measurement and calculation.

TABLE 2-3

SUMMARY OF ROOM TEMPERATURE TENSILE TESTS

Specimen No.	Density (g/cc)	Strain Rate (10^{-4}/ min)	Elastic Modulus (10^6 psi)	Shear Modulus (10^6 psi)	Poisson's Ratio ν	Fracture Stress (psi)
Si_3N_4-TS-01	3.33	6.6	44.2	17.4	0.27	59,650
Si_3N_4-TS-02	3.20	6.6	43.9	17.4	0.26	54,650

(Undesignated Norton Si_3N_4 received July 1971)

Stress-tensile strain and stress-radial strain curves for specimens Si_3N_4-TS-01 of this early test sequence[1] are reproduced as Figures 2-14 and 2-15, respectively. The material exhibited elastic behavior to failure or maximum load at room temperature. Plastic deformation at low strain rates was observed at 1800°F, however.[2] Load-deflection data (Figure 2-16) indicate nonelastic response in HS130 (Noralide NC132) silicon nitride at 2300 and 2500°F at 0.001 in/in/min strain rate.
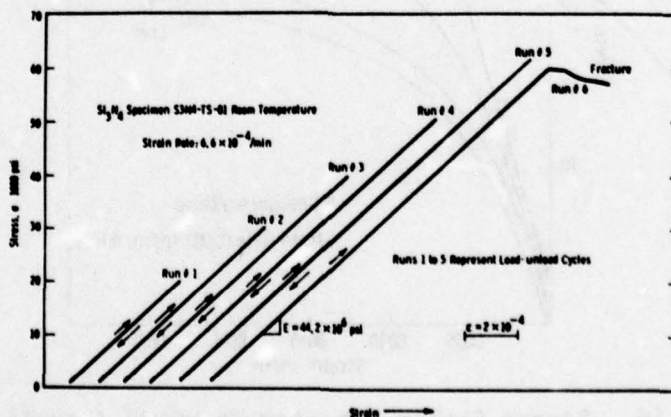
Figure 2-14. Stress-Tensile Strain Curves for Hot Pressed Silicon Nitride (Not Designated by Norton)

23

Figure 2-15 (graph):

Stress, σ 1000 psi

70

60 — Run # 5

50 — Run # 6

— Run # 4

40 — Si_3N_4 Specimen S3N4-TS-01

Room Temperature

— Run # 3

30 — Run # 2

20 — Run # 1

Poisson's Ratio: $\nu = \frac{\xi}{\xi_p} = 0.27$

10

$E_p = 16.5 \times 10^7$ psi $\xi = 4 \times 10^{-5}$

0
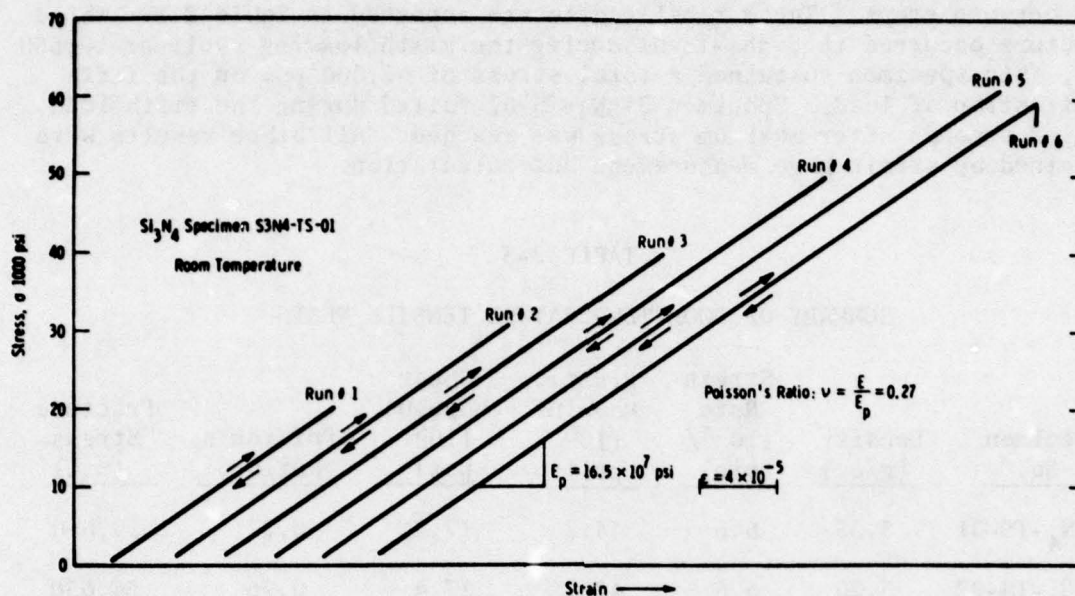
Strain →

Figure 2-15.   Stress-Radial Strain Curves for Hot Pressed
Silicon Nitride (Not Designated by Norton)

Figure 2-16 (graph):

Stress, ksi

35

30 — 2300 °F

25 — 2500 °F High

20 — 2500 °F Avg

2500 °Low

15

10

5

8 Specimens/Temp
Strain Rate 0.001 in/in/min

0005   0010   0015   0020   0025
Strain, in/in
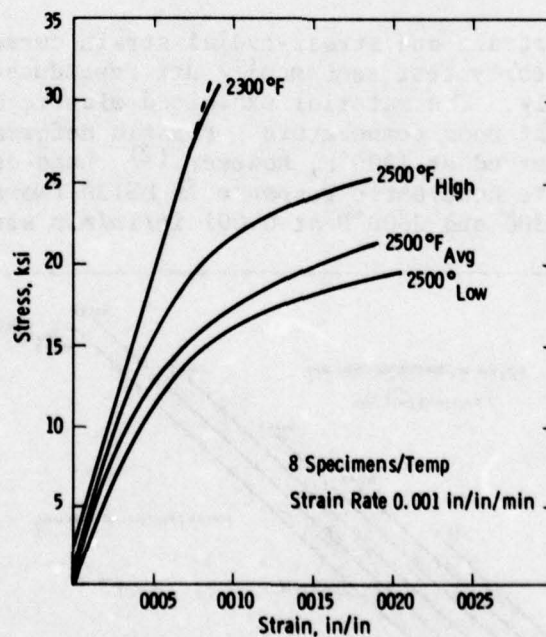
Figure 2-16.   Stress-Strain Behavior in HS130 (Noralide NC132)
Silicon Nitride at Elevated Temperatures

24

While the average tensile properties of Norton hot pressed silicon nitride tend to support the turbine vane application for temperatures up to 2300°F, very little margin of safety is provided. The high standard deviation indicates a high probability of failure. This was confirmed by static rig tests at 2200°F and 2500°F.[5,9,11]

The Tensile Strength of Norton NC203 Silicon Carbide is plotted as a function of temperature in Figure 2-17. Again, all data (Table 2-4) are tabulated as part of the Engineering Property Data Base. The reduction of strength with temperature was almost linear, with some indication of an inflection above 2300°F. These data were obtained from specimens of two different-sizes (1/4 inch dia x 1-1/2 gage length, and 1/4 inch dia x 2-1/2 gage length) at various strain rates between 0.1 and 0.001 inch/inch/minute.[6] No size effect or strain rate sensitivity was detected. A single test point was determined in helium at 2300°F.[2] Failure was consistent with the results obtained in an air atmosphere. The specimens, for the most part, failed within the gage length as shown in Figure 2-18.[4]
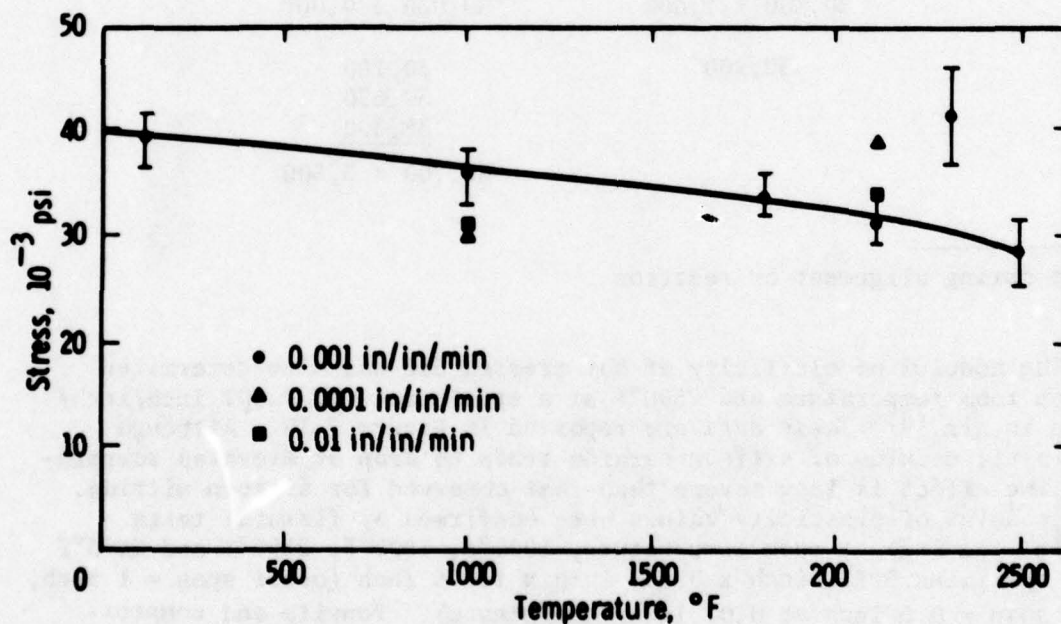
Figure 2-17. The Tensile Strength of Hot Pressed Silicon
Carbide (Noralide NC203)

25

TABLE 2-4

TENSILE PROPERTIES OF NORTON HOT PRESSED SILICON CARBIDE (Noralide NC203)

Strain Rate (in/in/min)	RT (72°F)	1000°F	1800°F	2100°F	2300°F	2500°F
			Tensile Strength (psi)			
0.001	32,200	47,100	35,950	25,450	35,150	28,950
	28,700	43,000	31,750	30,400	52,700	33,150
	45,150	30,100	36,400	28,950	37,800	18,900
	33,600	37,000		36,100	42,70C	*
	35,900	*		32,500	37,600	37,200
		26,250		35,000	41,405	23,900
						24,000
						29,800
	39,100	36,700	34,700	31,400	41,200	28,000
0.0001		29,400		39,150		
		31,250		41,300		
				36,600		
		30,300 ± 1,000		39,000 ± 9,000		
0.01		30,900		30,100		
				32,650		
				38,300		
				33,700 ± 3,500		

*Broke during alignment or reaction

The modulus of elasticity of hot pressed SiC was also determined between room temperature and 2500°F at a strain rate of 0.001 inch/inch/minute in air.[6] These data are reported in Figure 2-19. Although the elastic modulus of silicon carbide tends to drop at elevated temperature, the effect is less severe than that observed for silicon nitride. These modulus of elasticity values were confirmed by flexural tests (4-point loading) at room temperature, 1000°F, 1800°F, 2300°F and 2500°F using specimens 0.125 inch x 0.250 inch x 1.125 inch (outer span = 1 inch, inner span = 0.5 inch at 0.01 inch/inch/minute). Tensile and compressive outer fiber strains were measured with strain gages at room temperature.[1,3,4]

Comparing the two materials with respect to tensile properties, HS130 (Noralide NC132) silicon nitride is clearly superior to silicon carbide (Noralide NC203) at intermediate temperatures where maximum transient tensile stress is expected as a result of shutdown in a turbine application. The lower tensile modulus favors silicon nitride,
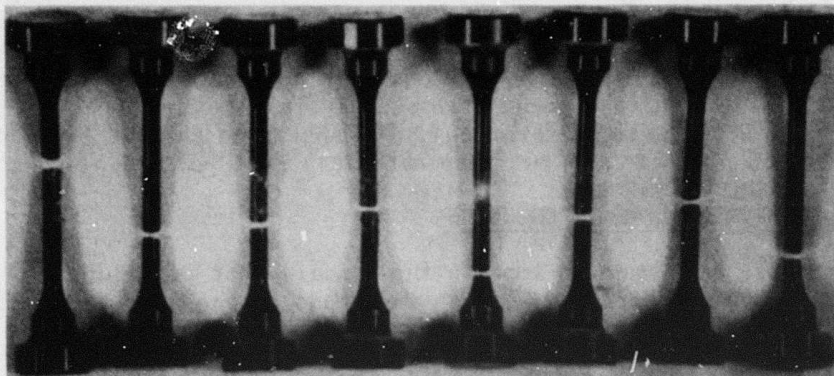
Figure 2-18. Failed Silicon Carbide Tensile Specimens
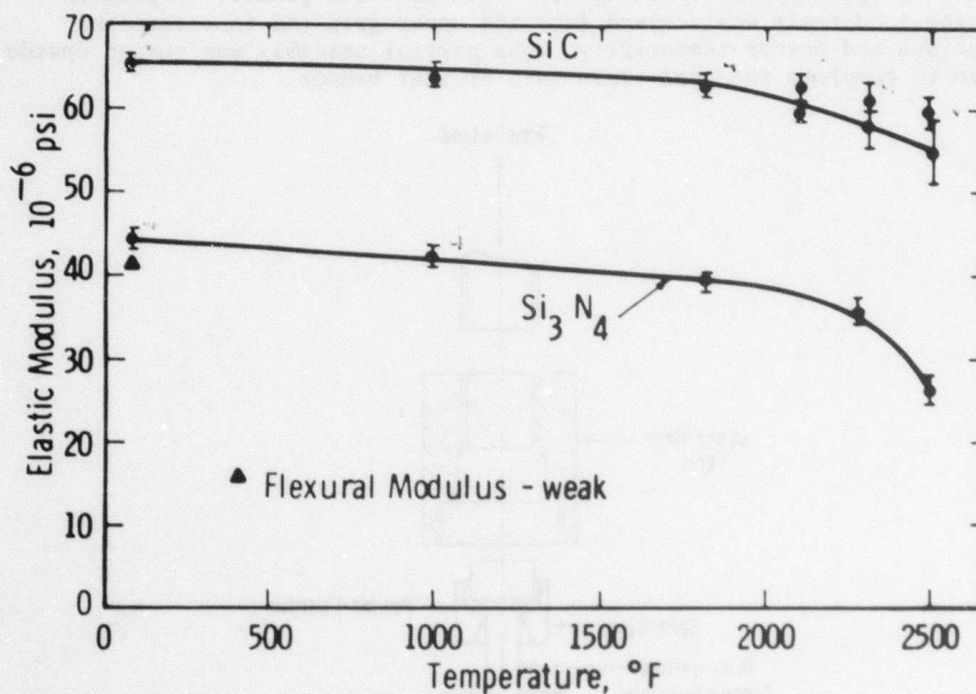
Figure 2-19. The Elastic Modulus of Hot Pressed Silicon
Carbide (Noralide NC203) as a Function of
Temperature Compared with HS130
(Noralide 132) Silicon Nitride

but lower thermal conductivity offsets this advantage completely as demonstrated by finite element stress analysis.[1] The high temperature strength of NC203 silicon carbide would appear to make it the choice for temperatures above 2300°F but vane materials must be strain accommodating.

2.2.4 EXPERIMENTAL TEST PROCEDURE

Attempts were made to improve the tensile test procedure.[8] A powder cushion was employed between the heads of the tensile specimens and each respective grip in an experimental method that was self-aligning. The gripping arrangement is illustrated in Figure 2-20 The split-seat was a diametric, split cylinder with a well for powder at one end and a tapered hole to center the specimen and contain the powder at the other.

Assembly was accomplished by slipping the lower grip over the button head of the specimen with the split-seat placed within the grip end. An eye dropper served to fill the well with powder. A portion of the load train was screwed into the upper-grip end to secure the specimen and powder temporarily. The partial assembly was turned upside down to complete the load train in a similar manner.
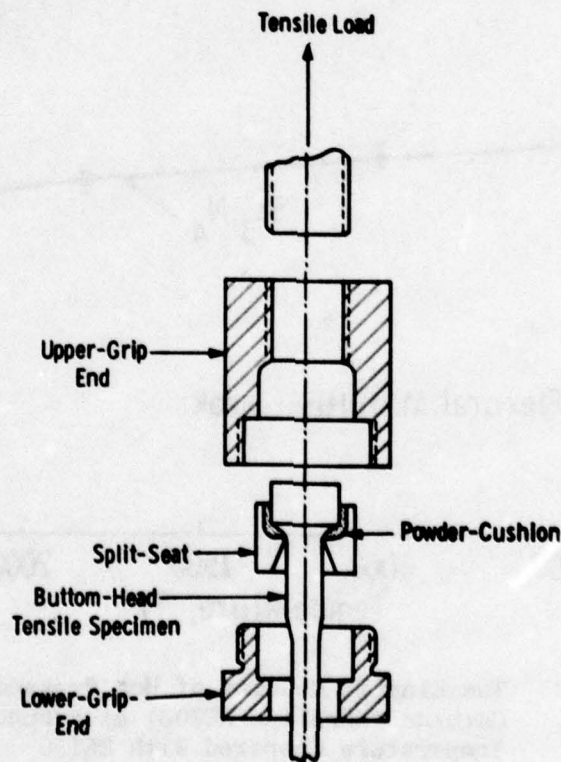
Figure 2-20. Powder Cushion Tensile Test

An instrumented steel specimen was used to demonstrate the technique initially at room temperature. Loads were applied in 100-lb increments to 500 lb and in 500-lb increments to 1500 lb. Tests were performed by two different operators using two different Satec universal testing machines. Eight powders were evaluated (Table 2-5).

TABLE 2-5

DESCRIPTION OF POWDERS

Powder	Internal Code	Description (Particle Size, etc.)
Nickel	Ni	Spherical particles, average 20 μm dia
Silicon Carbide	SiC-280	Average 44 m
Silicon Carbide	SiC-1500	Average 9 m
Silicon Carbide	SiC-EK	Average 5 m
Silicon Carbide	SiC-PPG	submicron, 15 m^2/g
Tungsten Diselenide	WSe$_2$	- 100 mesh
Boron Nitride	BN	- 325 mesh
Graphite	G	- 325 mesh

A vector analysis was used to define the resultant strain for each set of three strain gages. The amount of misalignment at each set of gages was calculated by dividing the absolute value of the resultant strain by the average strain of the three gages:

$$\% \text{ misalignment} = \frac{100x \sqrt{\varepsilon_1^2 + \varepsilon_2^2 + \varepsilon_3^2 - (\varepsilon_1\varepsilon_2 + \varepsilon_1\varepsilon_3 + \varepsilon_2\varepsilon_3)}}{1/3 (\varepsilon_1 + \varepsilon_2 + \varepsilon_3)}$$

A measure of the stress nonuniformity within the specimen's gage length was obtained at each load increment by dividing the difference between the highest and lowest values ($\varepsilon_H - \varepsilon_L$) of the nine strain gages by their average value (ε_{AV}):

$$\% \text{ nonuniformity} = \frac{\varepsilon_H - \varepsilon_L}{\varepsilon_{AV}} \times 100$$

29

Powders of a lubricating type such as graphite, boron nitride, molybdenum disulfide and tungsten diselenide were preferred. Particle size and distribution, material compliance and deformability appeared important to performance.

Graphite and boron nitride formed the most effective powder cushions, with graphite considered superior to boron nitride. Figure 2-21 a,b and c and Figure 2-22 a,b and c report the results of eight experiments with graphite and three experiments with boron nitride respectively. Error bars indicate the highest and lowest values obtained. Closed circles represent mean values. Six other powders are compared in Table 2-6.

In general, the percentage misalignment and the percentage stress nonuniformity decreased with increasing load. For most cases, loads <500 lb (corresponding to <10,000 psi) produced poor alignments. The shaded areas in Figures 2-21 and 2-22 represent the range of graphite and boron nitride powders, respectively. Because nine strain gages were considered in the analysis of stress uniformity, the stress nonuniformity appeared to be higher than the relative misalignment indications at each gage section. Better alignments and less data scatter were obtained in the center of the gage length than at the ends. A correlation between the resultant strain vectors at each of the three gage sections showed that the axes of most specimens were parallel to but not perfectly concentric with the loading axis.
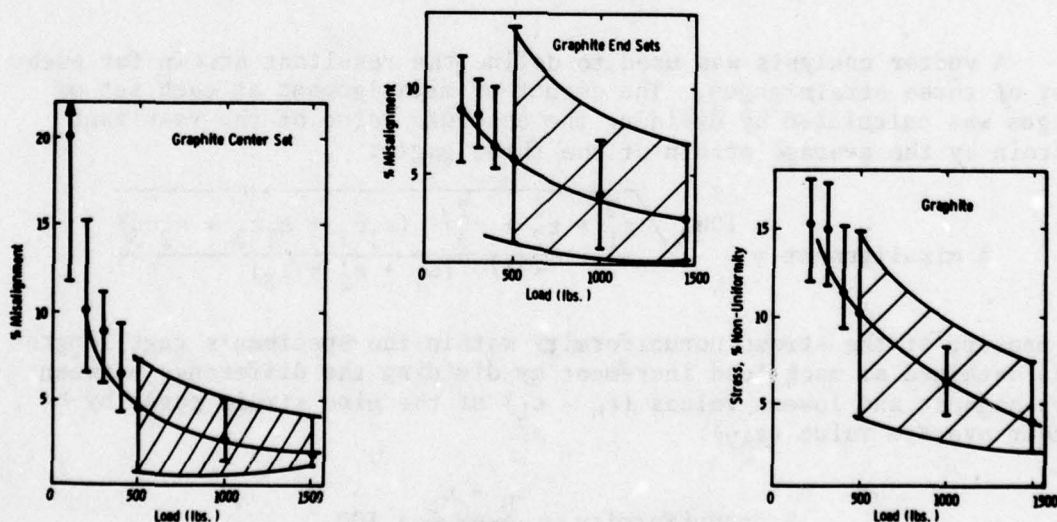
Figure 2-21. Effect of Graphite Powder in Powder Cushion Tensile Test
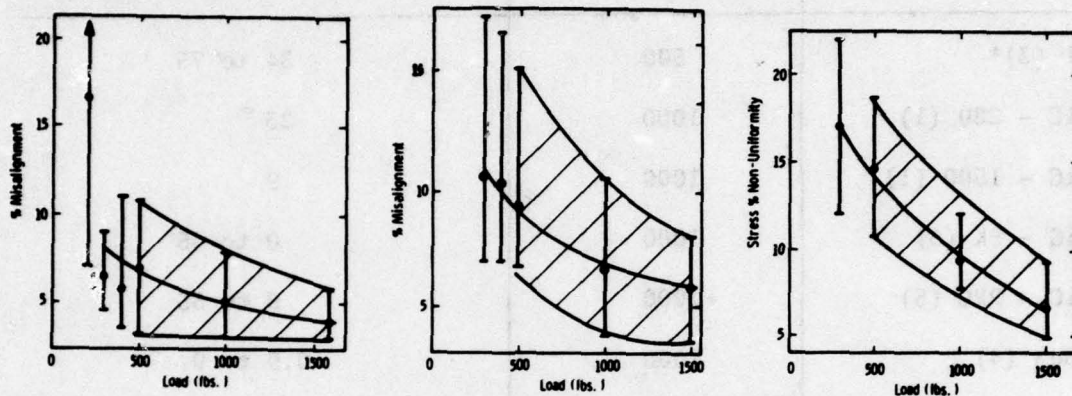
Figure 2-22. Boron Nitride Powder Performance in Powder
Cushion Tensile Test

The powder cushion technique represented a significant improvement
in tensile testing procedure because it required very little effort to
obtain acceptable load train alignment. Cost was reduced because strain
gages were eliminated. The need for precision machining of specimens
was removed in all areas except the gage sections and fillet areas.
Alignment within 3 percent was achieved. This reduced bending stresses
to levels below 1500 psi to produce an accuracy of ± 3500 psi for the
method.

31

TABLE 2-6

POWDER PERFORMANCE IN UNIAXIAL TENSILE TESTS

Powder	Load (lb)	Misalignment at Center (%)
Ni (3)*	500	34 to 75
SiC - 280 (1)	1000	23
SiC - 1500 (1)	1000	9
SiC - EK (6)	1000	0 to 45
SiC - PPG (5)	1000	9 to 55
WSe_2 (4)	1000	0.9 to 9

*( ) indicates number of tests

2.3 THE FLEXURAL PROPERTIES OF HOT PRESSED SILICON NITRIDE (NORTON HS130, NORALIDE NC132) AND HOT PRESSED SILICON CARBIDE (NORTON NORALIDE NC203)

2.3.1 THE TEST PROGRAM

The assessment of the flexural strength properties of hot pressed silicon nitride (Norton HS130 - Noralide NC132) and hot pressed silicon carbide (Norton Noralide NC203) from room temperature to 2500°F represented the nucleus of the test program to provide engineering property data for the design and performance analysis of ceramic stator vanes. Without a valid engineering property data base, a simulation of rotor blade perform- ance would have remained impossible.

In the flexural test mode it was possible to test a large number of specimens at specified temperatures within a temperature range. Test specimens are simple and therefore relatively inexpensive and easy to machine. The test setup and procedures are qualified under ASTM Standards and are well established in most laboratories with some custom modifica- tions and revisions indicated for temperatures above 2000°F.

Well over 200 silicon nitride test specimens were stressed to failure under conditions of 4-point loading from room temperature to 2500°F. Cross head motion or strain rate was varied between 0.2 and 0.0002 inch/min to provide an indication of strain rate sensitivity for samples which ranged in size from 1-1/8 x 1/8 x 1/8 inch to 6 x 1/2 x 1/4 inch. The number of silicon carbide specimens tested exceeded 150 before this work was discontinued following the catastrophic failure of the material tested as stator vanes in the first series of static rig tests at 2500°F.[7]

Ten repetitions per condition were specified with a minimum of 20 required where the population was developed to ascertain appropriate Weibull parameters. Particular attention was paid to billet to billet variability as described by the Weibull modulus so that statistical inference from flexural test data could be ascribed to the other test modes, i.e., tensile and shear, where statistical minimums only were maintained. Once the statistical characterization of a larger population was accomplished, transfer of that assessment in terms of standard deviation, failure probability and reliability appeared justifiable when comparisons and correlations proved favorable.

While the correlation of tensile strength and flexural properties was never fully substantiated, the only measure of tensile strength in the weak direction of hot pressed silicon nitride came from a Weibull analysis of the flexural data. Representative tensile test specimens could not be machined because of limited billet thickness: 1.25 to 1.30 inches. Miniature samples are always suspect because they are difficult to handle in specialized test setups.

33

2.3.2 THE TEST METHOD

Flexural testing for the most part was conducted under conditions of four-point loading in air, using an Instron machine equipped with a Centorr high temperature furnace.[1] Although initial measurements[1] were made with specimens 0.250 x 0.125 x 1.375 inch, ground longitudinally with a 200 grit diamond wheel on the tensile surface only, and employing maximum (outer) and minimum (inner) span distances of 1.0 and 0.5 inch, respectively,[1] the test specification was written for 0.250 x 0.125 x 1.125 ± 0.002 inch (width and height only) ground longitudinally on all four major surfaces with a 325 grit diamond wheel.[3] Sharp 90° corners were specified. Inner and outer span distances were designated at 0.875 and 0.375 inch, respectively, using a silicon nitride loading fixture with triangular knife edges (Figure 2-23).[3]

Figure 2-23. Si_3N_4 Flexural Test Fixture

The test matrix (Table 2-7)[3] was designed to develop data at a 0.95 confidence level from a minimum of 10 specimens per condition with a statistical evaluation of all accumulated data expected to define data deficiencies. Strain rates of 0.2, 0.02, 0.002, and 0.0002 inch/minute were actually employed over a test temperature range from RT (68°F) to 2550°F with intermediate points at 500, 1000, 1800, 2100, 2300, 2350 and 2500°F inclusively. Room temperature tests were run with strain gaged specimens in many instances to provide accurate measurement of elastic modulus.

Table 2-7

FLEXURAL FAILURE TEST MATRIX
(Tests/Billet on 10 Billets of 40)
Cross Rate (in/min)

Temperature (°F)	0.02[1]	0.002	0.0002[1]	Directions
RT	5	20[2]	5	2[3]
1000		10		strong
1800		10	5	2
2100		10		strong
2300		20[2]	5	2
2500		10		

1. Strain rate effects to be determined on three billets only.
2. To provide Weibull modulus for first billet at 0.90 confidence level.
3. Strong direction ⊥ to hot press, weak // to hot press direction.

NOTE: Weibull modulus in both directions was determined across ten billets from data provided at 0.99 confidence level.

In the specific case of large specimens tested in the beam and plate orientation to assess size and other geometric effects with respect to area and volume under stress, a special "Glo Bar" resistance heated furnace, oversized silicon nitride loading fixture and Universal test machine were employed.[5] Test specimen sizes included the following:

- 0.25 x 0.125 x 1.50 inches
- 0.25 x 0.50 x 1.50 inches
- 0.25 x 0.50 x 3.00 inches
- 0.25 x 0.50 x 4.50 inches
- 0.25 x 0.50 x 6.00 inches

tested under four-point, quarter-point loading at 0.002 inch/minute cross head motion. (See Table 2-8, page 52 for data.)

The sharp cornered specimen specification was inadvertently changed to include hand beveled corners well into the test program. Segregated results indicated a slightly higher average strength and larger standard deviation for the population with sharp corners. All results were assembled into a single data base, however.

2.3.3 SILICON NITRIDE FLEXURAL TEST RESULTS

Initial test measurements indicated an average room temperature flexural strength of 98,800 psi ± 6 percent (strong direction-normal to the hot pressing direction) for the first lot of hot-pressed silicon nitride supplied by Norton. This compared favorably with the mean value of 109,570 psi ± 8 percent reported by Norton using three-point loading.[1] Strength decreased with temperature from 74,900 psi ± 4 percent (room temperature - weak direction) to 54,000 psi ± 7 percent (1800°F) to 16,700 psi ± 11 percent (2550°F).

Remarkable improvements were made in the material over the life of the contract. A significant increase in the high temperature strength was demonstrated in the early billets of HS130 silicon nitride as shown by Figure 2-24 where HS130 is compared to HS110 with respect to weak direction flexural strength.[2] Anisotropy in the properties of hot pressed silicon nitride is illustrated in Figure 2-25 where strength versus temperature is plotted for the strong as well as weak directions of HS130. This characteristic persisted in any and all improved versions of the material and is considered inherent in the hot press densification process.

Strain or stress rate sensitivity was recognized in all forms of hot pressed silicon nitride tested, especially at elevated temperatures[2] as shown in Figure 2-26 where flexural strength varies directly with loading rate for specimens tested at 1800°F and above. At temperatures
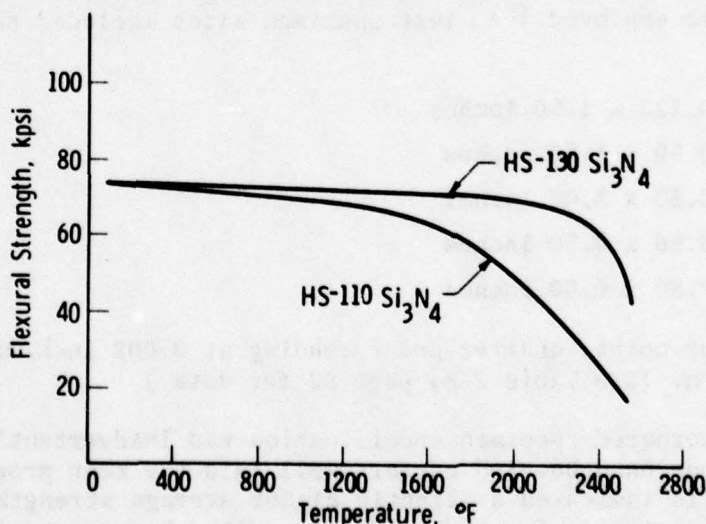
Figure 2-24. Strength versus Temperature for Norton Hot
Pressed Si_3N_4 (HS110 and HS130)

36
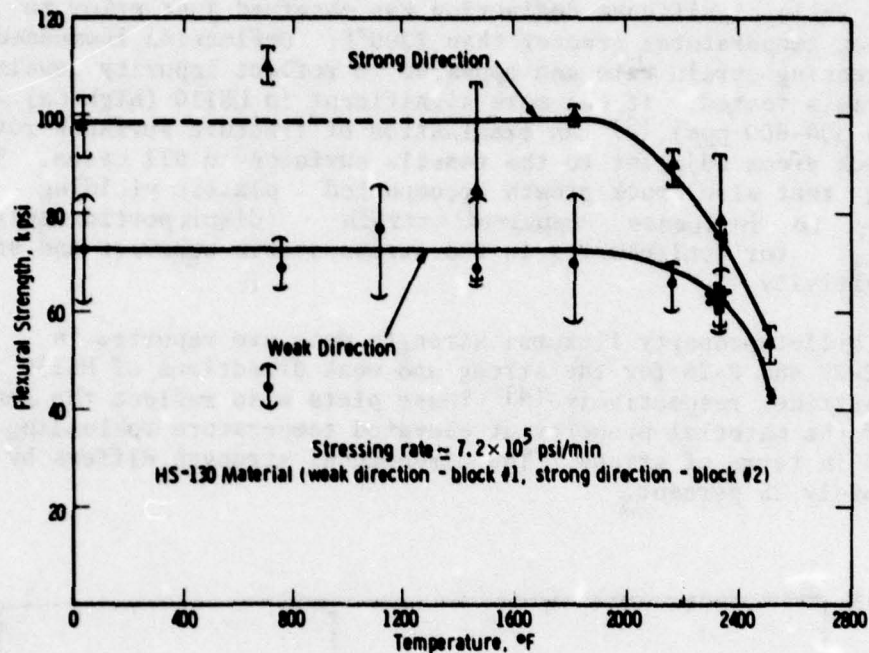
Figure 2-25. Strength versus Temperature for the Weak and Strong Directions of HS130 Si₃N4
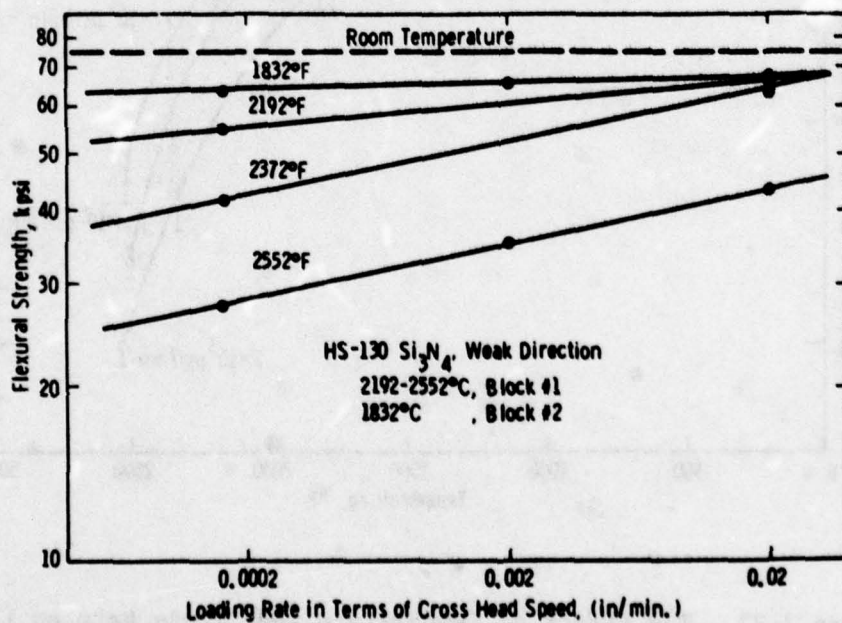
Figure 2-26. Log Plot of Strength versus Loading Rate at Various Temperatures (HS130 Si₃N₄)

37

below 2300°F, load deflection curves remained linear or elastic to fracture, while significant deflection was observed just prior to fracture at temperatures greater than 2300°F. Deflection increased with decreasing strain rate and appeared to reflect impurity levels in the materials tested. It was more significant in HS110 (high Ca) than in HS130 (Ca 300-800 ppm).[2] An examination of fracture surfaces revealed rough crack areas adjacent to the tensile surfaces in all cases. This indicated that slow crack growth accompanied plastic yielding or creep to influence apparent strain disproportionately thus accounting for nonlinearity in the stress-strain behavior and strain rate sensitivity.

The billet property flexural strength data are reported in Figures 2-27 and 2-28 for the strong and weak directions of HS130 silicon nitride, respectively.[4] These plots also reflect the sensitivity of the material property at elevated temperature to loading rate expressed in terms of stress. The directional strength differs by approximately 25 percent.
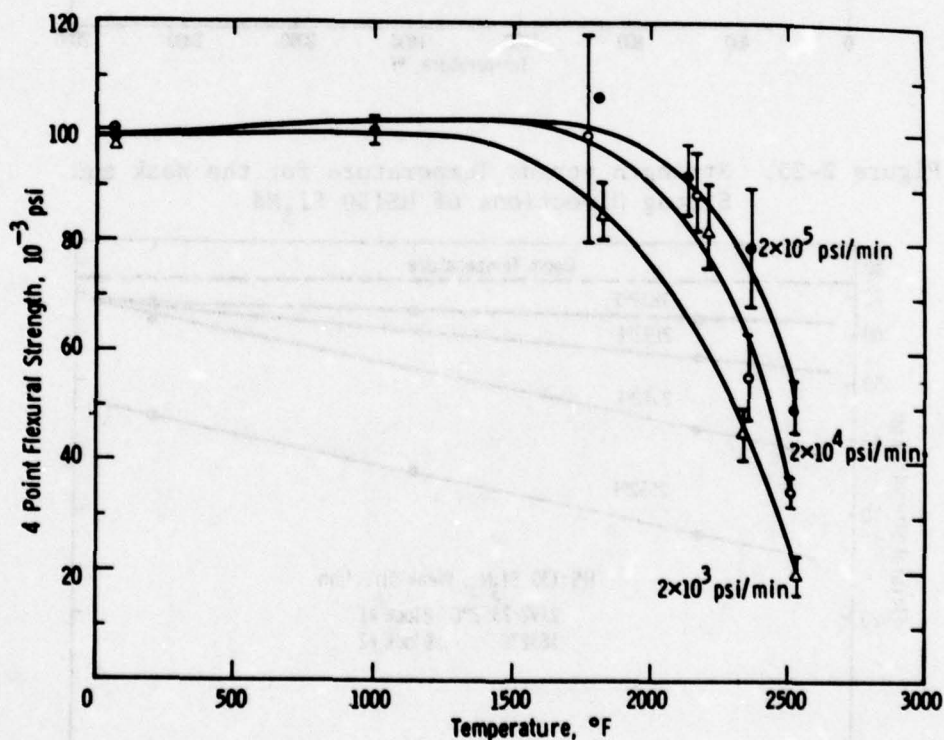
Figure 2-27. The Effect of Temperature and Stress Rate on the Flexural Strength of Norton HS130 Silicon Nitride (Strong/Perpendicular to Hot Press Direction)
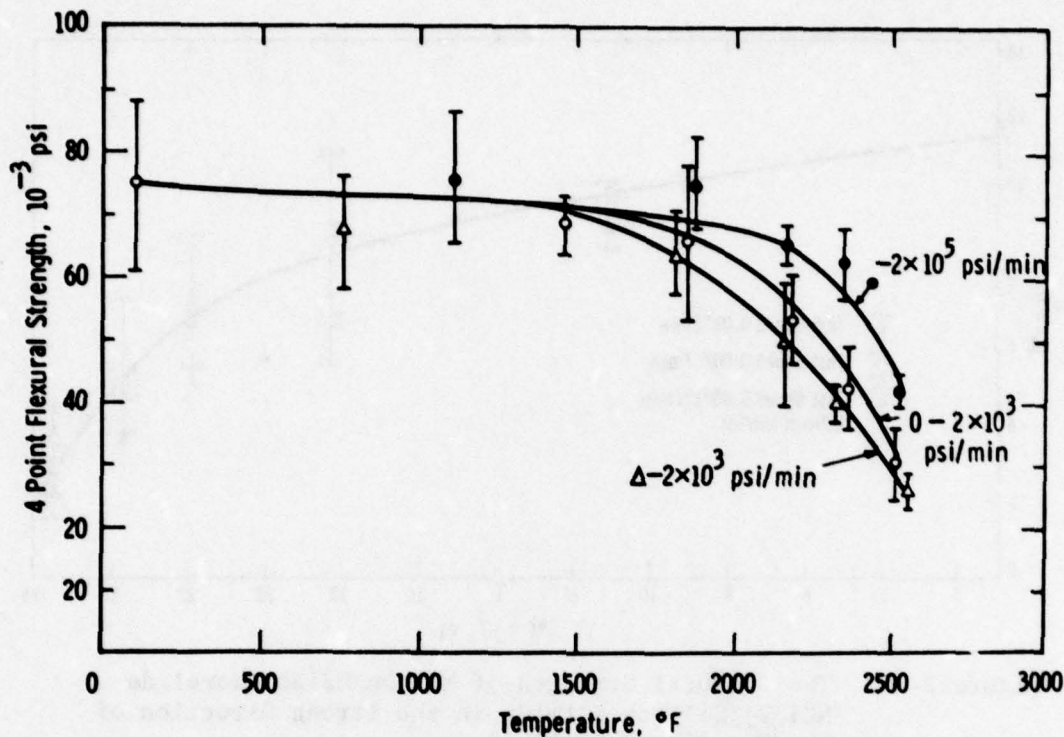
Figure 2-28. The Effect of Temperature and Stress Rate on the
Flexural Strength of Norton HS130 Silicon Nitride
(Weak/Parallel to Hot Pressing Direction)

The summary flexural strength properties of Norton HS130 (Noralide
NC132) appear in Figures 2-29 (strong) and 2-30 (weak). These data
incorporate the billet data with all available determinations on remnant
vane material to provide a comprehensive description of the basic
property. There appears to be a 40 percent difference between the
strong and weak directions of the material. The effect diminishes to
approximately 8 percent at 2300°F and seems to reverse at 2550°F. This
phenomenon must be attributed peculiarly to wide billet to billet
variability. The scatter of data on a billet to billet basis is widely
divergent, as indicated in Figure 2-31. There is clearly a need for
better reproducibility in billet manufacture.

The trend was toward higher strength as Norton produced a better
hot pressed silicon nitride product with time. Strength decreasing
defects, i.e., high and low density inclusions, common in early HS130
silicon nitride, were virtually eliminated in the remnant vane material
designated Noralide NC132. Whether or not anisotropy increased
significantly remains a question because it is difficult to account for
lower strength in the weak direction other than to attribute it to
billet variability and higher standard deviation of the billets.

39
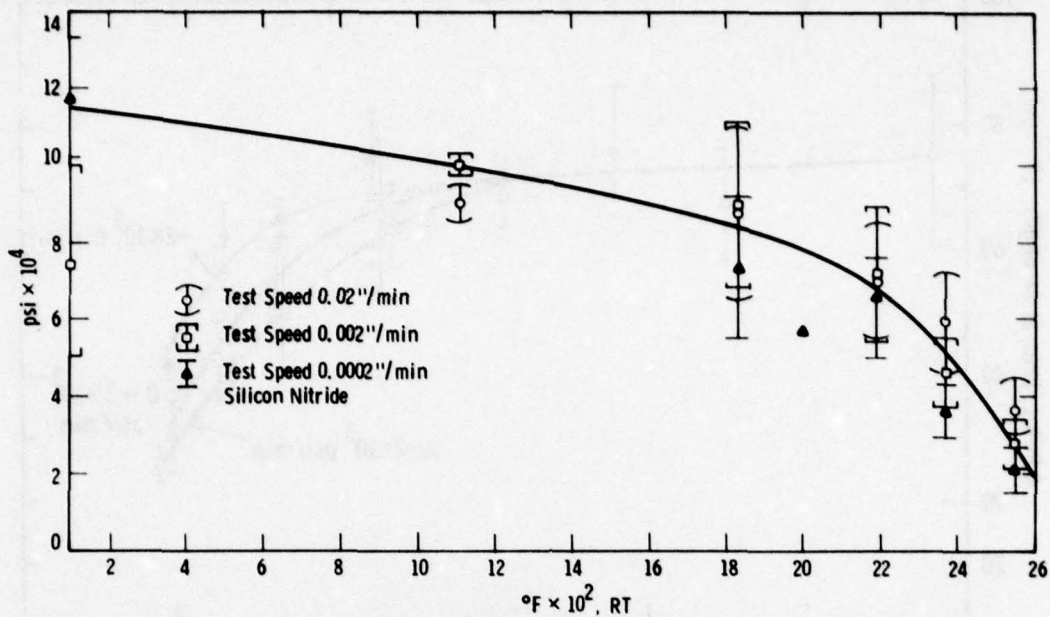
Figure 2-29. The Flexural Strength of Norton HS130 (Noralide
NC132) Silicon Nitride in the Strong Direction of
the Material (All Data)
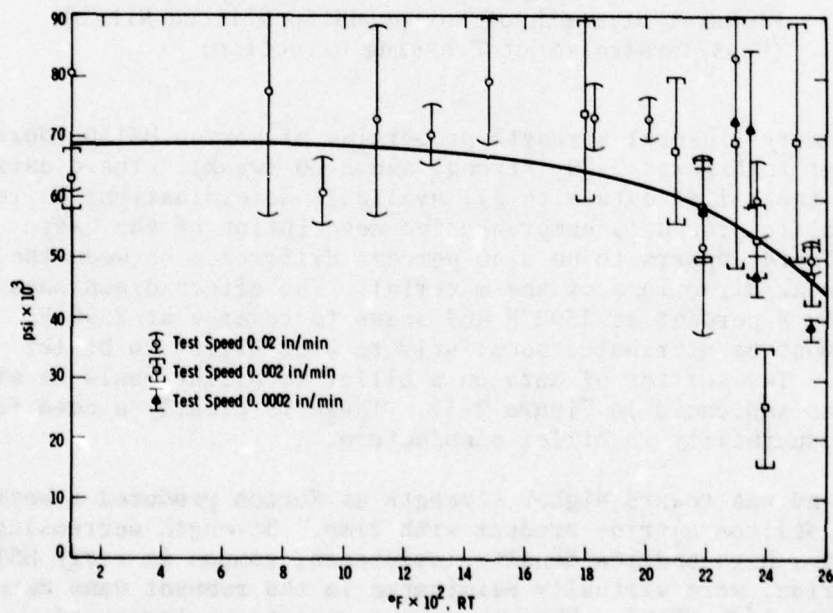
Figure 2-30. The Flexural Strength of Norton HS130 (Noralide
NC132) Silicon Nitride in the Weak Direction of
the Material (All Data)
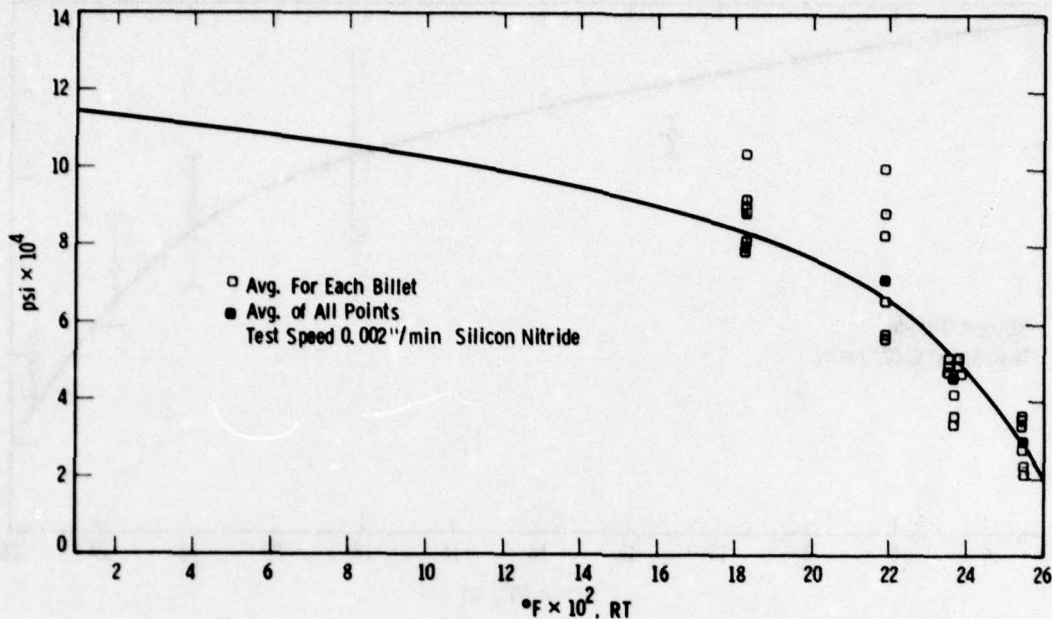
Figure 2-31.   Billet to Billet Variations of Flexural Strength
of Norton HS130 (Noralide NC132) Silicon Nitride
in the Strong Direction

The effect of strain rate sensitivity is diluted somewhat when
properties are averaged across billets and remnant material to define
the properties of a class of materials. These data are plotted for the
strong direction of Norton HS130 (Noralide NC132) in Figures 2-32, 2-33
and 2-34 for strain rates of 0.02, 0.002 and 0.0002, respectively.
Similar curves exist for the material in its weak direction. All data
and representations of that data are available in the Engineering Property
Data Base to be published by AMMRC independently sometime in the future.

2.3.4   SILICON CARBIDE FLEXURAL TEST RESULTS

Early in 1972 Norton produced a hot pressed silicon carbide material
worthy of consideration as a stator vane material. Flexural test specimens
of 0.125 x 0.250 x 2.0 inch size were prepared from 0.5 x 3.0 x 3.0 inch
blocks purchased from Norton for comparison with specimens purchased
directly from Norton.

The average strength of specimens prepared by Norton (320 grit
diamond ground) tested at Westinghouse in four-point bending was
100,900 ± 12 percent psi (four tests) as compared to 72,000 ± 13 percent
(4 tests) for specimens prepared by Westinghouse (220 grit diamond ground).
These preliminary data indicated that the strength of silicon carbide was
sensitive to surface finish.[2]

41
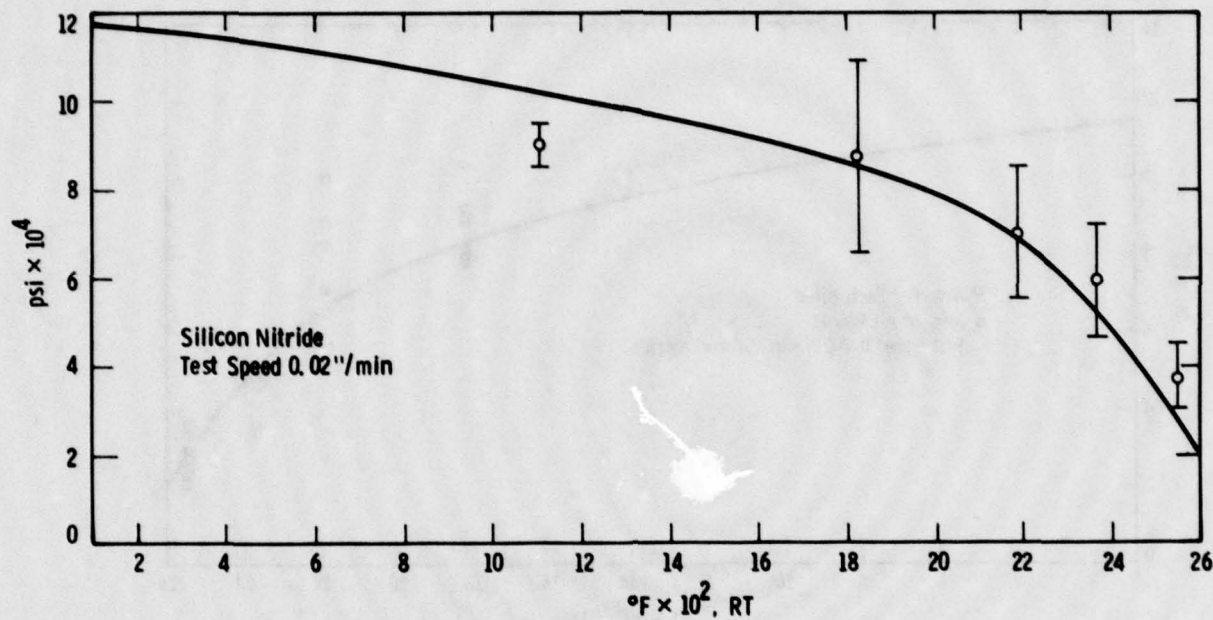
Figure 2-32. The Flexural Strength of Norton HS130 (Noralide
NC132) Silicon Nitride - Strong Direction, Strain
Rate 0.02 in/min Cross Head Motion
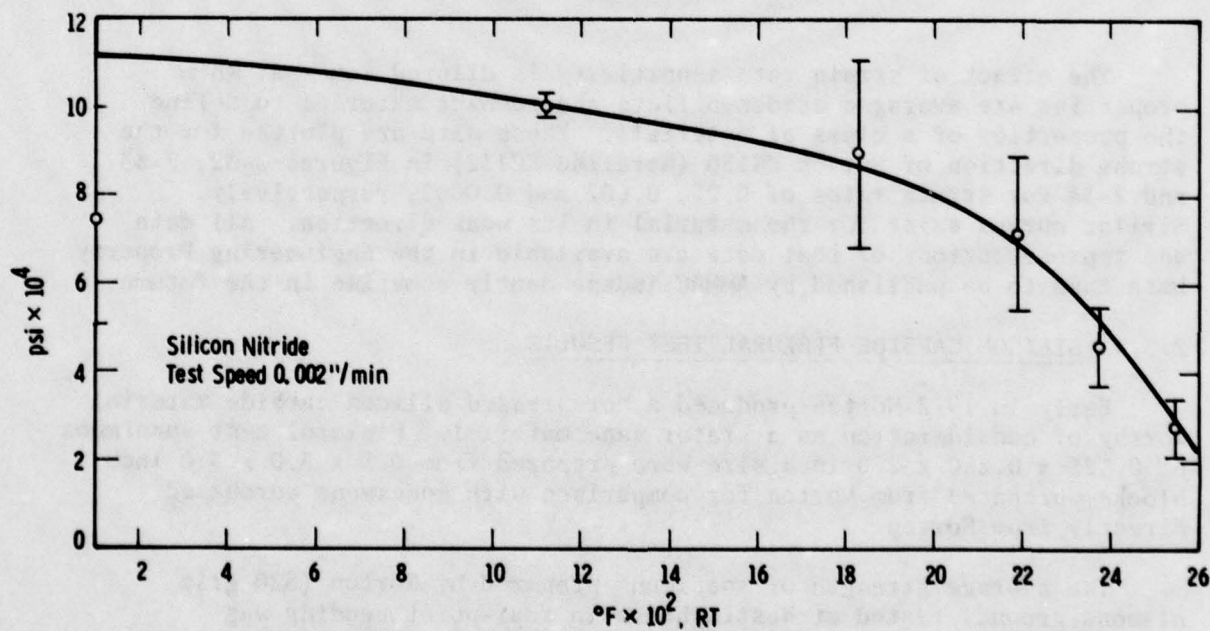
Figure 2-33. The Flexural Strength of Norton HS130 (Noralide
NC132) Silicon Nitride - Strong Direction, Strain
Rate 0.002 in/min Cross Head Motion

42
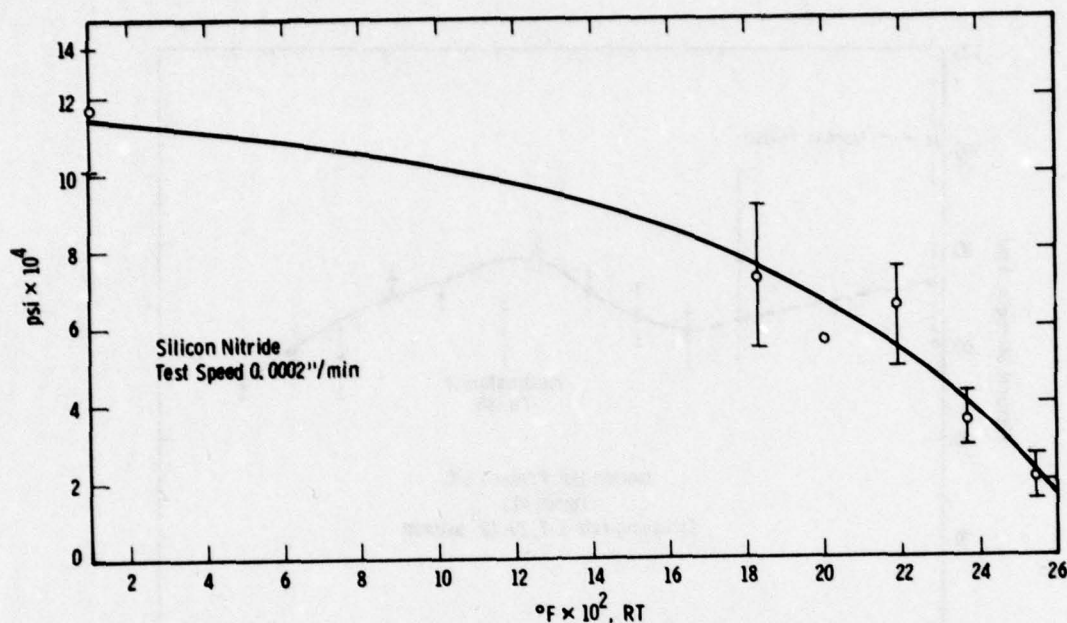
Figure 2-34.   The Flexural Strength of Norton HS130 (Noralide
NC132) Silicon Nitride - Strong Direction, Strain
Rate 0.0002 in/min Cross Head Motion

The flexural strength of this prototype silicon carbide material as
a function of temperature is presented in Figure 2-35. Too few tests
were performed to comment upon the minimum strength that occurred at
~800°F. The decrease in strength observed at temperatures above 1800°F
was significant. No strain rate sensitivity was detected in single
specimen tests at 2300°F in the range 0.2 - 0.0002 in/min cross head
speed.

Weibull statistical parameters were determined at 2372°F at a
cross head rate of 0.002 in/min for 20 specimens. A Weibull modulus,
m = 12.6 with normal stress, σ_o = 33,200 psi, indicated that the silicon
carbide tested was somewhat less volume sensitive than silicon nitride.[2]

Three 9 inch diameter x 1.30 inch thick billets were used to determine
the properties of Norton Noralide NC203 silicon carbide. The flexural
strength of the billet material as a function of temperature is reported
in Figure 2-36. Specimens were cut parallel and perpendicular to the hot
pressing direction but no significant indication of anisotropy was
detected.[4] There was a trend toward strain rate sensitivity, however,
as shown in Figure 2-37.[4] The slopes of the straight line data at
2290, 2370, and 2550°F, i.e., 0.0454, 0.0566 and 0.043, respectively,
indicated that silicon carbide was less susceptable to subcritical crack
growth than silicon nitride.[4]

43
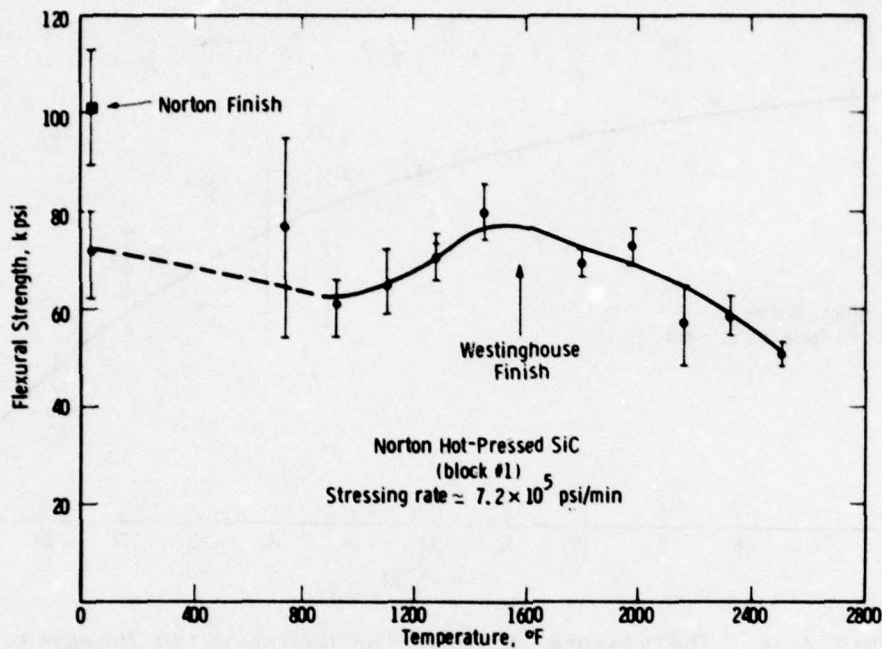
Figure 2-35. The Flexural Strength of Norton Hot Pressed SiC
(Prototype Material)
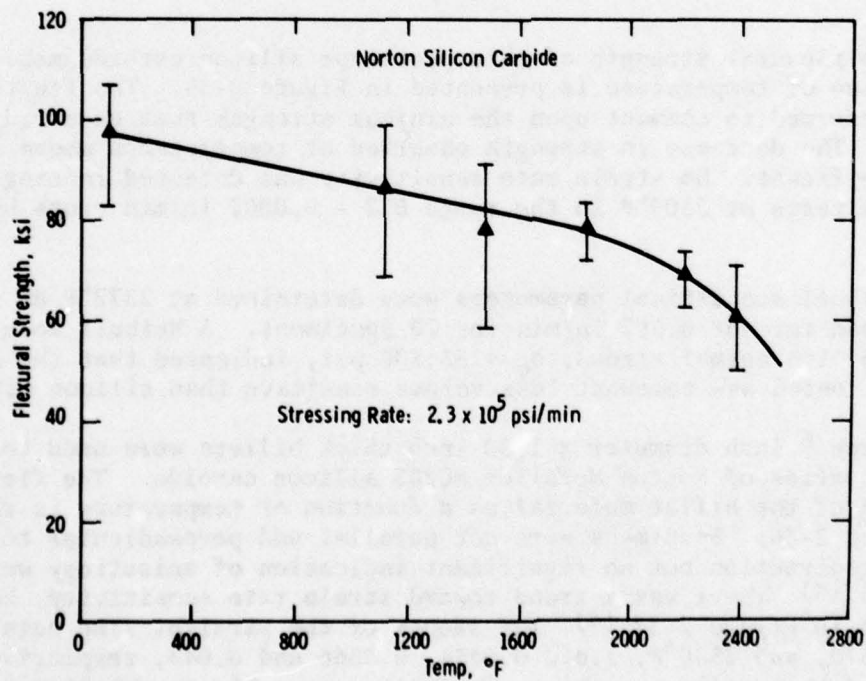
Figure 2-36. The Effect of Temperature on the Flexural Strength
of Norton Hot Pressed Silicon Carbide (Noralide NC203)

44
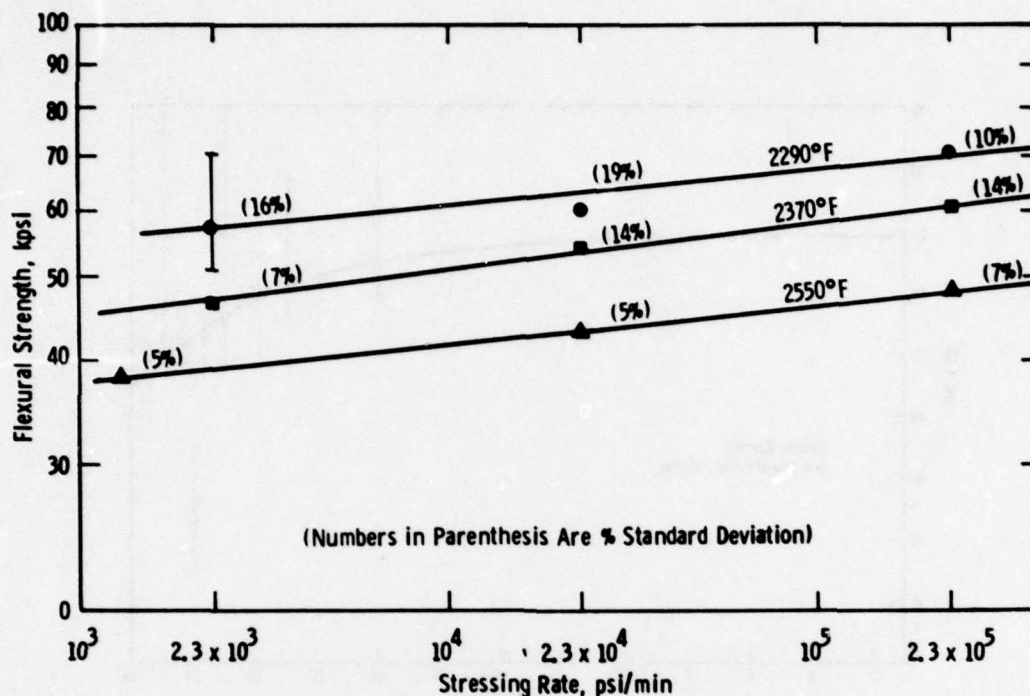
Figure 2-37. The Effect of Stress Rate on the Flexural Strength
of Norton Hot Pressed Silicon Carbide (Noralide NC203)

The flexural properties of hot pressed silicon carbide were particu-
larly sensitive to edge defects. Approximately 90 percent of the fracture
origins identified in flexural test specimens were observed at edges.
Specimen surface and edge condition clearly affect flexural strength results:
220 grit grinding - 73.0 $\pm$ 22% ksi, 320 grit with beveled edges-
96.6 $\pm$ 9% ksi.[4]

Summary data, which describe the flexural strength properties of
Norton Noralide NC203, appear in Figures 2-38 and 2-39. Billet results
from the characterization of the material and all appropriate data points
are shown. Strain rate sensitivity or the effect of strain rate on the
apparent flexural strength of hot pressed silicon carbide is evident from
the two figures. Error bars represent standard deviation which is high at
all temperatures.

2.3.5 STATISTICAL ASPECTS OF MATERIAL CHARACTERIZATION

As pointed out previously, the bulk of testing was conducted in the
flexural test mode with statistical inference to tensile and shear among
others.[3] When area and volume dependent failure probabilities,[10] or

$$\int \left(\frac{\sigma}{\sigma_o}\right) dA = KA\left(\frac{\sigma}{\sigma_o}\right)^m \quad \text{or} \quad \int \left(\frac{\sigma}{\sigma_o}\right)^m dV = KV\left(\frac{\sigma}{\sigma_o}\right)^m$$

45
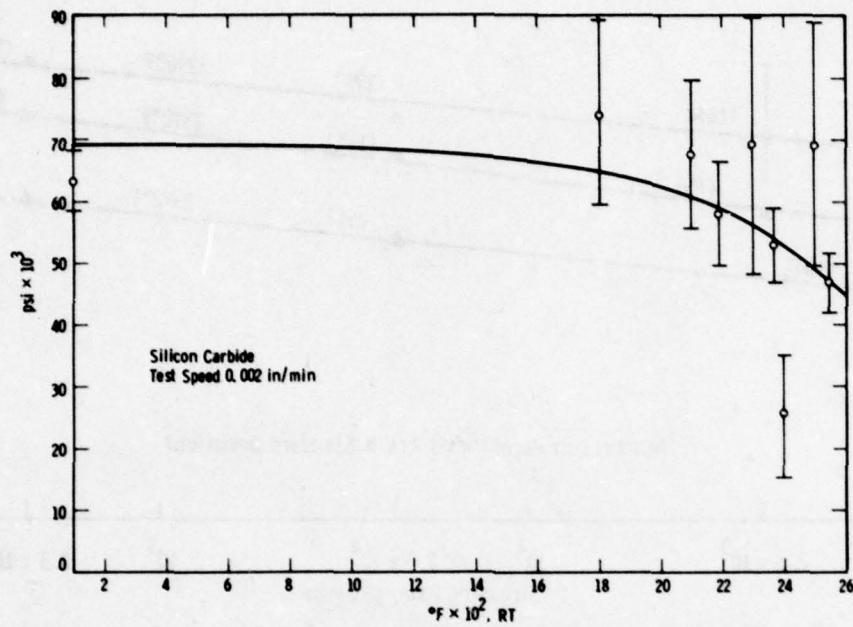
Figure 2-38. The Flexural Strength of Norton Noralide NC203
Silicon Carbide
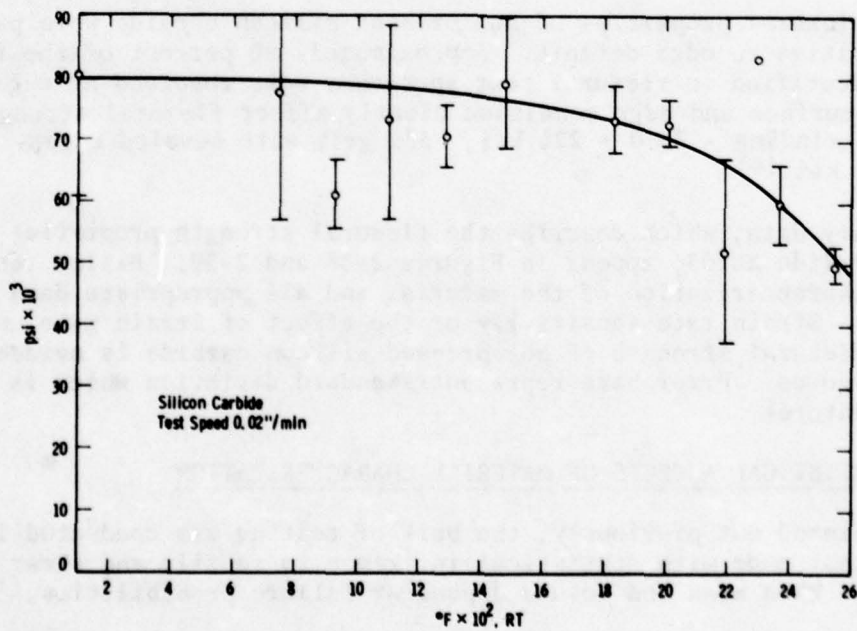
Figure 2-39. The Flexural Strength of Norton Noralide NC203
Silicon Carbide

were first plotted from three-point flexural strength data at room temperature supplied by Norton for HS130 Si3N4 billet certification, Figures 2-40 and 2-41 were produced to predict failure stress in silicon nitride for various test modes by application of Weibull Theory. The correlation of four-point flexural strength and available tensile data with the Weibull estimates was excellent. The Weibull area integral appeared appropriate for the prediction of tensile strength at room temperature, while the volume integral was preferred at 2375°F.(3)

Estimates of strength as a function of volume and/or area under stress were made for HS130 (NC132) silicon nitride and NC203 silicon carbide at room temperature, 1000, 1800 and 2300°F, using two and three parameter Weibull statistics(10) based on the four-point flexural strength measured as part of the experimental program.(5) Correlation of experimental tensile data with predicted results was best for the effective volume under stress, using two parameter Weibull, m = Weibull modulus and σ_0 = normalizing stress. Figures 2-42, 2-43 and 2-44 illustrate the results.

The best estimates of tensile strength for hot-pressed silicon nitride in the weak direction are 42,000 psi at room temperature, 39,500 psi at 1000°F, 35,000 psi at 1800°F and 22,000 psi at 2300°F based on Weibull theory of random flaw distribution (Figure 2-43). These data
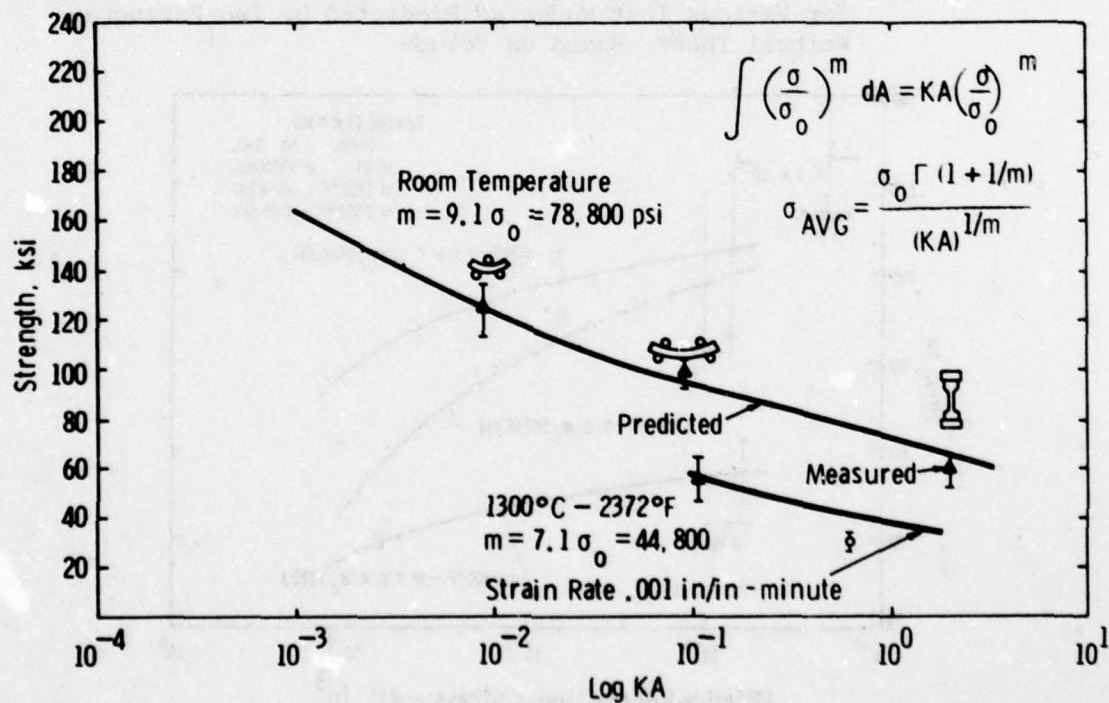
Figure 2-40. Predicted and Measured Failure Stress of Hot Pressed Silicon Nitride for Various Test Modes (Two Parameter Weibull Theory Based on Area)

47
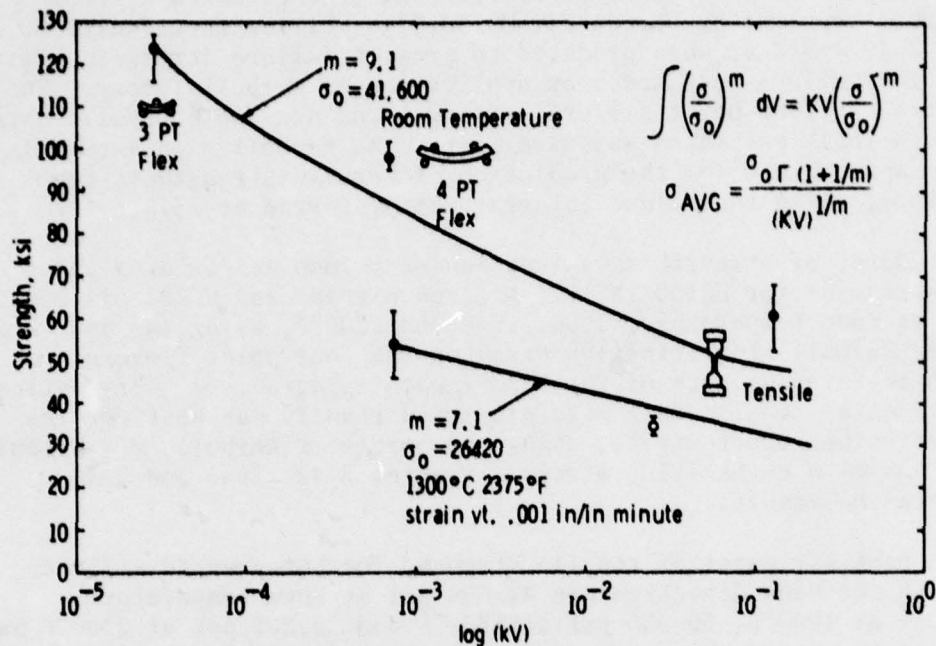
Figure 2-41. Average Failure Stress for Hot Pressed Silicon Nitride for Various Test Modes as Predicted by Two-Parameter Weibull Theory Based on Volume
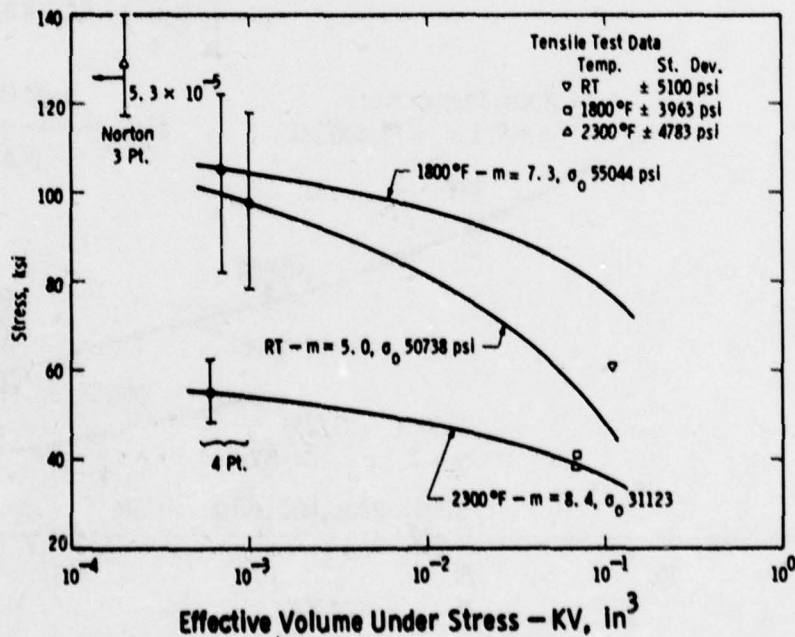
Figure 2-42. The Strength of Norton HS-130 Silicon Nitride (Strong Direction) as Predicted by Weibull Statistics Based on Volume
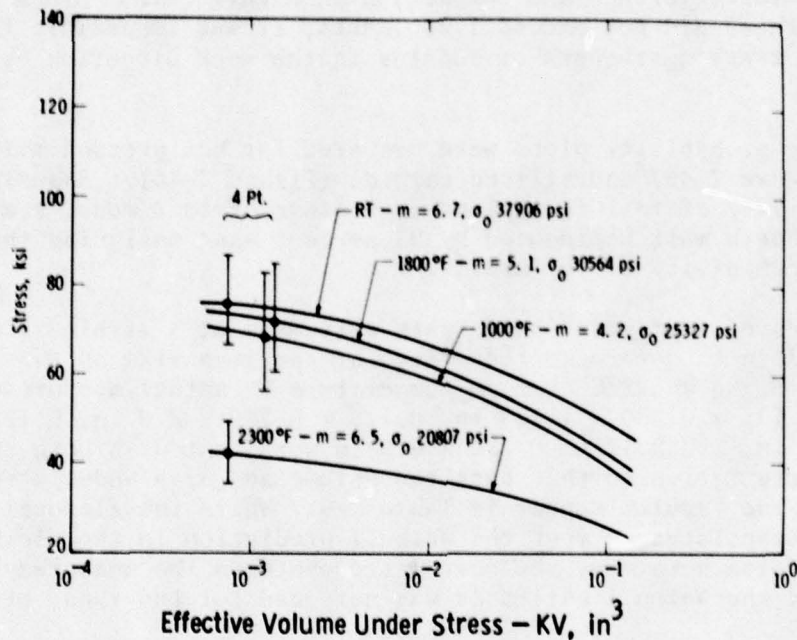
Figure 2-43. The Strength of Norton HS130 Silicon Nitride (Weak Direction) as Predicted by Weibull Statistics Based on Volume
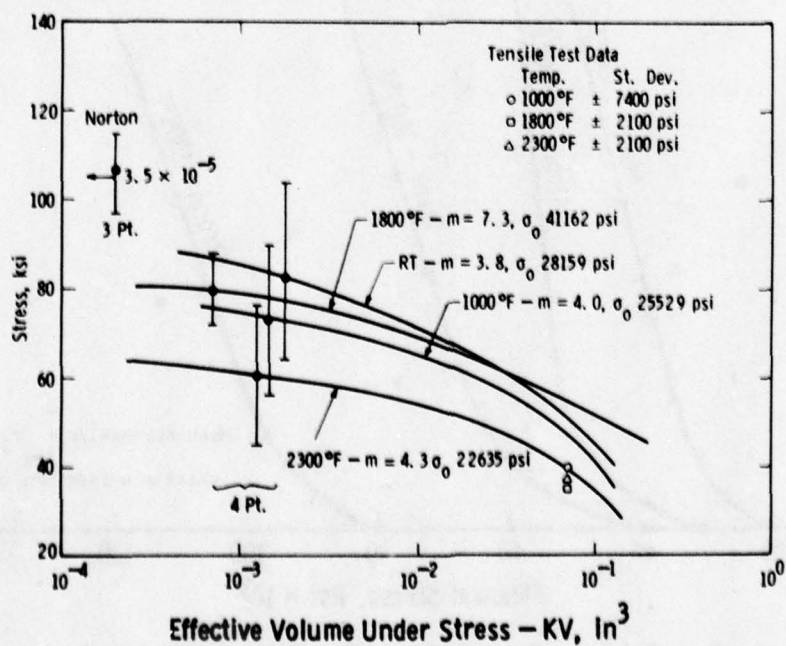
Figure 2-44. The Strength of Norton Hot-Pressed Silicon Carbide as Predicted by Weibull Statistics Based on Volume

are plotted for reference and comparison in Figure 2-12. Since the billet thickness did not exceed 1.25 inches, it was impossible to measure the tensile strength or modulus in the weak direction by actual test.[5]

Failure probability plots were prepared for hot pressed silicon nitride (Figure 2-45) and silicon carbide (Figure 2-46). Assuming the same probability of failure applies regardless of test mode, average tensile strength must be reduced by 25 percent when designing the 5 percent probability of failure.[5]

A series of four-point bend tests were made at a strain rate of 0.001 in/in/min to determine the effect of specimen size on the strength of Si_3N_4 and SiC at room temperature by actual measurement.[5] Specimens 0.125 x 0.250 x 1.125 in, 0.125 x 0.250 x 2.0 in, 0.125 x 0.250 x 3.0 in, and 0.125 x 0.250 x 6.0 in were tested in both the beam and plate orientation so that both the volume and area under stress were variables. The results appear in Table 2-8. While the flexural strength data are extrapolated to meet the Weibull prediction in the vicinity of the tensile size specimen, the correlation between the measured values, overall, and the Weibull estimates was not good for the range of sizes tested.
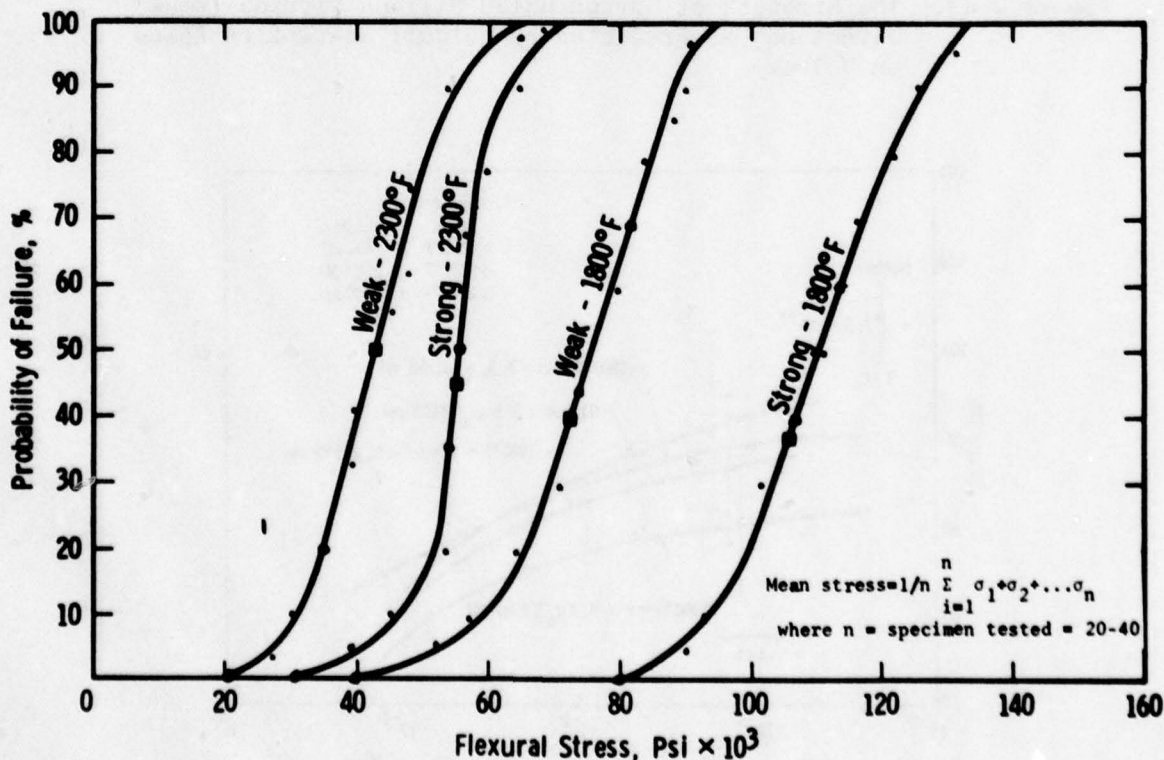
Figure 2-45. Failure Probability for Norton HS-130 Si_3N_4
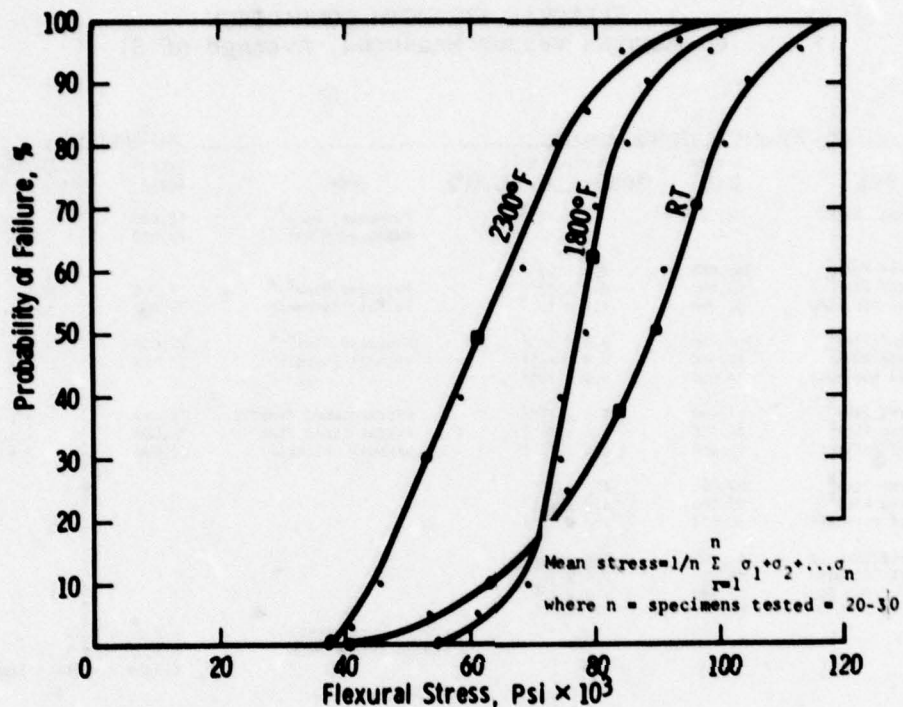
Figure 2-46.   Failure Probability for Norton Hot Pressed SiC

2.3.6   <u>AN ANALYSIS OF THE TIME-DEPENDENT FLEXURAL TEST</u>

The flexural testing and resultant data represent the strength and to some extent the creep properties of silicon nitride and silicon carbide as ceramic materials in a classical sense. As long as the stress-strain function is linear and remains the same for tension and compression, elastic beam theory can be used to determine stresses and strains. However, if the stress-strain function is nonlinear and/or the tensile behavior differs from compressive, the elastic treatment tends toward erroneous results. In such cases, a more complex analysis is indicated.

Nadai[11] presented the theory for bending of bars having a time-independent arbitrary law of deformation. Analyses of flexural creep are also prevalent in the literature.[12-16] A general theory for the bending of bars having a time-dependent arbitrary law of deformation is presented here. It is applicable to constant deformation rate tests and flexural creep tests as well. This representation is an extension and refinement of the work reported previously,[6,7] and as such supersedes rather than summarizes the activity specifically.

51

TABLE 2-8

FLEXURAL STRENGTH COMPARISON
(Estimates versus Measured, Average of 3)

Silicon Nitride (Strong Direction)			Silicon Carbide		
Mode	Stress (psi)	Specimen Size (Stressed Vol, KV, in^3)	Mode	Stress (psi)	Specimen Size (Stressed Vol, KV, in^3)
Flexural, base^P	98,500	1×10^{-3}	Flexural, base^P	80,000	3×10^{-3}
			Measured Flex^B	82,000	3×10^{-3}
Measured Flex^B	132,000	9.0×10^{-2}	Measured Flex^{P,B}	77,000	9.3×10^{-1}
Measured Flex^P	93,000	9.0×10^{-2}	Weibull Estimate	70,000	9.3×10^{-1}
Weibull Estimate	92,000	9.0×10^{-2}			
Measured Flex^B	100,000	9.4×10^{-1}	Measured Flex^{P,B}	72,000	5×10^{-1}
Measured Flex^P	85,000	9.4×10^{-1}	Weibull Estimate	58,000	5×10^{-1}
Weibull Estimate	78,000	9.4×10^{-1}			
Measured Flex^B	94,000	8.5×10^{-1}	Extrapolated Tensile	45,000	3×10^{-1}
Measured Flex^P	80,000	8.5×10^{-1}	Extrapolated Flex	71,000	3×10^{-1}
Weibull Estimate	69,000	8.5×10^{-1}	Weibull Estimate	52,000	3×10^{-1}
Measured Flex^B	80,000	4.9×10^{-1}			
Measured Flex^P	80,000	4.9×10^{-1}			
Weibull Estimate	60,000	4.9×10^{-1}			
Measured Tensile	61,000	9.9×10^{0}			
Weibull Estimate	42,000	9.9×10^{0}			
Extrapolated Flex	62,000	9.9×10^{0}			

P = Plate orientation   h x 2h x X in
B = Beam orientation   h x 1/2 h x X in
                              height x width x length

The analysis of the time-dependent flexure test assumes: (a) the bar has a constant cross section (rectangular, for simplicity); (b) it is loaded by forces directed perpendicular to the longitudinal axis; (c) cross sectional dimensions are small relative to the length in order to neglect shear stresses; (d) the rate of deflection is constant; and, finally (e) the cross sections remain planes during bending. The last assumption implies that the strains, ε, are linearly proportional to the distance, y, from the neutral axis:

$$\varepsilon = \frac{y}{R} \tag{1}$$

where R is the radius of curvature due to bending. The total strain, ε^*, across the height, h, of the specimen is therefore

$$\varepsilon^* = \frac{h}{R} = \varepsilon_t + \varepsilon_c \tag{2}$$

where ε_t is the maximum tensile strain at the outer tensile fiber and ε_c is the maximum compressive strain at the outer compressive fiber.

The equilibrium force equation is:

$$F = \int_{-h/2}^{h/2} \sigma(\varepsilon,t) \, dA_r = \frac{bh}{\varepsilon^*} \int_{\varepsilon_c}^{\varepsilon_t} \sigma(\varepsilon,t) \, d\varepsilon = 0 \tag{3}$$

where $\sigma(\varepsilon,t)$ is the stress, A_r is the area, and b is the specimen width. The applied moment, M, must be resisted by the specimen, resulting in the equilibrium:

$$M = \int_{-h/2}^{h/2} \sigma(\varepsilon,t) y \, dA_r = \frac{bh^2}{\varepsilon^{*2}} \int_{\varepsilon_c}^{\varepsilon_t} \sigma(\varepsilon,t) \varepsilon \, d\varepsilon \tag{4}$$

For the four-point flexure test in Figure 2-47,

$$M = \frac{Pa}{2} \tag{5}$$

for all points within the inner span; P is the applied load; and a is the moment arm. Also, the strain, ε^*, is proportional to the applied deflection. D_1.
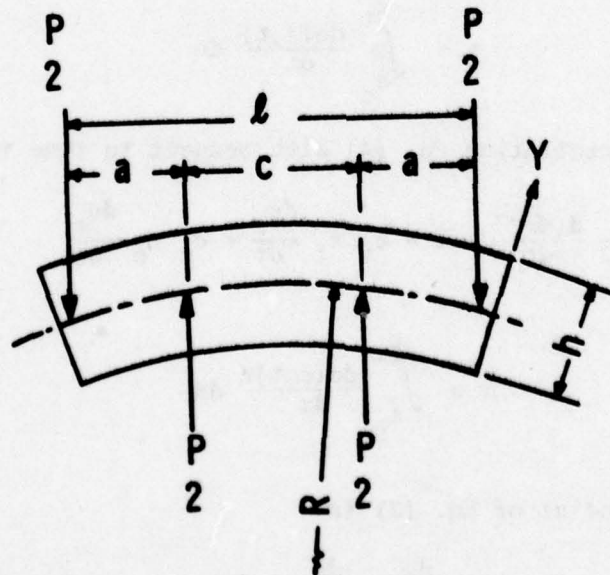
Figure 2-47. Bending of a Bar in Four-Point Flexure

For the case where the deflection, D_1, measures the relative vertical displacement of the inner span points to the outer span points, ϵ^* is given by:

$$\epsilon^* = k_1 D_1 = \frac{3}{a\ell - 4_a 2} D_1 \qquad (6)$$

where ℓ is the outer span length.

For the case where the deflection, D_2, measures the relative vertical displacement of the midpoint with respect to the inner loading points:

$$\epsilon^* = k_2 D_2 = \frac{h}{c^2} D_2 \qquad (7)$$

where c is the inner span length.

Differentiating Eq. (3) with respect to time, t, results in:

$$\frac{1}{bh} \frac{d(F\epsilon^*)}{dt} = 0 = \gamma + \sigma_t \frac{d\epsilon_t}{dt} - \sigma_c \frac{d\epsilon_c}{dt} \qquad (8)$$

where σ_t is the stress at the outer tensile fiber, σ_c is the stress at the outer compressive fiber, and

$$\gamma = \int_{\epsilon_c}^{\epsilon_t} \frac{d\sigma(\epsilon,t)}{dt} \, d\epsilon \qquad (9)$$

Similarly, differentiating Eq. (4) with respect to time results in:

$$\frac{1}{bh^2} \frac{d(M\epsilon^{*2})}{dt} = \lambda + \sigma_t \epsilon_t \frac{d\epsilon_t}{dt} + \sigma_c \epsilon_c \frac{d\epsilon_c}{dt} \qquad (10)$$

where

$$\lambda = \int_{\epsilon_c}^{\epsilon_t} \frac{d\sigma(\epsilon,t)\epsilon}{dt} \, d\epsilon \qquad (11)$$

Also the differential of Eq. (2) is

$$\frac{d\epsilon_t}{dt} + \frac{d\epsilon_c}{dt} = \frac{d\epsilon^*}{dt} \qquad (12)$$

54

By substitution, Eq. (10) can be written as:

$$\frac{1}{bh^2} \frac{d(M\varepsilon*^2)}{dt} = \lambda + \frac{\sigma_t \sigma_c}{(\sigma_c + \sigma_t)} \varepsilon* \frac{d\varepsilon*}{dt} + \frac{(\sigma_c \varepsilon_c - \sigma_t \varepsilon_t)}{\sigma_c + \sigma_t} \gamma \tag{13}$$

and

$$\frac{1}{bh^2} \left(2\frac{d\varepsilon*}{dt} \varepsilon* M + \varepsilon*^2 \frac{dM}{dt}\right) = \lambda + \frac{\sigma_t \sigma_c}{(\sigma_t + \sigma_c)} \frac{d\varepsilon*}{dt} \varepsilon* + \left(\frac{\sigma_c \varepsilon_c - \sigma_t \varepsilon_t}{\sigma_t + \sigma_c}\right) \gamma \tag{14}$$

If deflection and, therefore, the total strain, $\varepsilon*$, are held constant, then the stress relaxation version of Eq. (14) becomes

$$\frac{1}{bh^2} \left(\varepsilon*^2 \frac{dM}{dt}\bigg|_{\varepsilon*}\right) = \lambda + \left(\frac{\sigma_c \varepsilon_c - \sigma_t \varepsilon_t}{\sigma_t + \sigma_c}\right) \gamma \tag{15}$$

where $dM/dt \big|_{\varepsilon*}$ is the rate of moment change due to stress relaxation. Subtracting Eq. (15) from Eq. (14) produces

$$\frac{\sigma_t \sigma_c}{\sigma_t + \sigma_c} = \phi = \frac{1}{bh^2} \left[2M + \frac{\varepsilon*}{d\varepsilon*/dt} \left(\frac{dM}{dt} - \frac{dM}{dt}\bigg|_{\varepsilon*}\right)\right] \tag{16}$$

the general equation relating the outer fiber stresses to the moment and time.

For a constant moment creep test, dM/dt is zero. Therefore, the general equation for flexural creep becomes:

$$\frac{\sigma_t \sigma_c}{\sigma_t + \sigma_c} = \phi_c = \frac{1}{bh^2} \left[2M - \frac{\varepsilon*}{d\varepsilon*/dt} \cdot \frac{dM}{dt}\bigg|_{\varepsilon*}\right] \tag{17}$$

Equations (16) and (17) therefore relate the unknown values of σ_t and σ_c on the left to the measurable quantities on the right. Both moment and total strain must be determined as functions of time. The M and $\varepsilon*$ are instantaneous values. The dM/dt and $d\varepsilon*/dt$ are the slopes of the curves at those instaneous values. The $dM/dt\big|_{\varepsilon*}$ can be determined by running tests at several strain rates or for the creep tests at several constant loads. From these, moment-time curves at constant strain can be established and the required values determined from the slopes of the curves at the appropriate moment and time values.

It is necessary to have another function relating σ_t and σ_c in order to obtain exact values. Without knowledge of this function, it is impossible to establish boundaries within which most materials will fall. It can also be argued that material properties will usually fall closer to one or the other boundaries. For materials which undergo true plastic deformation, the tensile and compressive stress-strain curves

55

will be equivalent, i.e., σ_t will equal σ_c. Therefore, the first boundary is easily established. A large class of materials is highly resistant to deformation in the compressive mode. The second boundary occurs by letting the compressive stress be time-independent and linearly elastic. A simple compression test establishes which of the two conditions hold and in the elastic case establishes the compressive strain function, i.e., the modulus of elasticity.

For the first boundary condition, where tensile and compressive stress-strain relationships are the same, Eq. (16) becomes:

$$\sigma_t = \sigma_c = 2 \phi = \frac{2}{bh^2} \ [2M + \frac{\epsilon^*}{d\epsilon^*/dt} \ (\frac{dM}{dt} - \frac{dM}{dt}\Big|_{\epsilon_*})] \tag{18}$$

and Eq. (17) becomes:

$$\sigma_t = \sigma_c = 2 \phi_c = \frac{2}{bh^2} \ [2M - \frac{\epsilon^*}{d\epsilon^*/dt} \ \frac{dM}{dt}\Big|_{\epsilon^*}] \tag{19}$$

Also,

$$\epsilon_t = \epsilon_c = \epsilon^*/2 \tag{20}$$

For the second boundary condition, where the tensile side of the flexure bar follows a time-dependent arbitrary law of deformation and the compressive side behaves elastically, the moment deflection data can be analyzed incrementally under conditions of constant time by noting that for small changes:

$$\sigma t_i \ \Delta\epsilon_{t_i} = \sigma_{c_i} \ \Delta\epsilon_{c_i} \tag{21}$$

where

$$\Delta\epsilon_{t_i} = \epsilon_{t_i} - \epsilon_{t_{i-1}} \tag{22}$$

$$\Delta\epsilon_{c_i} = \epsilon_{c_i} - \epsilon_{c_{i-1}} = \epsilon_i^* - \epsilon_{t_i} - \epsilon_{c_{i-1}} \tag{23}$$

and

$$\sigma_{c_i} = \frac{\epsilon_{c_i}}{A} \tag{24}$$

56

where A is the elastic compliance (the reciprocal of the elastic modulus). By proper substitution in Eq. (22):

$$\varepsilon_{t_i}^2 + (\varepsilon_{c_{i-1}} - 2 \varepsilon_i^*) \varepsilon_{t_i} + [A \phi \varepsilon_{t_{i-1}} + (\varepsilon_i^* - A \phi)$$

(25)

$$(\varepsilon_i^* - \varepsilon_{c_{i-1}})] = 0$$

The quadratic equation can be solved for ε_{t_i}. Then, ε_{c_i}, σ_{c_i} and σ_{t_i} can be determined by substitution.

Analytical Results

The concept can be appreciated best by example. Moment/time and total strain/time values were generated to determine the outer fiber stress-strain relationships for the appropriate cases: elastic, time-independent arbitrary deformation law and time-dependent arbitrary deformation law.

For a constant rate of deflection the stress/strain/time relationships used in the synthesis of μ versus t and ε^* versus t curves were determined from an equation of the form:

$$\varepsilon = A\sigma + B \sigma^n t^m$$

(26)

where

$$A = 2 \times 10^{-7}$$
$$B = 2.2 \times 10^{-16}$$
$$n = 3$$
$$m = 1/2$$
$$\text{strain rate} = .01$$

When equivalent time-dependent deformation occurs in tension and compression:

$$\varepsilon_o = \varepsilon_t$$

(27)

If the material resists deformation in the compressive mode,

$$\varepsilon_c = A \sigma_c$$

(28)

57

Typical results of the tensile analysis for equivalent tensile and compressive deformation are shown in Figure 2-48. The elastic beam analysis produces a maximum stress that is 25 percent too high. The time-independent analysis underestimates the stress by 7 percent.
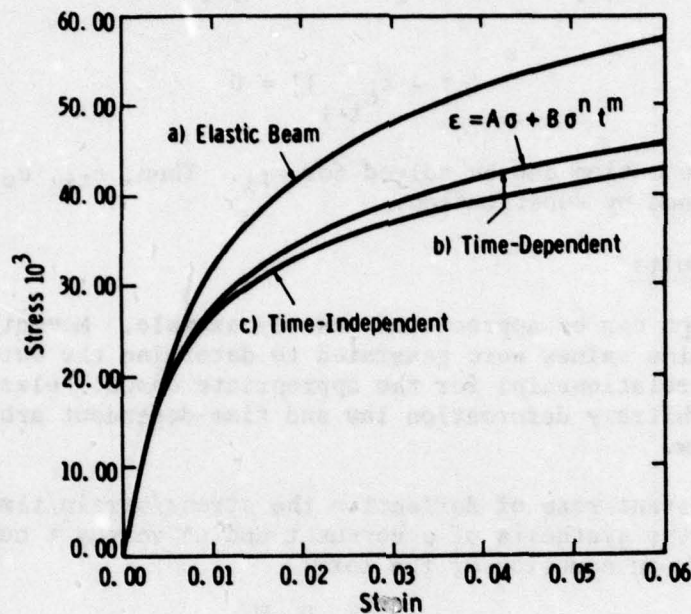
Figure 2-48. Outer Fiber Tensile Stress-Strain Relationships for Equivalent Tensile and Compressive Deformation as Determined from Elastic Beam Theory (a), Time-Dependent Deformation Theory (b) and Time-Independent Deformation Theory (c)

Figure 2-49 represents the tensile analysis for time-dependent tensile and elastic compressive deformation. In this case, the elastic beam theory not only produces a higher maximum stress, 78 percent, but the maximum strain is diminished by 26 percent. The time-independent analysis reduces the maximum stress by 7 percent.

The stress/strain/time relationships used to synthesize the moments and strain/time curves for creep were determined from Eq. (26) using the following parameters.

$A = 0.2$

$B = 8 \times 10^{-4}$

$n = 2$

$m = 1/2$

58
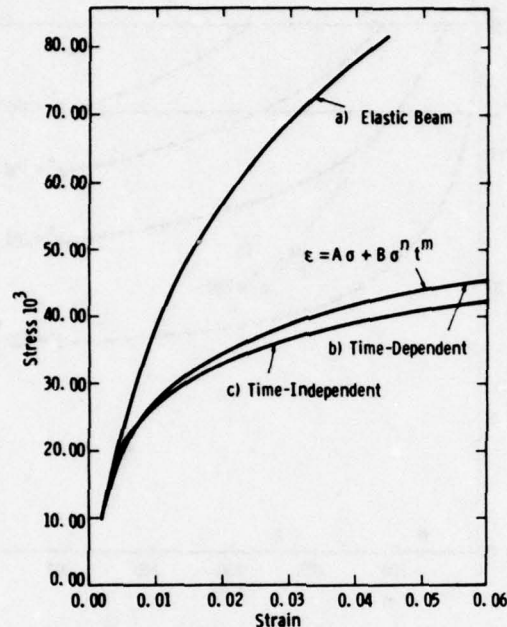
Figure 2-49. Outer Fiber Stress-Strain Relationships for Non-Linear Tensile and Linear Compressive Deformation as Determined from Elastic Beam Theory (a), Time-Dependent Deformation Theory (b), and Time-Independent Deformation Theory (c)

For equivalent time-dependent, nonlinear deformation in tension and compression, the creep data presented in Figures 2-50 and 2-51 were calculated for a constant moment of 100 $bh^2/6$ where the bar width, b, and the bar thickness, h, were both unity. This is equivalent to initially applying an elastic stress at the outside fibers of 100 units. Moment relaxation data were also calculated. These are represented by the dashed curves in Figure 2-50. The results of the analysis are plotted in Figure 2-52. The solid lines represent the stress-strain distributions within the bar at the given times. The dashed lines and circles are the outer fiber values. Initially, there is a rapid drop in stress and then a slower but continual stress decrease with time.

A comparison between creep for the constant moment flexural test and the expected creep for the constant stress uniaxial tensile test is made in Figure 2-53. Each was elastically stressed initially to the same value. Strains and strain rates differ considerably.

The creep and stress relaxation data of Figures 2-54 and 2-55 were calculated for a constant of 100 $bh^2/6$ for a bar width and thickness of unity in the case of time-dependent, nonlinear deformation in tension and linear elastic deformation in compression. The values of M, $dM/dt/\varepsilon'$

59
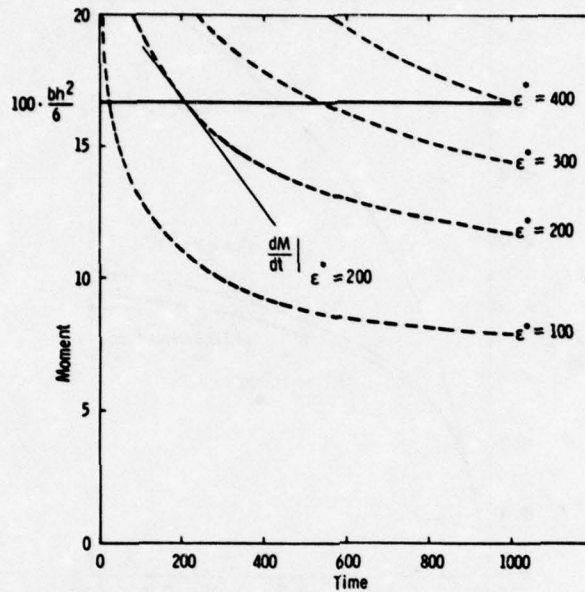
Figure 2-50. Constant Moment Line and Moment Relaxation Curves for a Calculated Example where Deformation in Tension and Compression Are Equal, Time-Dependent and Nonlinear
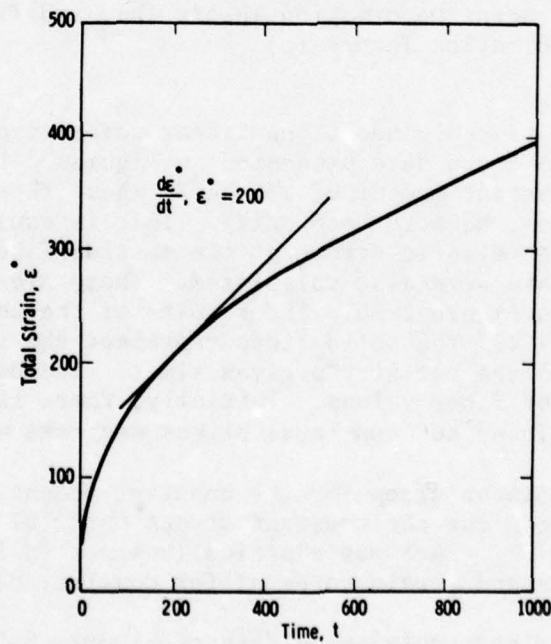
Figure 2-51. Total Strain Versus Time for a Calculated Example where Deformation in Tension and Compression Are Equal, Time-Dependent and Nonlinear

60
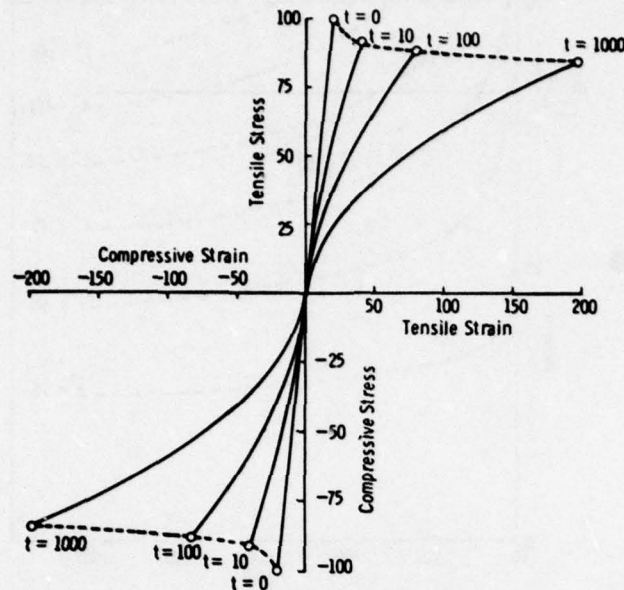
Figure 2-52.   Stress-Strain Distributions at Various Times during a
Constant Moment Flexural Creep Test for a Calculated
Example where Deformation in Tension and Compression
Are Equal, Time-Dependent and Nonlinear
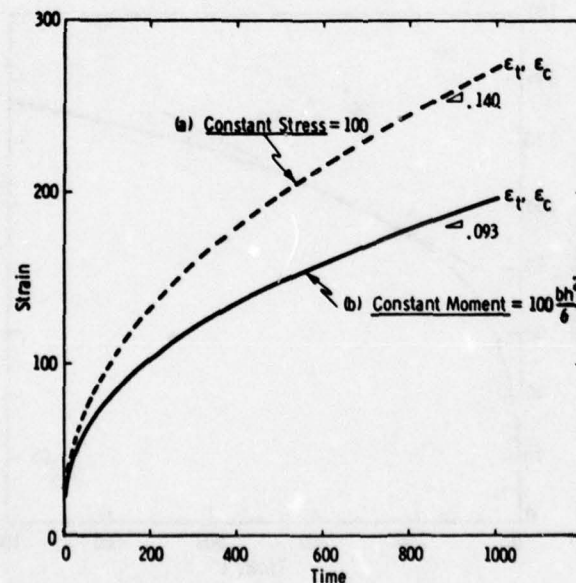
Figure 2-53.   Creep Curves for the Uniaxial Constant Stress Test and
the Flexural Constant Moment Test for a Calculated
Example where Deformation in Tension and Compression
Are Equal, Time-Dependent and Nonlinear

61
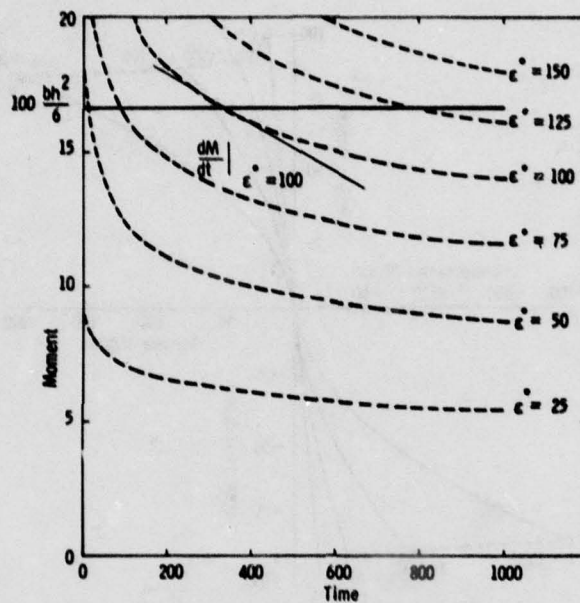
Figure 2-54. Constant Moment Line and Moment Relaxation Curves for a Calculated Example where Deformation in Tension Was Time-Dependent and Nonlinear, and Deformation in Compression was Linear-Elastic
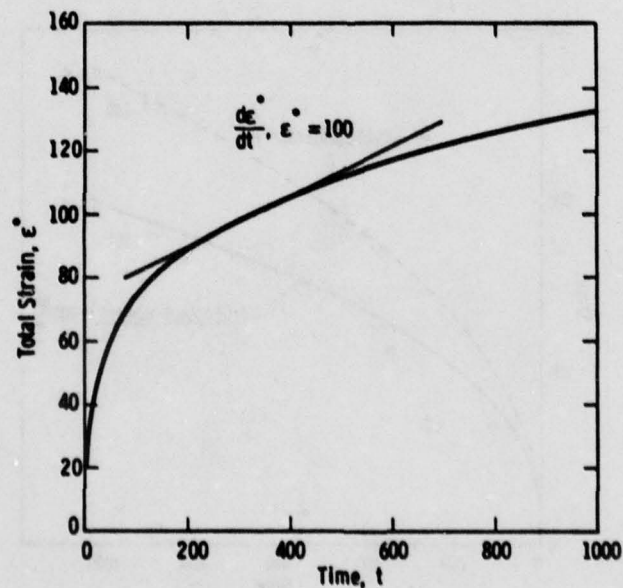
Figure 2-55. Total Strain Versus Time for a Calculated Example where Deformation in Tension Was Time-Dependent and Nonlinear and Deformation in Compression was Linear-Elastic

62

ε^*, and $d\varepsilon^*/dt$ at various times were determined as before. The results appear in Figure 2-56 as the stress-strain distribution within the bar at given times. The dashed line and circles represent outer fiber values. In this case the disparity in tensile stress with time is much greater than in the previous case, although the same tensile deformation equation is used.
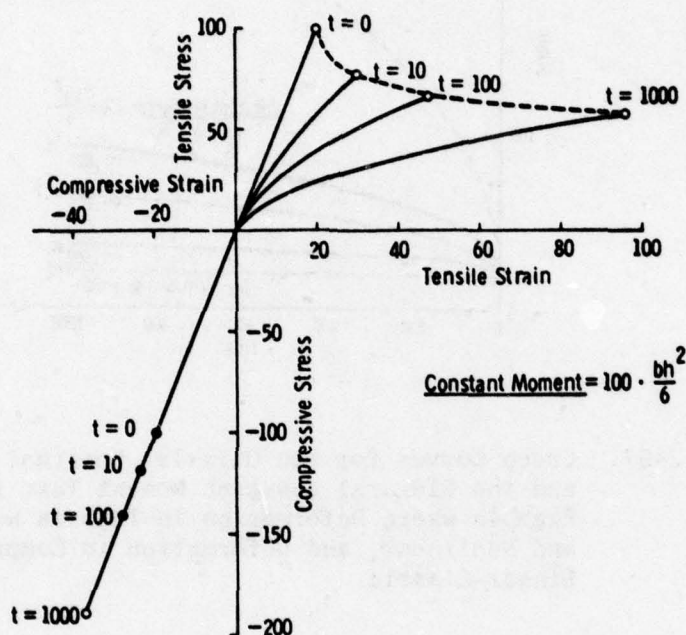
Figure 2-56. Stress-Strain Distributions at Various Times during a Constant Moment Flexural Creep Test for a Calculated Example where Deformation in Tension was Time-Dependent and Nonlinear, and Deformation in Compression Was Linear-Elastic

In Figure 2-57, a comparison is made between creep for this example of the constant moment flexural test and creep for the constant stress uniaxial tensile test. The flexural test for the present case produces even lower tensile strains and strain rates than for the previous case. The increase in flexural compressive strain over that of constant uniaxial compressive strain results from the bar regeneration requirement to maintain a force balance on the tensile and compressive sides. The curve for $\varepsilon^*/2$ versus time is included in Figure 2-57 because it represents the flexural creep curve normally reported. For materials that resist flow in compression, it is representative of an average only.

63
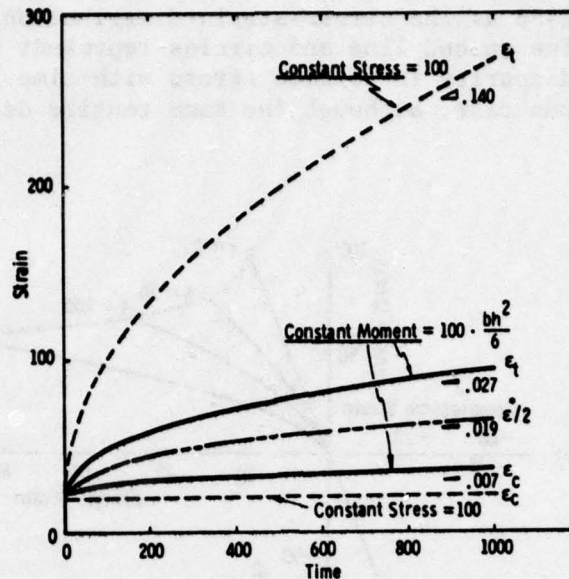
Figure 2-57. Creep Curves for the Uniaxial Constant Stress Test
and the Flexural Constant Moment Test for a Calculated
Example where Deformation in Tension was Time-Dependent
and Nonlinear, and Deformation in Compression Was
Linear-Elastic

The final example is the analysis of actual test data. Five samples
of HS130 (Noralide NC132) silicon nitride were tested at total strain
rates between 8×10^{-6} and 46×10^{-6}. The moment time and total strain/
time curves are shown in Figures 2-58 and 2-59, respectively. Analyses
were performed for a) an elastic beam, b) equivalent time-dependent
nonlinear tension and nonlinear compression and c) time-dependent
nonlinear tension and elastic compression. The outer fiber tensile
stress-strain curves were determined for each case (Figure 2-60). The
actual stress-strain values will fall within an envelope defined by the
curves b and c. Since silicon nitride resists flow in compression, the
curves in case (c) best describes the deformation behavior. Elastic
beam theory overestimates tensile strengths by 70 to 90 percent and
underestimates total strains by 10 to 25 percent.

64
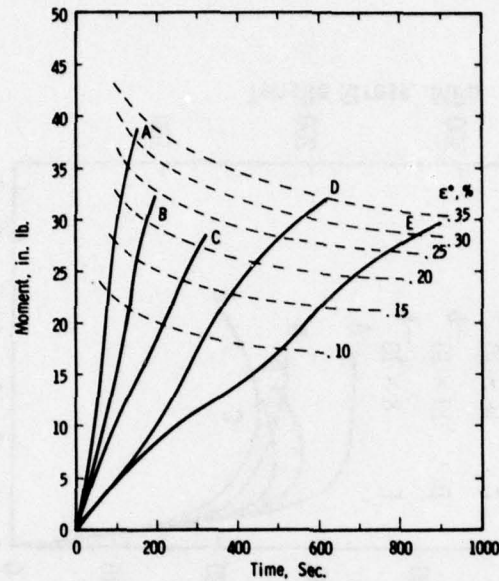
Figure 2-58. Moment-Time Curves for Flexural Tests on Norton HS130
(Noralide NC132) Silicon Nitride
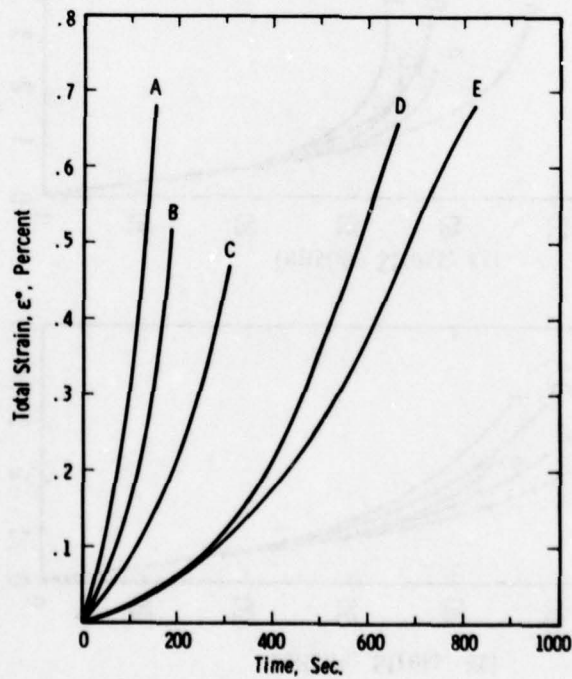
Figure 2-59. Strain-Time Curves for Flexural Tests on Norton HS130
(Noralide NC132) Silicon Nitride

65
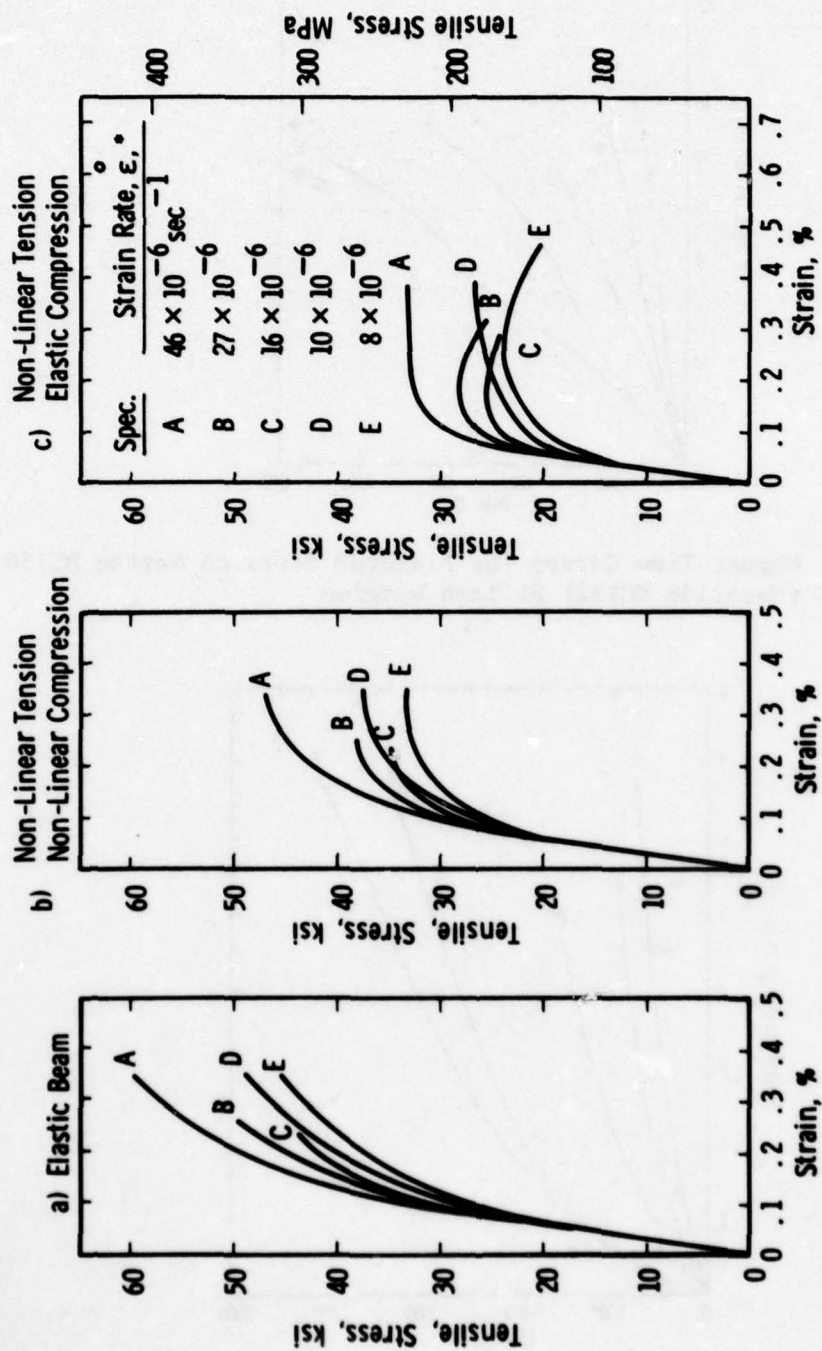
Figure 2-60. Stress-Strain Curves for Norton HS130 Silicon Nitride Calculated Using (a) Elastic Beam Method, (b) Equivalent Time-Dependent Nonlinear Tension and Compression Method and (c) Time-dependent Nonlinear Tension and Elastic Compression Method.

a) Elastic Beam

Non-Linear Tension
Non-Linear Compression

b)

c) Non-Linear Tension
Elastic Compression

Spec.	Strain Rate, $\dot{\varepsilon}$, $\sec^{-1}$
A	46×10^{-6}
B	27×10^{-6}
C	16×10^{-6}
D	10×10^{-6}
E	8×10^{-6}

Tensile Stress, MPa

Tensile Stress, ksi

Strain, %

2.4 CREEP PROPERTIES OF HOT PRESSED SILICON NITRIDE (NORTON HS130, NORALIDE NC132) AND HOT PRESSED SILICON CARBIDE (NORTON NORALIDE NC203)

2.4.1 BACKGROUND

The effects of creep and/or the stress rupture properties of materials are extremely critical in structural applications involving gas turbines, especially for hot/power section components. While the life determining property may be fatigue or some aspect of corrosion/erosion, i.e., oxidation or sulfidation, more often than not it is creep related stress rupture which becomes life limiting. This is certainly true where stress levels at elevated temperatures are high as in rotor blades, for example. The implication may be subtle in a low steady-state stress application like that of the stator vane, but transient thermal stresses peak in this case at temperatures which exceed the threshold of creep. Under such conditions failure may be averted by stress relaxation if indeed it is to be averted at all.

Creep/stress rupture properties represent an important design parameter, and become an essential part of any reasonable evaluation of component performance or life expectancy.

2.4.2 TENSILE CREEP AND STRESS RUPTURE TESTING

Every attempt was made to perform the creep/stress rupture tests by conventional methods. All data were presented in conventional form. A planned matrix (Table 2-9) was employed to bracket the material's performance (hot pressed Si_3N_4 and SiC) in terms of stress (5, 10, and 15 ksi) and temperature (1800, 2100, 2300 and 2500°F). A minimum of three specimens per condition per material was specified. Tests were performed in inert atmosphere (helium) and in air, using graphite, TD

TABLE 2-9

TEST MATRIX FOR TENSILE CREEP PROPERTIES
(TEST PLAN/TEST ACTUAL)

Stress	Temperature (°F)				
(psi)	1800	2100	2300	2400	2500
5,000	3/2	3/3	3/ 3	0/2	3/1
10,000	3/1	3/3	3/5	0/ 2	3/3
12,000	0/0	0/1	0/3	0/ 2	0/0
15,000	3/0	3/3	3/3	0/2	0/3

nickel-chrome, or silicon carbide grips, depending upon the specific
test requirement and the testing laboratory (Westinghouse R&D or
Westinghouse Astronuclear Laboratory - now Advanced Energy Systems
Division). The test matrix, as planned, was adjusted to eliminate
the high stress, high temperature and low stress, low temperature points
as testing proceeded. The creep strength of Si_3N_4 was so poor at 2500°F
that results were not meaningful. Too little strain occurred at 1800°F,
5000 psi for accurate measurements.

The typical creep specimen[2] is illustrated in Figure 2-61. Creep
testing in air was performed in 12,000 lb capacity lever-type (dead
weight) creep machines with 2800°F platinum-wound tube-type furnaces
installed which had 0.50 inch diameter view ports spaced 180° apart.
Specimen alignment was accomplished by a strain gage technique (see
Tensile Test Section 2.2.2, page 19). TD nickel chrome grips were
designed and used at 15,000 psi stress, 2300°F maximum (Figure 2-62).
Test temperatures were monitored with an optical pyrometer after
determining the temperature distribution with a platinum-10% rhodium
thermocouple.
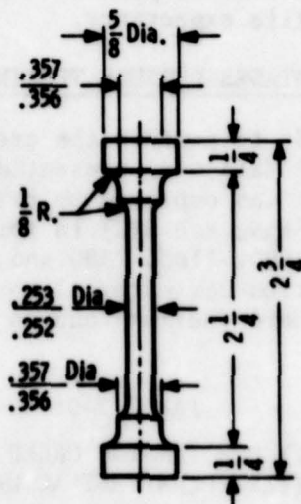
Figure 2-61. Creep Specimen

Attempts were made to measure creep strain initially with an optical
extensometer by sighting on silicon nitride targets cemented to the
specimen. When the cement reacted with the specimen, causing failure at
a target location, this method was abandoned in favor of targets which
were diffusion bonded in place. Cross-head travel proved to be an adequate
measure of creep strain when verified by the final dimensions of the specimen
after test, however.
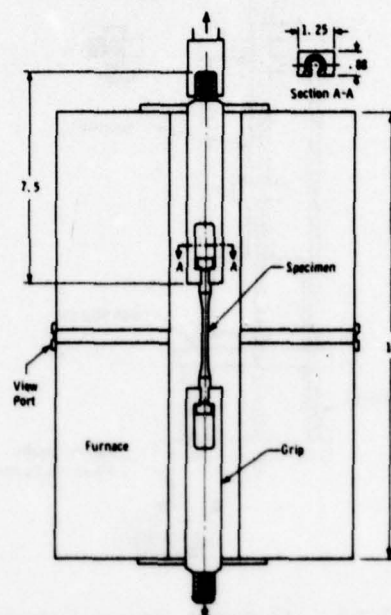
Figure 2-62.   Creep Test Setup with TD NiCr Grips

A ceramic rod-type extensometer (Figure 2-63) was eventually designed. This extensometer was attached to the specimen by wedging spring-loaded cross pieces into the radii at opposite ends of the gage length.

Tensile specimens, 5-1/2 inches long and 0.250 inch diameter (Figure 2-7), were used for tests in helium at 1 psig which employed a 20,000 lb capacity spring-type creep machine equipped with a Brew furnace (Figure 2-64). Creep strain was measured with a Gaertner M353A-10 optical extensometer sighted against graphite targets clamped to the 2.00 inch gage length of the specimen as shown in Figure 2-65. The strain measurements were difficult to make, however, because of poor contrast. Platinum/10% platinum-rhodium thermocouples were used to measure temperature and temperature distribution at first, but reaction between the thermocouple and the specimen precluded their use. An optical pyrometer was finally employed to monitor specimen temperature after the temperature distribution was adjusted to acceptable limits ($\pm$ 20°F at 2500°F over the 2.00 inch gage length).
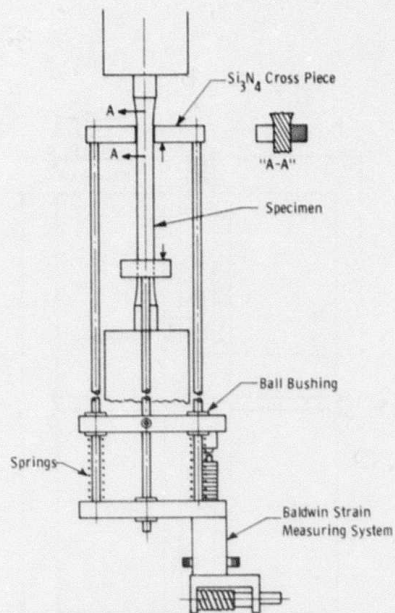
Figure 2-63.   Ceramic Creep Extensometer
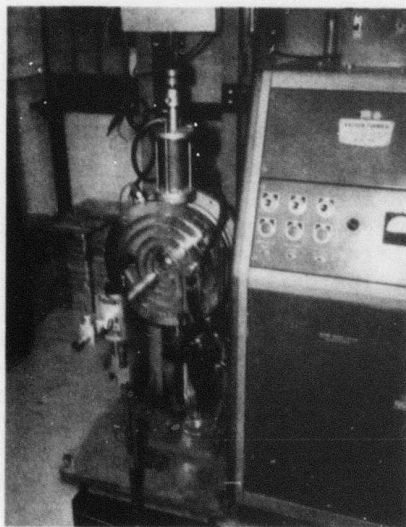
Figure 2-64.   Inert Atmosphere Creep Test Equipment, Including
Gaertner Optical Extensometer

70
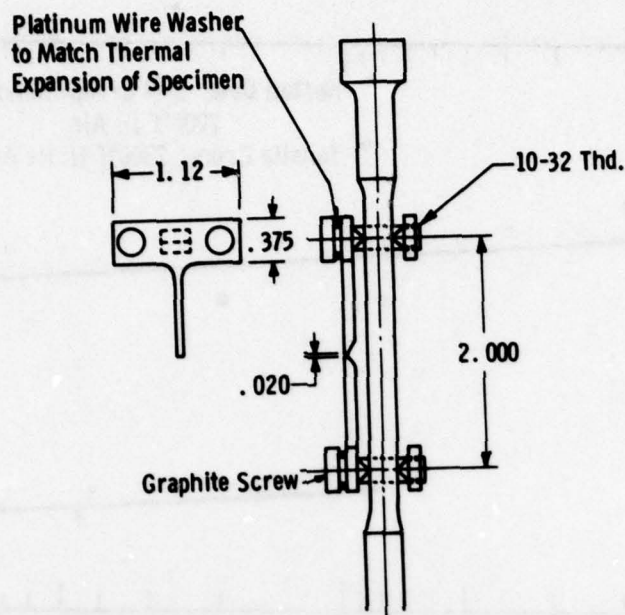
Figure 2-65. Graphite Extensometer Targets Used to Measure Creep
Strain Up to 2500°F in Inert Atmosphere

2.4.3 CREEP/STRESS RUPTURE TEST RESULTS

2.4.3.1 Silicon Nitride

A preliminary creep test on HS110 silicon nitride at 1800°F,
20,000 psi stress in air produced a steady-state creep rate of
3.5×10^{-6} in/in/hr. The specimen failed after 200 hours at 0.16 percent
elongation.[2]

Helium Atmosphere. The creep behavior of HS130 silicon nitride in
helium was investigated in a somewhat more systematic manner at first,
using an Instron machine and graphite grips.[2] Specimens were heated
inductively in a furnace capable of providing a uniform 3 inch hot zone
up to a maximum test temperature of 2500°F. Elongation was measured by
an LVDT, monitoring bottom RAM motion on the Instron machine with good
agreement between recorded strain and final specimen dimension.

The cursory creep results appear in Table 2-10.[2] Stress rupture
properties are plotted from these data in Figure 2-66. Test mode
obviously affects the results as shown by the inclusion of Norton data
obtained by three-point bending. Creep curves typically displayed the
three classic stages (Figure 2-67). When steady-state strain rate was

71
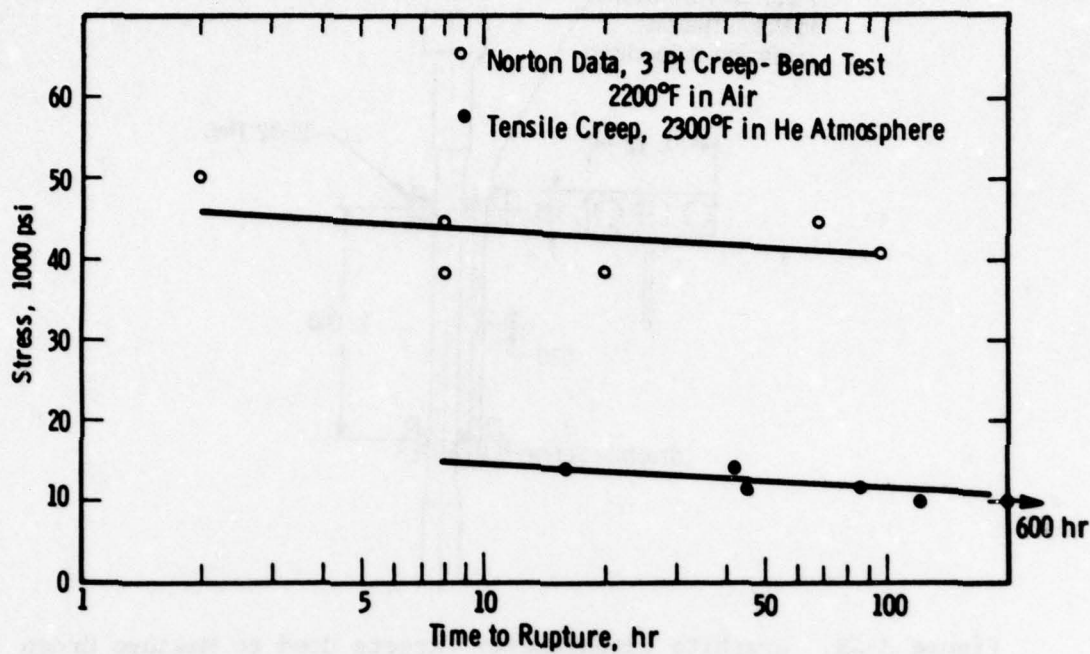
Figure 2-66.   Stress Rupture Properties of Si_3N_4
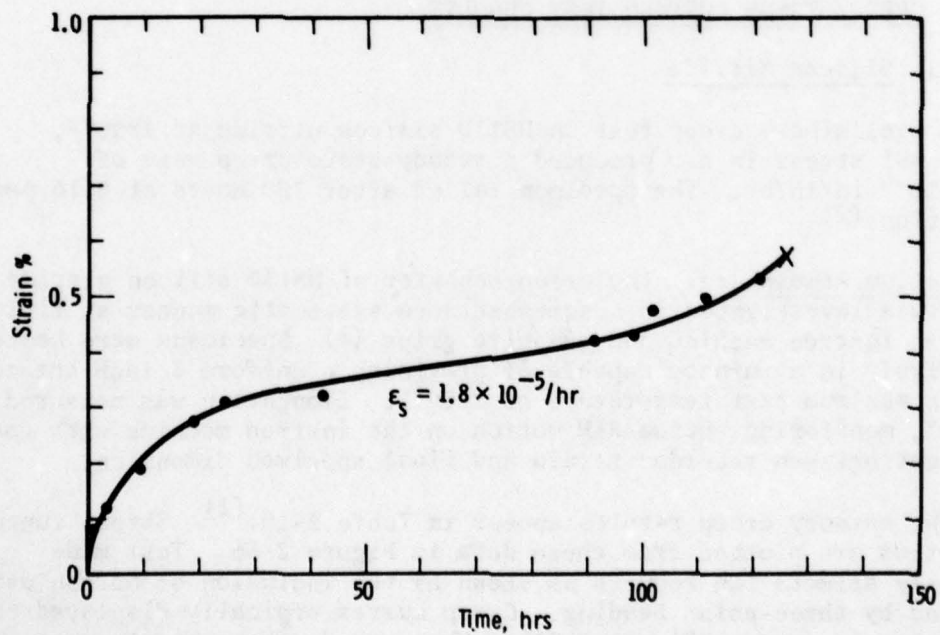
Figure 2-67.   Typical Creep Curve for HS130 Si_3N_4
10,000 psi, 2300°F

TABLE 2-10

CURSORY CREEP PROPERTIES OF HS130 Si_3N_4 IN HELIUM

Temperature ($^\circ$F)	Stress (1000 psi)	Time to Failure	Steady-State Creep Rate	Elongation (%)
2500	15	0.8 min	3×10^{-2}	0.32
2500	10	24 hr	2×10^{-3}	0.71
2300	10	129 hr (no failure)	1.8×10^{-5}	1.30
2300	10	600 hr	1.8×10^{-5}	0.58
2300	14	42.7 hr	3.6×10^{-5}	0.51
2300	14	17.2 hr	9.3×10^{-5}	0.53
2300	12	45.0 hr	1.8×10^{-5}	0.46
2300	12	86.8 hr	2.5×10^{-5}	--

plotted as a function of log stress (Figure 2-68) a low exponent, n = 1.3, in the relation $\epsilon = \sigma^n$ resulted. This provided the final indication of a creep mechanism since n < 2 suggests visco-elastic phenomena, i.e., a Nabarro-Herring diffusional creep or grain boundary sliding. Preliminary transmission electron microscopy supported the hypothesis of grain boundary sliding as the rate controlling process.[2]

Additional data from tests in helium permitted the stress rupture properties of HS130 silicon nitride to be developed more fully (Figure 2-69).[3] While the creep strength of the material appears to be adequate at 2300°F, performance at 2500°F is marginal at best, considering the 5000 psi gas bending stress requirement for a stator vane designed to operate for 10,000 hours in stationary turbine service.

HS130 offered a marked improvement in creep resistance over HS110. Since the Ca concentration in HS110 was an order of magnitude greater than for HS130 ($\sim$ 0.5 w/o for HS110 vs 0.03-0.06 w/o for HS130), impurity levels had to influence the properties of hot pressed silicon nitride appreciably.[3] That contention is supported by the plot of steady-state

73
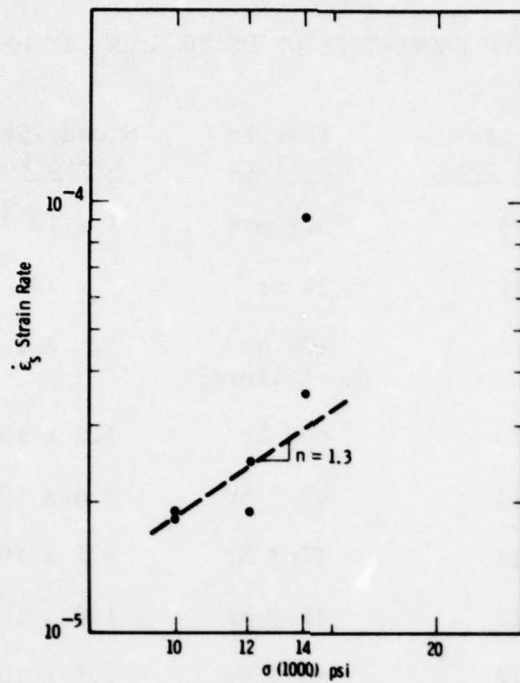
Figure 2-68. Strain Rate vs Stress for HS130 Si_3N_4 in Helium Atmosphere at 2300°F
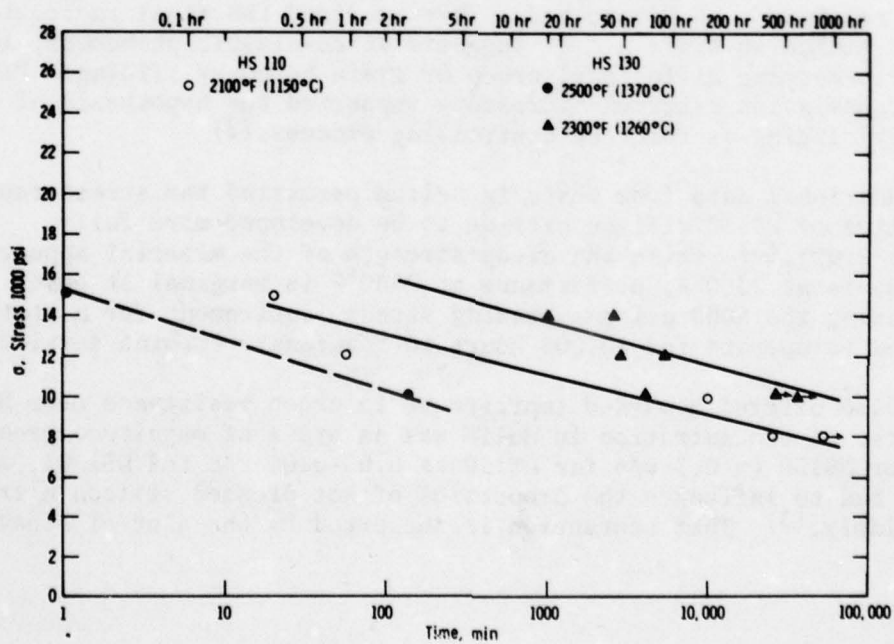
Figure 2-69. Stress-Rupture Properties of Silicon Nitride in He Atmosphere

creep rate as a function of reciprocal temperature in Figure 2-70 for
three levels of impurity. When the steady-state creep rate was expressed
by a generalized Arrhenius equation, activation energies for creep (ΔH)
were obtained as follows:

150 Kcal/mole - HS130 Si_3N_4 at 10,000 psi for 2300-2500°F

150 Kcal/mole - HS110 Si_3N_4 at 10,000 psi for 2050-2150°F
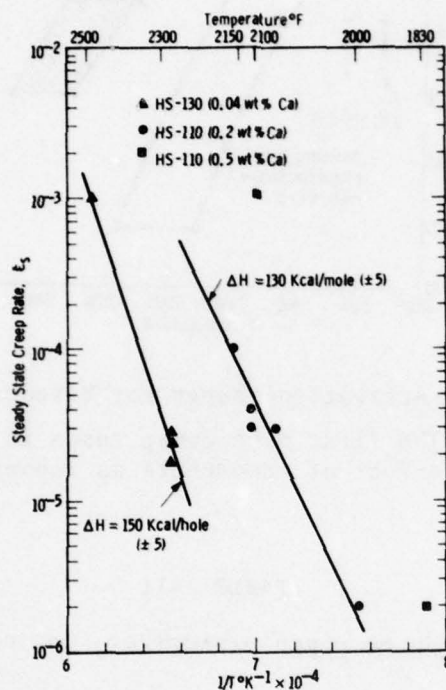
Figure 2-70.   Steady-State Creep Rate vs 1/T at
10,000 psi in He Atmosphere

The activation energy data are consistent with the observation that
creep deformation in hot pressed Si_3N_4 is controlled by grain boundary
sliding. The viscosity of the glass phase at the boundary is a dominant
factor when the mechanical strength of the material is considered,
particularly at elevated temperatures. Rosin, et al,[17] measured the
viscosities and the activation energies for viscous flow in SiO_2, SiO_2
doped with CaO and SiO_2 doped with Al_2O_3. Their data are compared with
the activation energies obtained for silicon nitride in Figure 2-71. If
the grain boundary glass phase in HS130 silicon nitride is 12 m/o as
reported[3] and the temperature dependence of ΔH for viscous flow of
SiO_2 plus 8 m/o CaO is assumed to be similar to that of pure SiO_2, curve B
is constructed to represent the glass phase composition. Favorable
agreement between the activation energies for creep in Si_3N_4 and viscous
flow in CaO doped SiO_2 strongly suggests that the creep behavior of Si_3N_4
which is sensitive to Ca concentration, is controlled mainly by the
properties of the grain boundary glass phase.

75
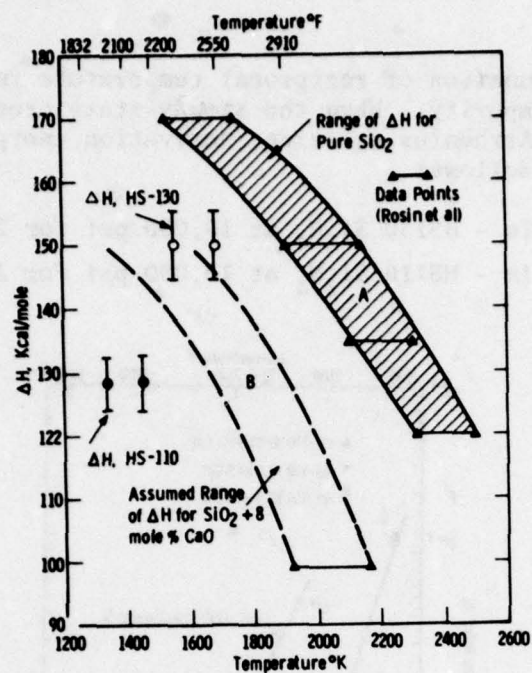
Figure 2-71.   Activation Energy for Viscous Flow

Results in Air.   The first nine creep tests in an air atmosphere
indicated a startling effect of atmosphere as reported in Table 2-11.[4]

TABLE 2-11

EFFECT OF ATMOSPHERE ON CREEP PARAMETERS, HOT PRESSED HS130 Si_3N_4

Test Temperature (°F)	Applied Load (1000 psi)	$\varepsilon_s hr^{-1}$ He	$\varepsilon_s hr^{-1}$ Air	Total Elong. (%) He	Total Elong. (%) Air	Comments
1800	10		1.5×10^{-7}			Term. 2000 hr
2050	10	2×10^{-5}		0.5		HS-110, 0.2% Ca
2100	10	2×10^{-6}		0.3		
2150	12			0.2		HS-110, 0.2% Ca
2200	10		1.6×10^{-5}		1.7	
2200	12					
2300	8		6×10^{-5}		3.1	
2300	10	2×10^{-5}	1×10^{-4}	0.6	3.3	
2300	12	3×10^{-5}		0.5	2.9	
2300	14	4×10^{-5}		0.5		
2400	10				2.8	
2500	10		2×10^{-3}		0.6	

76

Both creep rate and total creep strain are significantly higher in air than in helium. The phenomenon is clearly demonstrated in Figure 2-72 where typical creep curves of percent strain versus time are plotted for air and helium, respectively.
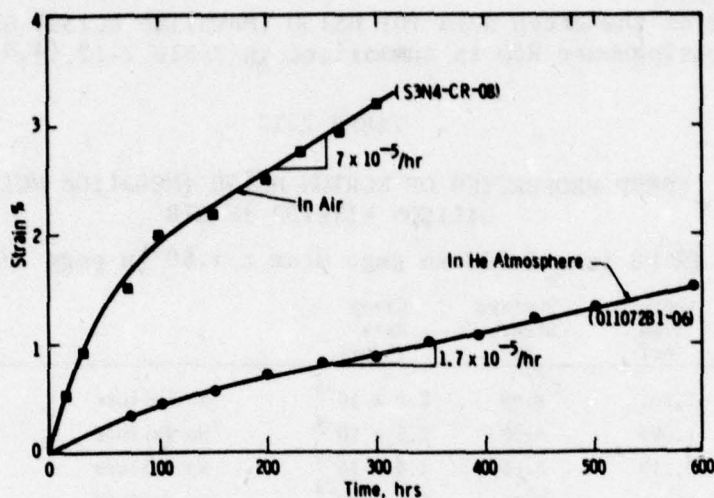
Figure 2-72. Creep Properties of Hot Pressed Si_3N_4 at 10,000 psi, 2300°F

There was a small reduction in the activation energy for creep in air as compared to the helium atmosphere (Figure 2-73).[4] However, ΔH remained high and continued to fall within the range of activation energies for viscous shear in silicate glasses.[1]
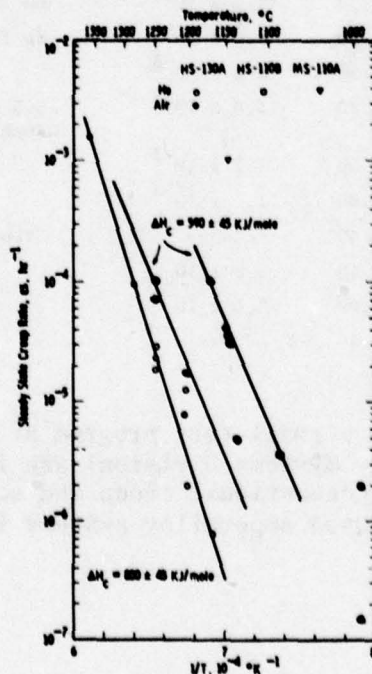
Figure 2-73. Effect of Temperature on the Creep Properties of Norton HS130 Silicon Nitride

77

The bulk of the creep data for HS130 (Noralide NC132) Si_3N_4 in air obtained at Westinghouse R&D is summarized in Table 2-12.[4,5,7].

TABLE 2-12

CREEP PROPERTIES OF NORTON HS130 (NORALIDE NC132) SILICON NITRIDE IN AIR

(3.00 in x 0.250 in gage diam x 1.50 in gage length)

Stress (psi)	Temp (°F)	Rupture Time (hr)	Rupture Strain (%)	Creep Rate (%/hr)	
10,000	1800	1,962	0.49	5.0×10^{-5}	No failure
10,000	2100	1,097	0.55	2.5×10^{-4}	No failure
10,000	2100	10,219	2.65	1.8×10^{-4}	No failure
15,000	2100	1,004	0.85	5.9×10^{-4}	No failure
15,000	2100	161	1.10	2.8×10^{-3}	Reaction in grip
15,000	2100	2,134	2.40	1.1×10^{-3}	
20,000	2100	17	0.33	8.5×10^{-3}	Tested previously
5,000	2300	1,826	4.50	1.4×10^{-3}	
5,000	2300	1,252	2.70	1.1×10^{-3}	
5,000	2300	978	1.05	4.0×10^{-4}	No failure
8,000	2300	2,282	3.50	1.0×10^{-3}	No failure
8,000	2300	331	1.00	1.2×10^{-3}	No failure
8,000	2300	515	3.30	6.0×10^{-3}	
10,000	2300	326	3.80	1.0×10^{-2}	5.5 in x 0.25 in diam x 2.00 in specimen failed at sight size
10,000	2300	322	3.30	7.2×10^{-3}	
10,000	2300	337	1.00	1.2×10^{-3}	
10,000	2300	128	2.40	--	Grip seats deformed
12,000	2300	736	3.40	3.5×10^{-3}	
15,000	2300	384	3.00	3.5×10^{-3}	
15,000	2300	2	1.40	--	

Supplementary results from a small test program at Westinghouse Astronuclear Laboratory (Advanced Energy Systems Division) are included in Table 2-13.[6] These data are plotted in conventional creep and stress rupture form for comparison with typically used superalloy systems in Figures 2-74, 2-75, 2-76 and 2-77.
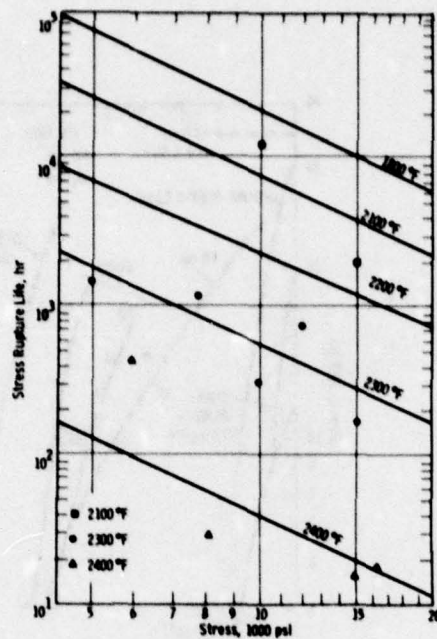
Figure 2-74.   Stress Rupture Properties of HS130
(Noralide NC132) Silicon Nitride
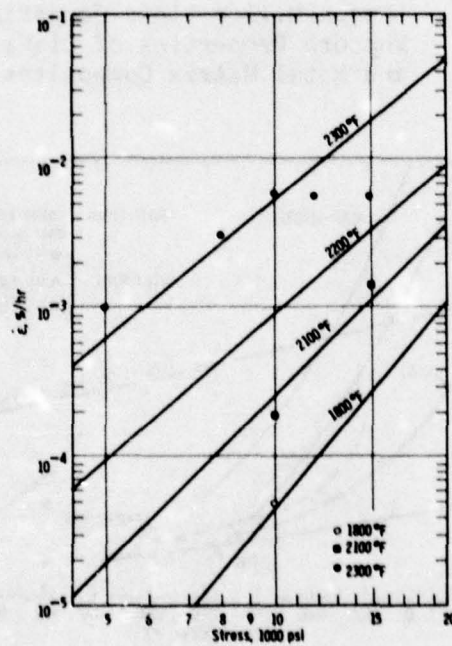
Figure 2-75.   Steady-State Creep Properties of
HS130 (Noralide NC132) Silicon Nitride

79
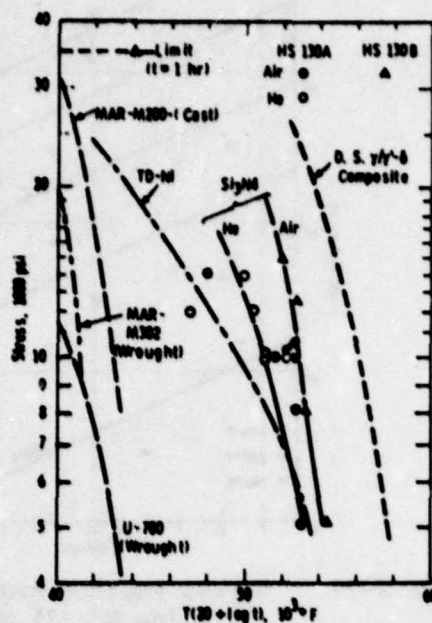
Figure 2-76. Larson-Miller Plots Comparing the Stress Rupture Properties of Si_3N_4 with Superalloys and Metal Matrix Composites
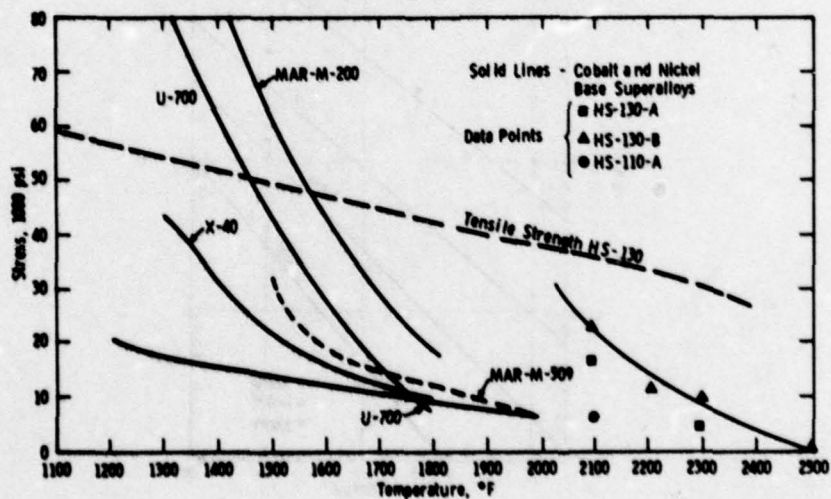
Figure 2-77. The 1000-Hour Stress Rupture Characteristics of of Si_3N_4 and Selected Superalloys

When selected data for stress rupture life at 2300°F are plotted as a function of stress for observed billet chemistry (Table 2-14) in Figure 2-78, two separate lines for HS130A and HS130B fit the results better than a single line to represent all data collectively.[5] The effect of Ca concentration as reflected by steady-state creep rate is evident in Figure 2-79 for temperatures of 2300 and 2100°F. Single datum points at 2500°F and 1800°F (10,000 psi stress) where creep rates approach 1.8×10^{-3} and 1.6×10^{-7}/hr respectively, are not shown.

While the effect of atmosphere on creep in HS130 Si_3N_4 (Noralide NC132) is apparent in Figures 2-78 and 2-79, the most significant aspect remains unidentified. Total elongation in helium rarely exceeds 1 percent, whereas 2.5 to 3.0 percent strain at rupture is characteristic of the hot-pressed silicon nitride in air. Since turbine rotor blading must meet a total strain requirement, creep life has been expressed in terms of maximum allowable tensile strain or 1 percent elongation . The data are reduced to reflect this strain criterion in Figure 2-80. Under conditions of 20,000 psi stress, the life estimates at 2100°F range from 500 to 2000 hours depending upon the calcium concentration of the parent HS130 (Noralide NC132) billet material. There is no need to impose a tensile strain requirement in stator vane applications because the steady-state stresses are not expected to exceed 4000 psi. If the vanes were to deform up to 3 percent by bowing, for example, the effect on performance would be inconsequential.[5]

It is generally agreed that creep deformation results from dislocation motion and/or diffusional creep. In the case of hot-pressed silicon nitride, grain boundary sliding, a diffusional process, presumably predominates.[5] Creep, therefore, can be expressed by:

$$\dot{\varepsilon} = A\,\sigma^n\,\exp^{\Delta H/RT}$$

where ΔH is the activation enthalpy for creep and n is an exponent equal to 2 (Figure 2-79) denoting grain boundary sliding.

Dislocations were identified in silicon nitride.[2] However, the dislocation density was very low and there was no detectable change in dislocation density as a result of creep deformation. The contribution of dislocation motion to creep strain was, at best, a few orders of magnitude less than the observed creep strain.
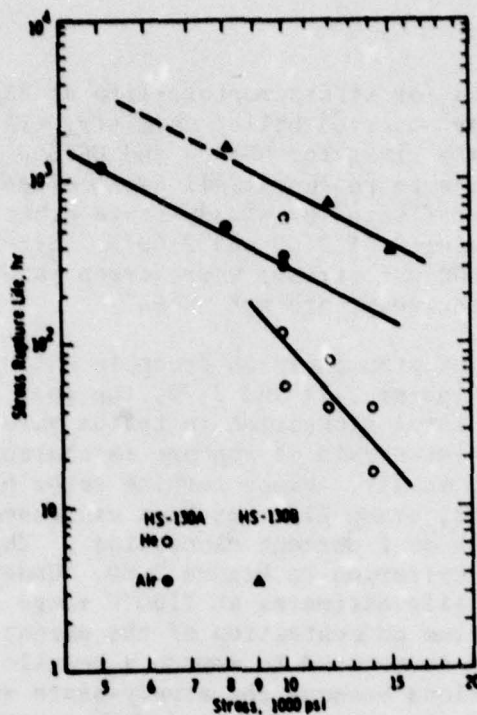
Figure 2-78. The Stress Rupture Properties of Norton HS130 Silicon Nitride at 2300°F
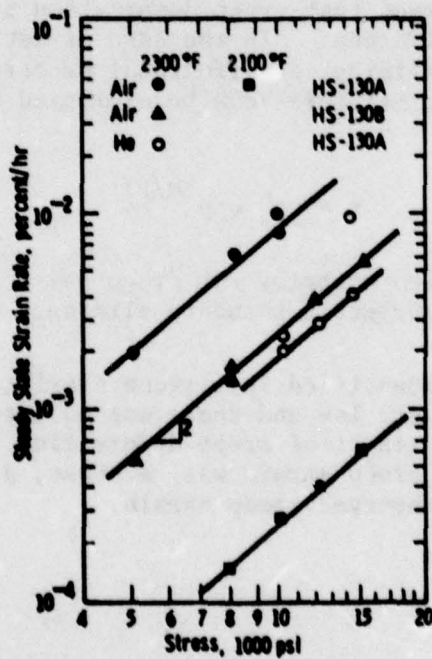
Figure 2-79. Steady-State Tensile Creep Properties of Norton HS130 Silicon Nitride

TABLE 2-13

SUPPLEMENTAL CREEP PROPERTIES FOR Si_3N_4
(Air Atmosphere-Silicon Carbide Grips)

Material	Temp (°F)	Stress (1000 psi)	Rupture Life (hr)	Rupture Strain (%)	Remarks
Si_3N_4 (NC132)	2200	16	7.5	5.2	Suspected grip deform
Si_3N_4 (NC132)	2200	14	0.5	0.15	
Si_3N_4 (NC132)	2200	12	---	---	Broke upon loading
Si_3N_4 (NC132)	2200	40	2.9	0.28	Failed due to temperature cycle
Si_3N_4 (HS130)	2400	6	450	6.7	
Si_3N_4 (HS130)	2400	8	52	4.3	
Si_3N_4 (HS130)	2400	8	20.1	1.9	
Si_3N_4 (HS130)	2400	4	1065	5.5	
Si_3N_4 (HS130)	2400	8	19	2.5	
Si_3N_4 (HS130)	2200	16	21	0.41	
Si_3N_4 (HS130)	2200	15	14	0.2	

TABLE 2-14

CHEMISTRY OF Si_3N_4 BILLETS
(In Weight Percent)

Group Designation	Ca	Na	K	Al	Fe	Mg
HS110-A	0.5	0.002-0.004	0.002-0.004	0.5-1.0	1.0	0.5
HS110-B	0.1-0.2	0.004-0.005	0.004-0.008	0.1	1.0	0.5
HS130-A	0.06-0.08	0.006-0.01	0.004-0.008	0.1-0.2	0.5	0.3-0.4
HS130-B	0.03-0.05	0.004-0.006	0.004-0.006	0.2	0.5	0.3-0.4

Since the grains cannot accommodate the deformation, grain boundary sliding leads to the initiation and steady-state growth of triple point grain boundary wedges which dominate creep deformation in Si_3N_4 (classical second stage of creep). The wedges coalesce to form stable cracks which characterize the third stage of accelerated creep to almost immediate failure. The viscosity of the glass phase at the grain boundary presumably influences the rate of grain boundary sliding.[5]

83
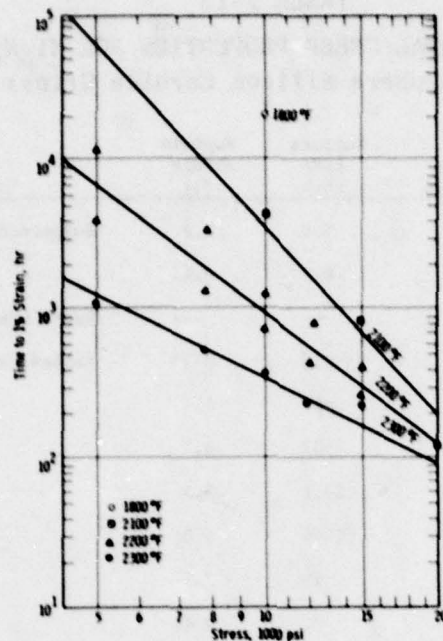
Figure 2-80.   The 1 Percent Tensile Creep Life of HS130
(Noralide NC132) Silicon Nitride

Three other creep experiments were run to clarify important aspects
of creep related phenomena. A 10,000 hour test of HS130 (Noralide NC132)
silicon nitride at 2100°F verified extrapolations from 1000-2000 hour
creep test data (Figure 2-81).[9]   In the second experiment four-point
flexural creep measurements were made on Noralide NC132 (HS130) for
comparison with the tensile creep results.   Steady-state creep rates in
the flexural mode were typically less than half those observed in pure
tension (Figure 2-82.)[6]
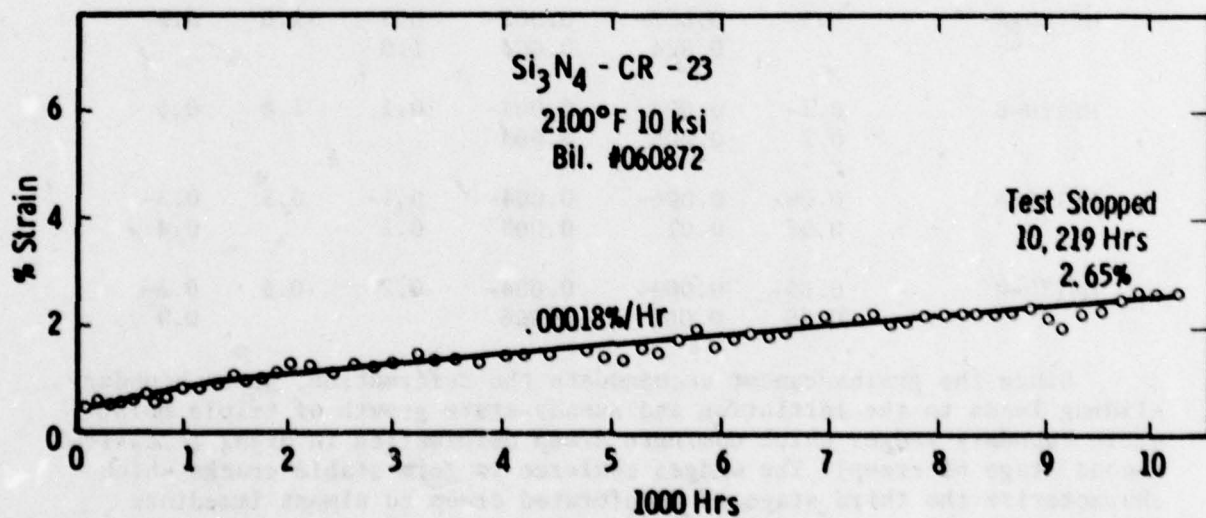
Figure 2-81.   Creep Life of Si_3N_4 (HS130/NC132) at 2100°F
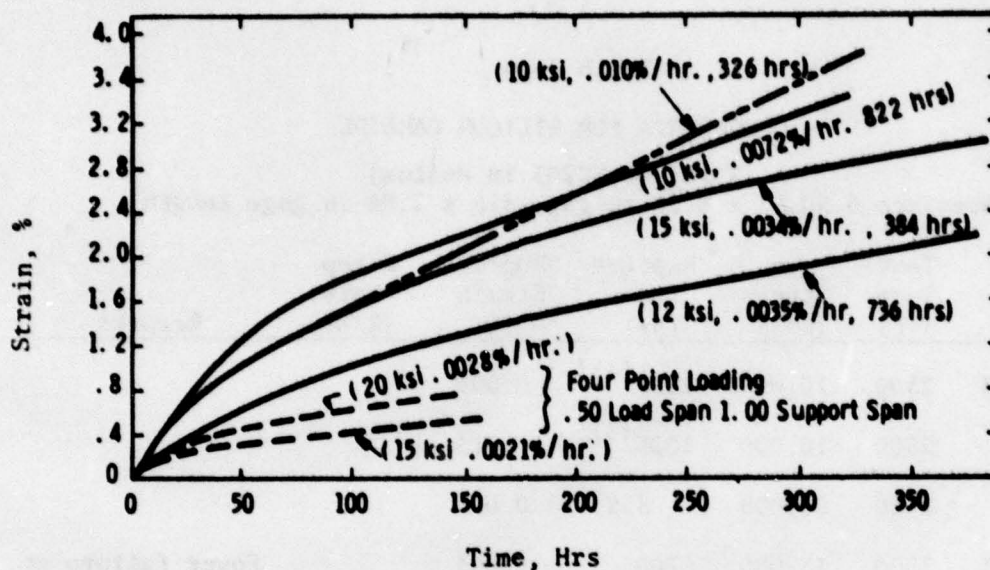
Figure 2-82. Creep of Norton HS130 Silicon Nitride
at 2300°F in Air

Finally, several specimens were preoxidized in air at 2500°F
(alumina muffle furnace) for tensile creep tests in helium at 15,000 psi
stress.[7] The results are summarized in Table 2-15. Preoxidation
increased the stress rupture life of Si_3N_4 in helium by the accommodation
of more strain to failure. While the results indicate an effect of
oxidation, the total creep strain in air is highest because the supply
of fresh oxide is continuous. In helium, some oxide was lost as a
result of the low partial pressure of the system.

TABLE 2-15

CREEP OF PREOXIDIZED Si_3N_4 (HS130)

(Tested in He at 2300°F, 15,000 psi stress)

	No Treatment	Preoxidized 200 hrs, 2500°F
Rupture life (hrs)	75, 44	503
Total Strain (%)	0.8, 0.7	1.17

85

2.4.3.2 Silicon Carbide

Preliminary tensile creep data for Norton hot pressed silicon car-
bide (Noralide NC203), obtained in helium using refractory metal grips
in a Brew furnace, indicated no significant creep at 2300 or 2500°F
after 1000 hours at a static stress of 10,000 psi.[4] One specimen
failed after 6 hours at 2500°F, 20,000 psi stress. Complete results
appear in Table 2-16.[6]

TABLE 2-16

CREEP DATA FOR SILICON CARBIDE

(Noralide NC203 in Helium)
(*Specimen* 5.50 in x 0.25 in gage dia x 2.00 in gage length)

Billet No.	Test Temp (°F)	Stress (psi)	Rupture Time (hr)	Rupture Strain (%)	Creep Rate (%/hr)	Remarks
872-2-14	2300	10,000	1008[4]	0.091		
	2500	10,000	1005[4]	0.013		
	2500	20,000	8.5	0.013		
872-8-41	2500	15,000	709	0.064		Power failure at 687 hours
872-7-28	2500	15,000	308	0.089		

It became difficult to determine the creep properties of NC203
silicon carbide in air.[6] Stress rupture measurements were extremely
erratic (Table 2-17) for creep strains that were consistently small.
In the final analysis, evidence of molten metal reaction between the
specimen and TD nickel-chromium grips, as illustrated in Figure 2-83,
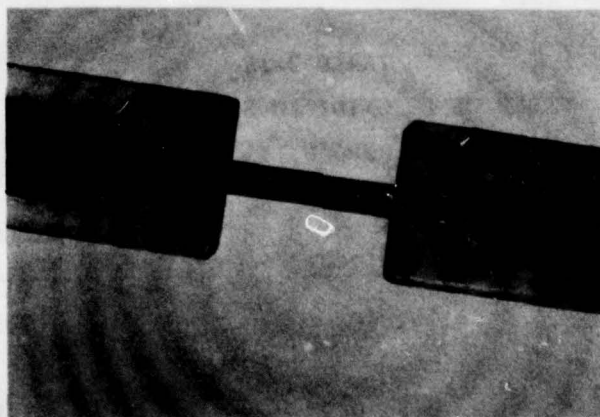
Figure 2-83. Molten Metal/Metal Oxide Silicon Carbide
Reaction *in* High Temperature Stress Rupture
Test (2300°F in Air)

86

made the test data meaningless. Early statements that silicon carbide was stress rupture limited could not be substantiated.[5]

The use of silicon carbide grips did not prove to be satisfactory.[6] Attempts to solve the reaction problem in air or obtain creep data in helium to 3000°F did not materialze because the Noralide NC203 material failed catastrophically in static rig vane tests at 2500°F.[7]

TABLE 2-17

CREEP PROPERTIES OF HOT PRESSED SILICON CARBIDE (NORALIDE NC203)

(In Air at 2300°F)

Stress (1000 psi)	Rupture Life (hr)	Rupture Strain (%)	Steady-State Creep Rate (%)	Remarks
10	<2100	0.3		Reaction with grip
10	650	0.3		
10	455	0.2		Reaction with grip
10	0	-		Failed on loading
10	83	0.4	1.7×10^{-3}	Reaction with grip
10	2131	0.4	9.5×10^{-5}	Did not fail
10	65	0.6	7×10^{-3}	Reaction with grip
15	619	-		SiC grips
15	2 min	-		
15	1 min	-		Reaction with grip
15	1 min	-		Reaction with grip

2.5 FATIGUE PROPERTIES OF HOT PRESSED SILICON NITRIDE (NORTON HS130/ NORALIDE NC132 AND HS110)

2.5.1 INTRODUCTION

The fatigue properties of the structural vane and blade materials used in gas turbines are very important if not critical. High cycle fatigue performance may be service-life limiting, while low cycle fatigue properties as measured mechanically may be indicative of transient thermal response.

The study of silicon nitride was comprehensive indicating extensive fatigue life and no apparent problems. Silicon carbide (Norton Noralide NC203) was never tested because the influence of creep tended to suggest infinite fatigue life. When the SiC failed in static rig tests at 2500°F, plans to determine fatigue properties were cancelled.

2.5.2 FATIGUE TESTING

All of the fatigue tests were performed in the high cycle fatigue machine represented schematically in Figure 2-84.[2] A flat specimen
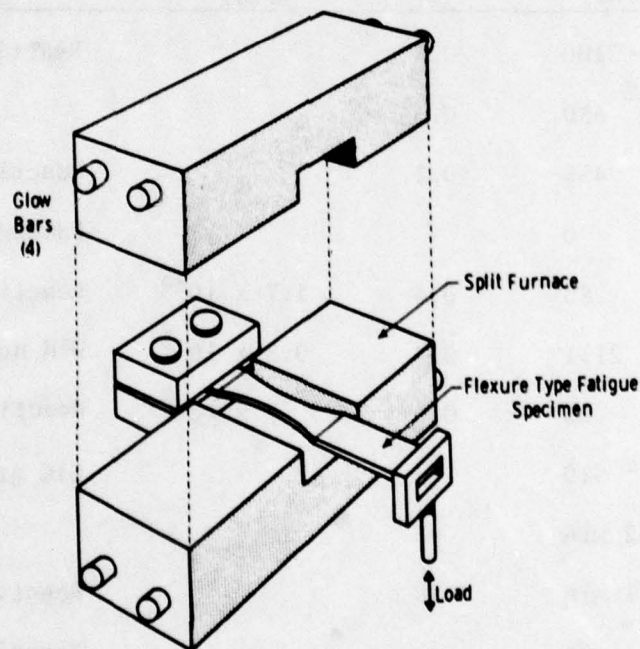
Figure 2-84. Fatigue Test

5.5 in. long x 1.0 in. wide (Figure 2-85) was clamped at one end while
free to move at the other under load applied by an eccentric driver at
1800 rpm. The maximum outer fiber tensile or compressive stress along
the centerline of the gage section was calculated from the cantilever
beam formula:

$$\sigma = \frac{6 \, P\ell}{b \, h^2} \tag{1}$$

where

> P = applied load
>
> ℓ = distance from the load end to the center of the gage section
>
> b = minimal width of the specimen at the gage section
>
> h = specimen thickness in the gage section
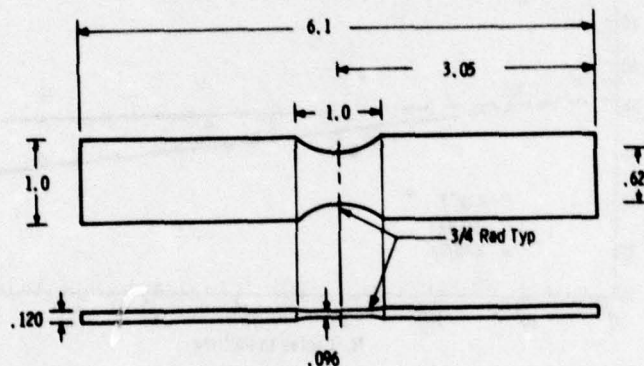
Figure 2-85. Silicon Nitride Fatigue Specimen

The Glo-bar furnace, which was open to the atmosphere, provided
stable temperatures up to 2350°F with variations of no more than 18°F
along the gage section.   A microswitch, placed within the furnace, was
used to terminate tests at the moment of specimen failure. Temperature
fluctuations exceeding ± 45°F would automatically shut off power to the
furnace and driver to ensure reliable results. Tests were run at 472,
2200 and 2350°F.[2]

Fracture surfaces were examined by scanning electron microscopy (SEM) and replica transmission microscopy, using standard two-stage plastic-carbon replication techniques. The flat surfaces near the fractured edge were examined by replica and thin foil transmission electron microscopy. Grain morphology was revealed by etching the specimen at 1380°F for 1 minute in a molten salt consisting of a mixture of 95 parts K_2CO_3 and 15 parts NaF.[2]

2.5.3 FATIGUE TEST RESULTS

Test results appear in Figure 2-86 and 2-87 for HS130 (Noralide NC132) and HS110, respectively. The dispersion of results around the best-fit straight line was very small. Data points marked (a) and (b) (Figure 2-87) were associated with large inclusions observed at the fracture surfaces.[2]
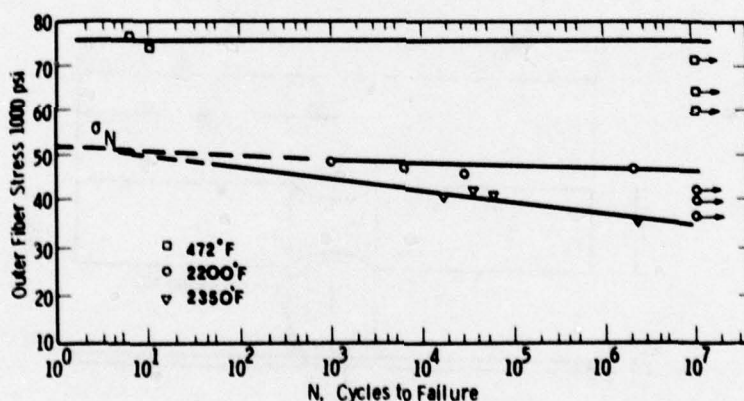
Figure 2-86. Cyclic Fatigue Behavior of Norton HS130 Hot Pressed Si_3N_4

The straight line extrapolations of the 2200 and 2350°F data to one cycle converge at a stress level of 51,000 psi. This was interpreted to indicate that the intrinsic, time-independent strengths were the same. The higher purity material, HS130, did not exhibit time-dependent fatigue behavior at 2200°F. Neither material displayed the phenomenon at 472°F.[2]
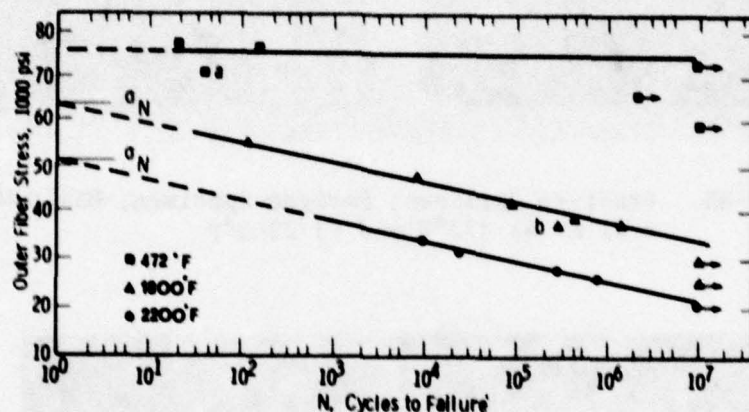
Figure 2-87. Cyclic Fatigue Behavior of Norton HS110 Hot
Pressed Si$_3$N$_4$

Typical fracture surfaces are shown in Figure 2-88. The sharp
facets and the numerous secondary cracks (dark lines on the replica)
indicate that failure occurred by intergranular cracking at 472°F as
well as at 2200°F. The less sharp appearance of Figure 2-88a is due
to a thin layer of oxide that apparently formed on the newly fractured
surface during the few minutes it took to remove the specimen from the
furnace. Similar features were observed on the fractured surfaces of
specimens tested at 1800°F (HS110) and 2350°F (HS130).

Dislocation structures near the outermost stressed surfaces of
specimens tested at 1800 and 2200°F appear in Figure 2-89. These
features represent selected areas of highly localized deformation. The
majority of the grains showed no evidence of a buildup of dislocations
over the original low density, typical of the as-received material
(Figure 2-90a). Helices and stacking faults were observed (Figure 2-89a,
center and top right, respectively). A high density of tangled dislo-
cations is identified in Figure 2-89b. The helical dislocations and
the tangles were not found in the as-received material and must have
formed as a result of the fatigue deformation. Similar observations
were reported on deformed reaction sintered Si$_3$N$_4$.[18]

91
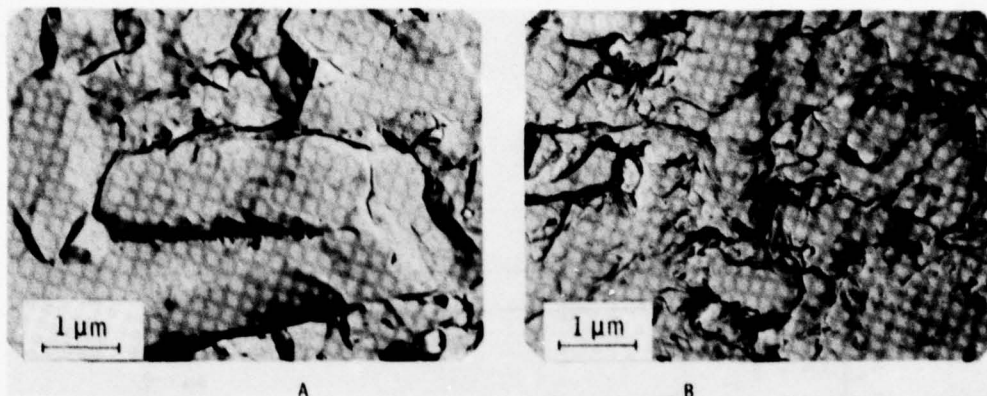
Figure 2-88.   Fracture Surfaces, Fatigue Specimen, HS110 Mate-
rial at a) 472°F and b) 2200°F
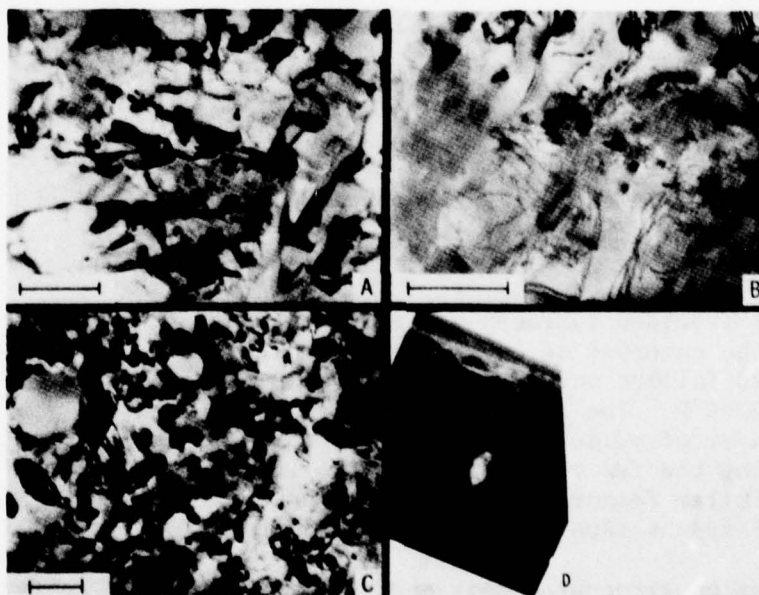
Figure 2-89.   Thin Foil Transmission Micrographs of Fatigue Speci-
mens (0.1 μm Scale Bars)

a.   Helices and stacking faults. Specimen tested at 1800°F
     and 20,000 psi. HS110 material.
b.   Localized deformation in a large grain. Specimens
     tested at 2200°F and 25,000 psi. HS110 material.
c.   Grain boundary sliding in specimen tested at 2350°F,
     and 40,000 psi. HS130 material.
d.   Failure which originated at an inclusion in c.
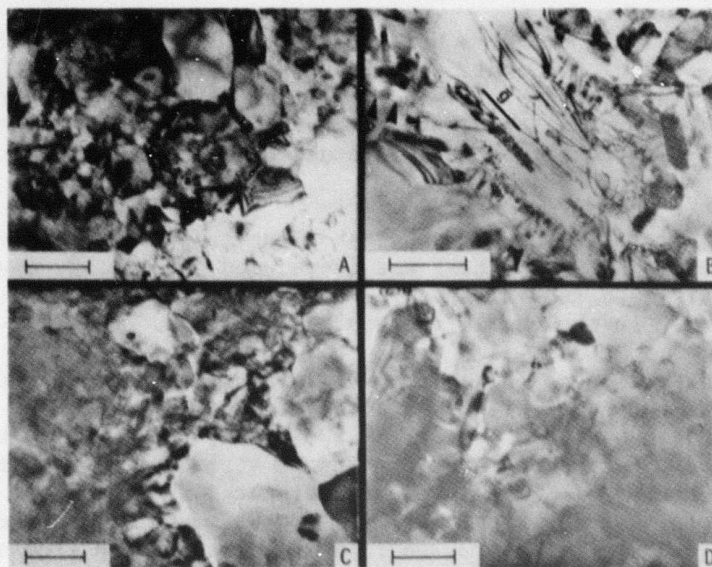
Figure 2-90. Thin Foil Transmission Micrographs of Creep Specimen, HS110 Material (0.1 µ Scale Bars)

a. As-received, not tested material, for comparison
b. Dislocation loops and helices occasionally observed in large grains. Tensile creep specimen, 1800°F, 20,000 psi
c. Tensile surface of a bend-creep specimen, ♦ hours at 2200°F, 38,000 psi. Note grain boundary sliding and separation
d. Same specimen as in c. Compressive surface. Note triple-point cavitations and boundary sliding.

A different mode of deformation was observed in specimens fatigued at 2350°F. Although evidence of localized dislocation motion was found, grain boundary sliding was more prominent (Figure 2-89c). The foil for this particular micrograph was cut from the interior of the specimen in an area of high stress concentration near a large inclusion (Figure 2-89d), the probable site of failure initiation. Triple-point cavitations and grain boundary separations are indicative of grain boundary sliding, for example, in alumina.[19]

A clear cut case cannot be made for the application of an elastic stress corrosion model for the fatigue behavior of Si_3N_4 at high temperatures. Although massive dislocation motion is not likely to occur in hot

pressed Si_3N_4 at temperatures below 3100°F,[20] the microstructures shown
in Figure 2-89 indicate that localized contributions from either disloca-
tion motion grain boundary sliding or diffusional creep cannot be ruled
out.[21] The latter visco-elastic mechanisms are probable because high
strength and high density in Si_3N_4 result from hot pressing in the
presence of a liquid phase.[2]

Tensile creep and bend creep tests were conducted to examine these
possibilities. The static test was introduced because visco-elastic
mechanisms are rate sensitive and may be affected by the high rates of
strain realized in the cyclic fatigue test. [2]

A flat specimen, 2 inches long, 1/2 inch wide and 1/8 inch thick,
prepared from the HS110 Si_3N_4 was placed in a four-point bend fixture
and subjected to a static load of 38,000 psi at 2200°F for 4 hours.[2]
A permanent set corresponding to a plastic strain of 0.01 on the outer
surface was measured. Thin foils were prepared from both the tensile
and the compressive surfaces. Typical microstructures are shown in Fig-
ure 2-90 (c and d). Figure 2-90b is a micrograph taken from a foil
prepared from the tensile-creep specimen. This particular specimen was
6 inches long, with a 1/4 inch diameter and 1 inch long gage section.
It failed at 1800°F under 20,000 psi stress after plastic strain of
0.0025 inch occurred. Figure 2-90b indicates that limited dislocation
motions occurred during creep deformation as evidenced by the helices
and the dislocation loops present in the large grain. Triple-point
cavitation and grain boundary separations are also detectable. The
latter, which are quite dominant in the bend creep specimen, occur
on both the tensile (Figure 2-90c) and compressive (Figure 2-90d)
surfaces.

By application of

$$\varepsilon = \rho bx \tag{2}$$

where ε is the plastic strain, ρ the dislocation density, b the Burger's
vector and x the average distance a dislocation moved, the dislocation's
contribution to the measured plastic strain was found to be less than
10^{-5}.[22] Therefore, the major contribution to the permanent deformation
during creep is derived from boundary sliding.

Boundary sliding was probably inhibited in the cyclic fatigue tests,
where the average strain rate was 3 in/in/min, or about six orders of
magnitude higher than the average strain rate in the creep tests. This
was certainly the case for temperatures up to 2200°F. [2]

Hillig and Charles[23] considered the fatigue failure of a brittle
material as an elastic medium. The time-dependent failure of the material

94

was attributed to a slow growth of preexisting flaws as a result of a corrosion process under load. Charles and Shaw[24] expressed the local rate of growth of the flaw as:

$$V = V_o \exp - [Q - V^*\sigma + B]/RT \qquad (3)$$

where Q represents the activation energy of the process, V^* the activation volume, σ the applied stress and B is related to the geometry of the crack tip. Developing Equation (3) further, Charles and Shaw obtained:

$$d(\sigma/\sigma_N)/d\ln t = - \frac{RT}{V^*\sigma_{th}} \qquad (4)$$

Here, the left-hand side is the slope of the line in a plot of σ/σ_N as a function of the life time, where σ is the applied stress for a given fatigue test, t is the time to failure, σ_N and σ_{th} are the time-dependent and the theoretical strengths of the material, respectively.

The fatigue data of Figure 2-87 are replotted in terms of σ/σ_N as a function of life time in Figure 2-91. The time-dependent strength, σ_N, for the particular mode of bending employed in the tests, was taken as the extrapolated value of σ at one cycle. At 1800°F, σ_N = 63,000 psi and at 2200°F, σ_N = 51,000 psi.[2]
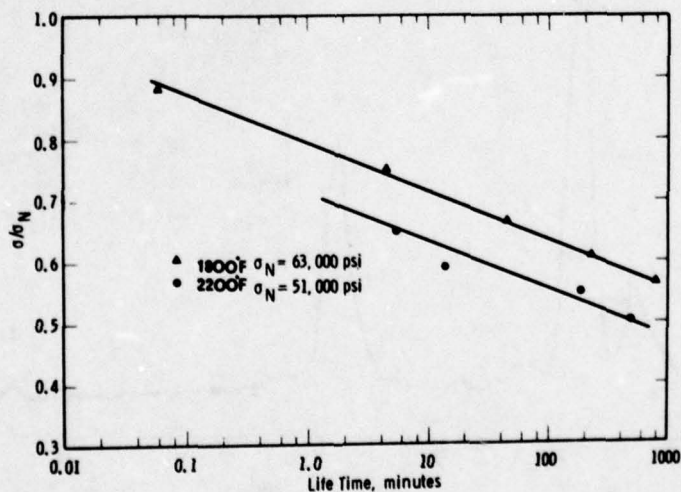
Figure 2-91. Normalized Stress as a Function of Life Time, HS110 Grade Si_3N_4

95

The theoretical strength of Si_3N_4 is 9×10^6 psi as calculated from $\sigma_{th} = E/S$. From Figure 2-91, $d(\sigma/\sigma_N/d\ln t = -0.08$. Activation volumes as calculated from Equation (4) become:

$$V^* \ (1800°F) \ \approx \ 4.6 \ cc/mole$$

$$V^* \ (2200°F) \ \approx \ 5.5 \ cc/mole$$

These results compare favorably with a value of 4.0 cc/mole, the activation volume for alkali metal ion diffusion in silicate glasses.[24]

Corrosion results (Figures 2-92 and 2-93) indicate that diffusion of Ca and Mg occurred, forming magnesium-calcium-silicates on the surface. These compositions have much lower melting points than the pure silicates.[25] It is quite plausible, in the absence of a plastic mechanism, that the fatigue life is controlled by slow crack growth occurring as a result of the formation of low melting glasses through a corrosion mechanism in air.[2]

Curve 645904-A

Phases: $Mg(Ca, Fe)SiO_3$ and $MgCa(SiO_3)_2$
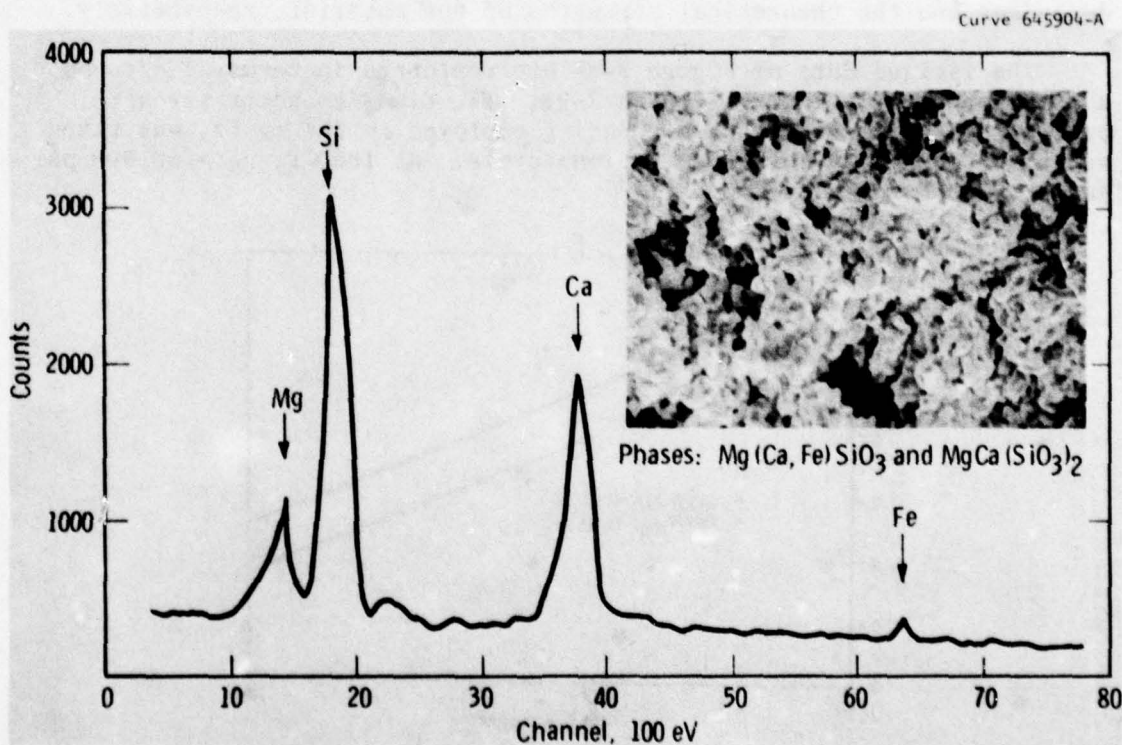
Figure 2-92. Nondispersive X-ray Analysis of Corrosion Layer, HS110 Material, 8 Hours at 2200°F in Air
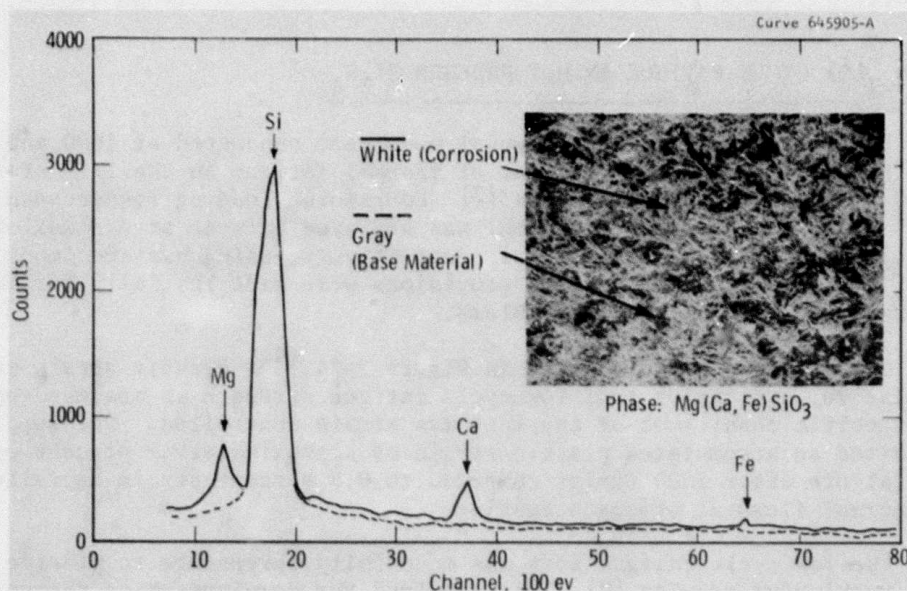
Figure 2-93. Nondispersive X-ray Analysis of Corrosion Layer, HS130
Material, 100 Hours at 2200°F in Air

Equation (3) provides an estimate of the activation energy from
Figure 2-91. If B in Equation (3) is independent of stress and tempera-
ture and $V^*\sigma$ is less than 0.5 kcal/mole:

$$Q \simeq \frac{R \, \Delta \, l \, nt}{\Delta \, \frac{1}{T}} \qquad (5)$$

For any given value of σ/σ_N, $Q \approx 65$ kcal/mole is obtained for the activa-
tion energy of the corrosion process. This value compares with 89.5 kcal/
mole obtained from studies of the kinetics of oxidation of hot pressed
Si_3N_4.[2]

Reference may be made again to the time-independent fatigue behavior
of HS130 material at 2200°F (Figure 2-86). The rate of oxidation of
HS130 is lower than that of the less pure HS110 material by more than
an order of magnitude. According to Hillig and Charles[23] certain con-
ditions of stress corrosion may sharpen flaws at a rate which just
balances the rounding effect of the stress concentration at the flaw
tip. Under such conditions, slow crack propagation will not occur and
a time-dependent fatigue behavior will not be observed. At room tempera-
ture neither oxidation nor plastic deformation occurs, and therefore no
time-dependent fatigue behavior is observed in HS130 silicon nitride.

2.5.4   LOW CYCLE FATIGUE IN HOT PRESSED Si$_3$N$_4$

Low cycle tests in the flexural mode were conducted at 1800 and 2300°F in air to model the effect of thermal fatigue on the life of HS130 silicon nitride components.[3]   Four-point loading (inner span - 0.375 inch, outer span 0.875 inch) was employed between stress maxima and minima of 20,000 and 5000 psi, respectively, using bar specimens 0.125 x 0.25 x 1.25 inches.   No provisions were made initially for load reversal to avoid alignment problems.

Cursory data are presented in Figure 2-94.[4]   Plastic strain was cumulative, indicating that low cycle fatigue strength as measured under the specific conditions of the test was strain controlled.   One specimen exhibited an accumulated plastic strain of approximately 2 percent without failure after 2000 cycles compared to 0.5 percent strain at failure for normal flexural strength testing.

The low cycle fatigue test was made fully reversible to provide more meaningful results.[6]   This required the development of the special KT silicon carbide fixture illustrated in Figure 2-95.   The actual test setup is shown in Figure 2-96.   Top and bottom surfaces of the test specimens were stressed alternately in tension and compression to complete each test cycle.
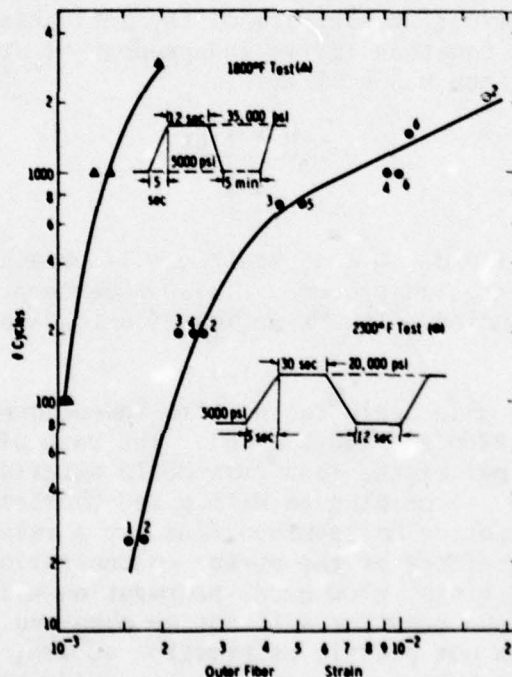
Figure 2-94.   Low Cycle Fatigue Results for Norton HS130
Si$_3$N$_4$ in Air
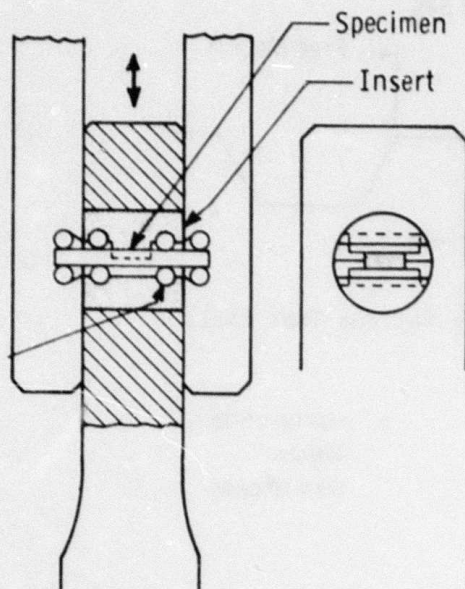
Figure 2-95.   Detail of Low Cycle
              Fatigue Fixture
              Loading Points
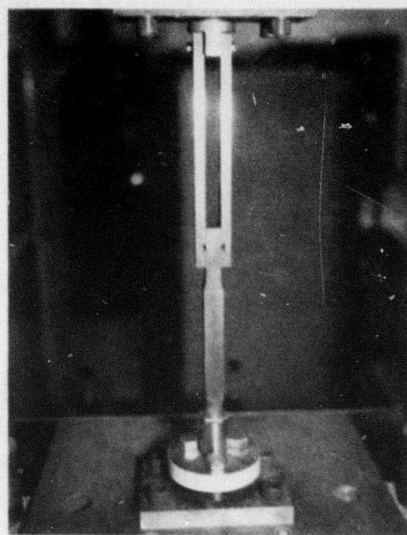
Figure 2-96.   Assembled Low Cycle
              Fatigue Fixture in
              Test Machine Without
              Furnace

Testing was performed on a Baldwin FGT universal test machine at
frequencies of 0.15 to 1.5 cycles per minute with 0.5 cycle per minute
(30 second hold time at maximum stress) most commonly employed. A
typical test cycle appears in Figure 2-97. Timers were added to the
machine control circuit to provide variable hold time capability at
selected stress levels. The machine was operated on load control with
a deflection control circuit operating to terminate the test upon speci-
men failure. When load was applied, reduced, and reapplied in the
fashion of a sine wave, no failures were recorded after 1500 cycles. [6]
Life ranged from 14 to 1640 cycles, however, when a hold time at maximum
stress was imposed. The fatigue characteristics of silicon nitride are
compared in Figure 2-98. Complete data are tabulated in Table 2-18.
Results for billets 7 and 10 appear to be erratic with an indication of
relatively short fatigue life. Billet 2, for which there were only two
values, performed in a significantly superior manner. HS130 silicon
nitride appeared to be sensitive to low cycle fatigue damage emanating
from some undefined characteristic of microstructure and composition. [7]

99
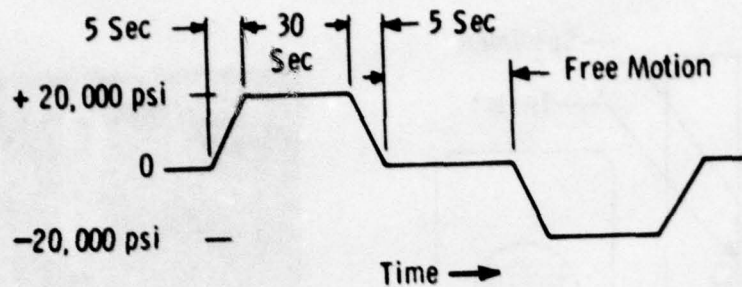
Figure 2-97. Typical Low Cycle Fatigue Test Cycle
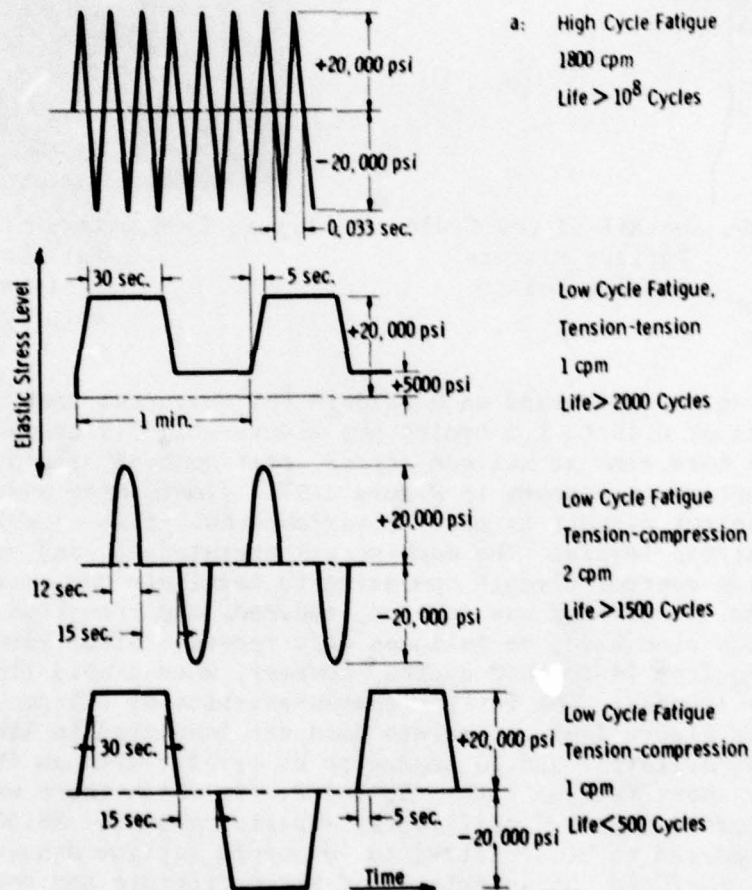
Figure 2-98. Schematic of Fatigue Response in HS130 Si_3N_4 at 2300°F in Air

100

TABLE 2-18

LOW CYCLE FATIGUE PROPERTIES*OF SILICON NITRIDE AT 2300°F

Test	Billet	Hold Stress (psi)	Time (sec)	Cycles to Failure	Remarks
1	10	None	None	139	Stopped
2	10	None	None	1190	Stopped
3	10	20,000	30	107	
4	10	20,000	30	14	No flaw indications
5	10	20,000	30	640	
6	10	20,000	30	78	
7	10	20,000	30	9	Flaw indication
8	10	20,000	30	5	Flaw indication
9	10	20,000	30	--	
10	10	20,000	30	22	Flaw indication
11	10	20,000	30	82	No flaw indications
12	7	20,000	30	293	
13	7	20,000	30	155	
14	7	20,000	15	213	
15	15	20,000	15	338	
16	2	30,000	30	606	
17	2	30,000	30	2095	

*Tension/Compression

101

2.6 THERMAL PROPERTIES

2.6.1 INTRODUCTION

The thermal properties of HS130 (Noralide NC132) silicon nitride and Noralide NC203 silicon carbide[26] were measured by the Battelle Memorial Institute (BMI) under subcontract to Westinghouse Research and Development. Specific heat, thermal expansion and thermal diffusivity as a measure of thermal conductivity were determined as a function of temperature from RT (68°F) to 2500°F.

2.6.2 SPECIFIC HEAT

Specific heat values were determined from enthalpy data obtained in a Bunsen ice calorimeter.[4] The apparatus is shown in Figure 2-99.

In the Bunsen ice calorimeter, heat given up by the specimen melted ice which was in equilibrium with outgassed distilled water in the closed calorimeter well. Mercury entered the systems from an external weight accounting source to make up the change in volume. The weight of the mercury making up the volume change was directly proportional to specimen
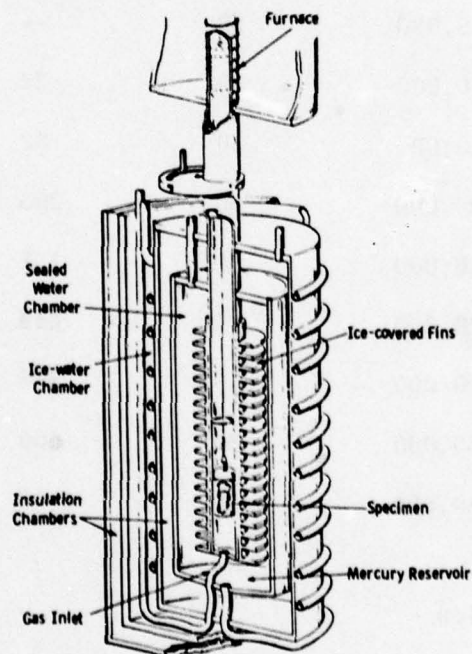
Figure 2-99. Battelle Ice Calorimeter

102

enthalpy or heat liberated by the specimen when cooling from an elevated temperature to the ice point. Specific heat was then calculated by the relation

$$C_p = \frac{dH}{dT}$$

where

    C_p = specific heat at elevated temperature

    H = enthalpy

    T = temperature

Samples were encapsulated in tantalum and heated in a furnace above the calorimeter well. Each specimen was dropped into the well and allowed to cool. Separate drops were made with an empty Ta capsule with equivalent surface emittance conditions to determine the contribution of heat from the specimen by difference. The process was repeated through the temperature range of interest to establish an enthalpy versus temperature curve which was used in conjunction with the specific heat equation to obtain the specific heat.

The specific heat of Norton HS130 (Noralide NC132) silicon nitride is reported in Figure 2-100 and Table 2-19. Comparative results for
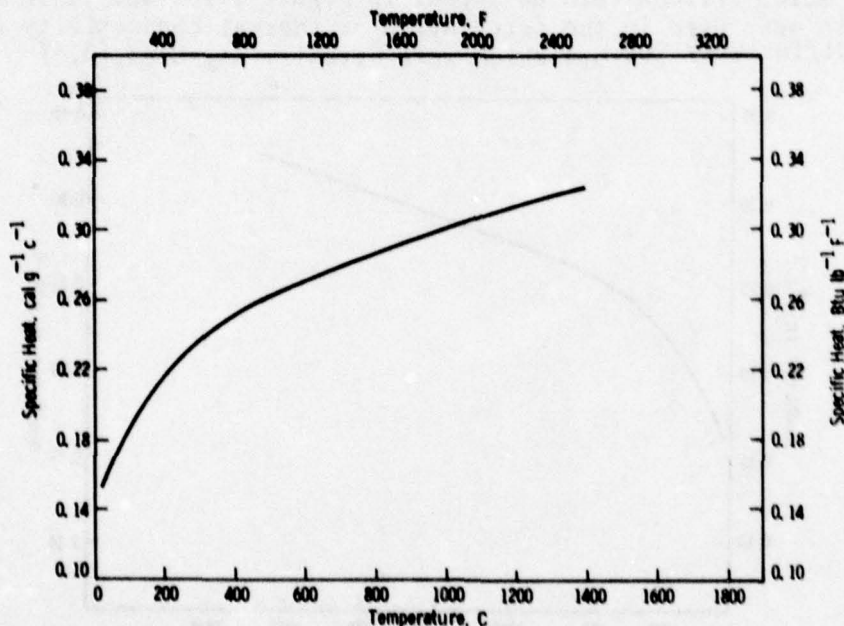
Figure 2-100. Specific Heat of Silicon Nitride

103

TABLE 2-19

SPECIFIC HEAT OF SILICON NITRIDE

Temperature		Specific Heat	
(°C)	(°F)	(cal g^{-1} C^{-1})	(Btu lb^{-1} F^{-1})
25	77	0.153	0.153
100	212	0.184	0.184
200	392	0.214	0.214
300	572	0.235	0.235
400	752	0.250	0.250
500	932	0.260	0.260
600	1112	0.269	0.269
700	1292	0.277	0.277
800	1472	0.284	0.284
900	1652	0.291	0.291
1000	1832	0.298	0.298
1100	2012	0.305	0.305
1200	2192	0.311	0.311
1300	2372	0.317	0.317
1400	2552	0.323	0.323

Noralide NC203 silicon carbide appear in Figure 2-101 and Table 2-20.[4] These data were used in the calculation of thermal conductivity from thermal diffusivity values which were actually measured.[3,4]
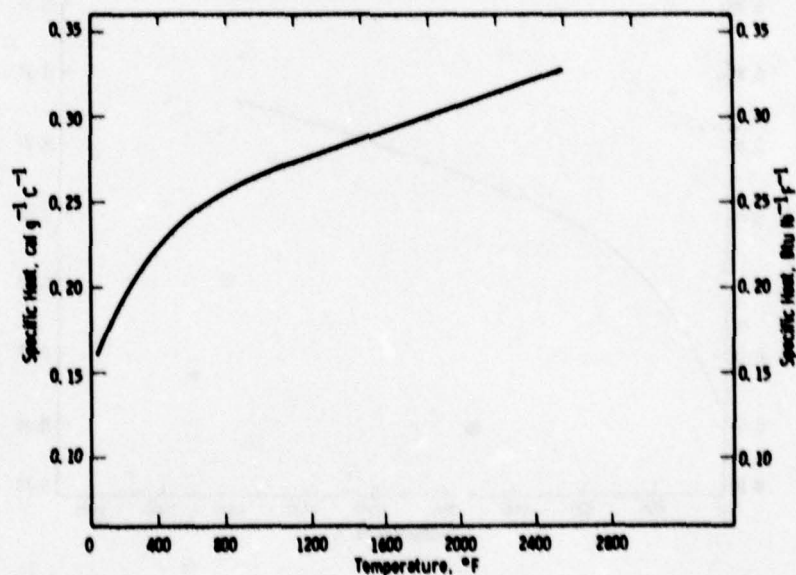
Figure 2-101. Specific Heat of Norton Hot Pressed Silicon Carbide

104

TABLE 2-20

SPECIFIC HEAT OF HOT PRESSED SILICON CARBIDE

Temperature		Specific Heat	
(°F)	(°C)	(Cal g^{-1} C^{-1})	(Btu lb^{-1} F^{-1})
77	25	0.162	0.162
212	100	0.195	0.195
392	200	0.224	0.224
572	300	0.243	0.243
752	400	0.256	0.256
932	500	0.265	0.265
1112	600	0.273	0.273
1292	700	0.280	0.280
1472	800	0.287	0.287
1652	900	0.294	0.294
1832	1000	0.301	0.301
2012	1100	0.308	0.308
2192	1200	0.315	0.315
2372	1300	0.322	0.322
2552	1400	0.328	0.328

2.6.3 THERMAL EXPANSION

Thermal expansion was measured directly by tracking the relative displacement of fiducial marks on the silicon nitride or silicon carbide specimens with telemicroscopes fitted with filar eye pieces.[2] The apparatus is illustrated schematically in Figure 2-102. Suitably marked
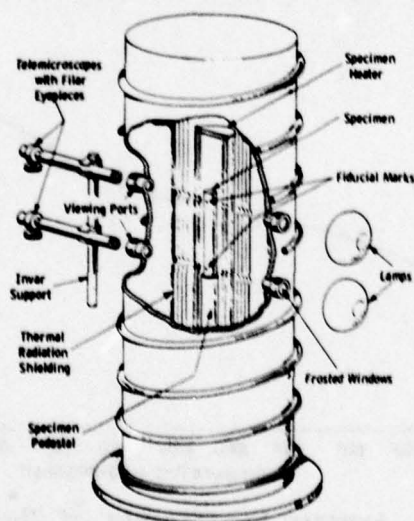
Figure 2-102. Battelle High Temperature Dilatometer for Direct View Expansion Measurements

105

specimens were supported within a tube furnace which was enclosed in an insulated vacuum/atmosphere chamber. Dilation on heating or cooling was tracked manually with the microscopes. Specimen temperature was measured by thermocouple or optical pyrometer. Dilations of the order or 7 x 10⁻⁶ inch were measured on specimens nominally 2-3/4 inches in length.

Data for HS130 silicon nitride are reported in Figures 2-103 and 2-104 and Table 2-21.(3) Comparative values for NC203 silicon carbide are presented in Figures 2-105 and 2-106 and Table 2-22.(4)
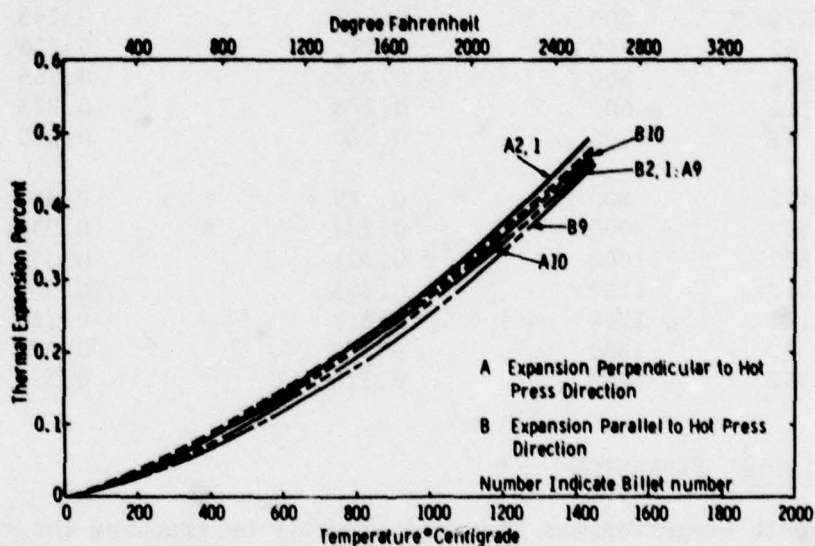
Figure 2-103. Thermal Expansion of Hot Pressed Silicon Nitride as a Function of Temperature
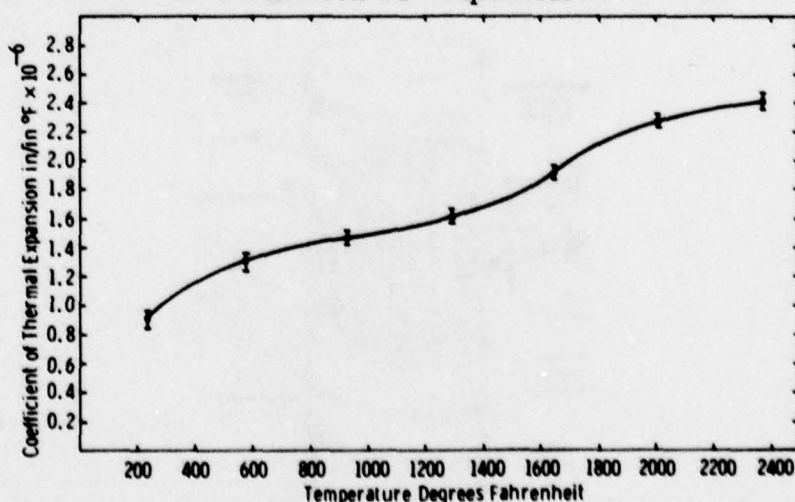
Figure 2-104. Average Coefficient of Thermal Expansion for Norton HS130 Si₃N₄ (Noralide NC132)

106

TABLE 2-21

AVERAGE THERMAL EXPANSION IN NORTON HS130 (NORALIDE NC132) SILICON NITRIDE

Temperature		Expansion (%)	
(°C)	(°F)	Parallel, Weak	Perpendicular, Strong
25	77	0.000	0.000
330	626	0.053	0.063
620	1148	0.143	0.145
975	1787	0.265	0.273
1092	1998	0.310	0.319
1179	2154	0.356	0.360
1296	2365	0.403	0.412
1367	2493	0.445	0.449
1227	2241	0.384	0.382
1107	2025	0.330	0.343
812	1494	--	0.210
496	925	--	0.109
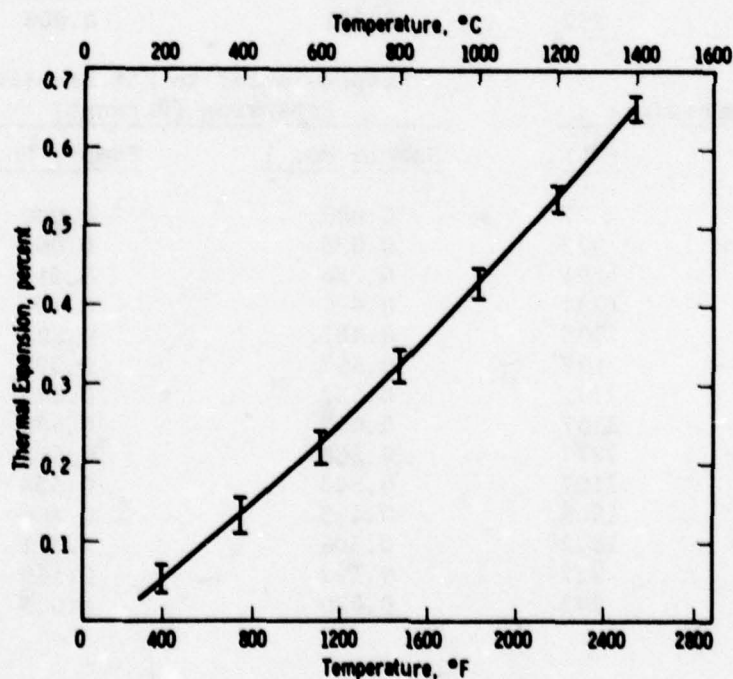
Figure 2-105.   Thermal Expansion of Norton Hot Pressed Silicon Carbide

107

TABLE 2-22

THERMAL EXPANSION OF SILICON CARBIDE

Temperature		Parallel to Hot Pressing Expansion (Percent)	
(°C)	(°F)	Sample No. 3	Sample No. 4
25	77	0.000	0.000
319	606	0.069	0.071
647	1197	0.217	0.219
965	1796	0.391	0.391
1091	1996	0.461	0.463
1193	2179	0.530	0.533
1303	2377	0.579	0.590
1370	2498	0.613	0.624
1249	2280	0.547	0.556
1155	2111	0.495	0.500
1049	1920	0.428	0.433
832	1530	0.303	0.309
501	934	0.150	0.152
122	252	0.001	0.004

Temperature		Perpendicular to Hot Pressing Expansion (Percent)	
(°C)	(°F)	Sample No. 1	Sample No. 2
25	77	0.000	0.000
300	572	0.075	0.069
644	1191	0.226	0.215
979	1794	0.426	0.434
1095	2003	0.487	0.503
1203	2197	0.567	0.575
1311	2392	0.632	0.645
1375	2507	0.667	0.680
1247	2277	0.588	0.602
1153	2107	0.523	0.534
1043	1909	0.463	0.466
828	1522	0.306	0.311
497	927	0.152	0.169
145	293	0.020	0.033
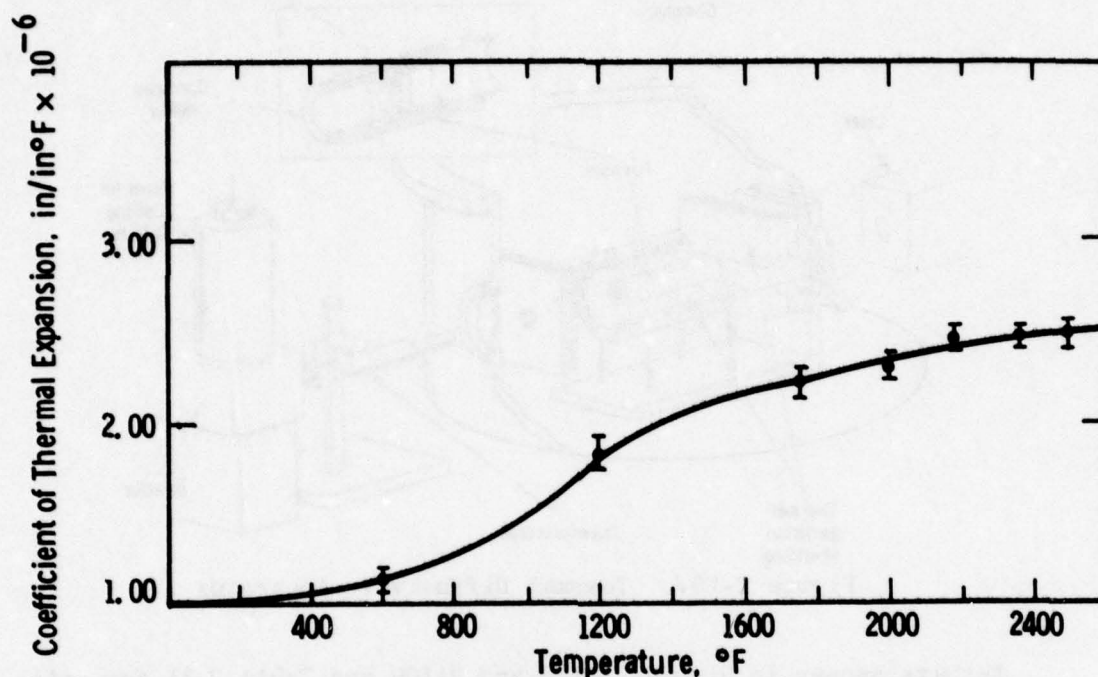
Figure 2-106. Average Coefficient of Thermal Expansion of Norton Noralide NC203 Silicon Carbide

2.6.4 THERMAL CONDUCTIVITY

Thermal conductivity was measured by a flash thermal diffusivity method, where diffusivity was determined by the transient behavior of a specimen subjected to a short-time thermal pulse on one of its sides.[2] The apparatus appears in Figure 2-107. A thin disc-shaped specimen was placed in the isothermal zone of a furnace and irradiated on the front face by a short-duration laser pulse. As the heat pulse traveled through the specimen, its back-face temperature rise was recorded as a function of time. The temperature-time history was related directly to the thermal diffusivity of the specimen by means of the equation

$$d = \frac{0.139L^2}{t_{1/2}}$$

where

d = thermal diffusivity

L = specimen thickness

$t_{1/2}$ = time required for back-face temperature to reach 1/2 its maximum temperature rise

109
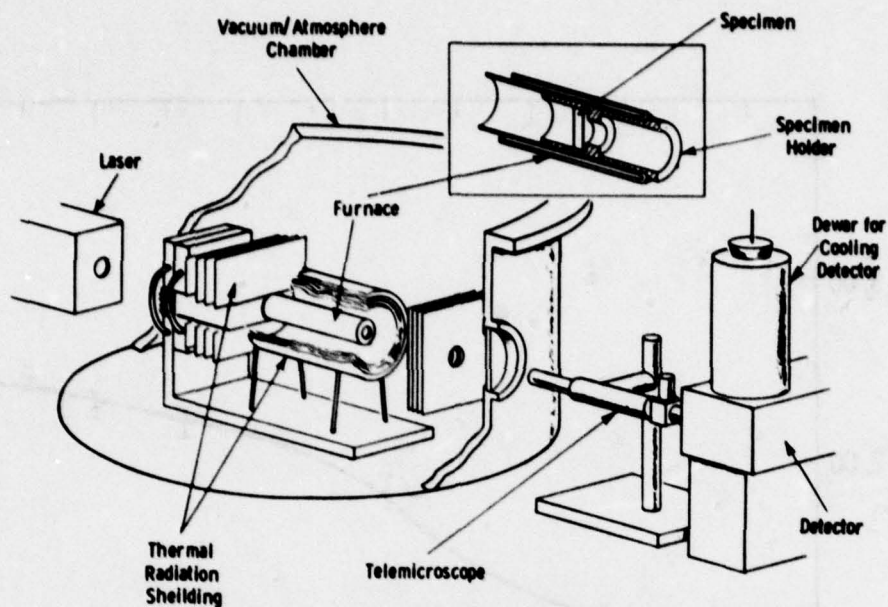
Figure 2-107. Thermal Diffusivity Apparatus

Results appear in Figures 2-108 and 2-109 and Table 2-23 for silicon nitride and Figure 2-110 and Table 2-24 for silicon carbide.

When thermal conductivity was derived as the product of thermal diffusivity, density and specific heat, the calculations yielded Figures 2-111 and 2-112 with Table 2-25 for silicon nitride[3] and Figure 2-113 with Table 2-26 for silicon carbide.[4]
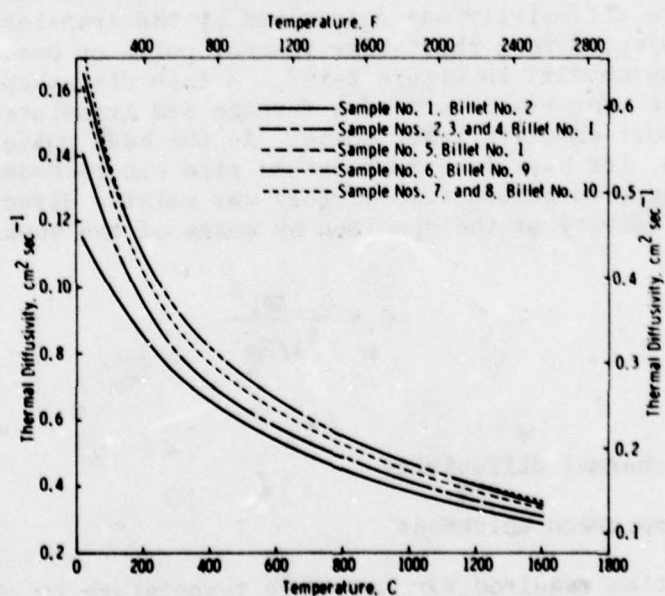
Figure 2-108. Comparison of Thermal Diffusivity Values for Heat Conducted Parallel to the Hot Pressing Direction in Silicon Nitride

110
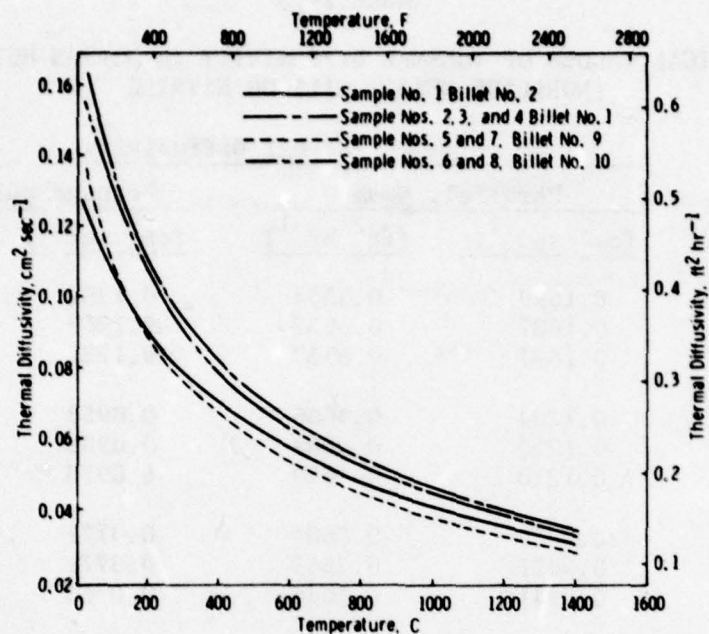
Figure 2-109.   Comparison of Thermal Diffusivity Values for Heat
Conducted Perpendicular to the Hot Pressing
Direction in Silicon Nitride
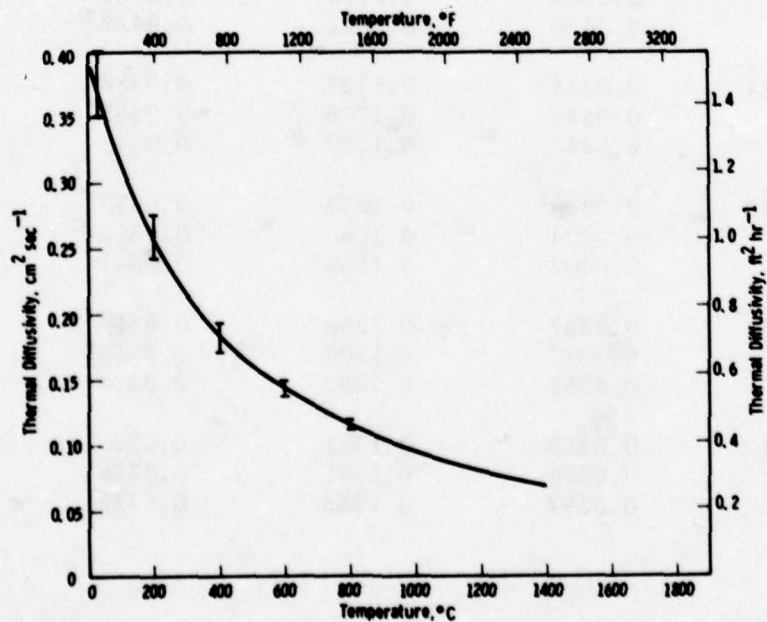
Figure 2-110.   Thermal Diffusivity of Norton Hot Pressed
Silicon Carbide

111

TABLE 2-23

TYPICAL VALUES OF THERMAL DIFFUSIVITY IN NORTON HS130 (NORALIDE NC132) SILICON NITRIDE

| Temperature | | Thermal Diffusivity | | | |
| | | Parallel, Weak | | Perpendicular, Strong | |
(°C)	(°F)	($cm^2 sec^{-1}$)	($ft^2 hr^{-1}$)	($cm^2 sec^{-1}$)	($ft^2 hr^{-1}$)
25	77	0.1699	0.6584	0.1259	0.4879
		0.1687	0.6537	0.1263	0.4894
		0.1687	0.6537	0.1237	0.4793
146	295	0.1204	0.4666	0.0958	0.3712
		0.1210	0.4689	0.0953	0.3693
		0.1210	0.4689	0.0973	0.3770
299	570	0.0930	0.3604	0.0771	0.2988
		0.0921	0.3569	0.0771	0.3011
		0.0941	0.3646	0.0769	0.2980
671	1240	0.0614	0.2379	0.0552	0.2139
		0.0621	0.2406	0.0546	0.2116
		0.0620	0.2403	0.0547	0.2120
992	1818	0.0474	0.1837	0.0424	0.1643
		0.0464	0.1798	0.0423	0.1639
		0.0470	0.1821	0.0419	0.1624
1101	2014	0.0444	0.1721	0.0388	0.1504
		0.0446	0.1728	0.0386	0.1496
		0.0441	0.1709	0.0386	0.1496
1211	2212	0.0406	0.1573	0.0359	0.1391
		0.0404	0.1566	0.0362	0.1403
		0.0402	0.1558	0.0361	0.1399
1291	2356	0.0387	0.1500	0.0335	0.1298
		0.0387	0.1500	0.0333	0.1290
		0.0387	0.1500	0.0334	0.1294
1378	2512	0.0359	0.1391	0.0326	0.1263
		0.0359	0.1391	0.0326	0.1259
		0.0357	0.1383	0.0328	0.1271

TABLE 2-24

THERMAL DIFFUSIVITY OF NORTON SiC

Temp (°F)	Parallel to Hot Pressing Thermal Diffusivity (cm^2 sec^{-1})	(ft^2 hr^{-1})	Temp (°F)	Perpendicular to Hot Pressing Thermal Diffusivity (cm^2 sec^{-1})	(ft^2 hr^{-1})
75	0.4043	1.5667	77	0.4162	0.6128
	0.4121	1.5969		0.4267	1.6535
	0.4157	1.6108		0.4317	1.6728
329	0.3004	1.1641	298	0.2800	1.0850
	0.2974	1.1524		0.2772	1.0742
	0.2974	1.1524		0.2835	1.0986
597	0.2186	0.8471	565	0.2044	0.7921
	0.2154	0.8347		0.2088	0.8091
	0.2231	0.8645		0.2059	0.7979
931	0.1430	0.5541	1186	0.1345	0.5247
	0.1431	0.5545		0.1359	0.5266
	0.1415	0.5483		0.1360	0.5270
1818	0.0991	0.3840	1791	0.0940	0.3643
	0.1002	0.3883		0.0967	0.3747
	0.1000	0.3875		0.0952	0.3689
1998	0.0882	0.3418	2026	0.0848	0.3286
	0.0868	0.3364		0.0843	0.3267
	0.0872	0.3379		0.0847	0.3282
2174	0.0797	0.3088	2194	0.0776	0.3007
	0.0802	0.3108		0.0789	0.3057
	0.0801	0.3104		0.0779	0.3019
2367	0.0743	0.2879	2363	0.0736	0.2852
	0.0743	0.2879		0.0781	0.2782
	0.0753	0.2918		0.0727	0.2817
2498	0.0697	0.2709	2494	0.0693	0.2685
	0.0697	0.2709		0.0694	0.2689
	0.0701	0.2717		0.0693	0.2685
2275	0.0784	0.3038			
	0.0782	0.3030			
	0.0772	0.2992			

113
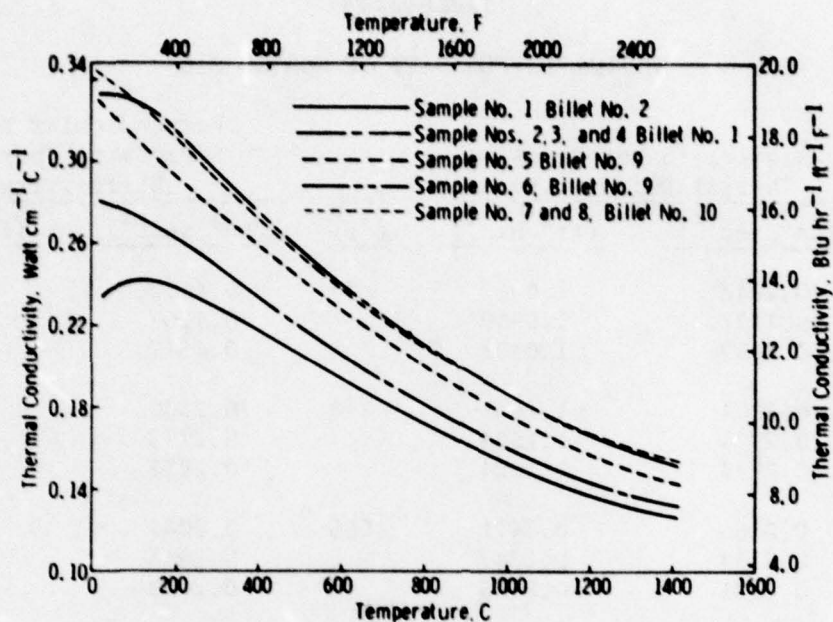
Figure 2-111. Comparison of Thermal Conductivity Values for Heat
Conducted Parallel to the Hot Pressing Direction
in Silicon Nitride
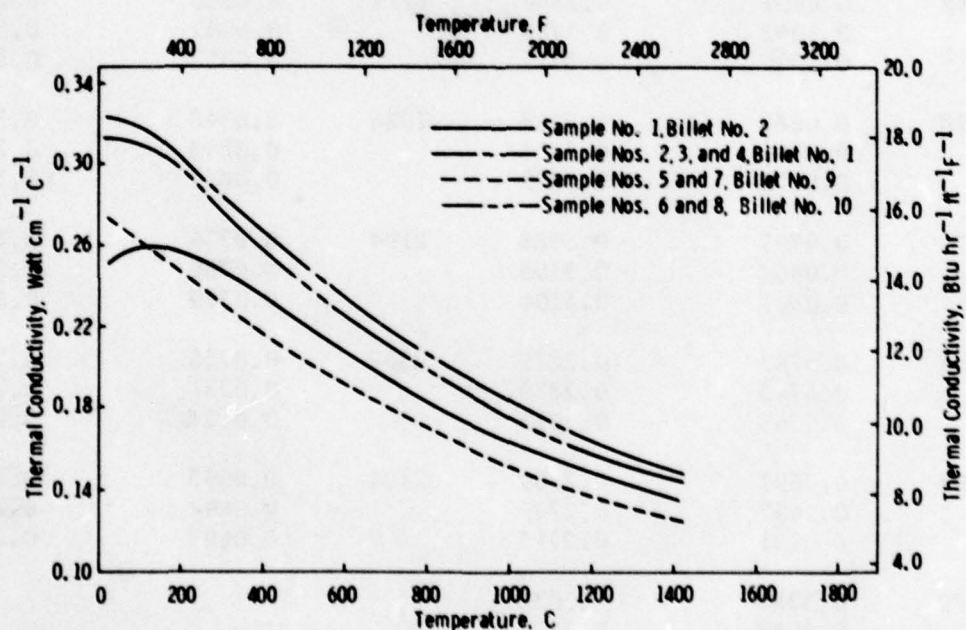
Figure 2-112. Comparison of Thermal Conductivity Values for Heat
Conducted Perpendicular to the Hot Pressing
Direction in Silicon Nitride

114

TABLE 2-25

TYPICAL VALUES OF THERMAL CONDUCTIVITY IN NORTON HS130 (NORALIDE NC132) SILICON NITRIDE

Temperature		Thermal Conductivity			
		Parallel, Weak		Perpendicular, Strong	
(°C)	(°F)	(watt cm^{-1} C^{-1})	(Btu hr^{-1} ft^{-1} F^{-1})	(watt cm^{-1} C^{-1})	(Btu hr^{-1} ft^{-1} F^{-1})
24	75	0.346	19.991	0.252	14.560
		0.343	19.818	0.253	14.618
		0.343	19.818	0.248	14.329
153	307	0.318	18.374	0.257	14.849
		0.320	18.489	0.256	14.791
		0.320	18.489	0.262	15.138
326	619	0.291	16.814	0.245	14.156
		0.288	16.640	0.247	14.271
		0.294	16.987	0.245	14.156
649	1200	0.224	12.942	0.201	11.614
		0.227	13.116	0.198	11.440
		0.226	13.058	0.199	11.498
986	1807	0.187	10.805	0.167	9.649
		0.184	10.631	0.167	9.649
		0.186	10.747	0.166	9.591
1099	2010	0.180	10.400	0.158	9.129
		0.181	10.453	0.157	9.071
		0.179	10.342	0.157	9.071
1204	2199	0.168	9.707	0.149	8.609
		0.167	9.649	0.150	8.667
		0.166	9.591	0.149	8.609
1313	2395	0.162	9.360	0.142	8.250
		0.162	9.360	0.141	8.147
		0.162	9.360	0.141	8.147
1371	2500	0.153	8.840	0.139	8.031
		0.152	8.782	0.138	7.973
		0.152	8.782	0.140	8.089

TABLE 2-26

THERMAL CONDUCTIVITY OF NORTON SiC

Temp (°F)	(watt cm^{-1} C^{-1})	(Btu hr^{-1} ft^{-1} F^{-1})	Temp (°F)	(watt cm^{-1} C^{-1})	(Btu hr^{-1} ft^{-1})
77	0.918	53.041	73	0.895	51.712
	0.941	54.370		0.913	52.752
	0.952	55.006		0.921	53.214
298	0.807	46.628	329	0.894	51.654
	0.799	46.165		0.885	51.134
	0.817	47.205		0.885	51.134
565	0.674	38.943	597	0.741	42.814
	0.689	39.810		0.731	42.236
	0.679	39.232		0.757	43.739
1186	0.510	29.467	931	0.549	31.721
	0.511	29.525		0.550	31.778
	0.512	29.583		0.544	31.432
91	0.385	22.245	1818	0.413	23.863
	0.396	22.880		0.418	24.152
	0.390	22.534		0.417	24.094
2026	0.358	20.685	1998	0.375	21.667
	0.356	20.569		0.370	21.378
	0.358	20.685		0.371	21.436
2194	0.334	19.298	2174	0.346	19.992
	0.340	19.645		0.349	20.165
	0.335	19.356		0.348	20.107
2362	0.323	18.663	2367	0.331	19.125
	0.315	18.200		0.331	19.125
	0.319	18.431		0.335	19.356
2494	0.309	17.854	2498	0.315	18.200
	0.309	17.854		0.315	18.200
	0.309	17.854		0.316	18.258
			2275	0.345	19.934
				0.344	19.876
				0.340	19.645

Figure 2-113. Thermal Conductivity of Norton Hot Pressed
Silicon Carbide

2.7 SHEAR PROPERTIES

2.7.1 INTRODUCTION

Ultimate shear strength and shear modulus for Norton HS130 (Nora-lide NC132) silicon nitride and Norton NC203 silicon carbide were determined by torsion tests at temperatures from RT (68°F) to 2500°F. Poisson's ratio, μ, was then calculated from the tension and torsion test data by the relationship:

$$\mu = \frac{E}{2G} - 1$$

where

E = elastic modulus in torsion

G = shear modulus

2.7.2 THE TEST METHOD

The torsion test itself and the test specimen are described in Figures 2-114 and 2-115, respectively. A 5000 inch/lb Baldwin-Lima-Hamilton
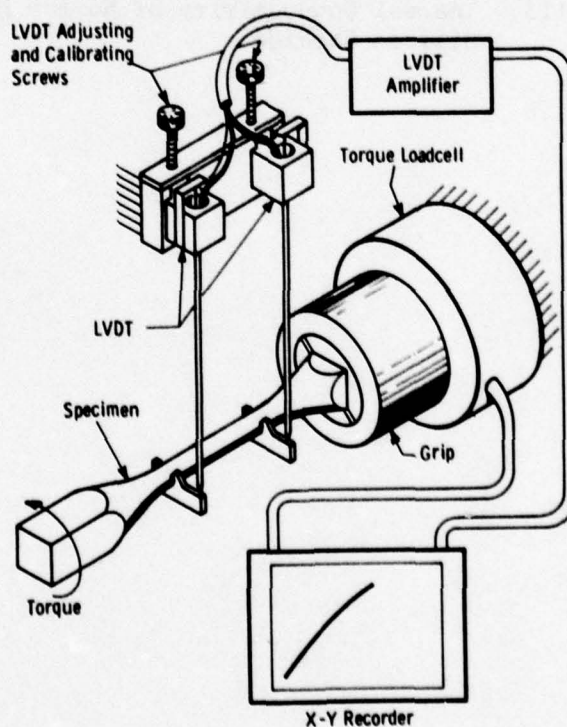
Figure 2-114. Torsion Test

118
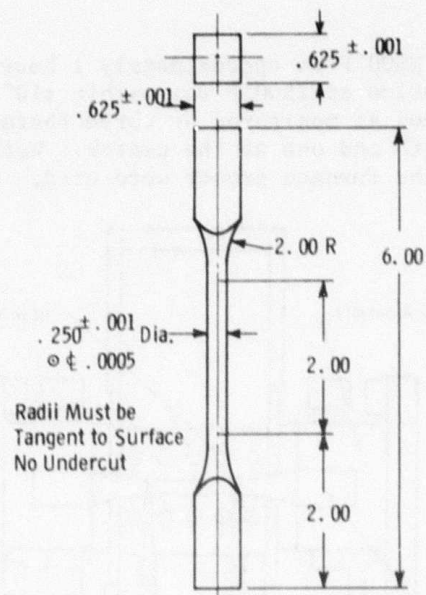
Figure 2-115. Torsion Specimen

torsion machine with adjustable loading rate from 0-1 rpm was actually
employed (Figure 2-116). Specimens were heated in a specifically
designed "Glo-bar" furnace which was capable of reaching the maximum
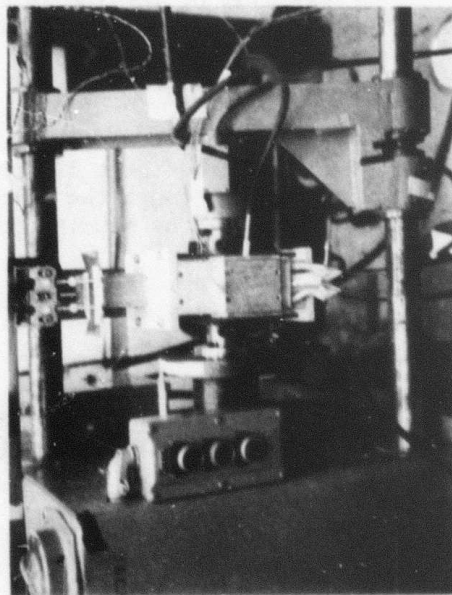
Figure 2-116. Torsion Machine and Assembled Torsion
Test Equipment

119

test temperature of 2500°F in approximately 1 hour (Figure 2-117). The temperature distribution at 2500°F was within ±10°F over the 2 inch gage length of the specimen as monitored by three thermocouples, one at each end of the gage length and one at the center. Water cooled grips located outside of the furnace proper were used.
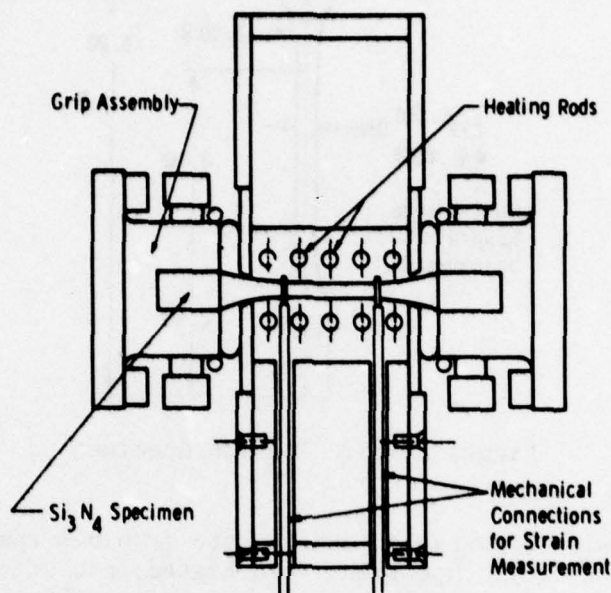
Figure 2-117. Cutaway View of Torsion Test Facility Showing Furnace Grips and Strain Readout

The angle of twist was measured by the rotation of alumina ceramic arms attached at each end of the specimen gage length with Xelox cement. Movement of the arms was transmitted through the furnace wall to miniature LVDT displacement transducers by alumina push rods.

An instrumented specimen with ceramic measuring arms in place is shown in Figure 2-118. Each specimen was aligned in the test machine by
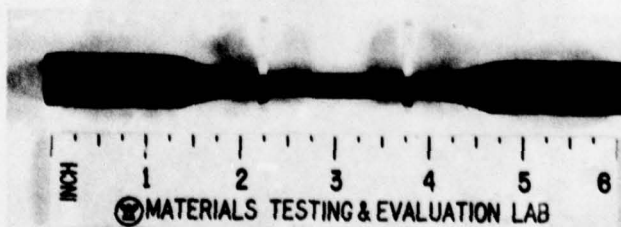
Figure 2-118. Torsion Specimen with Angle of Twist Arms and Strain Gage Torque Rosettes Mounted

120

means of a dial indicator so that eccentricity did not exceed 0.001 inch. Strain gages were used to assure that no bending stress was applied to the specimen when the stationary grips were tightened.

The displacement signals from the LVDT's were amplified by a two-channel Westinghouse amplifier. Torque and angle of twist were recorded simultaneously on an x-y recorder. Shear modulus and strain rate were recorded at room temperature, using strain gage torque rosettes bonded to the specimen gage section. These gages also served to check the angle-of-twist measuring system with agreement with 0.5 percent.

Shear modulus was calculated from the slope of the torque versus angle-of-twist curves. Specimens were twisted in both clockwise and counterclockwise directions to a maximum shear stress of 26,000 psi for Si_3N_4 and 20,000 psi for SiC, three times at each temperature. At the highest test temperature, the specimen was tested to failure to produce a full curve of torque versus angle of twist. Tests were performed at strain rates of 0.01 to 0.0003 rad/min (0.0003 rad/min proved to be the lowest strain rate obtainable). The total angle of twist was limited to 10° maximum to keep the error from the rotation of the arms to less than 1 percent. This angle was more than adequate for shear tests on high modulus brittle materials.

2.7.3 TEST RESULTS

Preliminary shear modulus and fracture strength measurements were made at room temperature on one sample HS130 silicon nitride at a strain rate of 8×10^{-4} in/in/minute.[2] A shear modulus of 18×10^6 psi and fracture stress of 68,600 psi were determined. The specimen was loaded to about 60,000 psi, then unloaded and reloaded to failure. No hysterisis was observed. At 1832°F, shear strength and shear modulus of 70,300 psi and 16.9×10^6 psi/in/in were obtained.[3]

Torque versus angle of twist curves were obtained to failure at the highest test temperature. Figure 2-119 is typical of HS130 Si_3N_4 at
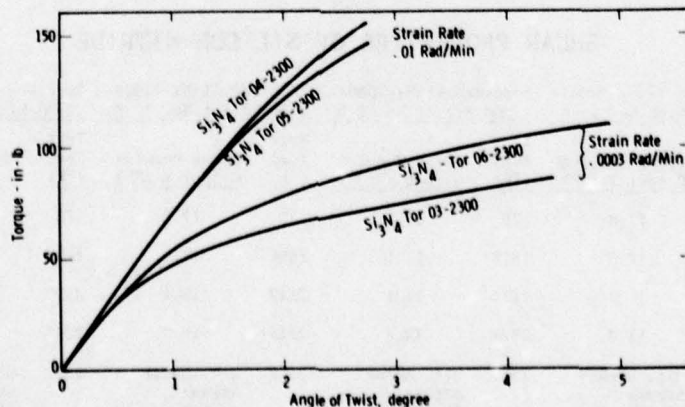
Figure 2-119. Torque vs Angle of Twist Curves for Silicon Nitride Tested at 2300°F

121

2300°F. No plasticity was evident in SiC specimens tested to 2500°F.[5] The effect of temperature on the shear modulus is shown in Figure 2-120
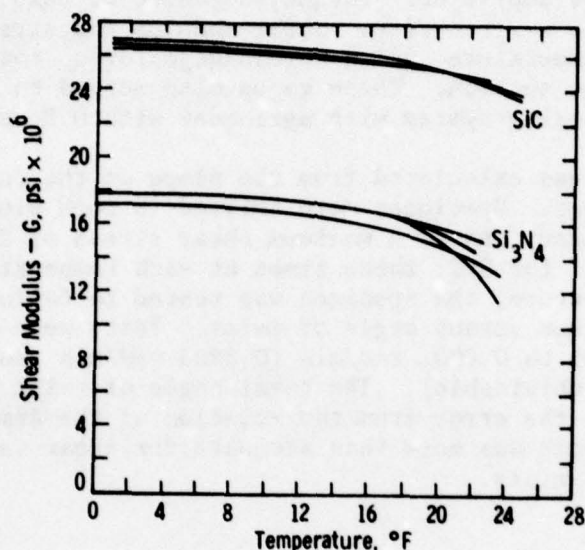
Figure 2-120. The Effect of Temperature on the Shear Moduli of Si₃N₄ and SiC

where data for silicon nitride and silicon carbide appear together for comparitive purposes. Summary tables were also prepared for silicon nitride (Table 2-27 and silicon carbide (Table 2-28).

TABLE 2-27

SHEAR PROPERTIES OF SILICON NITRIDE

Specimen Si₃N₄-TORO3-2300 Billet No. 10-A		Specimen Si₃N₄-TORO4-2300 Billet No. 9-B		Specimen Si₃N₄-TORO5-2300 Billet No. 10-B		Specimen Si₃N₄-TORO6-2300 Billet No. 9-A	
Test Temp (°F)	Shear Modulus G (psi x 10⁶)	Test Temp (°F)	Shear Modulus G (psi x 10⁶)	Test Temp (°F)	Shear Modulus G (psi x 10⁶)	Test Temp (°F)	Shear Modulus G (psi x 10⁶)
75	17.8	75	17.8	75	17.8	75	17.2
1800	17.0	1818	17.1	1830	17.0	1822	16.5
2135	16.0	2108	16.4	2119	16.4	2120	15.7
2340	13.7	2329	15.7	2319	15.2	2321	14.4
2340	Ult. Shear Stress 27,900 psi	2329	Ult. Shear Stress 50,950 psi	2319	Ult. Shear Stress 47,800 psi	2321	Ult. Shear Stress 36,000 psi
Strain Rate	0.003 rad/rad/min		0.01 rad/rad/min		0.003 rad/rad/min		0.01 rad/rad/min

122

TABLE 2-28

SHEAR PROPERTIES OF SILICON CARBIDE

Specimen SiC-TORO1- 2300 Billet No. 872-2-1		Specimen SiC-TORO2- 2500 Billet No. 872-7-2		Specimen SiC-TORO3- 2500 Billet No. 872-8-3	
Test Temp ($^\circ$F)	Shear Modulus G (psi x 10^6)	Test Temp ($^\circ$F)	Shear Modulus G (psi x 10^6)	Test Temp ($^\circ$F)	Shear Modulus G (psi x 10^6)
75	26.6	75	27.0	75	26.6
1808	25.6	1808	25.9	1811	25.8
2100	25.0	2104	24.9	2108	24.9
2296	24.6	2306	24.3	2307	24.5
		2493	23.5	2507	23.8
2296	Ult. Shear Stress 37,200 psi	2493	Ult. Shear Stress 23,200 psi	2507	Ult. Shear Stress 41,750 psi
Strain Rate	0.001 rad/rad/min		0.001 rad/rad/min		0.001 rad/rad/min

It was possible to obtain representative values for Poisson's ratio for the two materials as supplementary data from the shear and tensile properties. Results appear in Table 2-29.

TABLE 2-29

POISSON'S RATIO FOR Si$_3$N$_4$ AND SiC

Material	RT	1800°F	2100°F	2300°F	2500°F
HS130 (NC132) - Si$_3$N$_4$	0.25	0.16	0.13	0.19	--
NC203 - SiC	0.22	0.21	0.22	0.22	0.19

2.8 COMPRESSIVE PROPERTIES

Only cursory determinations of compressive properties were made because ceramic materials classically exhibit extreme strength in the compressive mode. It was inconceivable that vane or blade failures could result from the compressive stresses normally associated with startup and acceleration of a gas turbine to peak load.

A standard load frame (Figure 2-121) was used to generate compressive strength and compressive creep data for HS130 silicon nitride. The
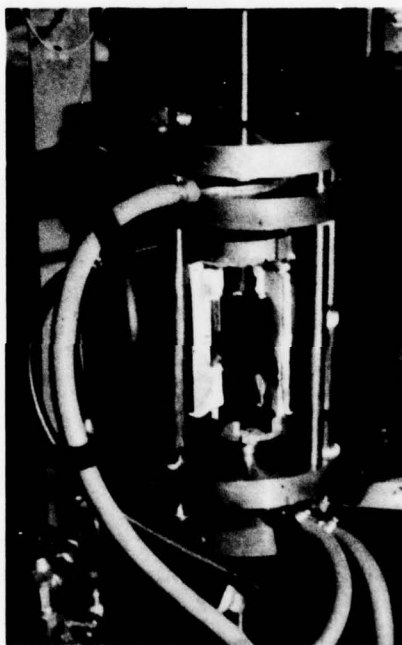
Figure 2-121. Compressive Strength and Creep Machine

compressive strength of Si_3N_4 exceeded 450,000 psi at room temperature in duplicate tests of 1 inch long by 3/8 inch diameter specimens loaded between KT silicon carbide platens.[3] The compressive creep curve shown in Figure 2-122 was produced from similar specimens stressed at 100,000 psi at 2300°F.

Silicon carbide was not tested in the compressive mode because the preliminary data for silicon nitride indicated properties far superior to any stress requirement.
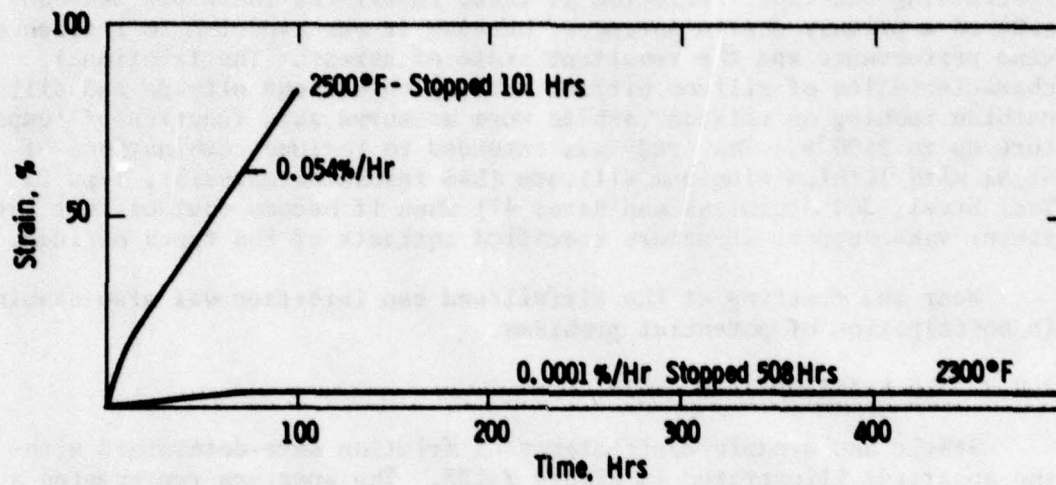
Figure 2-122. Compressive Creep of Silicon Nitride

2.9 FRICTION AND RELATED PROPERTIES

2.9.1 INTRODUCTION

The three-piece stator vane was designed to encourage freedom of motion at the interfacial functions between the airfoil section and its restraining end caps. Friction at these interfaces therefore was considered a primary design parameter because it was expected to influence vane performance and the resultant state of stress. The frictional characteristics of silicon nitride rubbing on silicon nitride and silicon carbide rubbing on silicon carbide were measured as a function of temperature up to 2500°F. The study was extended to include combinations of Si_3N_4 with lithium aluminum silicate (LAS insulator material, Type 21 Tool Steel, 304 Stainless and Benes 41) when it became obvious that the stator vane support structure specified contacts of the types defined.

Wear and fretting at the airfoil/end cap interface was also examined in anticipation of potential problems.

2.9.2 THE FRICTION TEST

Static and dynamic coefficients of friction were determined with the apparatus illustrated in Figure 2-123. The specimen represented a
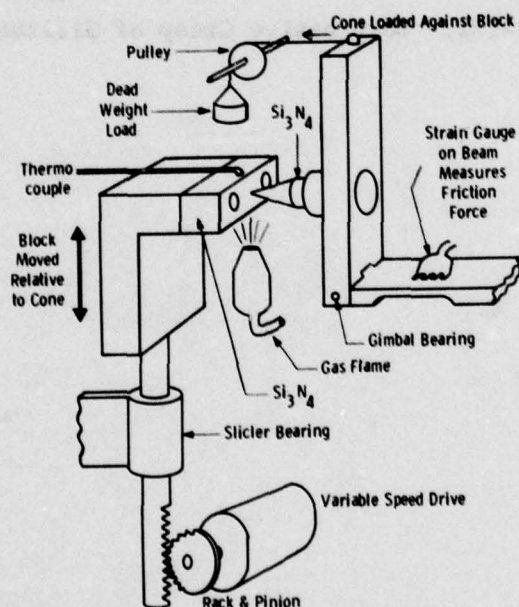
Figure 2-123. Schematic Drawing of Friction Apparatus

126

stylus with a 1/16 inch diameter flat nose transversed by a motor driven flat block at a prescribed rate, under a predetermined control load.[1] A strain gage in the stylus mount served to measure the force necessary to overcome friction. Temperatures up to 600°F were achieved by blowing hot air against the friction surface. The temperature range was extended upward to 1900°F through the use of a gas burner. Final test temperatures of 2500°F required an oxy-acetylene torch.

2.9.3 TEST RESULTS

Preliminary results for silicon nitride versus silicon nitride (HS130 material) are presented in Table 2-30.[1] The stick-slip character of the frictional properties are described in Figure 2-124.

TABLE 2-30

STATIC AND DYNAMIC FRICTION CHARACTERISTICS

Si_3N_4 vs Si_3N_4

Load		Speed	Temp	Static Friction Force	Static Friction	Dynamic Friction
(lb)	(psi)	(inch/min)	(°F)	(lb)	Coefficient	Coefficient
5	1700	10	R.T.	1.0	0.20	0.20
5	1700	10	R.T.	1.2	0.24	0.24
5	1700	10	600	1.3	0.26	stick-slip
5	1700	10	600	1.4	0.28	stick-slip
5	1700	10	1000	1.8	0.36	stick-slip
5	1700	10	1000	2.3	0.46	stick-slip
5	1700	10	1800	8.5	1.70	stick-slip
5	1700	10	1850	7.3	1.46	stick-slip
5	1700	10	1900	7.9	1.58	stick-slip
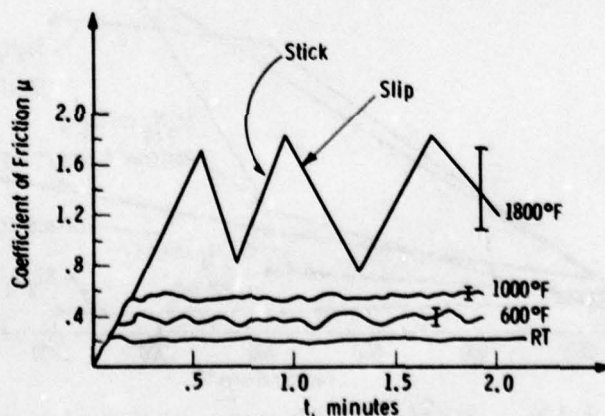
Figure 2-124. Static and Dynamic Friction Characteristics of Si_3N_4 vs Si_3N_4

127

The breakway coefficient of friction for silicon nitride/silicon
nitride is recorded as a function of temperature in Figure 2-125.(2)
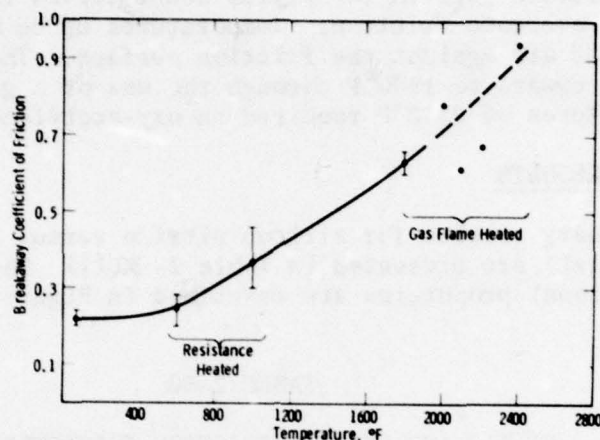
Figure 2-125.   Breakway Coefficient of Friction of Silicon
             Nitride vs Silicon Nitride as a Function
             of Temperature

Similar data for Si3N4 against a variety of metals and nonmetals
appear in Figure 2-126.(3) Frictional effects for Si3N4 against LAS
(lithium alumina silicate, an insulator material) and SiC/SiC are sum-
marized in Tables 2-31(3) and 2-32,(4) respectively.
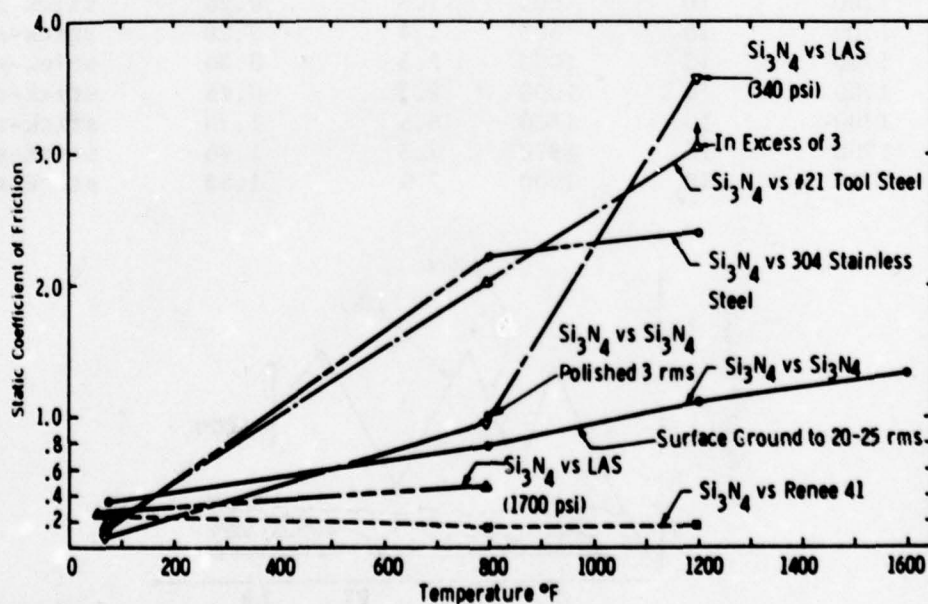
Figure 2-126.   Static Coefficient of Friction for Hot Pressed
             Silicon Nitride vs Various Materials

128

TABLE 2-31

COEFFICIENTS OF FRICTION FOR Si_3N_4 vs LAS

Tip		Plate	Load (psi)	Temp (°F)	Static (lb)	Static Coef	Dynamic
$Si_3N_4 \left(\begin{smallmatrix}\text{polished}\\\text{2-3 rms}\end{smallmatrix}\right)$	vs	LAS (Ground Parallel)	340	RT	0.11	0.11	stick-slip
$Si_3N_4 \left(\begin{smallmatrix}\text{polished}\\\text{20-25 rms}\end{smallmatrix}\right)$	vs	LAS (Ground Parallel)	340	RT	0.09	0.09	stick-slip
$Si_3N_4 \left(\begin{smallmatrix}\text{polished}\\\text{2-3 rms}\end{smallmatrix}\right)$	vs	LAS (Ground Perpendicular)	340	RT	0.10	0.10	stick-slip
$Si_3N_4 \left(\begin{smallmatrix}\text{polished}\\\text{20-25 rms}\end{smallmatrix}\right)$	vs	LAS (Ground Perpendicular)	340	RT	0.11	0.11	stick-slip
$Si_3N_4 \left(\begin{smallmatrix}\text{polished}\\\text{2-3 rms}\end{smallmatrix}\right)$	vs	LAS (Ground Parallel)	1700	RT	1.07	0.21	stick-slip
$Si_3N_4 \left(\begin{smallmatrix}\text{polished}\\\text{20-25 rms}\end{smallmatrix}\right)$	vs	LAS (Ground Parallel)	1700	RT	1.3	0.26	stick-slip
$Si_3N_4 \left(\begin{smallmatrix}\text{polished}\\\text{2-3 rms}\end{smallmatrix}\right)$	vs	LAS (Ground Perpendicular)	1700	RT	1.23	0.24	stick-slip
$Si_3N_4 \left(\begin{smallmatrix}\text{polished}\\\text{20-25 rms}\end{smallmatrix}\right)$	vs	LAS (Ground Perpendicular)	1700	RT	1.3	0.26	stick-slip
$Si_3N_4 \left(\begin{smallmatrix}\text{polished}\\\text{2-3 rms}\end{smallmatrix}\right)$	vs	LAS (Ground Parallel)	340	600	0.76	0.76	stick-slip
$Si_3N_4 \left(\begin{smallmatrix}\text{polished}\\\text{20-25 rms}\end{smallmatrix}\right)$	vs	LAS (Ground Parallel)	340	600	0.79	0.79	stick-slip
$Si_3N_4 \left(\begin{smallmatrix}\text{polished}\\\text{2-3 rms}\end{smallmatrix}\right)$	vs	LAS (Ground Perpendicular)	340	600	0.72	0.72	stick-slip
$Si_3N_4 \left(\begin{smallmatrix}\text{polished}\\\text{20-25 rms}\end{smallmatrix}\right)$	vs	LAS (Ground Perpendicular)	340	600	0.52	0.52	stick-slip
$Si_3N_4 \left(\begin{smallmatrix}\text{polished}\\\text{2-3 rms}\end{smallmatrix}\right)$	vs	LAS (Ground Parallel)	1700	600	1.53	0.31	stick-slip
$Si_3N_4 \left(\begin{smallmatrix}\text{polished}\\\text{20-25 rms}\end{smallmatrix}\right)$	vs	LAS (Ground Parallel)	1700	600	1.59	0.33	stick-slip
$Si_3N_4 \left(\begin{smallmatrix}\text{polished}\\\text{2-3 rms}\end{smallmatrix}\right)$	vs	LAS (Ground Perpendicular)	1700	600	2.65	0.53	stick-slip
$Si_3N_4 \left(\begin{smallmatrix}\text{polished}\\\text{20-25 rms}\end{smallmatrix}\right)$	vs	LAS (Ground Perpendicular)	1700	600	2.8	0.56	stick-slip
$Si_3N_4 \left(\begin{smallmatrix}\text{polished}\\\text{2-3 rms}\end{smallmatrix}\right)$	vs	LAS (Ground Parallel)	340	1200	------SAMPLE CRACKED-------		
$Si_3N_4 \left(\begin{smallmatrix}\text{polished}\\\text{20-25 rms}\end{smallmatrix}\right)$	vs	LAS (Ground Parallel)	340	1200	3.67	3.67	stick-slip
$Si_3N_4 \left(\begin{smallmatrix}\text{polished}\\\text{2-3 rms}\end{smallmatrix}\right)$	vs	LAS (Ground Perpendicular)	340	1200	4.31	4.31	stick-slip
$Si_3N_4 \left(\begin{smallmatrix}\text{polished}\\\text{20-25 rms}\end{smallmatrix}\right)$	vs	LAS (Ground Perpendicular)	340	1200	2.67	2.67	stick-slip

TABLE 2-32

STATIC COEFFICIENT OF FRICTION FOR HOT-PRESSED SILICON CARBIDE (SiC/SiC)

(Load-1700 psi, Test speed-0.01 inch/min)

Temp (°F)	Static	Dynamic	Temp (°F)	Static	Dynamic
RT	0.35	0.25	2100	1.82	Stick-Slip
1000	0.60	Stick-Slip	2100	2.00	Stick-Slip
1800	1.25	Stick-Slip	2200	1.85	Stick-Slip
1800	1.40	Stick-Slip	2300	2.50	Stick-Slip
2000	1.46	Stick-Slip	2400	2.85	Stick-Slip
2000	1.68	Stick-Slip	2500	Samples would not break loose with a force of > 15 lb static	

2.9.4 WEAR AND FRETTING

Wear and fret tests were used to supplement the friction data and to simulate the effect of motion at the end cap airfoil interface.[3] The specimen geometry and test fixture are shown in Figure 2-127. The entire apparatus is illustrated in Figure 2-128.
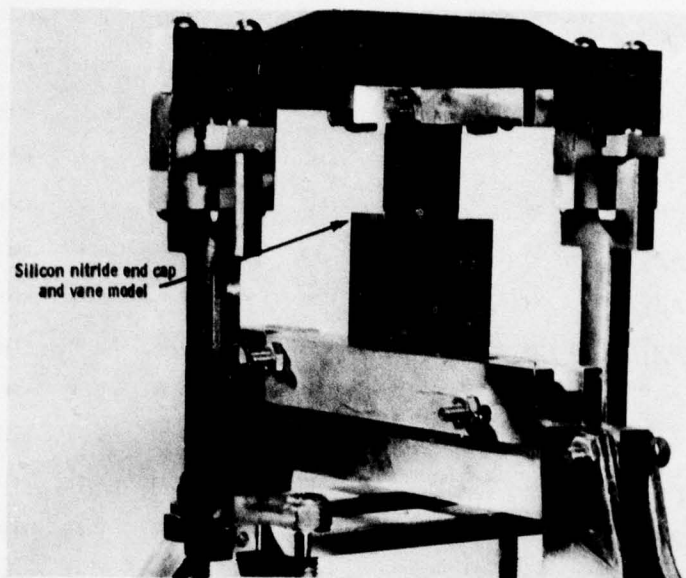
Figure 2-127. Wear and Fret Test Apparatus
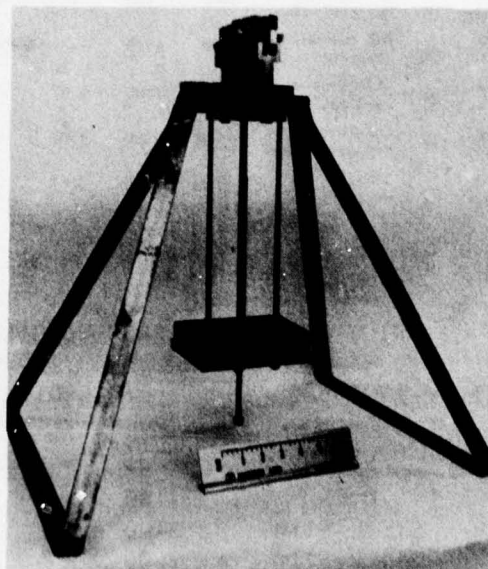
Figure 2-128. Wear and Fret Test Apparatus (Rocking Motion Is in the Plane of the Ruler)

Silicon nitride was tested against silicon nitride at 2300°F for
1 hour (3600 cycles) at 11.0 lb load, and for 1/2 hour (1800 cycles) at
19.8 lb load.[3] Fretting increased markedly at the higher load as shown
in Figure 2-129. The white deposit appeared to be powdered silicon nitride
with some silicon dioxide. Measurements indicated that the coefficient
of friction, as measured in the friction and wear apparatus, decreased
from approximately 1.0 to 0.8 as wear increased with time at 2300°F.

Model of vane and end cap
after 3600 cycles at
11 lbs load 2300°F

Same surfaces after an additional
1800 cycles at 19.8 lbs, 2300°F
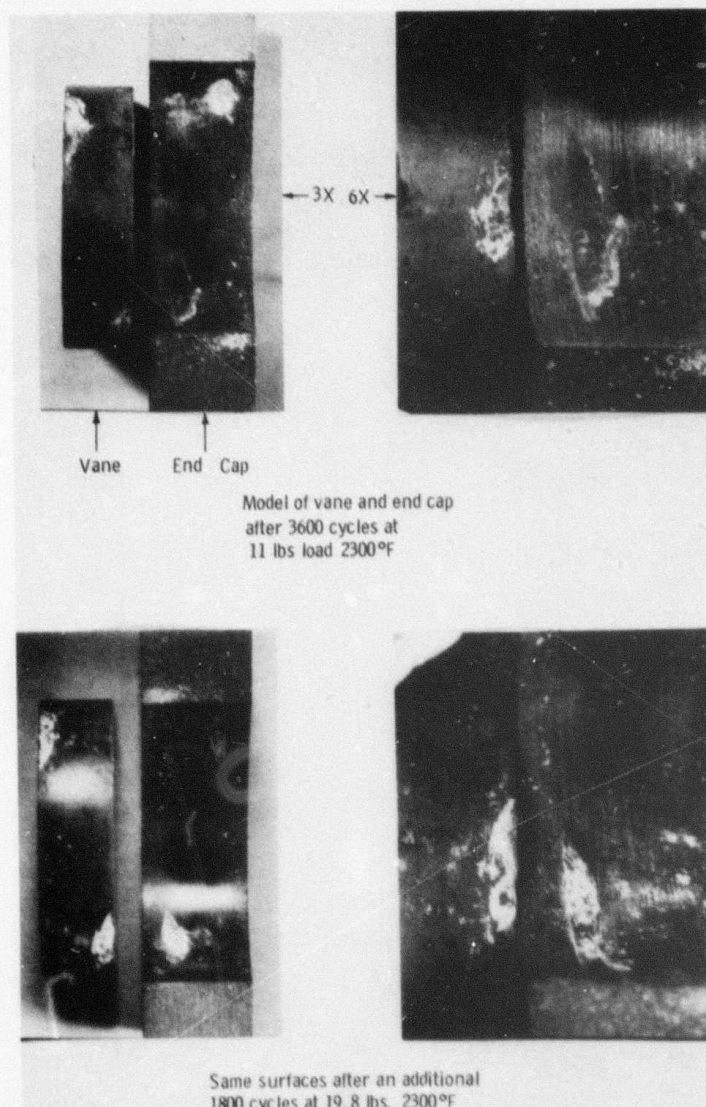
Figure 2-129.   Surface of Wear and Fret Specimens of Hot
Pressed Silicon Nitride

These results signaled a potential problem in the contact area between the airfoil and end cap in the three piece vane design if contact and thermal stresses caused crack propagation from the chipped areas. The motion imposed in this test exceeded that expected in the part by a factor of 5, and each cycle represented a single turbine start. No, problems of this type were encountered in any of the static rig tests, however.

2.10 FLEXURAL TESTS OF LITHIUM ALUMINA SILICATE (LAS) INSULATOR MATERIAL

2.10.1 INTRODUCTION

Lithium alumina silicate (LAS) insulators of the 8.00 inch radius configuration[4] were tested in both the 2200°F and initial 2500°F static rig tests.[5,6,7] All LAS insulators developed cracks, caused principally by transient thermal stresses at the upstream circumferential edge or by edge loading at the downstream circumferential edge. As a part of the evaluation of the failed insulators, flexural tests, in 4-point loading at room temperature, were conducted on both untested insulator remnant material and material removed from one of the failed insulators at an apparently undamaged location (2200°F static rig tests[5]). Specimens which had been heat treated to 2000°F for 2 hours to permit the healing of machining damage and specimens ground in both the longitudinal (lengthwise) and transverse (widthwise) directions were also tested.[9]

2.10.2 RESULTS

The specimens were 1.125 x 0.125 x 0.25 inch ground approximately to the specification used to make the insulators in the static rig tests. The results are given in Figure 2-130. Transverse grinding lowered the average strength to approximately 65 per cent of that for the material ground longitudinally. Heat treatment had very little effect. The insulator exposed in the 2200°F static rig tests was shown to degrade. Test results were scattered widely.
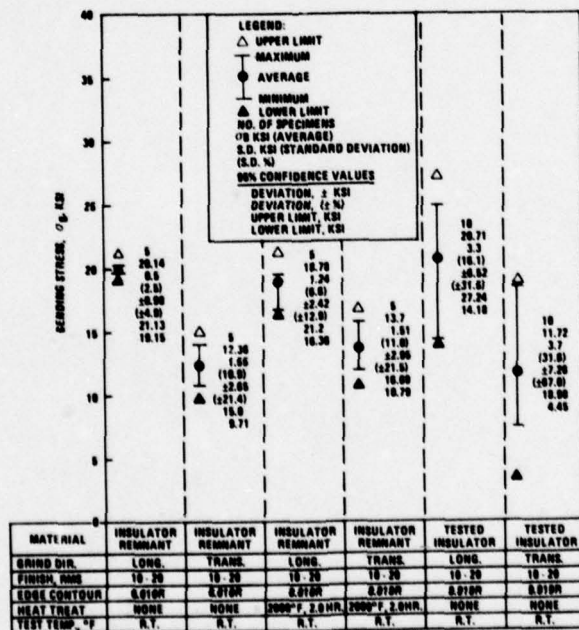
Figure 2-130. Flexural Test Results for Cervit C140 LAS Insulator Material at Room Temperature

133

Temperatures in the static rig at insulator locations apparently exceeded 2000°F as indicated by local melting. This condition contributed to the insulator failure observed.(4)

2.11 PROPERTIES OF BORON NITRIDE INSULATOR MATERIAL

2.11.1 INTRODUCTION

The (Carbonundum Combat "M") properties of a hot-pressed boron nitride insulator material were characterized to verify the vendor data used in design calculations. Specimens were prepared from five pieces of hot-pressed boron nitride cut from the billets used to manufacture insulators for static rig tests at 2500°F.[9] The list of properties measured includes: density, flexural strength versus temperature, strength in compression; Poisson's ratio, elastic modulus, sonic velocity, flexural creep, thermal expansion and thermal conductivity.

2.11.2 DENSITY

The density of each of five pieces was measured by water immersion. Results appear in Table 2-33.

TABLE 2-33

THE DENSITY OF "COMBAT M" BORON NITRIDE

Piece No.	1	2	3	4	5
Density (g/cc)	2.11	2.13	2.14	2.12	2.13
Water Absorption (%) 100 Hours in 50% Humidity	0.007	0.004	0.005	0.004	0.006

2.11.3 FLEXURAL STRENGTH

Flexural strength was determined up to 2000°F in four-point loading for a load span of 0.50 inch over an outer support span of 1 inch.[9] Nominal specimen dimensions were 0.125 inch thick 0.250 inch wide and 1.25 inch long. In the "B" direction of the material (Figure 2-131)
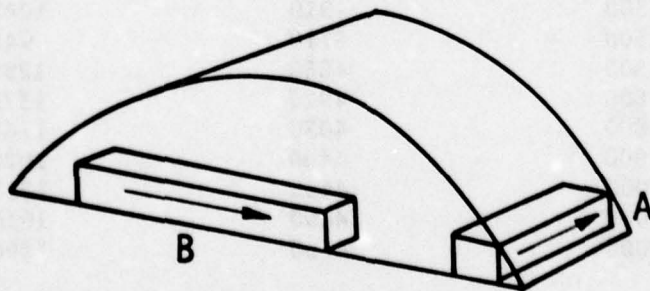
Figure 2-131. Specimen Orientation in Boron Nitride Insulator Materials

135

grinding marks ran longitudinally while in the "A" direction the grind-
ing marks were transverse. Final grinding was done with A; 320 grit
diamond wheel. The flexure specimen specification is shown in Fig-
ure 2-132. Three specimens from each direction were tested for each
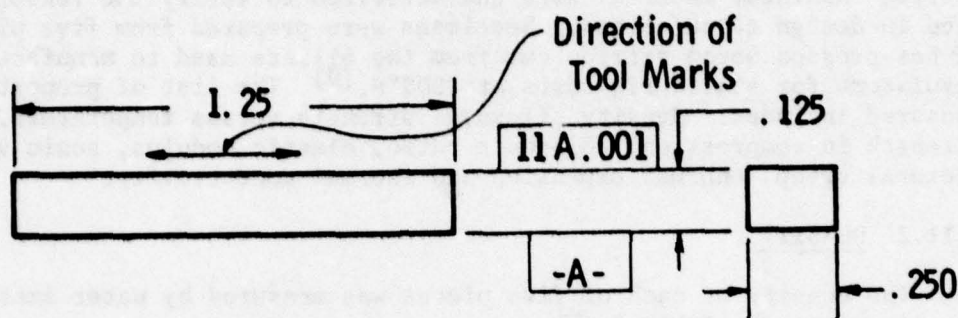
Figure 2-132. Flexural Specimen

temperature condition. Flexural strength is reported in Table 2-34.
The results are plotted as a function of temperature in Figure 2-133.

TABLE 2-34

THE FLEXURAL STRENGTH OF HOT-PRESSED BORON NITRIDE

Temperature (°F)	Ultimate Flexural Strength (psi)	
	"A" Direction	"B" Direction
RT	4090	10650
RT	3990	11350
RT	3950	11800
1200	4040	11850
1200	4100	10950
1200	4260	
1500	4910	10450
1500	5110	9480
1500	4550	12500
1800	4920	13750
1800	4050	11400
1800	4460	10200
2000	4650	12150
2000	4490	16100
2000	4560	13000

136
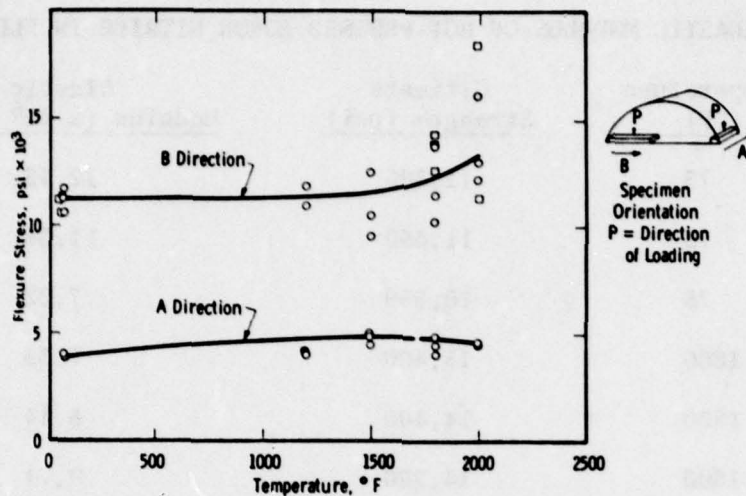
Figure 2-133. The Effect of Temperature on the Flexural
Strength of Boron Nitride Insulator
Material

Other flexure tests were conducted on 0.125 inch thick, 0.250 inch
wide and 2 inch long specimens (Figure 2-134) at test temperatures of
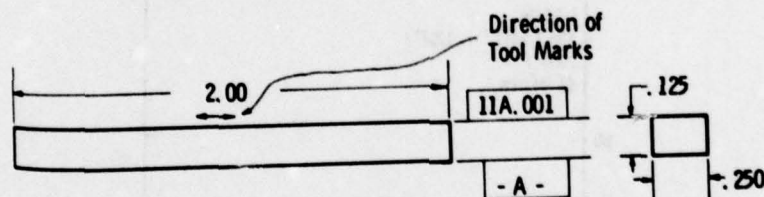
Figure 2-134. Flexural Specimen for Stress-Strain Determinations

75°F, 1800°F and 2000°F using a three-rod deflectometer to obtain
stress-strain curves. These specimens were cut from the "B" direction
orientation. Results appear in Table 2-35. A typical stress-strain
curve (2000°F) is shown in Figure 2-135.

137

TABLE 2-35

ELASTIC MODULUS OF HOT-PRESSED BORON NITRIDE IN FLEXURE

Temperature (°F)	Ultimate Strength (psi)	Elastic Modulus (x 10^6 psi)
75	11,300	12.43
75	11,450	11.38
75	10,550	7.22
1800	15,400	7.33
1800	14,400	8.44
1800	14,200	9.71
2000	18,600	6.58
2000	11,250	6.91
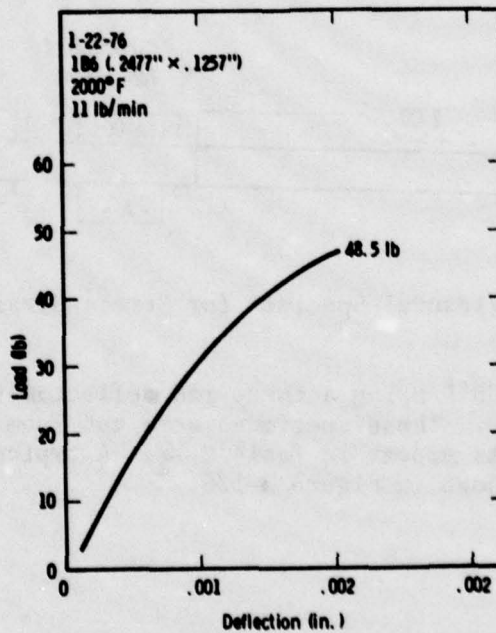
Figure 2-135. Typical Load Deflection Curve for Boron Nitride Insulator Material (2000°F)

2.11.4 TESTS IN COMPRESSION

Compression tests were conducted at 75°F, 1500°F, 1800°F and 2000°F, using specimens illustrated in Figure 2-136. At 75°F, specimens from both directions were strain gaged to provide elastic modulus and Poisson's ratio data for comparison with sonic velocity test results.[9] Results are shown in Table 2-36. The material acted isotropically in all compression tests.
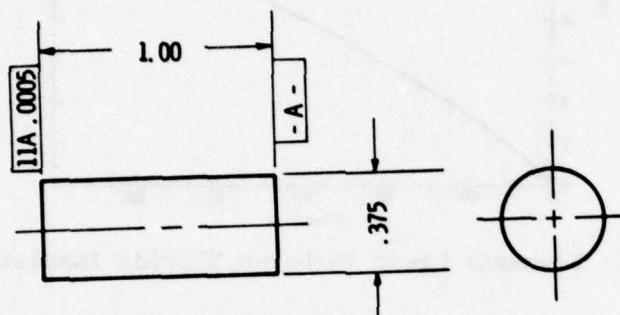
Figure 2-136. Compression Specimen

TABLE 2-36

COMPRESSION RESULTS FOR HOT-PRESSED BORON NITRIDE

Temp (°F)	Ultimate Strength (psi)	Elastic Modulus (x 10⁶ psi)	Poisson's Ratio
75	25,350	1.24	0.053
75	27,250	8.91	0.114
1500	23,500	No Data	No Data
1800	36,150	No Data	No Data
1800	37,400	No Data	No Data
2000	36,700	No Data	No Data

2.11.5 FLEXURAL CREEP TESTS

Flexural creep tests were conducted at 1800°F and 5000 psi on a "B" direction specimen and at 1800°F and 2500 psi on "A" direction specimens. Loading spans and specimen configuration were the same as those used in the flexural strength tests. Flexural creep data are illustrated in Figure 2-137.

139
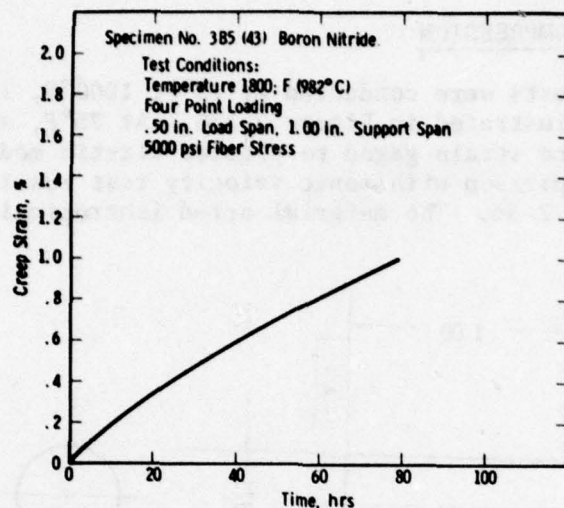
Figure 2-137. Flexural Creep in Boron Nitride Insulator Material

2.11.6 SONIC VELOCITY MEASUREMENT

Elastic and shear moduli were computed from the extensional and torsional wave velocities through *cylindrical specimens of the material* (Figure 2-138). Poisson's ratio was calculated from the E and G values obtained.
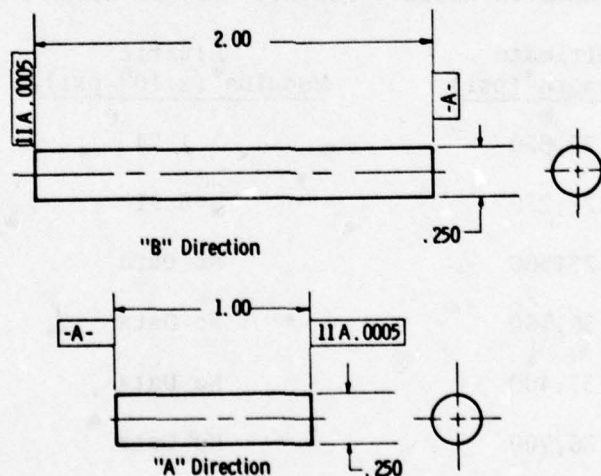
Figure 2-138. Thermal Expansion and Sonic Velocity Test Specimens

2.11.7 THERMAL EXPANSION

Thermal expansion of 1800°F was measured with a quartz tube dilatometer using specimens 0.25 inch diameter x 2 inches long (Figure 2-138).

140

For the "A" direction, two 1-inch long pieces were stacked together. The "B" direction measurements were duplicated because of the low thermal elongation obtained. Thermal expansion curves appear in Figures 2-139, 2-140 and 2-141.
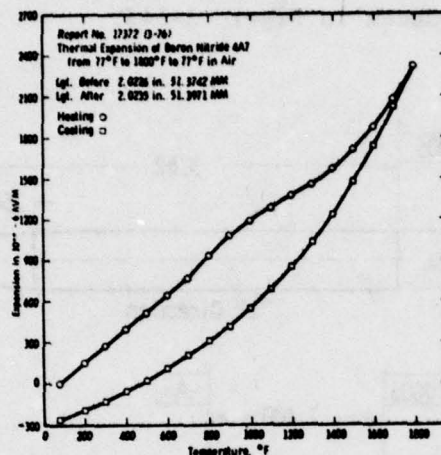
Figure 2-139. Thermal Expansion of Boron Nitride Insulator Material Parallel to the Hot-Press Direction "A" (Across Insulator)
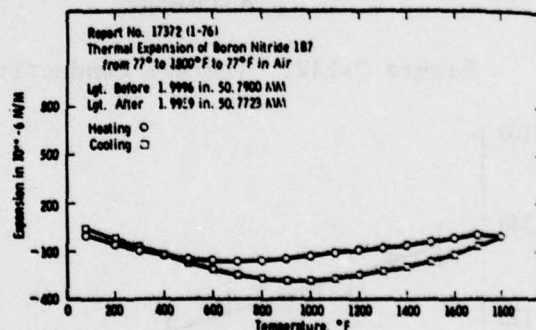
Figure 2-140. Thermal Expansion of Boron Nitride Insulator Material Perpendicular to the Hot-Press Direction "B" (Through the Insulator).
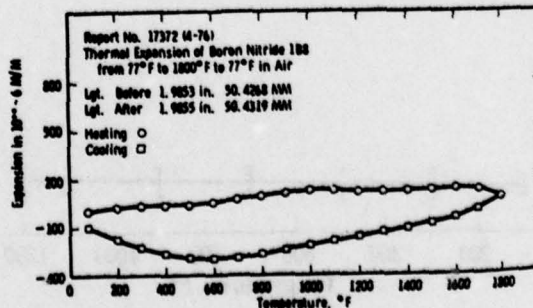
Figure 2-141. Thermal Expansion of Boron Nitride Insulator Material Perpendicular to the Hot Press Direction "B" (Repeat Determination)

141

2.11.8 THERMAL CONDUCTIVITY

The thermal conductivity was determined in both the "A" and "B" directions by a comparative bar technique, using specimens described in Figure 2-142. Both specimens could not be made to the same specification because the bulk dimensions of the material did not permit it. Test results are also reproduced in Figure 2-143.
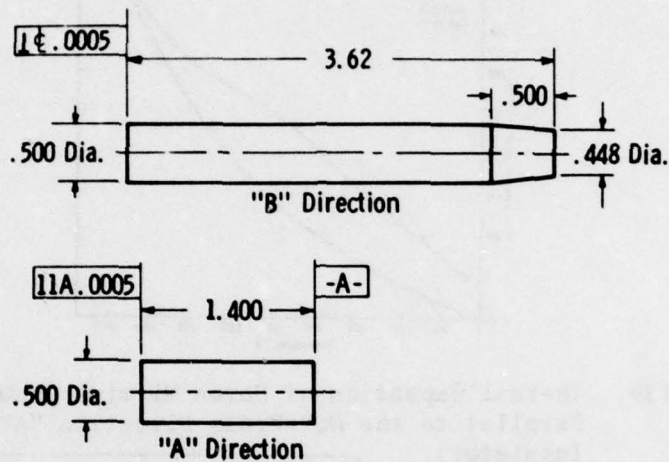
Figure 2-142. Thermal Conductivity Specimen
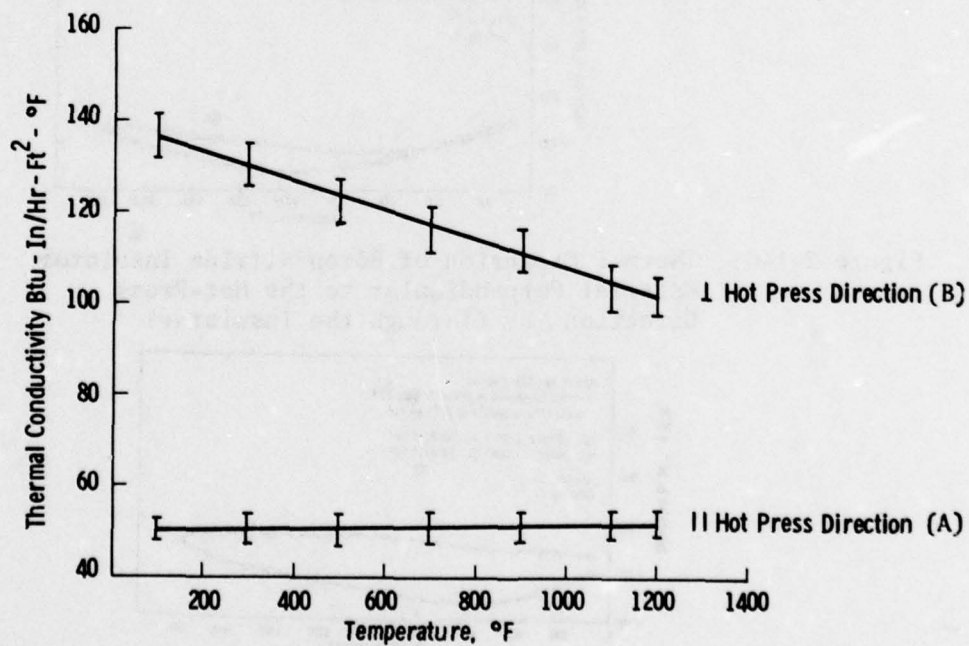
Figure 2-143. Thermal Conductivity in "Combat M" Boron Nitride

142

SECTION 3

THE MICROSTRUCTURE OF CERAMIC STATOR VANE MATERIALS

3.1 INTRODUCTION

As stated previously, hot pressed materials (dense silicon nitride and dense silicon carbide) used for the fabrication of stator vane components were purchased for this program exclusively from the Norton Company. Three different types of silicon nitride (HS110, HS130 and NC132) were evaluated. Except for a few small preliminary billets and the first three 9 inch diameter x 1-1/2 inch thick billets,[3] which were delivered for property determinations, only one variety of silicon carbide, designated Noralide NC203, was examined.

The full extent of material characterization was not realized with the determination of the engineering property data base for component design, analysis and performance review. Density and composition became an important part of the materials and processes acceptance specifications, while the definition of microstructure, including prominent features and defects, not only contributed to an understanding of the material's ability to function but also provided a key to material improvement. Detrimental impurities, for example, were reduced in concentration or eliminated from HS110 silicon nitride to produce HS130, a silicon nitride material which exhibited superior room temperature and high temperature strength properties.[2] Further improvement in room temperature strength resulted when the large inclusions characteristic of HS130 were removed by powder classification in the production of NC132 silicon nitride materials.[5]

143

3.2 HOT PRESSED SILICON NITRIDE

All evidence suggested that Norton hot pressed silicon nitride HS130 was prepared by milling the blended powder with tungsten carbide media. Densification probably occurred in a BN coated graphite susceptor die, using magnesium oxide (MgO) as the sintering additive. Changes in the process to control the starting Si_3N_4 powder were reflected in the lower concentrations of impurities (WC, Al and Ca) in HS130 relative to HS110 material.[2] Classification of the milled Si_3N_4 powder appeared responsible for significant decreases in the WC concentration in later billets of HS130 and all billets of NC132 silicon nitride.[6]

3.2.1 DENSITY AND COMPOSITION

Since the density of other possible crystalline constituents in silicon nitride hot pressed with MgO was greater than the theoretical density of β-Si_3N_4(3.18 g/cc), fully dense Si_3N_4 billet material was expected to exhibit a density of greater than 3.18 g/cc. Tungsten contamination (as either WC or WSi_2), for example, would tend to increase bulk density appreciably. The density of HS130 material ranged from 3.17 to 3.21 g/cc,[3] while that of NC132, although containing less tungsten, ranged from 3.21 to 3.27 g/cc.[5] These data suggest that the HS130 material contained porosity to some degree even though this conclusion was never supported fully by physical evidence other than occasional layered shading in the radiographs of components or the random retention of dye penetrant on the surface of end caps.[4,8]

The cation impurities, as determined by emission spectrographic analyses, found in HS110 and all billets of HS130 (Noralide NC132) are compared in Table 3-1. HS130 was shown to contain approximately 1/10 the Al and Ca content of HS110, and there was evidence to suggest better control of W and C contamination during the early stages of HS130 production.[2] The billet chemistry in the latter phases of HS130 manufacture revealed that a level of relative consistency in composition had been achieved. There was very little compositional difference between HS130 and NC132 silicon nitride.[5]

The magnesium content, as determined by wet chemical analysis, indicated that approximately 1-1.5 w/o MgO was used as a hot pressing additive in HS130 and NC132.[5] This represented a significant decrease as compared to HS110.[2]

3.2.2 MICROSTRUCTURAL CHARACTERIZATION OF Si_3N_4

General Features

The microstructure of hot pressed Si_3N_4 was determined from 1 cm x 1 cm x 3 mm specimens mounted in Kold Mount. Wet abrasive paper was used for rough polishing down to 600 grit. Final polishing was done

144

TABLE 3-1

SUMMARY SPECTROGRAPHIC CHEMICAL ANALYSIS OF HOT PRESSED SILICON NITRIDE

Group Designation	Al	B	Ca	Cr	Mn	Mg	Fe	W	C
NBS No. 57 (Refined Si)	0.67	--	0.73	--	--	0.01	0.65	--	0.09
HS110	0.9	0.055	0.5	0.105	0.015	0.7	0.7	~3	0.3
HS110	0.2	<0.005	0.04	0.035	0.08	~1%	1.0		
HS130	>0.1	<0.002	0.1	0.02	0.018	>0.1	>0.1	~3%	0.42
HS130	0.1	0.001	0.03	0.04	0.04	0.7	0.7		
HS130	0.08	0.0035	0.1-0.8	0.05	0.055	>0.2	<0.3	~1%	0.14
HS130 (NC132)	>0.1-0.07	<0.001-0.002	0.06-0.03	0.06-0.04	0.06-0.05	>0.2	~0.3	~1%	0.14
HS130 (NC132)	>0.1-0.07	0.007-0.003	0.06-0.04	0.06-0.034	0.07-0.05	>0.2->0.1	>0.3->0.1	0.5-<0.3	0.07-0.04

on cloth with Linde B solution. The specimens were preheated, etched in a eutectic mixture consisting of 93 gm K_2CO_3 and 15 g Na from 1/2 to 4 minutes and then cleaned ultrasonically. Surface replicas were prepared using a two-stage carbon replication shadowed with palladium. The replicas were examined in a Siemens Micrograph operating at 100 kV. (The high voltage was used so that diffraction patterns could be obtained from grains and other debris extracted from the surface.)[1]

The major crystalline phase in all Norton hot-pressed Si_3N_4 materials was β-Si_3N_4.[1] Occasionally, traces of α-Si_3N_4 and Si_2N_2O were identified by X-ray diffraction. The presence of α-Si_3N_4 was also confirmed by transmission electron microscopy.

Figures 3-1a, b and c show the typical microstructure of hot-pressed Si_3N_4 (HS130) as revealed by etching 75 seconds at 1350°F.[1] Four types of grains were basically identified. Small equiaxed grains from about 1 μm to 4 μm appeared most frequently. A few larger equiaxed grains of the order of 8-10 μm and a few elongated grains typically 2 x 10 μm were also observed. The grains in these groups were identified as β-Si_3N_4 by electron diffraction; a finding in general agreement with the observations of Evans and Sharp.[27] Occasionally, small round dimples were seen within the grains (Figure 3-1c). While this phenomenon could

a   b   c
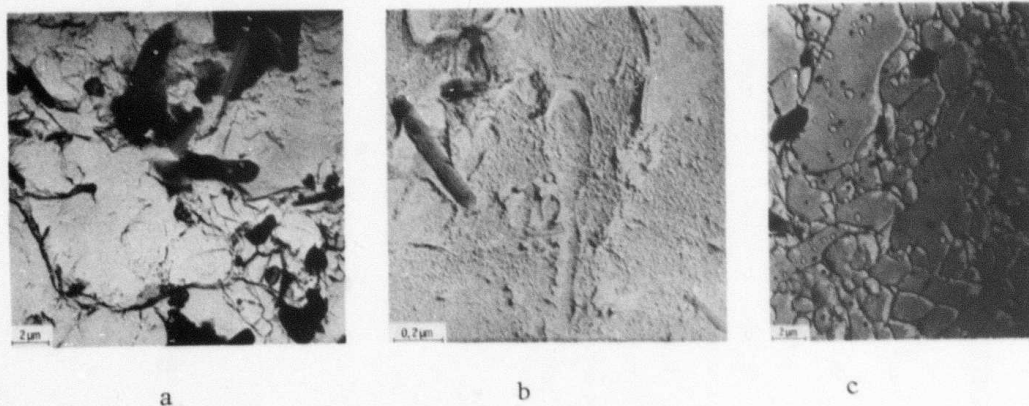
Figure 3-1.   Silicon Nitride (HS130) Micrographs
  a.   Replica Transmission Micrograph- Over Etched 4 min. at 1350°F
  b.   High Magnification - Two-Stage Carbon Replica
  c.   Two-Stage Carbon Replica Etched 75 sec. at 1350°F

be attributed to surface pitting as a result of etching or polishing, it was more likely that these dimples represented small subgrains as observed by transmission microscopy. A fourth type of grain appeared most infrequently, accounting for less than 1 percent by volume.[1] These very large elongated grains, about 10 μm wide and up to 50 μm long, were indexed predominantly as α-Si_3N_4. Their grain boundaries were mainly continuous, although discontinuities were observed.

Other examples of grain morphology as revealed by transmission electron microscopy are shown in Figure 3-2. The diffraction pattern (Figure 3-2a) was taken through the largest diffraction aperture covering the entire micrograph area. The absence of a ring pattern indicates a nonrandom distribution of grain orientation.[1] Figure 3-2b, the grain morphology was developed by etching a fracture in concentrated hydrofluoric acid (HF). The grain size in such a microstructure was difficult to describe and measure, however, fiber lengths rarely exceeded 10 μm with diameters no more than 1 μm.[2]

a   b
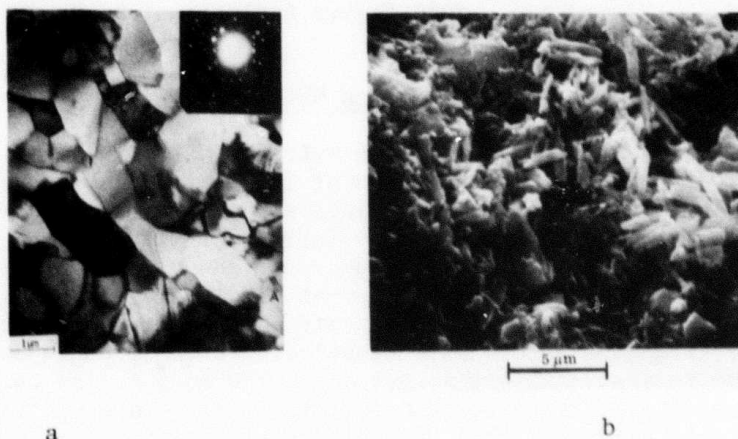
Figure 3-2.   Grain Morphology in Si_3N_4 (HS130)
a.   Transmission Micrograph (100 kV) -
     Absence of Ring Pattern Indicates
     Nonrandom Grain Orientation.
b.   Etched Fracture Surface, Revealing
     Fibrous Grain Structure

Pole-figure analysis[3] indicated some preferred orientation in hot-pressed Si_3N_4 (HS130). Figure 3-3 is a reproduction of a (210) pole-figure from a specimen obtained from billet 309902-2. The hot-pressing direction is vertical (from top of page). The pole-figure and histogram indicate that about 15 percent of the grains are oriented, with the basal planes within 20° of the hot-pressing direction or, conversely, with the C axes within 70° of the hot-pressing direction.

Hot Pressing Direction
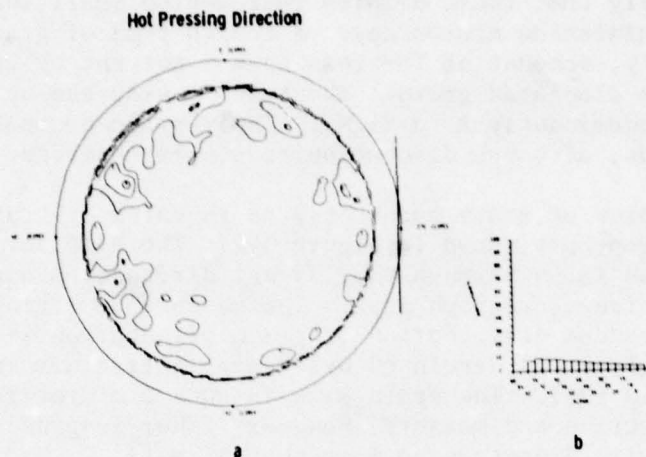
Figure 3-3. Pole Figure Analysis of Si_3N_4 (HS130)

Impurities in High Density Silicon Nitride

Although hot-pressed silicon nitride (HS130) was nominally 98 percent pure, the distribution of impurities was apparently not random. Macroscopically, large inclusions were observed which were directly related to the premature failure of flexural and fatigue specimens. The three flexural specimens shown in Figure 3-4 were selected from a group of 20 tested at 2350°F, in air, at a cross-head velocity of 0.02 in/min to illustrate the effect. The average strength of this group was 69,000 psi. The decrease in strength due to inclusions amounted to approximately 35 percent. The most common large inclusion was a particle of free silicon (Figure 3-4a). This particular particle was located below the most highly stressed portion of the tensile surface. The micrograph indicates clearly that failure originated at the particle-matrix interface.[2]

Another frequently observed inclusion was an iron-rich particle (Figure 3-4b). Probe analysis indicated that inclusions of this type were iron-silicon intermetallic compounds.[2] A rarely found inclusion is shown in Figure 3-4c. Here the particle was magnesium rich, probably a magnesium silicate located at the bottom of the round hole.[2]

The foreign inclusions shown in Figures 3-5a and b also affected fatigue tests. The free silicon inclusions apparently acted as stress raisers, and slow crack growth was induced at the particle matrix interface (Figure 3-5b.) Failure of the specimen could have been initiated by the fatigue failure of the soft silicon inclusions.[2]

148
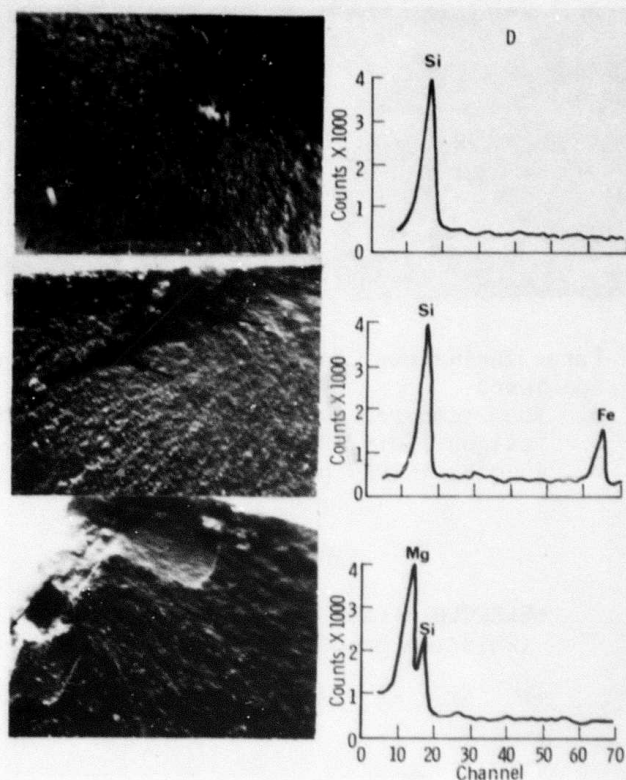
Figure 3-4. Common Inclusions on Fractured Surfaces of Si_3N_4 (HS130)
- a. Silicon inclusion failed at 58,000 psi, light micrograph, 35X
- b. Iron-rich inclusion failed at 45,500 psi, SEM micrograph, 130X
- c. Mg-rich inclusion failed at 57,800 psi, SEM micrograph, 140X

Extensive X-ray radiography was conducted on flexural test specimens in an attempt to correlate detectable flaws with strength degradation.[3] Groups of ten specimens from each of five HS130 Si_3N_4 billets were radiographed. Almost all specimens from billets 1, 2 and 3 (Table 3-2) were shown to contain high density inclusions. No high density inclusions were observed in specimens machined from billets 9 and 10. After testing all 50 specimens, it was quite obvious that the majority of the fractures from tests at 1800°F and 2370°F were not associated with high density inclusions. Premature failures were frequently associated with white, powdery particles of the type described in Figure 3-6.
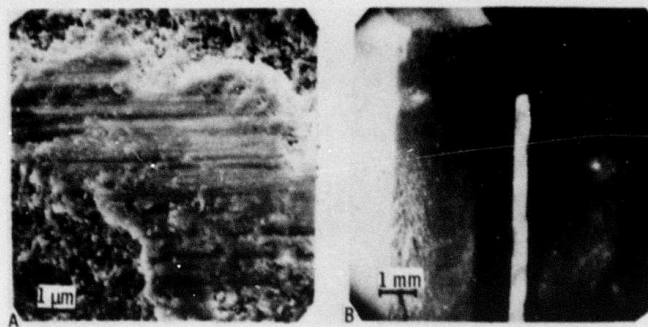
Figure 3-5. Large Inclusions Causing Premature Failures in Fatigue
Specimens
a. Room temperature, HS110 failure - 60,000 psi.
Fatigue limit 70,000 psi
b. 2350°F, 40,000 psi. HS130 failure after 8 min.

TABLE 3-2

SELECTED BILLET CHEMISTRY FOR Si_3N_4
(Emission Spectrographic Analysis)

Billet No.	Al	B	Ca	Cr	Fe	K	Mg	Mn	Na	Ni	Ti	W	C
011072 B1 (HS110)	0.8	0.01	0.5	0.2	0.6	0.01	0.6	0.02	0.01	0.01	0.01	~ 3	0.41
309902-1 (HS130)	0.1	0.001	0.03	0.04	0.7	0.004	0.7	0.04	0.02	0.01	0.02	~ 4	0.43
309902-2 (HS130)	0.1	0.02	0.07	0.04	0.6	0.003	0.8	0.03	0.004	0.01	0.02	~ 3	0.41
309902-3 (HS130)	0.2	0.01	0.03	0.04	0.6	0.003	0.7	0.03	0.006	0.01	0.02	~ 3	0.36
309902-9 (HS130)	0.08	0.001	0.03	0.04	0.4	0.006	0.6	0.03	0.008	0.01	0.02	0.5	0.07
309902-10 (HS130)	0.09	0.004	0.04	0.04	0.5	0.004	0.5	0.03	0.008	0.01	0.02	0.3	0.04

ACCURACY: W and Fe by visual reading: accuracy 0.3 to 3 times amount present.

All other elements by direct reading: accuracy ± 50% of amount present.

Scanning electron micrographs of other defects are shown in
Figure 3-7. Microprobe traces taken across these inclusions showed a
lower concentration of Si and a higher nonuniform concentration of
carbon, as compared to bulk Si_3N_4. A few of the inclusions were removed
using a WC tool and subjected to Debye-Scherrer X-ray diffraction.
Faint lines, corresponding to hexagonal BN, were seen along with strong
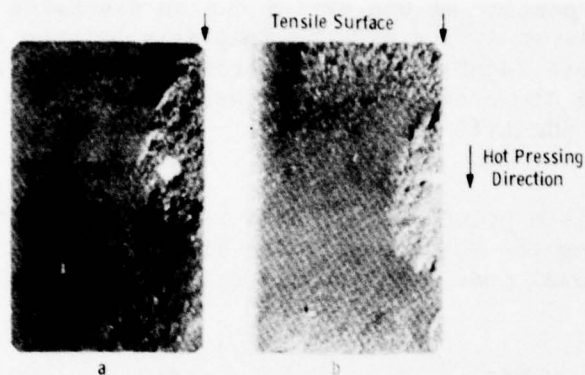
Figure 3-6. Light Micrographs Showing Orientation of Lenticular, Non-Densified Silicon Nitride Inclusion in Flexural Test Specimens
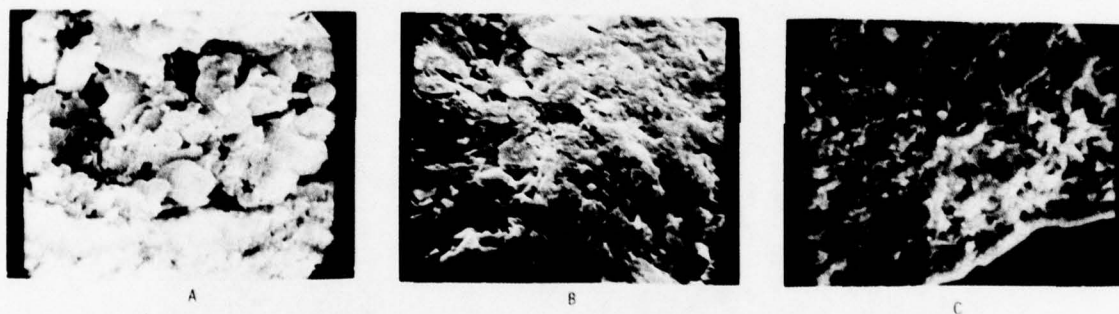
Figure 3-7. Scanning Electron Micrographs of Defects in HS130 Si_3N_4
    a. White Powdery Inclusion - 2800X
    b. BN Powder - 5500X
    c. Powdery Consolidated Si_3N_4 - 2000X

lines from β-Si3N4. Laser source emission spectroscopy also confirmed silicon, but boron was only found in an inclusion from billet 1. These white powdery inclusions were considered to be small agglomerates of nondensified Si_3N_4 which occasionally contained BN.[3]

The anisotropy observed in the strength of silicon nitride may be attributed to layering, inclusions, and/or voids rather than to preferred orientation of grains.[2] Figure 3-8a represents a composite micrograph of replicas taken from three perpendicular faces of a hot-pressed billet. No apparent differences in grain orientations can be detected but, in

151

all cases, a bimodal distribution of grain sizes was measured. About 80 percent of the grains were equiaxed and varied in size from 0.5 to 2 μm. Another 20 percent of the grains had an elongated appearance with the short axis between 1-2 μm and the long axis between 4-10 μm. Both types of grains were identified by electron diffraction as β-Si3N4. About 1 percent of the elongated grains were larger - up to 30 μm long. These grains were identified as α-Si3N4.

Figure 3-8b is a print (2X) of an X-ray radiograph taken from specimens cut along the thickness of the billet so that, when tested in a four-point flexural mode, the tensile axis was parallel to the
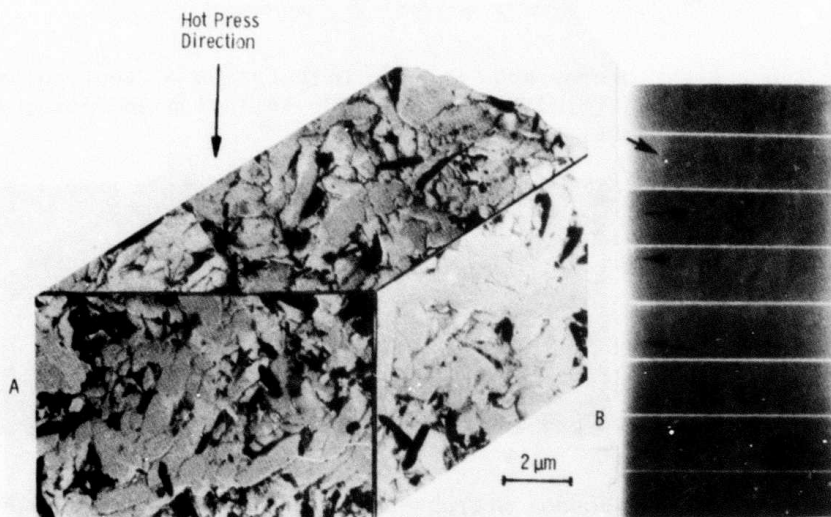
Figure 3-8. Typical Features of an As-Received Si3N4 Billet (HS130)
a. Composite replica micrograph showing grain morphology on three perpendicular faces
b. Radiograph of specimens cut along the billet thickness showing flaws and variable density layers

hot-pressing direction. Close examination of the radiograph shows two possible reasons for the lower strength displayed by these specimens.[2] The variations in intensity indicate layers of varying density which may result from gradients in pressure along the pressure axis during hot-pressing. The boundaries between the zones of varying density could cause a decrease in strength when the applied stress acts perpendicular to these boundaries. There are also numerous flaws

152

(marked by arrows). The dark flaws indicate inclusions of higher density than the parent material, while the white flaws indicate areas of lower density, possibly small cracks.

Almost all of the indicated flaws were elongated in the same orientation. Therefore, each could represent spherical flaws (particles or voids) which were squashed to a lenticular shape during hot-pressing. If the fracture strength of the material follows the Griffith relation:

$$\sigma = A \sqrt{\frac{\gamma E}{c}} \tag{1}$$

where γ is the fracture energy, E the elastic modulus and c the critical crack size, a lenticular flaw would contribute a different crack length c, depending on the orientation of the flaw with respect to the applied stress σ. Figure 3-8b implies that c is larger when the applied stress is directed parallel to the hot-pressing direction, hence the lower strength measured in this orientation. Although an estimate for c can be obtained, comparison of the fracture stress, σ, with the flexural test data was not possible because the exact location of the flaws with respect to the tensile surface was not known.[2]

In the case of these flexural strength specimens, Eq. (1) is applicable if an assumption is made that the inclusions define the size of a critical flaw.[2] Since γ and A were not determined for the particular test conditions:

$$\sigma \sqrt{c} = \text{constant} \tag{2}$$

where σ is the stress at the flaw and c is the flaw size. The estimated flaw sizes for inclusions identified in Figure 3-4 were 290 μm, 220 μm and 140 μm, respectively.[2] With stress levels at the flaw corresponding to σ = 40,000 psi for the silicon particle, which lay below the surface; σ = 45,500 psi for the iron rich particle; and σ = 57,800 psi for the magnesium-rich inclusion: $c_{\mu m}$ and $\sigma \sqrt{c}$ x 10 become:

	Particle A	Particle B	Particle C
c μm	290	220	140
$\sigma \sqrt{c}$ x 10^6	680	675	685

Such inclusions were regarded as critical flaws that caused serious degradation in the strength of the material.

On a microscopic scale, impurities were not generally associated with grain boundaries in HS130.[1] Individual particles or clusters of particles were observed. Typical examples are shown in Figures 3-9a, b

153

and c. A row of particles in an α-grain were less than 300Å in diameter (Figure 3-9a). These particles were too small to be identified by electron diffraction. Similarly, a cluster of impurities of less than 200Å in diameter is shown in an α-grain by dark field illumination in Figure 3-9b. One or two extra spots were observed in the diffraction pattern (arrow); however, positive identification was impossible. Larger particles about 1000Å in diameter appear in Figure 5-9c. Elastic strain fields were associated with these larger particles. A few particles were located in the grain boundary defined by the dislocation network (marked gb in the micrograph).

a   b   c
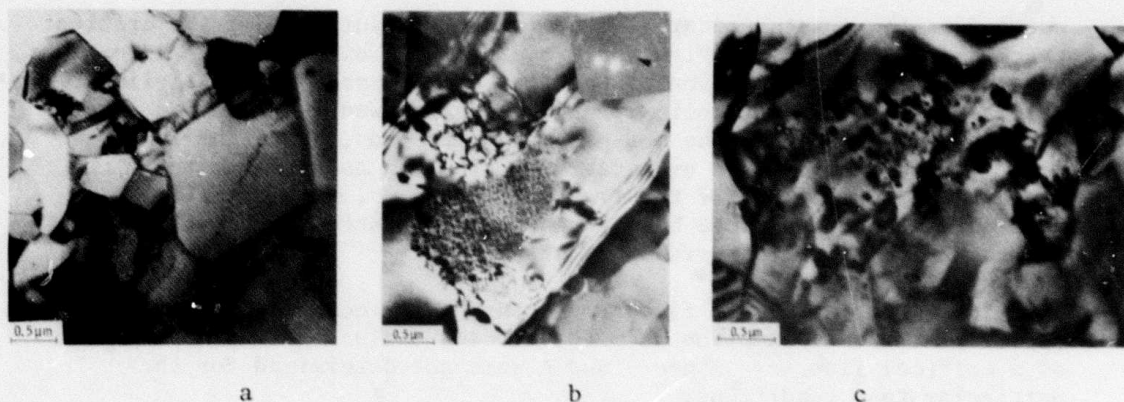
Figure 3-9.   Transmission Micrograph Displaying Impurities in HS130 Silicon Nitride
a.   Chain of impurities across a grain (100 kV)
b.   Dark field image of $\bar{g}$ showing a cluster of impurities (again 800 kV)
c.   Round impurities associated with strain fields (800 kV)

Voids were only observed occasionally.[1] It was difficult to decide whether a void was originally present or whether it was the result of a grain being lost during thinning and handling. Since the voids shown in Figure 3-10 display a sharp contrast transition, they represent true voids, rather than being a result of thinning. Other-wise, low angle ion bombardment would have produced a more gradual transition in contrast across the edge of the void.

The distribution of the major impurity elements was determined by microprobe analysis.[2] Typical results for the HS110 material are shown in Figure 3-11. Similar results, with lower levels of calcium

154

Figure 3-10.   Typical Pores in Hot-Pressed Silicon Nitride
(HS130) (800 kV, 15° Thinning)
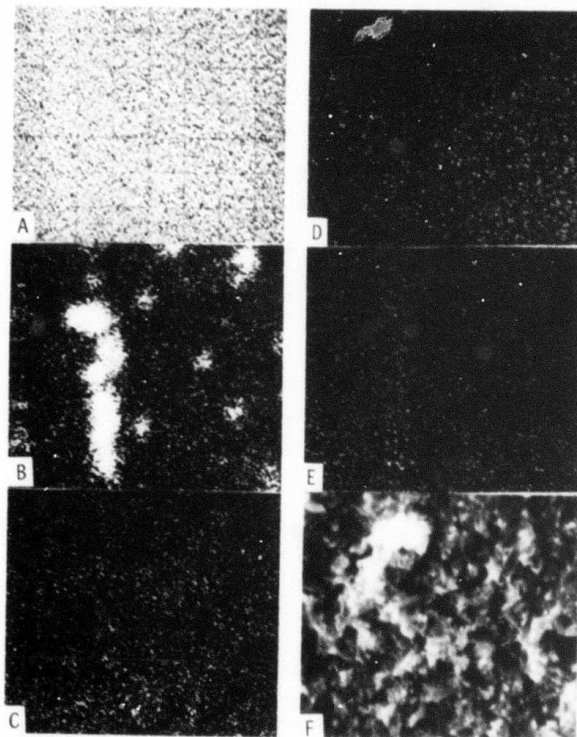
Figure 3-11.   Distribution of Impurity Elements by Microprobe Analysis
of HS110 Material.   1600X
a)   Si K_α, 400 c/s   b)   Fe K_α, 62 c/s   c)   Mg K_α, 76 c/s
d)   Ca K_α, 40 c/s   e)   Al K_α, 76 c/s   f)   Reference scanning
electron micrograph.   Note segregation of iron, without
depletion of Si.

155

and aluminum, were obtained for HS130 material. The scanning of the five elements was done over the same area, but no correlation between the signatures of the various elements was obvious, nor was it possible to state whether the elements were concentrated in the boundaries or the grain interior.[2] This was due to the fact that the probe beam diameter was about 2 μm, which was of the order of the grain size. Figure 3-12 indicates numerous clusters of iron which, in a few cases, extend over 50 μm in length. Most of these clusters were about 10 μm diameter. There was no apparent change in intensity of the silicon count over the iron-rich areas. This was interpreted to indicate that iron was present as an iron-silicon compound.[2]
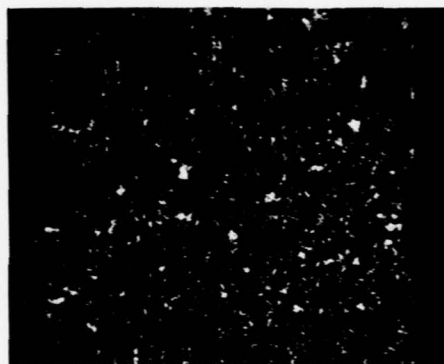
Figure 3-12. Low Magnification (335X) Microprobe Scanning Micrograph Showing Fe Distribution in HS130 Grade Material. (Clusters are about 10 μm in Diameter.)

Impurity distributions on a microscopic level are shown in Figure 3-13. Figure 3-13a is a replica transmission micrograph taken from the fractured surface of a fatigue specimen near the fracture origin. This particular specimen failed prematurely in a fatigue test.[2] It is possible that the concentration of fine impurity particles was the source of failure. Figure 3-13b shows an area occasionally found in thin foil transmission micrographs, identifying a cluster of particles within a large grain. These particles were too small for a positive identification by electron diffraction. Strain fields (dark semi-rings) are associated with the particles. These may originate with the hot-press cycle when differential thermal contraction occurs between the particles and the Si_3N_4 matrix as a result of cooling.[2]
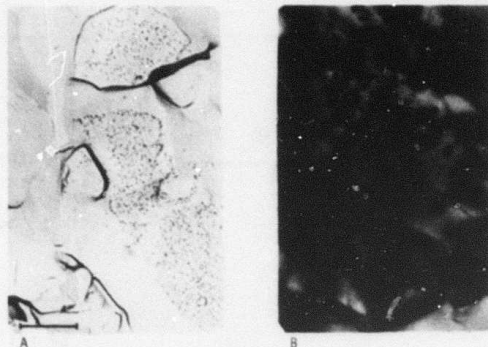
Figure 3-13. Microscopic Distribution of Impurity Particles (0.5 μm
              Scale Bars)
              a. Two stage carbon replica, fracture surface, premature
                  failure of fatigue specimen (HS110)
              b. Transmission micrograph (HS130)

Additional information concerning the distribution of major
impurities in silicon nitride was obtained by Auger analysis.[3]
Specimens of square cross section (0.1 x 0.1 in) were placed in a vacuum
chamber and evacuated overnight at a pressure of 10^{-9} torr. The speci-
mens were then broken to expose a virgin fractured surface. Since
extensive examination of a large number of fracture surfaces indicated
that the fracture was predominantly intergranular at all temperatures
between RT and 2500°F, particular attention was paid to the grain
boundary phase.

Semiquantitative results were obtained by measuring the peak-to-peak
height (I_x) of the major peak of each element present.[3] From the known
relative sensitivity, S_x, of each element with respect to a silver
standard and the scale factor, K_x, the concentration of element x in
atomic percent is given by

$$C_x = \frac{I_x 100}{S_x K_x} \Bigg/ \Sigma \frac{I_a}{S_a K_a} \tag{3}$$

where the sum is over one peak from each element present on the surface.

A typical Auger trace of a freshly fractured surface of HS130
silicon nitride is shown in Figure 3-14. Similar traces were obtained
for HS110 material. The major cation impurities were Ca, Na, K and Mg,
which combined with silicon, oxygen and nitrogen to represent the
grain boundary composition.[3]

157
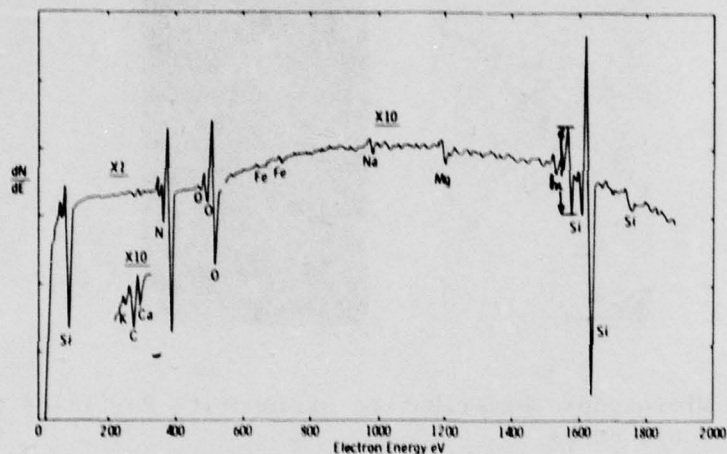
Figure 3-14. Typical Auger Trace of a Fresh Fracture Surface (HS130)

It was possible to reveal the transition and bulk composition by sputtering the fresh fractures in argon to remove material 2500Å from these surfaces in 40Å increments. The results of analyses after sputtering for both grades of Si3N4 (HS110 and HS130) appear in Figure 3-15. Nitrogen and iron increased in the bulk composition, while oxygen and the alkalies decreased.(3)
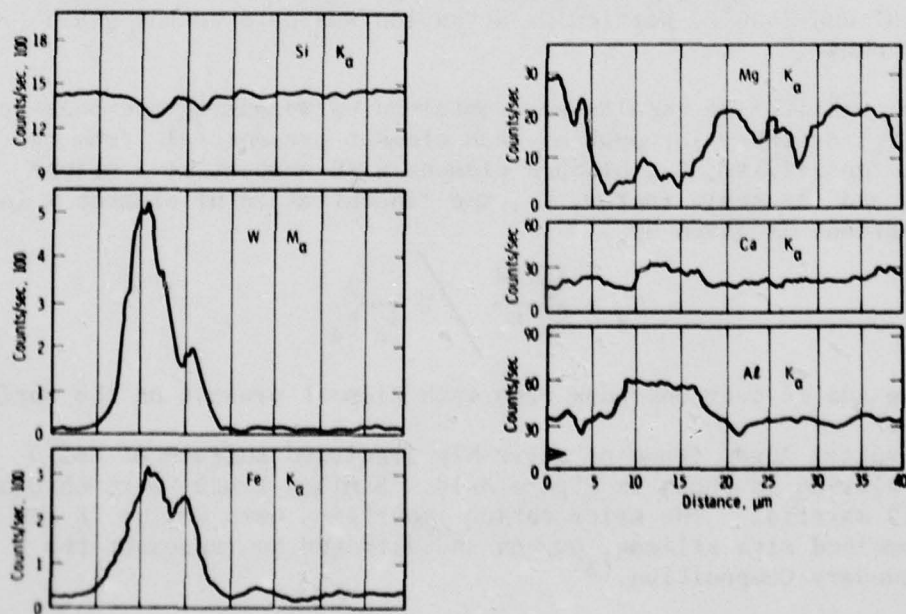
Figure 3-15. Element Distribution Profiles in Hot-Pressed Silicon Nitride (HS110 and 130) by Auger Analysis

The oxygen concentration converted from Auger profiles (Table 3-3) was consistent with AMMRC neutron activation analysis which showed 2-5 and 6-9 percent oxygen in HS130 and HS110 silicon nitride, respectively.[3] The high level of oxygen at the boundary indicated a glass phase composition approaching:

HS110: $2MgO \cdot 2Al_2O_3 \cdot 9CaO \cdot 22SiO_2$

HS130: $CaO \cdot MgO \cdot 8SiO_2$
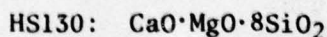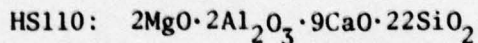
TABLE 3-3

CONCENTRATION OF ELEMENTS
WITHIN THE Si_3N_4 GRAIN (w/o)

(Data Converted from Auger Profiles)

	Si	N	O	Fe	Al	Mg	Ca
HS110	balance	34	8	1.2	1.4	0.9	0.8
HS130	balance	36	6.5	1.2	---	0.7	---

The high concentration of CaO in the boundary glass phase was considered significant in that it could account for the substantial difference in high temperature creep strength between the HS110 and HS130 Si_3N_4. Creep data suggested that a major contribution to the observed deformation came from grain boundary sliding. The effect of Ca, and to a lesser degree Al, K and Na, could be related to an appreciable decrease in the viscosity of silicate glasses with small additions of CaO.[5]

The combined effect of the alkaline earth and alkali metals, Ca, Na and K, on the high temperature strength of hot-pressed silicon nitride is indicated in Figure 3-16, where cation concentration is plotted against average flexural strength.[3] At 2370°F, for example, a reduction in strength from 55,000 to 30,000 psi was measured when the Ca concentration changed from 0.03 to 0.09 w/o. The effect of composition on the creep properties was considered even more significant.

While Ca^{++} appears to be detrimental to high temperature strength properties of hot-pressed silicon nitride, a study of wetting indicated that small concentrations of Ca in the glass phase are essential if the molten glass phase is to wet Si_3N_4 grains to achieve high density.[5] Therefore, calcium cannot be eliminated completely for the benefit of high temperature strength.
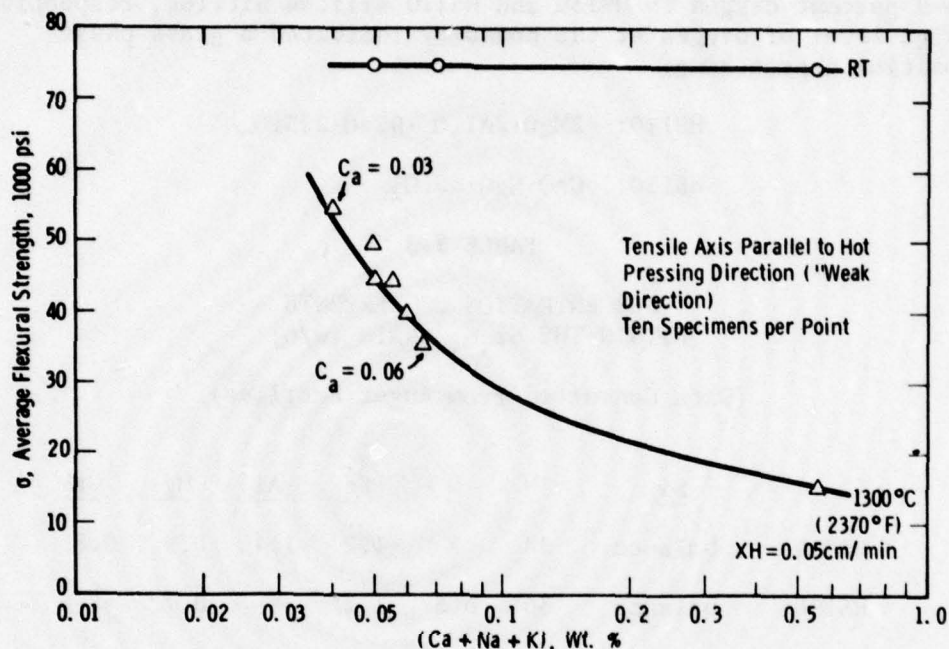
Figure 3-16.   Effect of Impurities on the Flexural Strength
(4 Point Bend) of Silicon Nitride (HS130)

Dislocation Structures in High Density Silicon Nitride

Evans and Sharp[20] and Butler[27] discussed the dislocation
structures in β phase Si_3N_4. While the observations reported were in
general agreement with their work, dislocation structures were also
observed in the very large, elongated α grains.[1]   The dislocation
structures in both the α and β phases are similar.

To determine Burger vectors in both the α and β phases, grains
extracted during surface replication were examined.[1]   These extracted
grains were thin enough for high voltage transmission microscopy. By
the nature of their formation they presented suitable conditions for
examinination of slip behavior at room temperature. Normally, in a
brittle material like Si_3N_4, the critical stress for dislocation motion
is much higher than the fracture stress (at least at low temperatures).
Only at the fracture surface do sufficiently high stresses develop to
cause dislocation motion.[1]   Consequently, the thin extracted grains
provided the fracture surfaces for transmission microscopy.

160

Examples of slip bands observed in α and β grains are shown in Figure 3-17. In both examples, the dislocations are mostly of the screw type. Furthermore, the conditions of $\bar{g}.\bar{b} = 0$ or $\bar{g}.\bar{b} \neq 0$ are consistent only with a Burger's vector of the type c [0001].[1] Other examples of tilting experiments are given in Table 3-4, from which the conclusion was drawn that the most common Burger's vector for both α and β was c [0001]. This had been observed previously for the β phase only.[20]
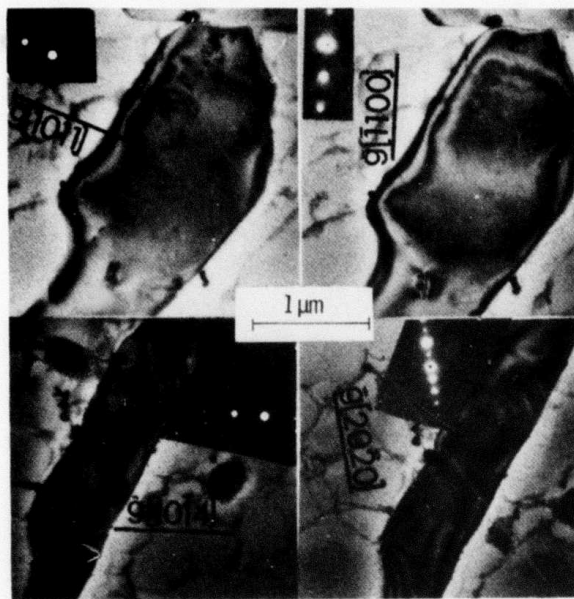
Figure 3-17. Room Temperature Slip Traces in Extracted Si_3N_4 Grains - Tilt Analysis Consistent with B.V. C[0001]. Note That Dislocations Are Almost All of the Screw Type. (800 kV) Top row: β grain [1101] ZA. Bottom row: α grain [0110]ZA Left: g.b≠0   Right: g.b=0

Two more examples of commonly observed dislocations in the large α grains are shown in Figure 3-18a and b. The dislocation segments that are in contrast and the segments that are out of contrast (arrows Figure 3-18a) probably comprise a low angle twist boundary. Near-edge dimples are shown in Figure 3-18b (note dislocations of opposite signs identified by arrow). Common dislocation boundaries in β grains are shown in Figure 3-19. Other common features observed in β grains appear in Figure 3-20. Note dislocation tangles (Figure 3-20a and b) and what might be bundles of stacking faults in Figure 3-20c and d.

TABLE 3-4

CONDITIONS FOR DISLOCATION VISIBILITY AND NONVISIBILITY FOR $\bar{b}=c$ [00010]

g	$\bar{g}.\bar{b}=0$	$\bar{g}.\bar{b}\neq0$	Phase
$\bar{2}022$		X	β
$3\bar{3}00$	X		β
$02\bar{2}2$		X	β
$2\bar{2}00$	X		β
$10\bar{1}4$		X	α
$20\bar{2}0$	X		α
$10\bar{1}2$		X	α

a   b

Figure 3-18.   Dislocation Structure in HS130 Silicon Nitride
      a.   2 Grain $\bar{g}$ = [0$\bar{1}$127], [$\bar{1}$2$\bar{1}$1] ZA (100 kV)
      b.   Near Dimples (arrow) in a α Grain
          $\bar{g}$ = [10$\bar{1}$2], [$\bar{1}$3$\bar{2}$2] ZA (100 kV)
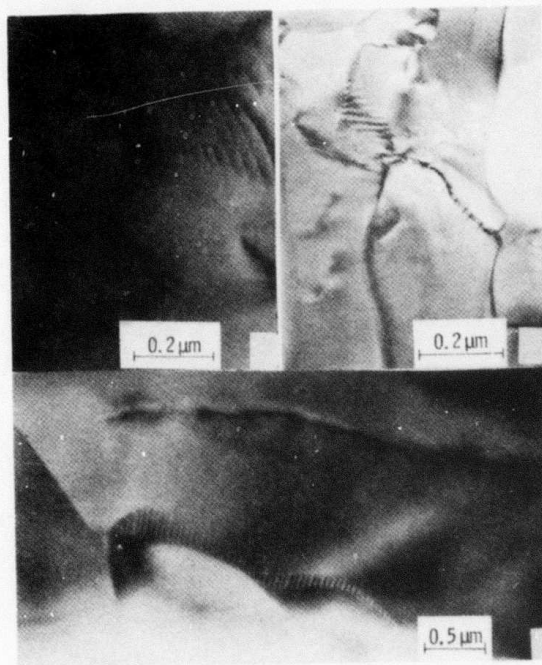
Figure 3-19. Examples of Frequently Observed Grain Boundary
Dislocation Networks and Faults
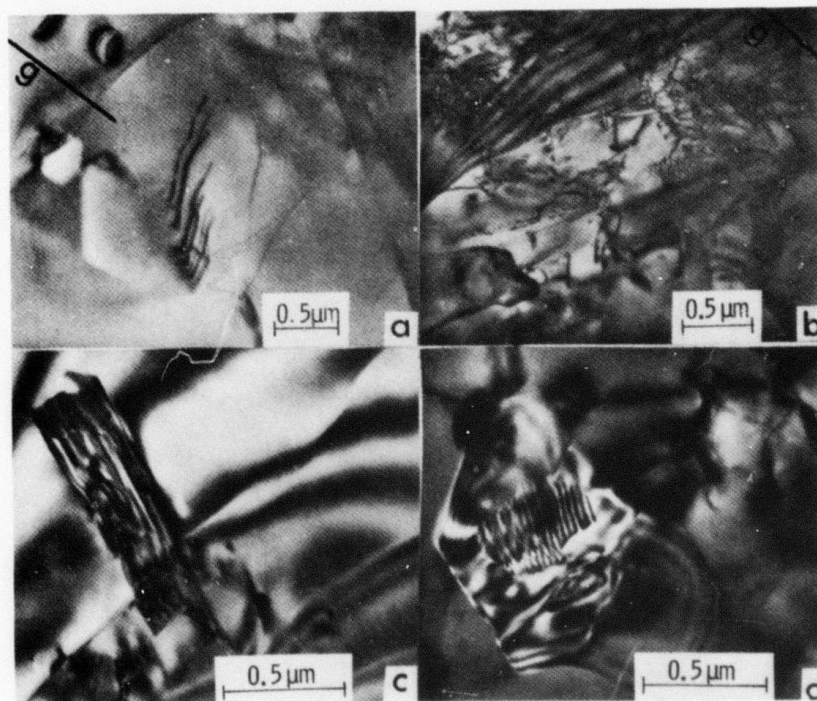
Figure 3-20. Examples of dislocation (a and b) and possible fault
structures (c and d) in β grain. Note tangles in b
and grain boundary network in a. (800 kV)

164

3.3 HOT-PRESSED SILICON CARBIDE

All evidence suggests that the Norton hot-pressed silicon carbide was also prepared for densification by milling with WC media. The hot-pressing additive in this case was apparently Al_2O_3. Tungsten carbide contamination decreased while boron concentration showed a marked increase in billets of late manufacture.[3,7]

3.3.1 DENSITY AND COMPOSITION

The theoretical density of SiC is 3.21 g/cc. Since the density of the Al_2O_3 hot-pressing aid and the WC contaminants are greater, one would expect the fully dense material to have a bulk density greater than 3.21 g/cc. As shown in the Property Certification Tables,[3,4] the density of NC203 SiC ranged between 3.28 and 3.33 g/cc.

Typical spectrographic analysis of the major impurities in Norton hot-pressed SiC is given in Table 3-5. The main impurity element was aluminum, which was added as alumina presumably to promote liquid phase sintering. Tungsten represented another major impurity which was present mainly in the form of WC, a residue of the ball milling operation. The source of iron contamination was not determined. It may have resulted from a crushing operation or it may have occurred as a natural impurity in the starting powder.[3]

TABLE 3-5

SPECTROGRAPHIC CHEMICAL ANALYSIS OF HOT PRESSED
SILICON CARBIDE (NC203)

Group Designation	Al	B	Ca	Cr	Fe	Mg	Mn	W	C
NBS No. 57 (Refined Si)	0.67	--	0.73		0.65	0.01	--		0.09
SiC	>1.0%	0.04	<0.003	<0.001	0.1	<0.001	<0.001	>1.0%	~27.5%
SiC	>1.0	0.05-0.02	0.01-0.02	<0.003	0.1			>0.3	
SiC	>1.0	0.06-0.02	0.03-0.007	<0.003	0.1			>0.3	

Powder X-ray diffraction data appear in Table 3-6.[3] WC was identified as the only impurity phase. Al_2O_3 was not detected, indicating that it was either not present in sufficient quantity or, more probably, that it was present as a constituent of an amorphous grain boundary phase.

The distribution of the impurities and the additives in hot-pressed SiC are illustrated in Figure 3-21. Alumina was the major constituent

165

of the grain boundary phase, which also contain a dispersion of W-rich particles.[3] Although the probe beam was defocused for an oxygen scan, it was apparent that the grain boudnary phase contained oxygen also. An overlap of Fe and W peaks was observed. This is similar to that reported previously for Si_3N_4. In both cases the source of W appeared to be the ball milling media. During hot-pressing at 3700°F, a reaction apparently occurred between W, Fe and Si which resulted in the formation of a W-Fe-Si compound. Unfortunately, this compound could not be identified by powder X-ray diffraction in either SiC or Si_3N_4.[3]

TABLE 3-6

POWDER X-RAY DIFFRACTION DATA FOR HOT-PRESSED SiC
(NC203) NORTON BILLET 472-3

(SiC Phase is a Mixture of the Hexagonal II and IV Polymorphs)

d($\overset{\circ}{A}$)	Relat. Intensity*	Phase	d($\overset{\circ}{A}$)	Relat. Intensity*	Phase
3.47	W	unknown	1.23	VW	SiC,WC
2.82	W	WC	1.22	VW	SiC
2.62	M	SiC	1.15	VW	WC
2.58	W	SiC	1.13	W	SiC
2.51	S	SiC,WC	1.09	W	SiC
2.35	M	SiC	1.045	W	SiC
2.18	W	SiC	1.015	VW	SiC,WC
2.10	VW	SiC	1.00	W	SiC
2.00	W	SiC	0.99	W	SiC
1.87	W	WC	0.975	W	SiC
1.68	W	SiC	0.955	W	SiC,WC
1.60	VW	SiC	0.942	W	SiC,WC
1.54	S	SiC	0.915	W	SiC
1.45	VW	SiC,WC	0.89	VW	SiC
1.42	W	SiC,WC	0.865	W	SiC
1.33	VW	SiC	0.840	W	SiC
1.31	VW	SiC	0.790	W	SiC
1.29	W	SiC,WC			
1.26	W	SiC,WC			

Referring specifically to the last eight billets received, the tungsten content was typically less than 0.3 w/o.[7] The aluminum concentration was reasonably uniform at a concentration slightly greater than 1.0 w/o. This is significant because it represents a standard of quality control in the blending process where alumina is apparently the hot-pressed additive employed. Boron, which was low in billet 050873, rose significantly from 300 to 800 ppm.[7] Boron, in some form, was apparently added deliberately during the fabrication of these later billets. The calcium content was reduced to levels approaching the alkali metals. It is impossible to comment on the significance of calcium, however.

---

*W = Weak
VW - Very Weak
 S=Strong
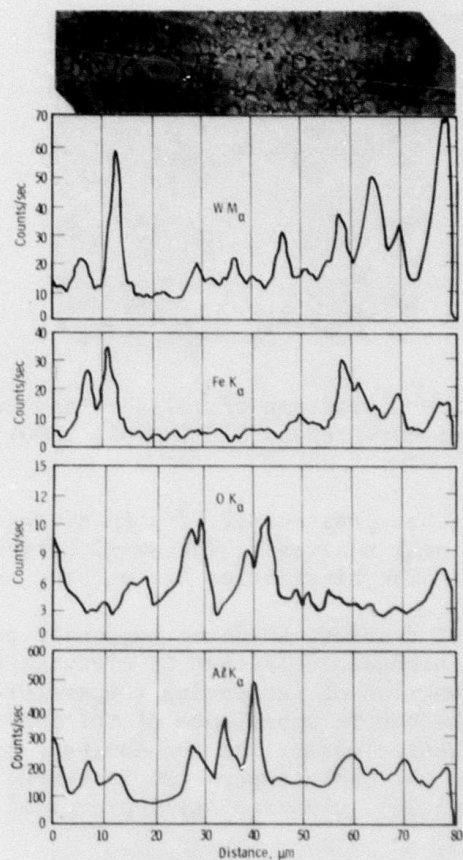
Figure 3-21. Microprobe Line Traces. Beam Path Marked
on Micrograph.
a. Hot Pressed SiC, (Norton 472).
b. Black Particles, W(Fe) Silicide
c. White Particles, Free Si
d. Al_2O_3 in Grain Boundaries

Twenty-eight elements were identified in the analyses. Most of
these represented trace impurities which may or may not affect the
performance of silicon carbide.[7]

3.3.2 THE MICROSTRUCTURE OF SILICON CARBIDE

General Fractures

Grain morphology is illustrated in Figure 3-22, a scanning electron
micrograph of a polished and etched specimen (electrolitic etch 20 KOH,
6 volt 25 sec). Equiaxed grains, which vary in size from about 1 μm to

167
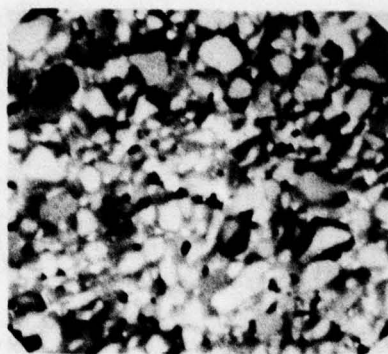
Figure 3-22. SEM Micrograph of Polished and Etched Surface
of Hot-Pressed SiC (NC203, 2000X)

10 µm, are typical of hot-pressed SiC.[3] An average grain size of 3 µm
was established by lineal analysis. The small bright particles are WC
or W-rich inclusions. The black holes are etching cavities.

An examination of fracture surfaces suggested a gradual transition
in failure mode from predominantly that of cleavage to predominantly
intergranular as a function of increasing temperature.[3] Frequent
cleavage steps and the smooth appearance of the fracture surface (Fig-
ure 3-23) indicated that cleavage was the dominant mode of failure at
room temperature. As the test temperature increased to 1470°F, (Fig-
ures 3-24, 3-25, and 3-26), cleavage still prevailed, but the fracture
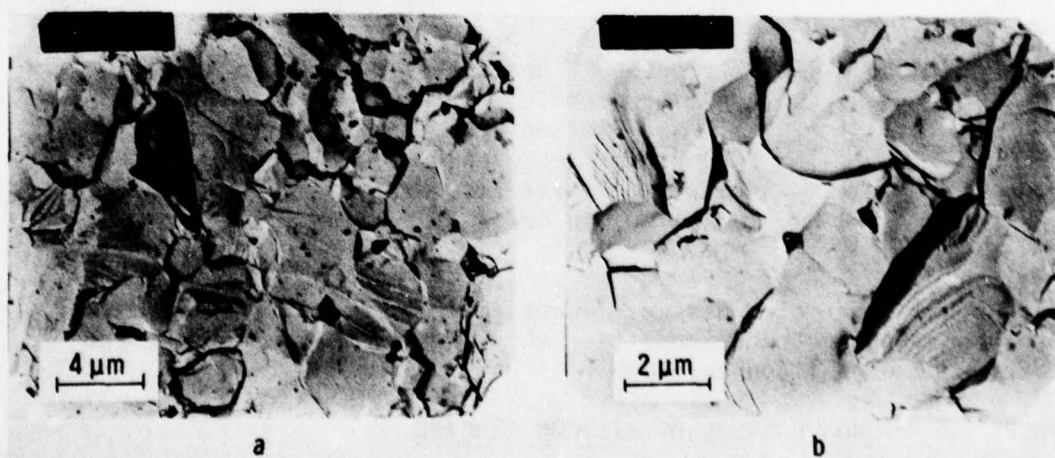
Figure 3-23. Replica Transmission Micrographs of Room Temperature
Fracture Surfaces - Norton Hot Pressed SiC (NC203)

168
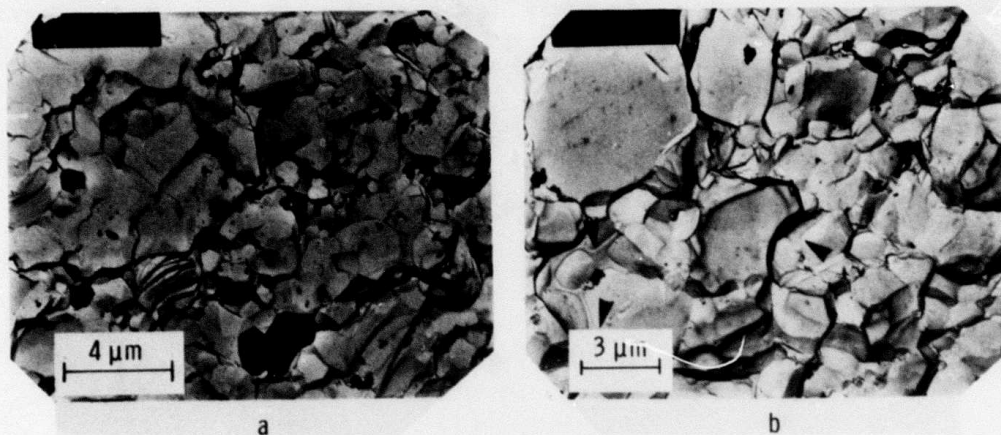
Figure 3-24. Replica Transmission Micrograph of 752°F Fracture
Surfaces - Norton Hot Pressed SiC (NC203)

Figure 3-25. Replica Transmission Micrographs of 1115°F Fracture
Surfaces - Norton Hot Pressed SiC (NC203)

surface became rougher and secondary intergranular cracking was visible.
Furthermore, large areas of a grain boundary phase were frequently
exposed. This phase appeared to have been molten at some previous time.
The rounded nature of the grain edges was consistent with a liquid-phase
sintering phenomenon that involves partial dissolution at the grain-
boundary interface. At 1832°F there was little evidence of cleavage.
Intergranular cracking appeared dominant in Figure 3-27. The small
square particles (Figure 3-27b) probably resulted from nucleation of a
corrosion product.[3]

169
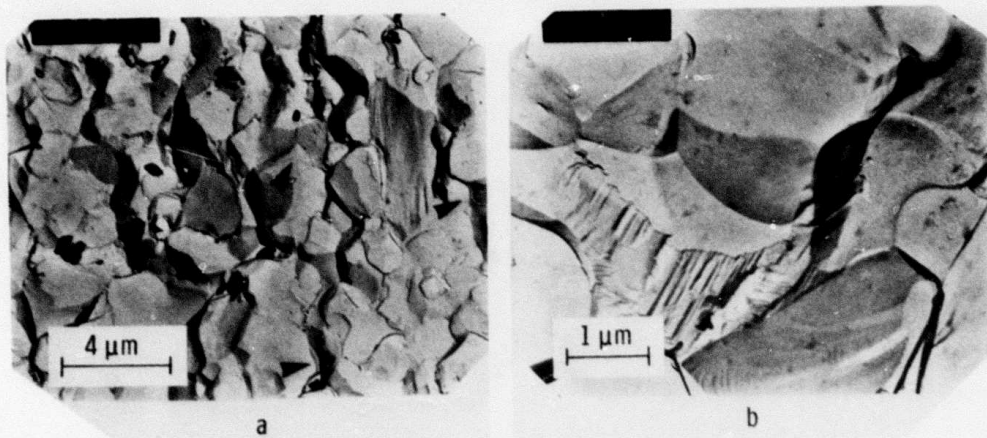
Figure 3-26.   Replica Transmission Micrographs of 1472°F Fracture
Surfaces - Norton Hot-Pressed SiC (NC203)
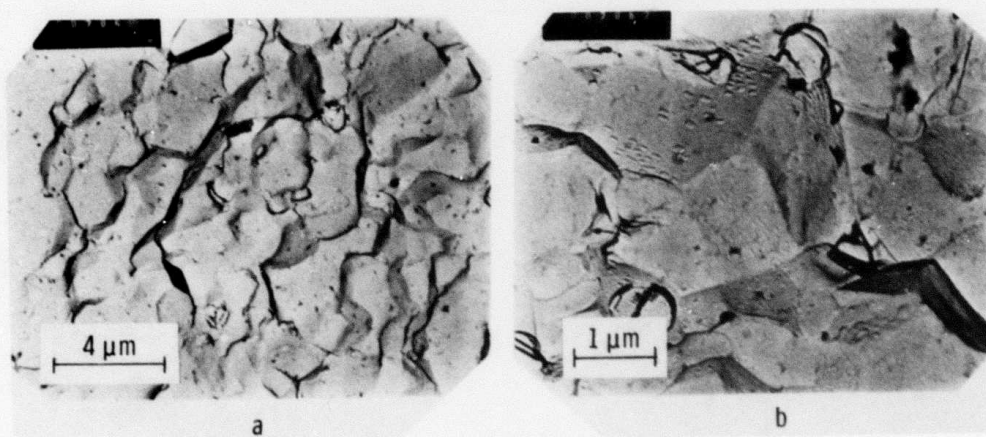
Figure 3-27.   Replica Transmission Micrograph of 1832°F Fracture
Surfaces - Norton Hot-Pressed SiC (NC203)

Figure 3-28 shows SEM micrographs of fracture surfaces of specimens
tested at 1115°F and 2000°F, respectively. The large grain in the center
of Figure 3-28a exhibited evidence of cleavage. The entire area shown
in Figure 3-28b contains the grain boundary phase which is somewhat
lighter than the grain proper, indicating a higher molecular weight than
SiC.[3]   This light phase was interpreted to be an Al_2O_3-rich boundary
phase. Nondispersive X-ray analysis (Figure 3-29) indicated that the
grain boundary phase was rich in Fe. Intergranular cracking was the
dominant mode of failure at 2000°F.

170

a   b
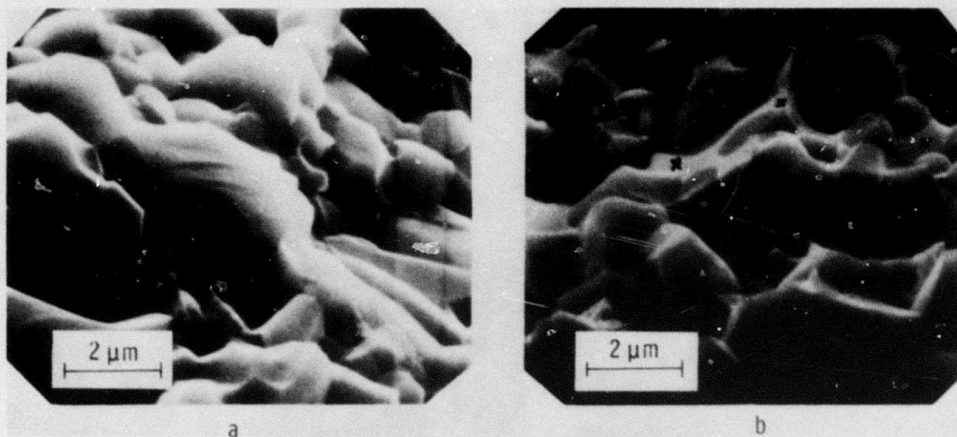
Figure 3-28.   SEM Micrograph of Fracture Surfaces of Hot-Pressed
                SiC (NC203)
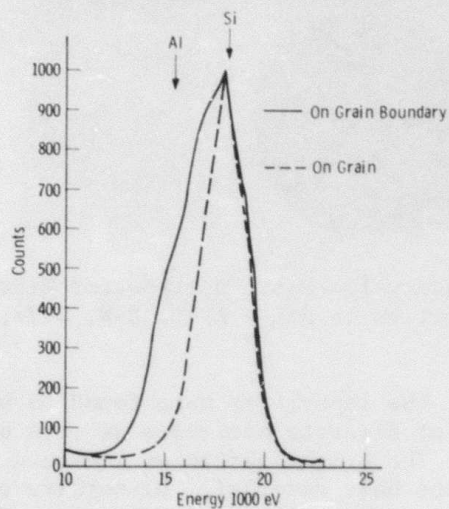
Figure 3-29.   Nondispersive X-Ray Analysis, Fracture Surface -
                Norton Hot-Pressed SiC (NC203)

Impurities in Silicon Carbide

The qualitative distribution of the major impurity elements in SiC
are described in Figure 3-30. These are images of five elements obtained
by secondary-ion-mass-spectroscopy.[4] The relative intensities do not

171

relate to concentration. The traces indicates a relatively uniform distribution of all elements, with Al indicated in the highest concentration based on particle density.
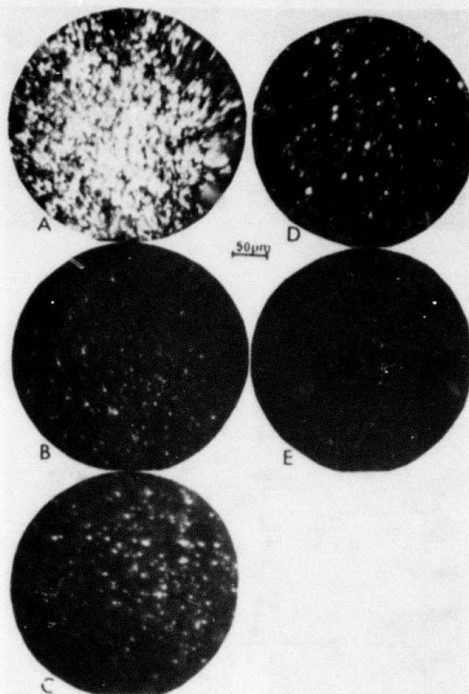
Figure 3-30.   Secondary-Ion-Mass Spectrometer Micrographs of Major Impurities in SiC - A-Al, B-W, C-Ti, D-B and E-Fe

On a finer scale, the impurities were found to be concentrated primarily in the form of discrete particles as seen by the SEM micrograph in Figure 3-31. The bright particles indicate areas of higher mass, as compared to the base material. Dispersive energy analysis showed that the particles were either rich in Al or W.[4] Based on the X-ray diffraction and probe analyses, these particles were structurally similar to Al_2O_3 or WC, although the exact composition of the particles was not determined.

Exposure to high temperatures for a long period of time in inert atmospheres, apparently caused a loss of Al_2O_3 from SiC. This is shown in the SEM micrograph, Figure 3-32. The surface examined represented a creep specimen in test for over 1000 hours at 2500°F. Aluminum was not present in any of the many bright particles.[4]

172
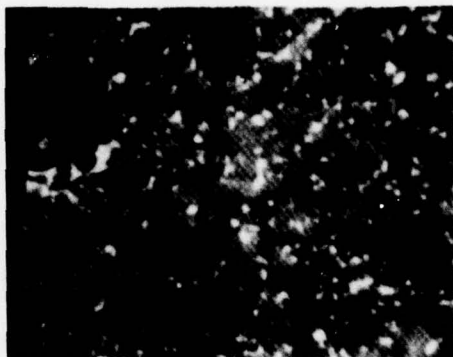
Figure 3-31. SEM Micrograph of Polished SiC (NC203) Showing
Impurities (2000X)
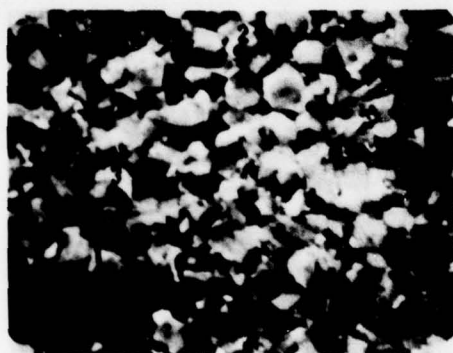
Figure 3-32. SEM Micrograph, Thermally Etched, Hot Pressed SiC
(NC203) Creep Specimen, (Particles Show Si, W and
Traces of Ti and Fe - No Al)

High magnification transmission micrographs appear in Figures 3-33
and 3-34. When compared to Figures 3-31 and 3-32, there are indication:
of a high distribution of foreign particles arranging in size from a
few microns in diameter to about 1000Å. The dark field micrograph
clearly indicates particles at the grain boundaries. However, the dif-
fraction pattern was not clear enough for positive identification.[4]

Figure 3-34 also reveals a few particles within the grain (A). T
occurrence of a high density of stacking faults and dislocations was
most interesting.[4] It is possible that these faults constitute ver
active sites for the nucleation of failure. The cleavage and genera
low strength of SiC at low temperatures may be related to its inher
faulty structure.

173

Figure 3-33. Transmission Electron Micrographs Showing Inclusions
in Grain Boundaries of Hot Pressed SiC (NC203)
A - Bright Field; B - Dark Field (1000 kV)

3.3.3 CHEMICALLY VAPOR DEPOSITED SILICON CARBIDE

Chemically vapor deposited silicon carbide is a high purity, non-conductive material that is extremely difficult to etch. Microstructural features were observed by examining fracture surfaces. Figure 3-35 shows a log-magnification replica transmission micrograph of a specimen fractured at room temperature.[3] Long columnar grains, about 3-5 μm wide, are typical of this material. Failure by cleavage is clearly evident.

Higher magnification micrographs appear in Figure 3-36. Figure 3-36a demonstrates secondary cracking along large-angle grain boundaries. A change in the direction of the cleavage steps delineates the columnar grain (Figure 3-36b). This micrograph also shows a fine granular sub-structure within the columnar grains (arrows).

Fracture surfaces prepared at high temperature (>2000°F) could not be examined due to the formation of a corrosion layer.[3]

174
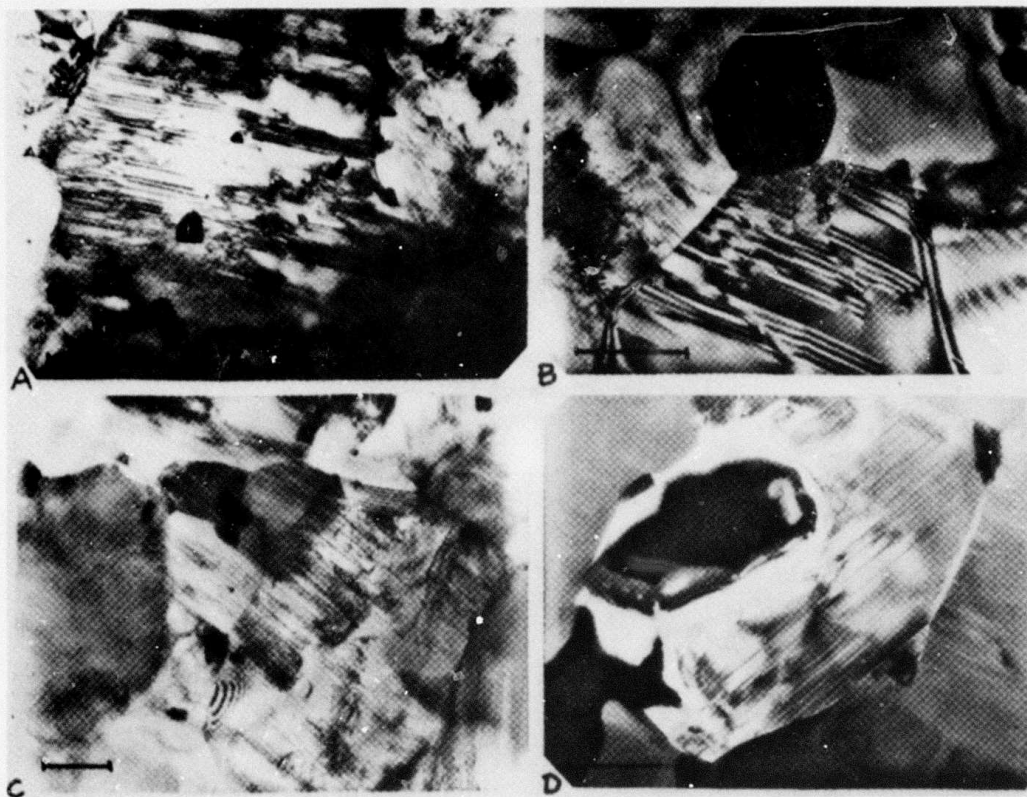
Figure 3-34.   Typical Microstructures in Hot Pressed SiC
(NC203) (1 μm Scale Bar)
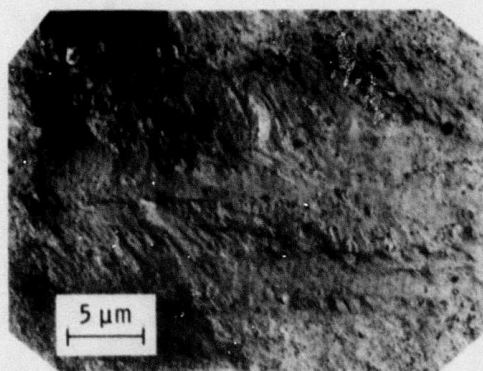
Figure 3-35.   Columnar Structure in CVD-SiC Long Grains
(Energy Research)

A   B
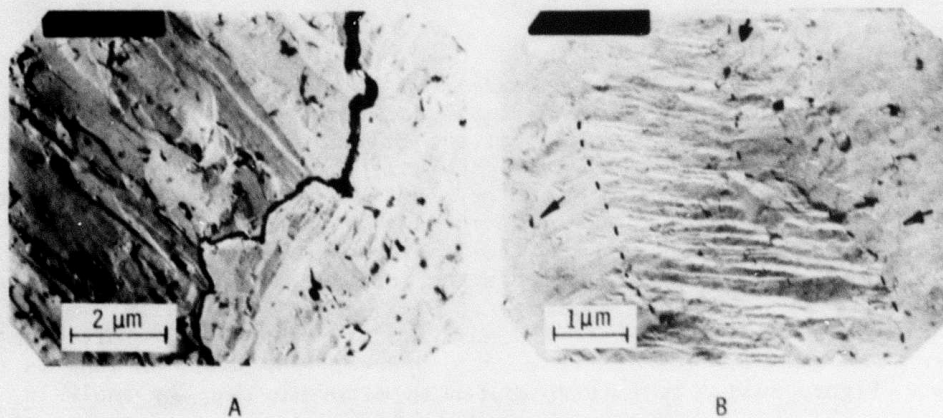
Figure 3-36.   Replica Transmission Micrograph Room Temperature
Fracture Surfaces - CVD-SiC (Energy Research)

SECTION 4

ENVIRONMENTAL STABILITY OF Si_3N_4 AND SiC

4.1 THERMODYNAMIC PROPERTIES

4.1.1 <u>INTRODUCTION</u>

Silicon nitride and silicon carbide are effective as high temperature structural materials because a protective surface layer, containing predominantly silica (SiO_2), is formed in highly oxidizing atmospheres. Usefulness at high temperature does not depend solely upon intrinsic stability, but also upon the stability of the protective oxide layer. The SiO_2 layer could be consumed from the surface of Si_3N_4 and SiC either by straight volatilization or by reaction with Si_3N_4 or SiC at the Si_3N_4-SiO_2 or the SiC-SiO_2 interface, respectively. A thermodynamic analysis of the decomposition and volatilization of Si_3N_4, SiC and SiO_2, and of the interfacial reactions of Si_3N_4 and SiC with surface SiO_2 are presented here.

The hot pressed silicon nitride and silicon carbide, developed specifically for high-temperature structural applications, were prepared by the hot-pressing or sintering of the respective powders with a densification aid. The additives influenced the formation of extraneous phases in small quantities, e.g., oxynitride and mixed silicates, in the hot-pressed bulk material and also in the surface oxide during oxidation. These phases complicated the problem because detailed phase equilibria and thermodynamic properties data were not available for a complete analysis of the stability of Si_3N_4 and SiC materials. Since such information was lacking, the analysis was necessarily limited to pure Si_3N_4, SiC and SiO_2. The effect, however, was small as long as the concentration of the extraneous phases remained small. <u>The analysis, therefore, is useful in an assessment of the potential performance of commercial silicon nitride and silicon carbide materials in various environments.</u>

4.1.2 <u>DECOMPOSITION AND VOLATILIZATION REACTIONS</u>

Silicon nitride dissociates into Si (solid or liquid depending on the temperature) and N_2 gas according to the reaction:

$$Si_3N_4(s) \rightarrow 3\ Si(s,\ell) + 2\ N_2(g) \tag{1}$$

177
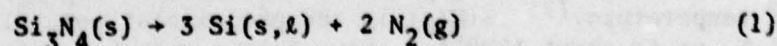
The pressure of $N_2(g)$ formed by the dissociation of Si_3N_4 is shown in Figure 4-1 as a function of temperature.[7] The dissociation N_2 pressure at $1600^\circ K$, the proposed use temperature for Si_3N_4, is only 2.8 x 10^{-4} atm.[28] At $2151^\circ K$ where the N_2 pressure reaches 1 atm, Si_3N_4 dissociated completely. This dissociation can be suppressed if Si_3N_4 is used in a high ambient N_2 pressure environment.
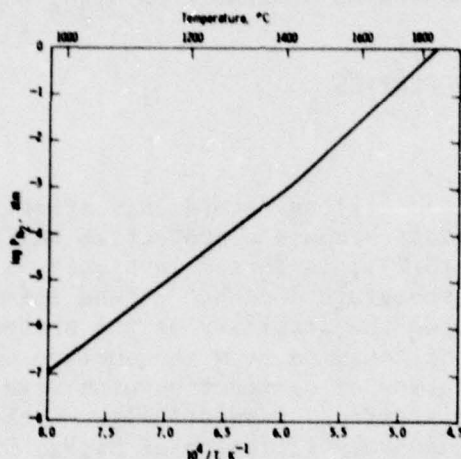
Figure 4-1. Dissociation Pressure of Nitrogen over Si_3N_4 (s)

The vaporization behavior of Si_3N_4 is complex and remains only partly characterized with regard to the nature of the volatile species. The various possible reactions in the volatilization of Si_3N_4 include:

$$2\ Si_3N_4(s) \rightarrow 6\ SiN(g) + N_2(g) \tag{2}$$

$$4\ Si_3N_4(s) \rightarrow 6\ Si_2N(g) + 5\ N_2(g) \tag{3}$$

$$Si_3N_4(s) \rightarrow 3\ Si(g) + 2\ N_2(g) \tag{4}$$

$$2\ Si_3N_4(s) \rightarrow 3\ Si_2(g) + 4\ N_2(g) \tag{5}$$

$$Si_3N_4(s) \rightarrow Si_3(g) + 2\ N_2(g) \tag{6}$$
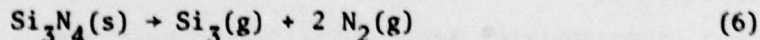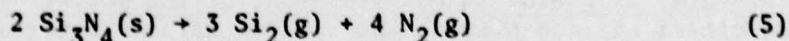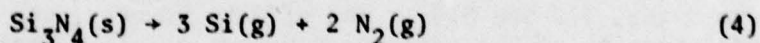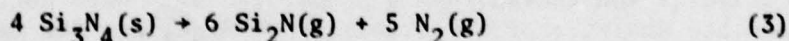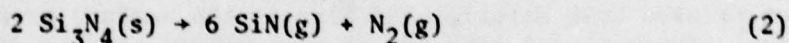
The partial pressures of the volatile species, $SiN(g)$, $Si_2N(g)$, $Si(g)$, $Si_2(g)$ and $Si_3(g)$, calculated according to reactions (2) to (6) in a N_2 environment of 1 atm pressure are shown in Figure 4-2 as a function of temperature.[7] $SiN(g)$ is the predominant volatile species over Si_3N_4 up to about $1600^\circ K$. Above that temperature $Si(g)$ becomes predominant. The partial pressure of both $SiN(g)$ and $Si(g)$ at $1600^\circ K$ is

178
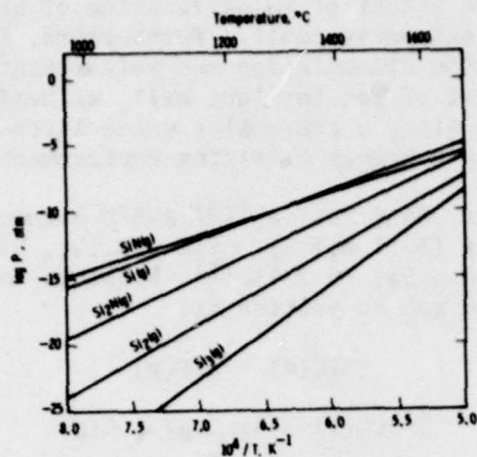
Figure 4-2. Partial Pressures of Various Volatile Species Over
Si_3N_4 (s) in 1 Atm Pressure N_2 Environment

only 4×10^{-10} atm, which is extremely small. The partial pressures of
$Si_2N(g)$, $Si_2(g)$ and $Si_3(g)$ are even smaller. High ambient N_2 pressure
will reduce the volatilization of Si_3N_4 still further. The partial
pressures of the volatile species in a N_2 atmosphere of 7.75 atm pressure,
which is characteristic of gas turbine operation at 10 atm total pres-
sure, are shown in Figure 4-3. The partial pressures of $SiN(g)$ and
$Si(g)$ at 1600°K are now reduced to 3×10^{-10} and 1×10^{-10} atm, respec-
tively.[7] The partial pressures of other volatile species are reduced
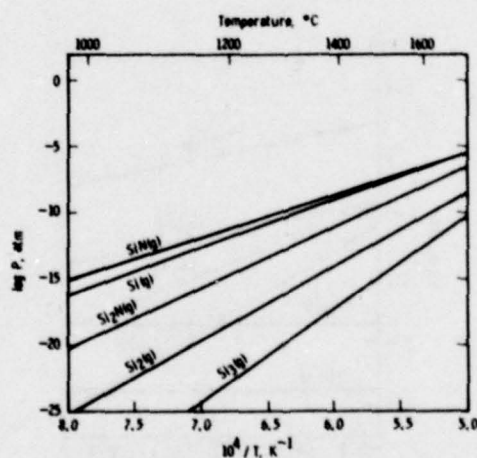
Figure 4-3. Partial Pressure of Various Volatile Species Over
Si_3N_4 (s) in 7.75 Atm Pressure N_2 Environment

179

similarly. Thus, the extent of volatilization of Si_3N_4 at the proposed use temperatures is extremely small. Furthermore, the formation of volatile species by the dissociation and volatilization of Si_3N_4 in environments like that of gas turbines will, at best, represent a localized condition, since a protective oxide layer should form very quickly over Si_3N_4 in a highly oxidizing environment.

According to the JANAF Tables,[28] β-SiC decomposes at 3259°K into a vapor mixture of Si (32.1 mol %), Si_2C (20.1%), SiC_2 (45.4%), Si_2 (1.8%), SiC (0.28%) and Si_3 (0.23%).[7] Possible reactions in the volatilization of SiC can be written as:

$$SiC(s) \rightarrow SiC(g) \qquad\qquad\qquad (7)$$

$$2\, SiC(s) \rightarrow Si_2C(g) + C(g) \qquad\qquad\qquad (8)$$

$$SiC(s) \rightarrow Si(g) + C(g) \qquad\qquad\qquad (9)$$

$$2\, SiC(s) \rightarrow Si_2(g) + 2\, C(g) \qquad\qquad\qquad (10)$$

$$3\, SiC(s) \rightarrow Si_3(g) + 3\, C(g) \qquad\qquad\qquad (11)$$

$$2\, SiC(s) \rightarrow SiC_2(g) + Si(s,\ell) \qquad\qquad\qquad (12)$$
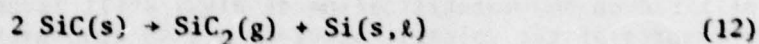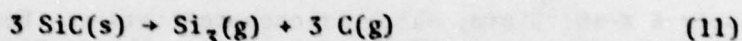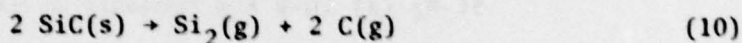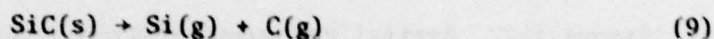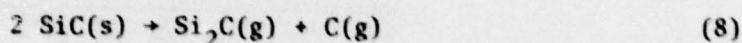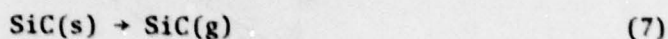
The partial pressures of various volatile species over SiC at 1600 and 2000°K, calculated for reactions (7) to (12), are shown in Figures 4-4 and 4-5, respectively, as functions of carbon potential. The carbon potential ranges chosen represent the regions over which SiC(s) is stable
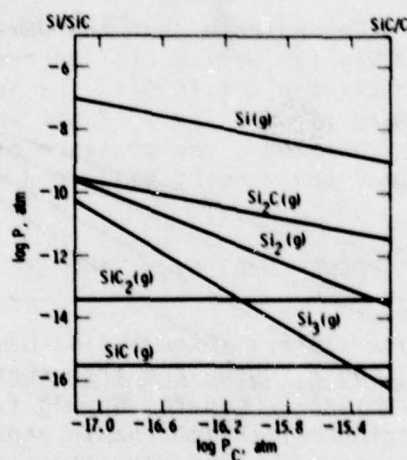
Figure 4-4.   Partial Pressures of Various Volatile Species Over SiC (s) at 1600°K.

180
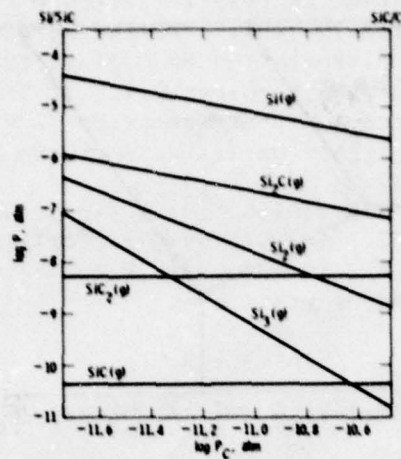
Figure 4-5. Partial Pressures of Various Volatile Species Over SiC (s) at 2000°K

at each temperature. The carbon potentials at the extreme left and extreme right in both figures represent the Si/SiC phase boundary and the SiC/C phase boundary, respectively.[7] It is apparent that the predominant volatile species over SiC(s) is Si(g), at both 1600 and 2000°K. At 1600°K, the maximum partial pressure of Si(g) over SiC(s) is 1×10^{-7} atm, which is insignificant for most applications. The partial pressures of other volatile species are even smaller. At 2000°K, however, the partial pressure of Si(g) could be as high as 4.2×10^{-5} atm. This might limit the use of SiC at such high temperatures in certain environments, e.g., under dynamic vacuum conditions where the volatile species will be removed continuously from the system.[7]

Figures 4-4 and 4-5 also indicate that the partial pressures of Si(g), $Si_2(g)$, $Si_3(g)$ and $Si_2C(g)$ over SiC(s) decrease as the carbon potential increases. For example, at 1600°K, the partial pressure of Si(g) at the SiC/C interface is only 1×10^{-9} atm compared to 1×10^{-7} atm at the Si/SiC interface. Therefore, the presence of carbon deposited on bare SiC from the ambient environment will tend to lower its volatility.[7]

4.1.3 STABILITY OF OXIDE FORMED OVER Si_3N_4 AND SiC

A thermochemical phase diagram (Figure 4-6) has been constructed for the Si-N-O system at 1600°K, using the free energy data for Si_3N_4 and SiO_2 from the JANAF Tables[28] and for Si_2ON_2 from Blegen.[29] This diagram represents the regions of thermodynamic stability for Si_3N_4, Si_2ON_2 and SiO_2 as a function of oxygen and nitrogen partial pressures. It follows from this diagram that upon heating in an oxidizing environment,

181
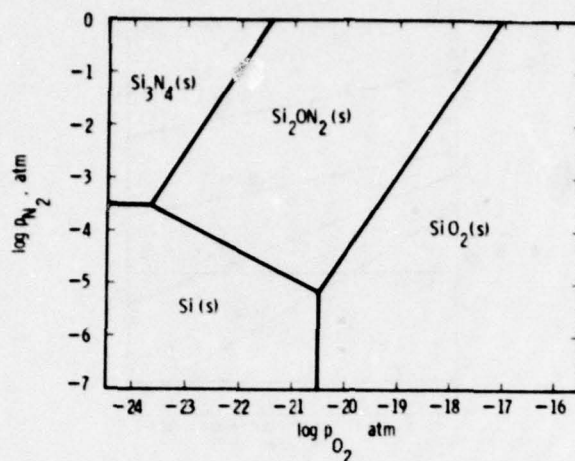
Figure 4-6. Thermochemical Diagram for the Si-O-N System at 1600°K

a duplex oxide layer consisting of Si_2ON_2 and Si_3N_4 should form on the Si_3N_4 surface. Depending upon the kinetics of the reaction and the duration of oxidation, the Si_2ON_2 in the oxide layer may oxidize almost completely to SiO_2.

Various experimental investigations of oxidation conducted on different Si_3N_4 materials failed to identify duplex layers of Si_2ON_2 and SiO_2. Furthermore, Si_2ON_2 has been detected only rarely in the oxide scales. However, the bulk of the evidence suggests that the oxide layer formed on Si_3N_4 consists predominantly of SiO_2, a species which provides protection against further oxidation in oxidizing environments.

In the Si-C-O system, the only known condensed phases are SiC and SiO_2. Figure 4-7 shows the thermochemical diagrams for the silicon-carbon-oxygen system at 1300 and 1600°K, respectively. The ordinate scale gives the pressure of the carbon monomer; the abscissa gives the oxygen partial pressure and the pressure ratio for carbon monoxide to carbon dioxide. The thin diagonal lines in the diagrams give the carbon monoxide pressures. The thicker lines separate the regions of existence for Si(s), SiC(s), and SiO_2(s). Carbon monomer pressures higher than those for solid carbon have no meaning. These diagrams indicate that upon oxidizing SiC at high oxygen partial pressures, a surface layer of SiO_2 should form.

The protective film of predominantly SiO_2(s) forms on the surfaces of Si_3N_4 and SiC in oxidizing atmospheres according to the reactions:

$$Si_3N_4(s) + 3\ O_2(g) \rightarrow 3\ SiO_2(s) + N_2(g) \tag{13}$$

(a) 1300°K   (b) 1600°K
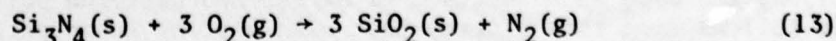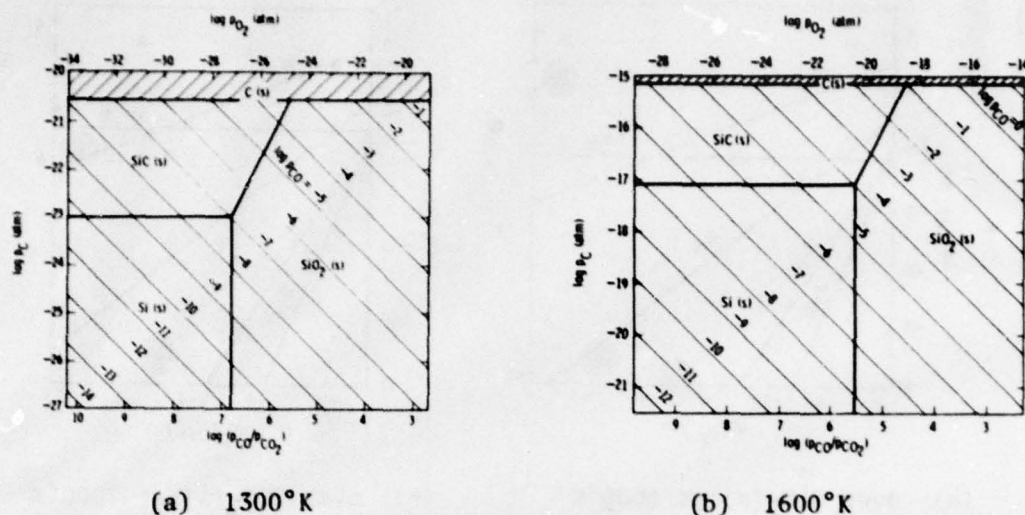
Figure 4-7. Thermochemical Data for the Si-C-O System

$$2 \ SiC(s) + 3 \ O_2(g) \rightarrow 2 \ SiO_2(s) + CO(g) \tag{14}$$
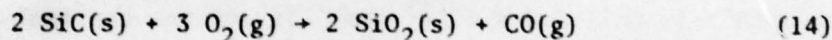
The volatilization of this surface $SiO_2(s)$ can result in the formation of various gaseous species according to the reactions:

$$SiO_2(s) \rightarrow SiO_2(g) \tag{15}$$

$$2 \ SiO_2(s) \rightarrow 2 \ SiO(g) + O_2(g) \tag{16}$$

$$SiO_2(s) \rightarrow Si(g) + O_2(g) \tag{17}$$

$$2 \ SiO_2(s) \rightarrow Si_2(g) + 2 \ O_2(g) \tag{18}$$

$$3 \ SiO_2(s) \rightarrow Si_3(g) + 3 \ O_2(g) \tag{19}$$
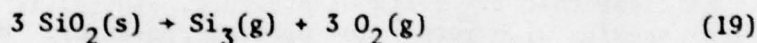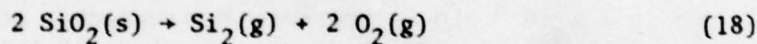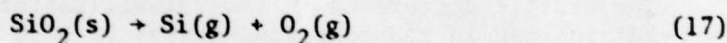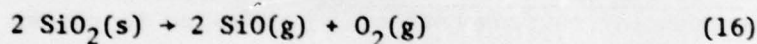
The partial pressures of the gaseous species formed according to reactions (15) and (19) have been calculated and are shown in Figure 4-8 at 1600 and 2000°K, respectively, as a function of ambient oxygen partial pressure.[7] The oxygen partial pressure at the extreme left of these figures (3.2×10^{-21} and 4.0×10^{-15} atm at 1600 and 2000°K, respectively) represents the oxygen partial pressure below which SiO_2 is not thermo-dynamically stable. It is apparent that $SiO_2(g)$ is the predominant gaseous species over $SiO_2(s)$ in high ambient oxygen pressures, while $SiO(g)$ becomes the predominant species in low oxygen partial pressure environments. Also, the partial pressure of $SiO_2(g)$ formed over $SiO_2(s)$

183
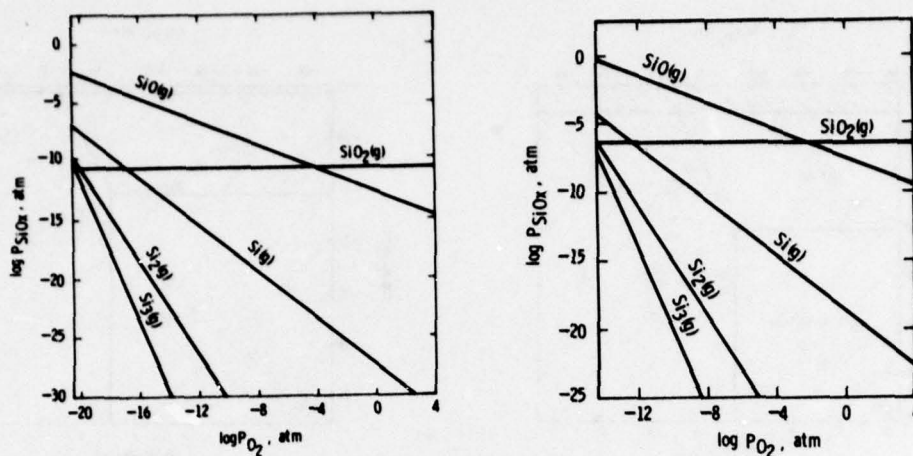
(a)   over $SiO_2(s)$ at 1600°K   (b)   over $SiO_2(\ell)$ at 2000°K

Figure 4-8.   Partial Pressure of Various Volatile Species

at 1600°K is only 3.8×10^{-11} atm.   It remains constant irrespective of the ambient oxygen pressure.   The partial pressure of SiO(g) is lower than that of the $SiO_2(g)$ down to about 1×10^{-4} atm oxygen pressure, but increases rapidly at lower oxygen pressures.   Similar behavior is indicated at 2000°K.   Thus, the volatilization of SiO_2 is insignificant in highly oxidizing environments, e.g., in air, in gas turbines, etc., but it becomes very critical in reducing environments, e.g., in vacuum, due to the formation of SiO(g).   Hence, the usefulness of Si_3N_4 and SiC in reducing environments will be limited to rather low temperatures.

The drastic difference in the volatilization behavior of $SiO_2(s)$ in oxidizing and in reducing atmospheres is also illustrated in Figure 4-9, where the partial pressures of gaseous species formed in 1 atm O_2 and in 1×10^{-8} atm O_2 pressure environments, according to reactions (15) and (19), are shown as a function of temperature.[7]   Again, it is clear that at 1 atm O_2 pressure, $SiO_2(g)$ is the predominant vapor species with rather low partial pressures.   However, in 1×10^{-8} atm O_2 pressure (reducing conditions), SiO(g) becomes the predominant species at temperatures above ~1250°K.   Under such reducing conditions, the SiO(g) partial pressure could be as high as 2×10^{-4} atm at 2000°K.

In addition to volatilization, the protective surface layer of $SiO_2(s)$ can be consumed by reaction with substrate Si_3N_4 or SiC according to the reactions:

$$Si_3N_4(s) + 3SiO_2(s) \rightarrow 6\ SiO(g) + 2N_2(g) \qquad (20)$$

$$SiC(s) + 2\ SiO_2(s) \rightarrow 3\ SiO(g) + CO(g) \qquad (21)$$

184
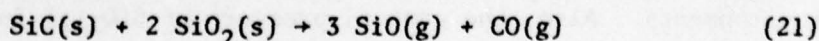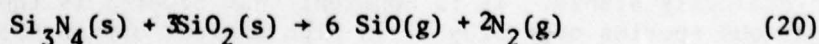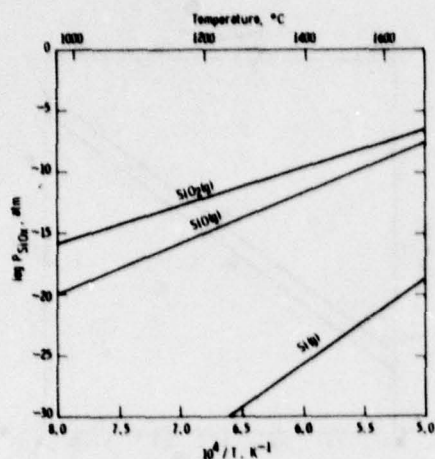
(a) 1 Atm Pressure Oxygen
     Environment
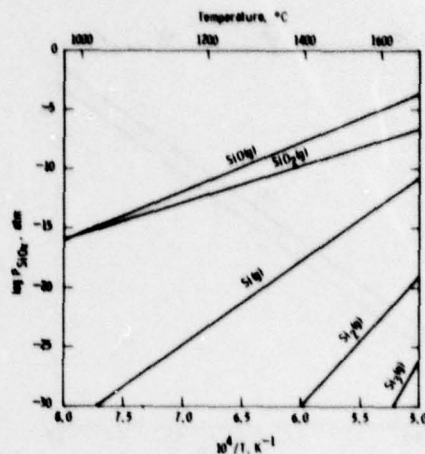
(b) 10^{-8} Atm Pressure O_2
     Environment

Figure 4-9. Partial Pressures of Various Volatile Species Over
            $SiO_2(s,\ell)$

These reactions result in the formation of SiO(g) and other gaseous
species at the $Si_3N_4(s)$-$SiO_2(s)$ and $SiC(s)$-$SiO_2(s)$ interfaces.[7] Assum-
ing stoichiometric formation of gaseous products, the equilibrium partial
pressures of SiO(g) formed according to reactions (20) and (21) have
been calculated. The equilibrium SiO(g) pressures for Si_3N_4 and for SiC
substrates are shown in Figure 4-10 as a function of temperature. High
SiO(g) pressures at high temperatures could cause rupture of the protec-
tive $SiO_2(s)$ layer with subsequent accelerated oxidation. More impor-
tantly, if all of the surface $SiO_2(s)$ reacts according to reactions (20)
and (21), then a bare Si_3N_4 or SiC surface will be exposed, causing
"active" oxidation of Si_3N_4 or SiC by the formation of SiO(g) according
to the reactions:

$$2 \, Si_3N_4(s) + 3 \, O_2(g) \rightarrow 6 \, SiO(g) + 4 \, N_2(g) \qquad (22)$$

$$SiC(s) + O_2(g) \rightarrow SiO(g) + CO(g) \qquad (23)$$
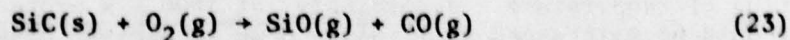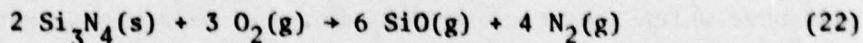
This could only happen in environments with very low oxygen partial
pressures. Wagner[30] developed a theory to interpret the transition
between "active" oxidation (by formation of gaseous SiO) of Si found at
low oxygen partial pressures, and "passive" oxidation (by formation of
a protective layer of SiO_2) which occurs at high oxygen partial pressures.

185
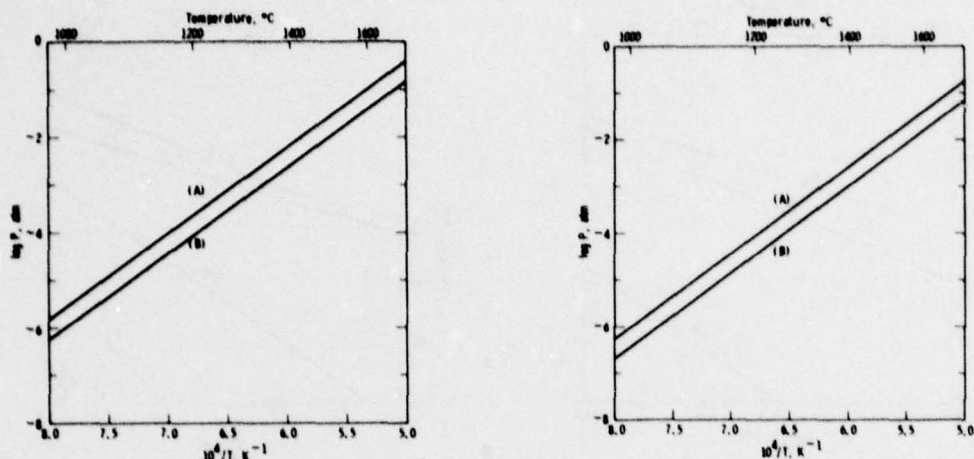
(a)   At the Si₃N₄ Interface (A)   (b)   At the SiC-SiO₂ Interface A
      on Si₃N₄ (B)   on SiC (B)

Figure 4-10.   Equilibrium Pressures of SiO(g) and the O_2 Partial
Pressures, $P_{O_2}^*$, above which a Protective SiO_2
Layer Should be Maintained (B)

He derived the following equation for calculating the value of O_2 partial
pressure, $P_{O_2}^*$, below which no oxide is maintained on the surface of
silicon:

$$P_{O_2}^* \cong 0.4 \, P_{SiO(eqm)}$$

where $P_{SiO(eqm)}$ is the equilibrium partial pressure of SiO(g) at the
Si-SiO₂ interface. Extending this theory to the oxidation of Si₃N₄ and
SiC, the values of the O_2 partial pressure, $P_{O_2}^*$, below which all the
surface SiO₂ reacts to form SiO(g) according to reactions (20) and (21),
and above which a protective SiO₂ layer is maintained, have been cal-
culated. These values of $P_{O_2}^*$ are also shows in Figure 4-10 as a func-
tion of temperature. Accordingly, at 1600°K a protective layer of SiO₂(s)
should be maintained on 1) Si₃N₄ down to ambient oxygen pressure of
8 x 10⁻⁴ atm, and 2) SiC down to 3.6 x 10⁻⁴ atm. However, at 2000°K,
the protective layer of SiO₂ is expected to be maintained only down to
O₂ pressure of 3.5 x 10⁻¹ atm on Si₃N₄, and 1.8 x 10⁻¹ atm on SiC. Below
these oxygen pressures, "active" oxidation of Si₃N₄ and SiC can occur,
thus limiting their usefulness as structural materials.

Thermodynamically, the above analysis for Si₃N₄ is not completely
correct, since (as shown in Figure 4-6) the oxide in equilibrium with
Si₃N₄ should be Si₂ON₂ and not SiO₂. However, experimental investiga-
tions have shown that SiO₂ is the predominant oxide formed on Si₃N₄.

186

For this reason, the above analysis can be used to assess at least approximately the behavior of Si_3N_4 in environments with different oxygen partial pressures. From a purely thermodynamic equilibrium point of view, however, the Si_2ON_2 and SiO_2 coexistent interface should be analyzed rather than the $Si_3N_4-SiO_2$ interface presented. Silicon oxynitride and SiO_2 could react according to the reaction:

$$Si_2ON_2(s) + SiO_2(s) \rightarrow 3\ SiO(g) + N_2(g) \qquad (24)$$
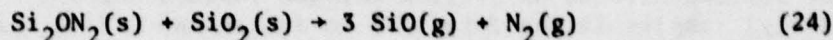
where $SiO(g)$ is formed at the $Si_2ON_2 - SiO_2$ interface. The equilibrium $SiO(g)$ pressure at this interface at $1600°K$ would be 8.04×10^{-4} atm. This is comparable to the equilibrium $SiO(g)$ pressure at the "assumed" $Si_3N_4-SiO_2$ interface shown in Figure 4-10.

4.2 OXIDATION OF SILICON NITRIDE AND SILICON CARBIDE

4.2.1 EXPERIMENTAL PROCEDURE

Oxidation experiments were conducted by continuous thermogravimetry, using an automatic Cahn electrobalance with a sensitivity of 2 μg.[1] The silicon nitride or silicon carbide (Norton HS130 and NC203, respectively) samples in the form of 1 cm square and 0.2 cm thick plates were cut from the hot-pressed billets and polished with up to 6 μm diamond paste. The polished specimen was suspended from the balance with a sapphire fiber and held in the hot zone of a platinum-resistance furnace in a flowing oxygen atmosphere. The changes in the weight of the specimen were continuously recorded on a strip chart recorder.

Most of the oxidation experiments were conducted in dry oxygen at 1 atm pressure. The oxygen gas was dried by passing it through anhydrous calcium silicate and phosphorus pentoxide before passing it over the specimen suspended from the balance.

In order to study the effect, if any, of the oxygen partial pressure on the oxidation of Si_3N_4, thermogravimetric experiments were conducted at 2500°F in O_2-Ar gas mixtures with oxygen partial pressures of 0.01, 0.05, 0.1, 0.3, 0.5, 0.7 and 0.9 atm at a total pressure of 1 atm. Similarly, in order to study the effect of nitrogen partial pressure on the oxidation kinetics of hot-pressed Si_3N_4, experiments were conducted using N_2-O_2-Ar gas mixtures with varying nitrogen partial pressures of 0.1, 0.2, 0.3, 0.4, 0.5, 0.6 and 0.7 atm at a fixed oxygen partial pressure (0.2 atm) and fixed total pressure (1 atm).

After oxidation, the surfaces of the specimens were analyzed by X-ray diffraction, scanning electron microscopy and electron microprobe analysis to completely characterize the oxidation products formed at different temperatures.

4.2.2 SILICON NITRIDE (NORTON HS130) - Results

The initial oxidation experiments were performed at different flow rates of oxygen from 500 to 5000 ml/min, with the gas velocities in the reaction tube (∿2 cm diameter) ranging between 2.6 to 26 cm/sec. The oxidation rates were found to be independent of the oxygen flow rate at all temperatures in the range 1800 to 2550°F, indicating that the oxidation of Si_3N_4 was not controlled by gas transport in the surface boundary layer. Flow rate in all subsequent oxidation experiments was maintained at 500 ml/min.

Effect of Temperature

The weight change data for oxidation of Si_3N_4 in 1 atm dry oxygen at different temperatures are summarized in Figure 4-11. No detectable
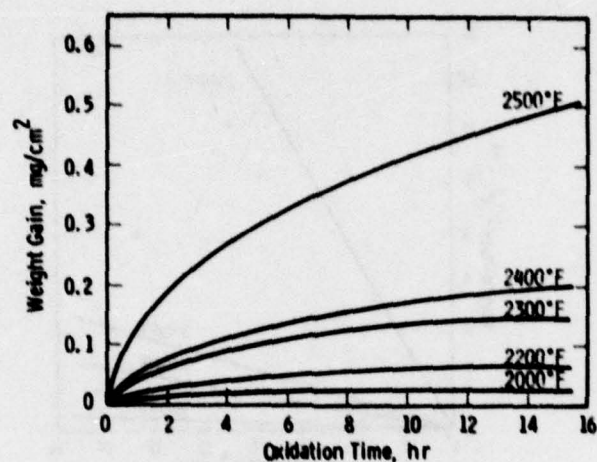
Figure 4-11. Weight Change vs Time Curves for Commercial Hot-
Pressed Si_3N_4 in Dry Oxygen at 1 Atm Pressure

weight gain was observed for oxidation at 1832°F, and below.[2] The
weight gain vs time curves at all temperatures approximate the classical
parabolic behavior, which can be represented by the equation:

$$W^2 = K_p \cdot t$$

where W is the weight gain at time t, and K_p is the parabolic rate con-
stant. Plots of the square of the weight gain (W^2) as a function of
time (t) for different temperatures of oxidation are shown in Fig-
ure 4-12, where the straight lines represent a region of parabolic oxi-
dation behavior.

The parabolic rate constants (K_p) for the oxidation of silicon
nitride, obtained from the slopes of the straight lines in Figure 4-12,
are shown in Figure 4-13 as a function of temperature. Using the
Arrhenius equation:

$$K_p = A \exp(-E/RT)$$

where E is the activation energy, R is the gas constant and T the abso-
lute temperature, an activation energy of 375 kJ/mol is obtained for the
oxidation of hot-pressed Si_3N_4 in 1 atm oxygen in the temperature range
1800 to 2550°F.

The weight gain versus time curves for oxidation of Si_3N_4 at 2500°F
in O_2-Ar gas mixtures with oxygen partial pressures from 0.01 to 0.9 atm

189
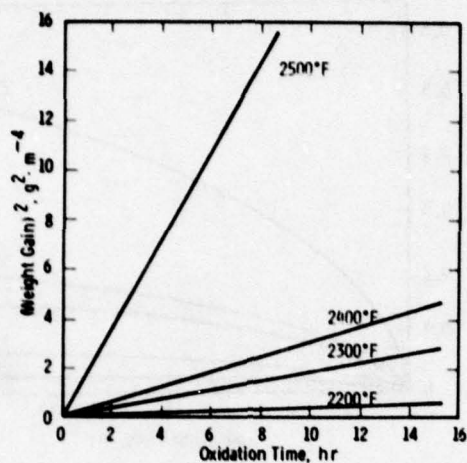
Figure 4-12.   Parabolic Plots for Oxidation of Hot-Pressed
Si₃N₄ in Oxygen at 1 Atm Pressure
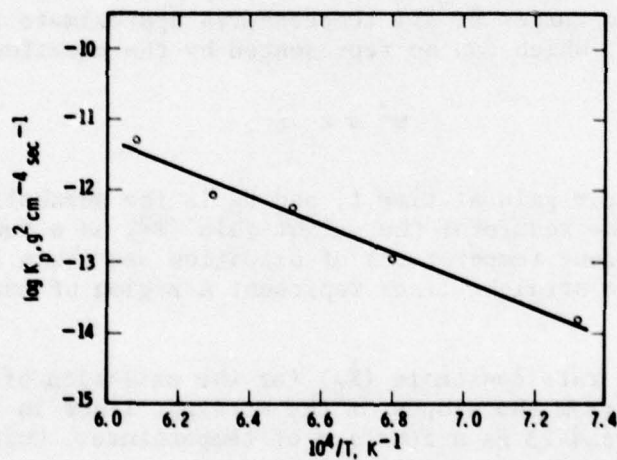
Figure 4-13.   Parabolic Rate Constants for Oxidation of
Commercial Hot-Pressed Si₃N₄ in Oxygen at
1 Atm Pressure as a Function of Temperature

were identical to those obtained in pure oxygen. <u>Similarly, the weight
gain versus time curves for oxidation in N₂-O₂-Ar gas mixtures were iden-
tical to those obtained in pure oxygen.</u> Also, the oxidation products
formed in these gas mixtures were similar to those obtained in pure
oxygen. Even though the range of oxygen and nitrogen partial pressures

used was quite small, the oxidation rate of hot-pressed Si_3N_4, within the "passive" oxidation region, is evidently independent of ambient oxygen and nitrogen partial pressures.

The surface morphologies of the oxide films formed on Si_3N_4 after oxidation in pure oxygen for 30 hours at various temperatures are shown in scanning electron micrographs (Figure 4-14). The oxide formed at 1800°F was completely glassy and severely cracked.[2] At 2000°F, a long needle-like crystalline phase, inferred to be mainly enstatite ($MgSiO_3$) by energy dispersive X-ray analysis, begins to appear. The amount of this needle-like phase increases with increasing temperature of oxidation, and at 2400 and 2500°F the surface is completely covered with this enstatite phase. In addition to the enstatite phase, the surfaces of the oxidized specimens appear to contain another phase, most probably cristobalite (SiO_2) as identified later by X-ray diffraction analysis.

The scanning electron micrograph of a transverse section of a Si_3N_4 specimen oxidized for 30 hours at 2300°F is shown in Figure 4-15 along with the energy dispersive X-ray scans in both Si_3N_4 substrate and the oxide film thereon.[2] While only the silicon peak could be detected in the unoxidized Si_3N_4 substrate, peaks representing Mg, Al, Ca, Fe, Mn, Na and K were identified in the scan of the oxide film.* These elements concentrate in the oxide film during the oxidation process. The concentration of these elements in the oxide film was confirmed by scanning X-ray (Figure 4-16) of the oxidized Si_3N_4 surfaces, using an electron beam microprobe analyzer.[2] Although, these microprobe pictures illustrate the oxidation products formed at 2300°F only, similar behavior was observed at all oxidation temperatures in the range 2000 to 2550°F.

The identity of the oxidation products formed at various temperatures was established by taking X-ray Debye-Scherrer patterns of the surface scrapings from oxidized silicon nitride specimens. The unoxidized material contained predominantly β-Si_3N_4 with traces of Si_2ON_2. The amount of β-Si_3N_4 in the surface scrapings decreased as the amount of other phases increased with increasing temperature of oxidation, while the amount of Si_2ON_2 appeared to remain constant. The cristobalite (SiO_2) phase first appeared in specimens oxidized at 1800°F; its concentration was observed to increase in specimens oxidized at 2000 and 2200°F, and level off in specimens oxidized above these temperatures. Enstatite ($MgSiO_3$) and clino-enstatite ($MgSiO_3$) phases appeared in specimens oxidized at 2200°F; again their concentration increased with increasing temperature of oxidation.[2]

---

*The Au Pd peaks in the scan are from the surface film of an Au-Pd alloy deposited on an oxidized silicon nitride specimen to obtain a conducting surface for scanning electron microscope examination.
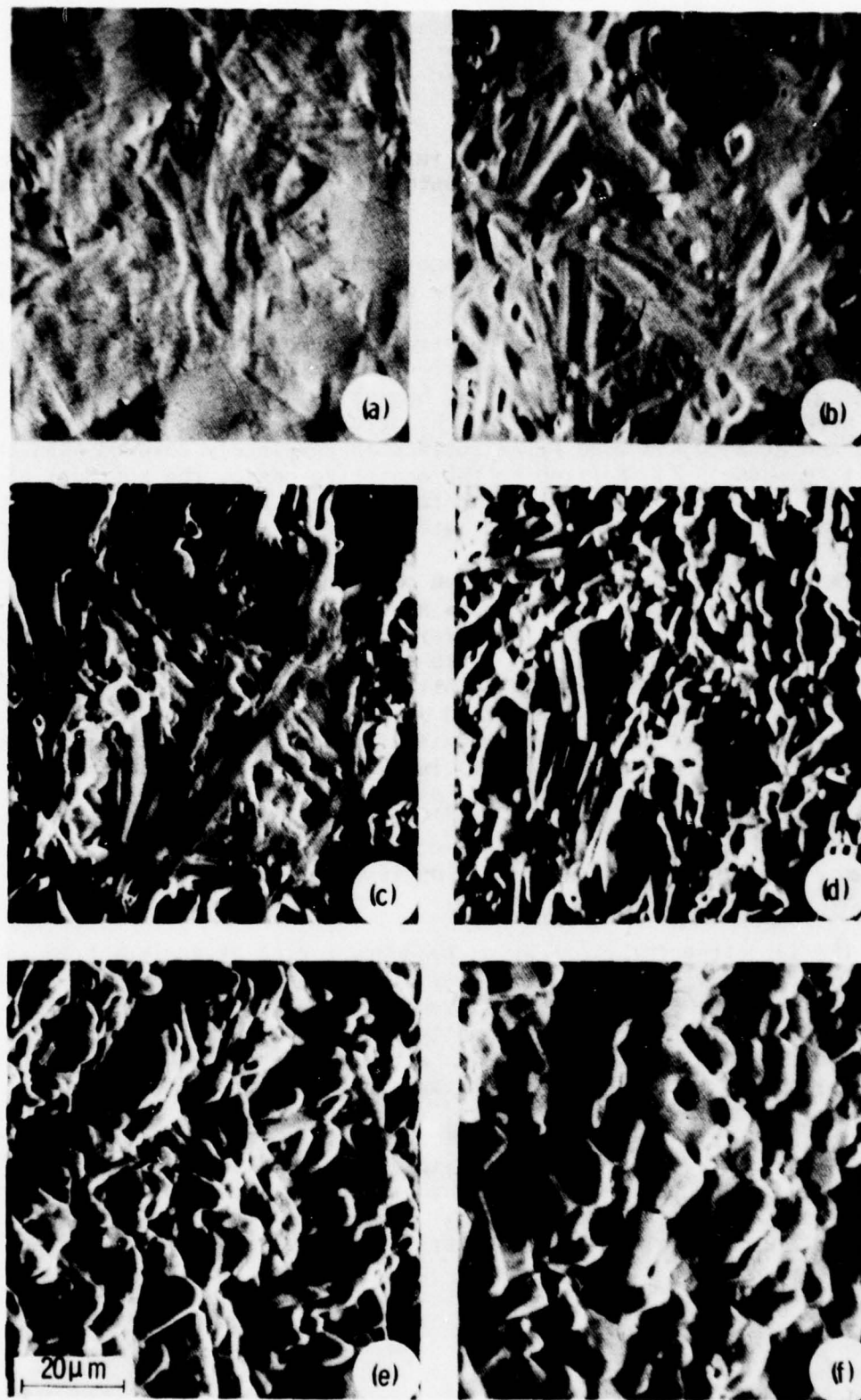
Figure 4-14.   Scanning Electron Micrographs of Surfaces of Silicon Nitride
Oxidized for 30 Hr in Oxygen at 1 Atm Pressure; (a) 1800°F,
(b) 2000°F, (c) 2200°F, (d) 2300°F, (e) 2400°F, (f) 2500°F

192
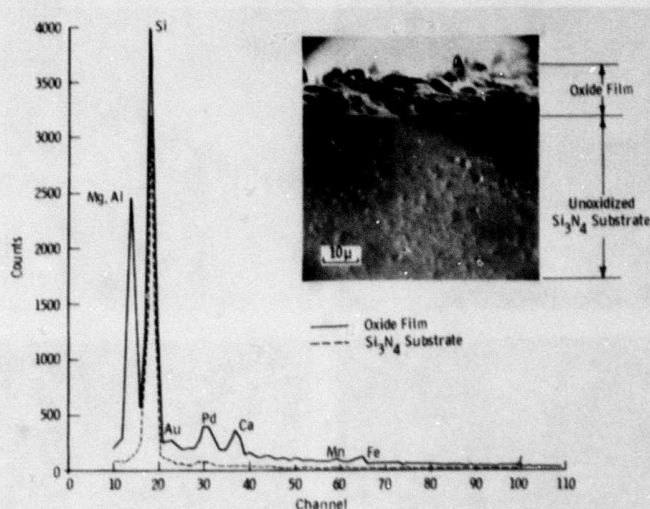
Figure 4-15.   Scanning Electron Micrograph of a Transverse Section of
              Si3N4 Specimen Oxidized at 1260°C for 30 Hours in 1 Atm
              Oxygen, With Energy-Dispersive X-ray Analysis in the Oxide
              Layer and in Si$_3$N$_4$ Substrate.

The existence of cristobalite (crystalline SiO$_2$) at 1800°F suggests
that additive and impurity elements (mainly Mg and Ca) affect the
devitrification of silica glass and reduce its viscosity.[1]   Even though
X-ray diffraction analysis did not detect any phases containing Ca, Na,
K, Fe, Al and Mn, these elements were definitely present in surface
oxide film as indicated by energy dispersive X-ray analysis and micro-
probe scans discussed earlier.   These additive and impurity elements,
therefore, must either form crystalline mixed silicates, such as
diopside (MgO·CaO·2 SiO$_2$), with surface silica in amounts too small to
be detectable by X-ray diffraction analysis, or they dissolve in
surface silica to form an amorphous glassy phase.   A mixed silicate phase,
diopside (MgO·CaO·2 SiO$_2$), was detected in this investigation in oxide
film formed on Si$_3$N$_4$ after 4000 hours of oxidation at 2500°F.[9]

The parabolic nature of the rate curves indicates that the oxidation
of hot-pressed silicon nitride is controlled by a diffusional mechanism.
The many possible diffusional reactions which could occur during oxida-
tion of hot-pressed Si3N4 are shown schematically in Figure 4-17.   As
suggested by various experiments[32-42] on the oxidation of Si, SiC
and Si3N4, the growth of the oxide layer on Si3N4 is expected to occur
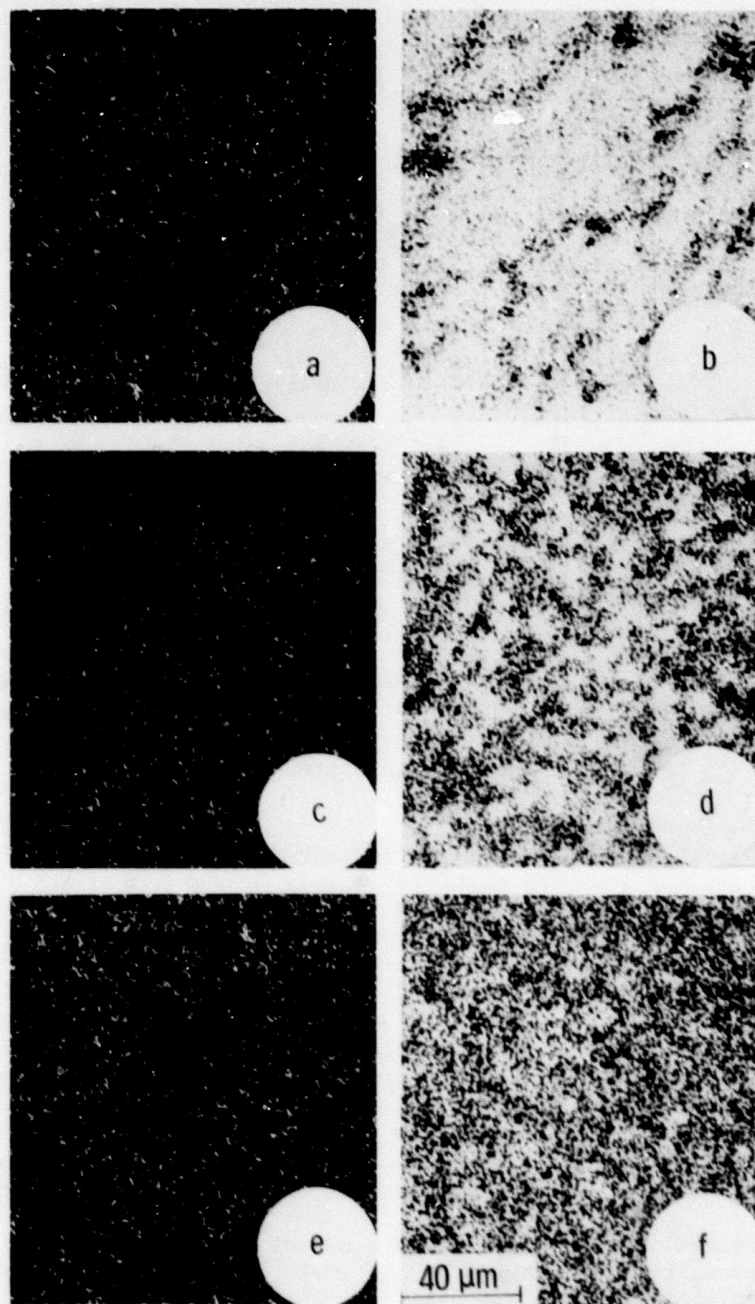
Figure 4-16. Scanning X-ray Pictures Showing Concentrations of Various
Elements in Unoxidized Si_3N_4 and in the Surface Oxide on
Si_3N_4. (a) Mg $K\alpha$ - Unoxidized Si_3N_4; (b) Mg $K\alpha$ - Oxide;
(c) Ca $K\alpha$ - Unoxidized Si_3N_4; (d) Ca $K\alpha$ - Oxide;
(e) Fe $K\alpha$ - Unoxidized Si_3N_4; (f) Fe $K\alpha$ - Oxide

Si$_3$N$_4$ | Oxide | O$_2$ Gas

O ions or O$_2$ molecules

N ions

N atoms ← N$_2$ molecules

SiO(g)   O$_2$(g)

Mg, Ca, etc ions
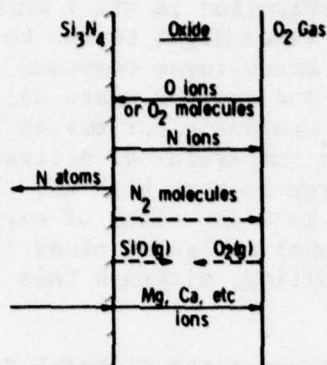
Figure 4-17.   Schematic Representation of Various Reactions Possible During Oxidation of Hot-Pressed Si$_3$N$_4$. (Dashed Lines Indicate Transport in Pores and Fissures in the Oxide Film.)

by inward diffusion of oxygen ions or molecules. Table 4-1 lists the values of activation energies for the parabolic oxidation of Si, Si$_3$N$_4$ and SiC, which might be expected to show similar oxidation kinetics since SiO$_2$(s) is formed in all three cases. Even though there is wide variation in literature values of the activation energies, the activation energy of 375 kJ/mole for oxidation of hot-pressed Si$_3$N$_4$

TABLE 4-1

COMPARISON OF ACTIVATION ENERGIES

System	Temp Range (°C)	Activation Energy (kJ/mole)	Reference
Hot-pressed Si$_3$N$_4$ in O$_2$	1000-1400	375	Present work
Powder Si$_3$N$_4$ in O$_2$	1065-1340	256	32
Powder Si$_3$N$_4$ in Air	1065-1340	285	32
Powder Si$_3$N$_4$ in O$_2$ or Air	1100-1300	147	33
Powder SiC in O$_2$	900-1600	65-85	34
Powder SiC in O$_2$	1300-1550	191	35
Powder SiC in O$_2$	1200-1500	277	36
Powder SiC in O$_2$	900-1300	210	37
Powder SiC in Air	900-1300	336	37
Si in O$_2$	900-1200	125-130	38, 39, 40
O$_2$ Diffusion in Fused SiO$_2$	925-1225	298	41
O$_2$ Diffusion in Fused SiO$_2$	850-1250	122	42

determined in this investigation is still much higher than the highest value reported. A high value might be due to diffusion of oxygen ions or molecules through an oxide layer composed of not only silica, but also magnesium silicate and various mixed silicates such as diopside. Literature data are not available for oxygen diffusion in magnesium silicate or diopside for comparison of activation energies. The fact that the activation energy is very high and the oxidation rate of hot-pressed silicon nitride is independent of oxygen partial pressure suggests that a diffusional mechanism other than inward oxygen ion diffusion is rate controlling, although this cannot be stated with certainty.

Nitrogen gas evolution at the $Si_3N_4(s)-SiO_2(s)$ interface must be accounted for in the oxidation of Si_3N_4. There are three processes (as shown in Figure 4-17) by which this nitrogen gas may be removed from the interface. First, nitrogen atoms may diffuse outward through the oxide film and recombine at its surface to form N_2 molecules. Second, nitrogen can be removed from $Si_3N_4(s)$-oxide interface by inward diffusion of nitrogen into the silicon nitride substrate. The possibility and extent of this process depends upon stoichiometry and the diffusion rates in hot-pressed silicon nitride material. The third process, which most probably occurs in the oxidation of hot-pressed silicon nitride, is the formation of N_2 bubbles at the $Si_3N_4(s)$-oxide interface. When nitrogen pressure within such bubbles exceeds the ambient pressure, the bubbles burst to form a pore network at the surface as seen in Figure 4-14.

In addition to the transport of gaseous species as discussed above, one also has to account for the observed concentration of Mg, Ca, Fe, Al, etc., in the oxide film. It appears certain that during oxidation of Si_3N_4, these elements, which are predominantly present in a grain boundary glass phase in the starting material, diffuse outward from the grain boundaries. Thus, the diffusion of these cations outward from the glass phase and through the oxide film may be the rate controlling process in the oxidation of hot-pressed silicon nitride. Considering the complexity of the system, the fact that a single straight line can be drawn on an Arrhenius type plot (Figure 4-13 and a single value of activation energy obtained may be quite fortuitous. Even then, the high value of activation energy (375 kJ/mole) for oxidation of hot-pressed Si_3N_4 compares favorably with activation energies for cation (Mg^{++}, Ca^{++}) diffusion in oxides and silicates, e.g., 331 kJ/mole for Mg^{++} diffusion in MgO,[43] 281 kJ/mole for Mg^{++} diffusion in Mg_2SiO_4,[44] and 376 to 397 kJ/mole for Ca^{++} diffusion in several compositions in the $CaO-SiO_2$ system.[45,46] Furthermore, the oxidation rate of hot-pressed silicon nitride has been found to increase with an increasing amount of MgO additive, and also with an increasing concentration of Ca, Na and K impurities. This evidence also lends credence to the hypothesis that the oxidation of hot-pressed silicon nitride is controlled by the diffusion of additive and impurity cations (mainly Mg^{++} and Ca^{++}) from the grain boundary glass phase through the surface oxide film.[4]

196

Effect of Oxidation on Flexural Strength

Hot-pressed Si_3N_4 (HS-130) specimens, in the form of 1/8 x 1/4 x 1-1/8 inch rectangular bars, were oxidized at different temperatures for extended periods of time in atmospheric air to determine the effect of oxidation on mechanical properties. After oxidation, the flexural strengths were measured under conditions of four-point loading, using a strain rate of 0.002 inch per minute.

Figure 4-18 shows the flexural strength after different periods of oxidation at 2000°F.[9] The flexural strength decreased from ∿100 ksi for the unoxidized material to 65 ksi after about 400 hours of oxidation at 2000°F. With further oxidation, the strength appeared to remain constant. Similarly, the 2200°F strength after different periods of oxidation at 2200°F is shown in Figure 4-19. Here again, a sharp decrease in strength in the first few hundred hours of oxidation was observed, after which the strength became stable at ∿60 ksi.[9]
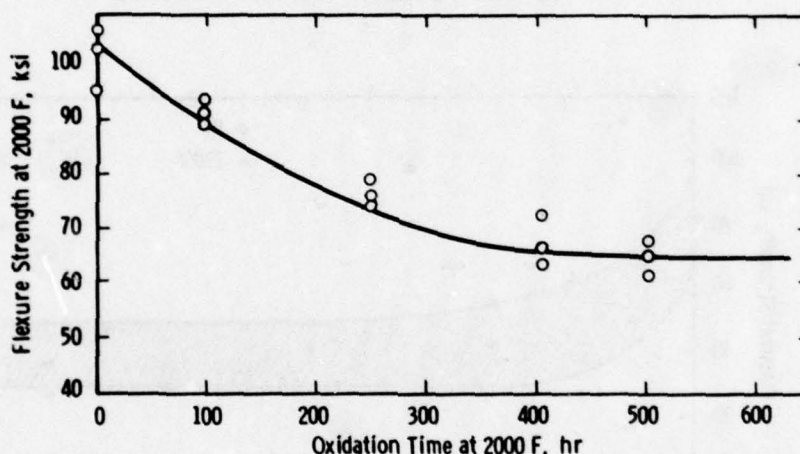
Figure 4-18. Effect of Oxidation on the Strength of Hot-Pressed Si_3N_4

Both the room temperature and 2300°F strengths were measured on specimens oxidized at 2500°F. These data appear in Figure 4-20 as a function of oxidation time where both room temperature and 2300°F strengths are shown to decrease by oxidation. The 2300°F strength after long-term oxidation at 2500°F stabilized at ∿40 ksi.[9]

The reduction in strength was apparently caused by surface degradation which occured during oxidation at elevated temperatures. Such degradation was evident in the surface appearance of the Si_3N_4 specimen
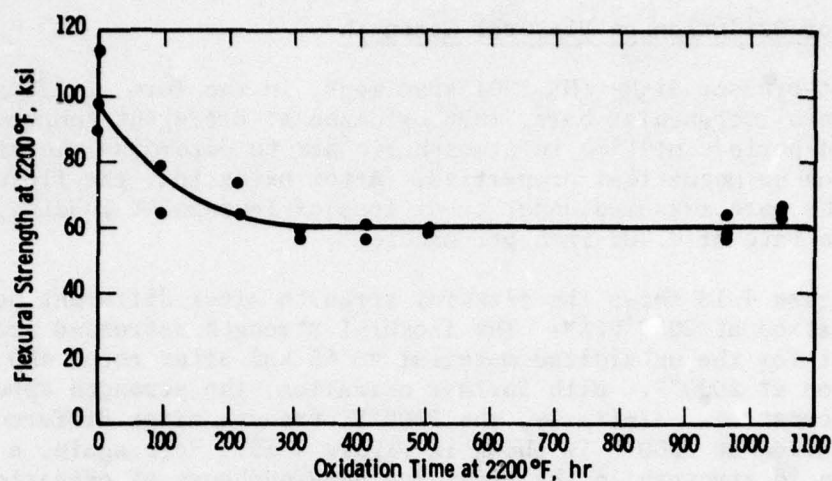
Figure 4-19.   Effect of Static Oxidation on Strength
of Hot-Pressed Silicon Nitride
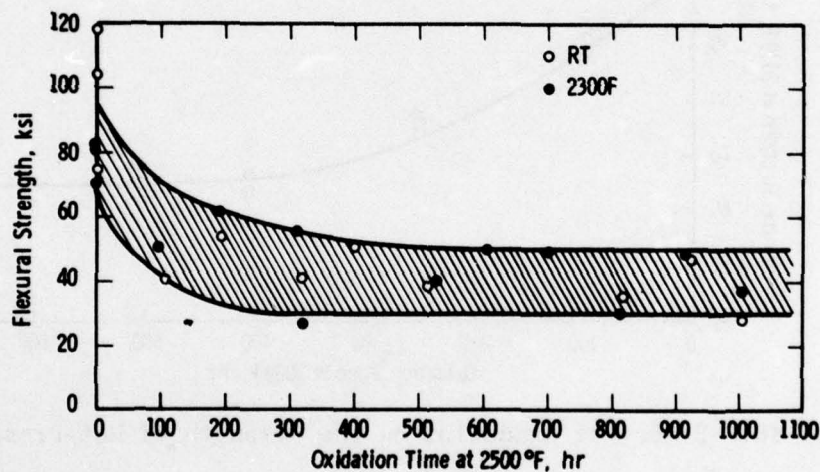
Figure 4-20.   Oxidation Time at 2500°F

shown in Figure 4-21 after 2096 hours of oxidation at 2500°F, both
before and after removing the surface oxide. The specimen surface was
characterized by microcavities which become visible when the oxide
was removed. The predominant oxidation product on hot-pressed Si_3N_4
after long-term oxidation at temperatures in the range 2000-2500°F
was $MgSiO_3$.[9] This $MgSiO_3$ could react with the Si_3N_4 substrate,
causing formation of microcavities on the surface. This phenomenon
is clearly evident in Figure 4-22 where scanning electron micrographs
of the fracture surface of an oxidized Si_3N_4 are shown. The fracture
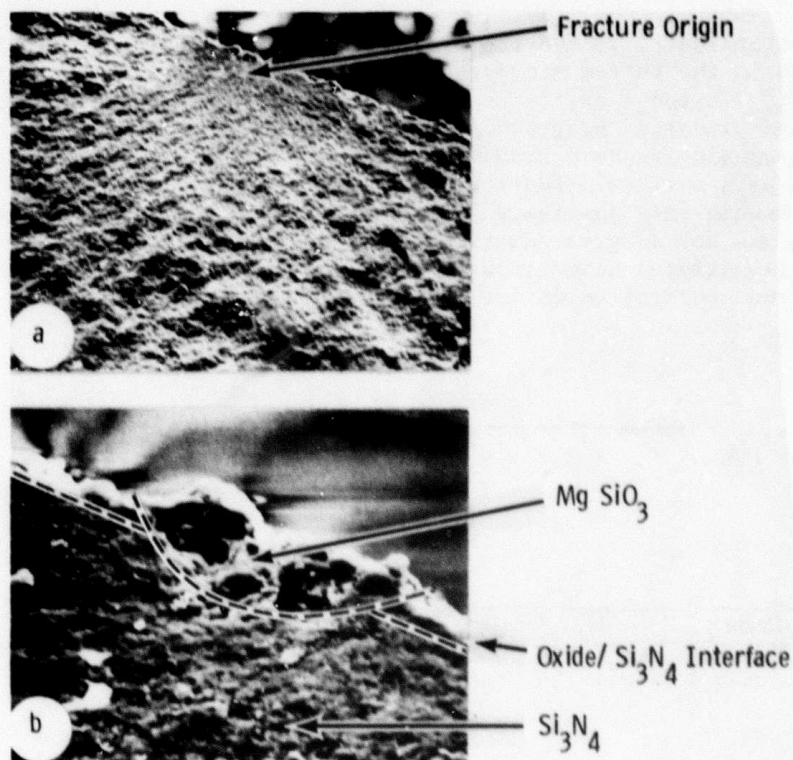
Figure 4-21. Scanning Electron Micrographs of the Fracture Surface of a Hot-Pressed Si_3N_4 Specimen Oxidized for 625 Hours in Air at 2500°F; (a) Area Indicating Fracture Origin, 105X (b) Magnified View of the Fracture Origin, 1050X
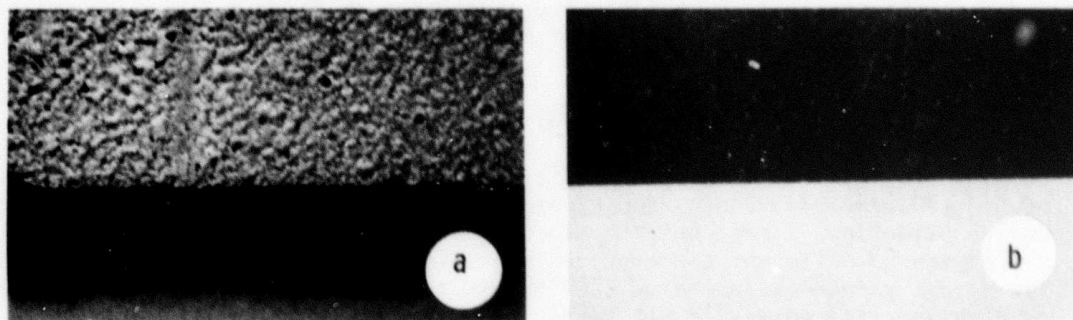
Figure 4-22. Surface of a Si_3N_4 Specimen after 4096 Hr of Oxidation in Air at 2500°F; (a) With Surface Oxide, (b) After Removing Surface Oxide. (5X)

199

origin is indicated in the top micrograph. This area of origin is magnified in the bottom micrograph. Energy dispersive analysis indicated that $MgSiO_3$ formed a cavity on the surface as shown in the bottom micrograph. As oxidation progressed, sharp microcavities formed on the surface, causing a sharp reduction in the strength of the material. However, with further oxidation, at some stage the microcavities on the surface became only shallower and wider, and the further effect on strength was not as great as from the formation of initial sharp cavities. This is illustrated schematically in Figure 4-23. Thus, after the first few hundred hours of oxidation, the strength remains practically constant.[9]
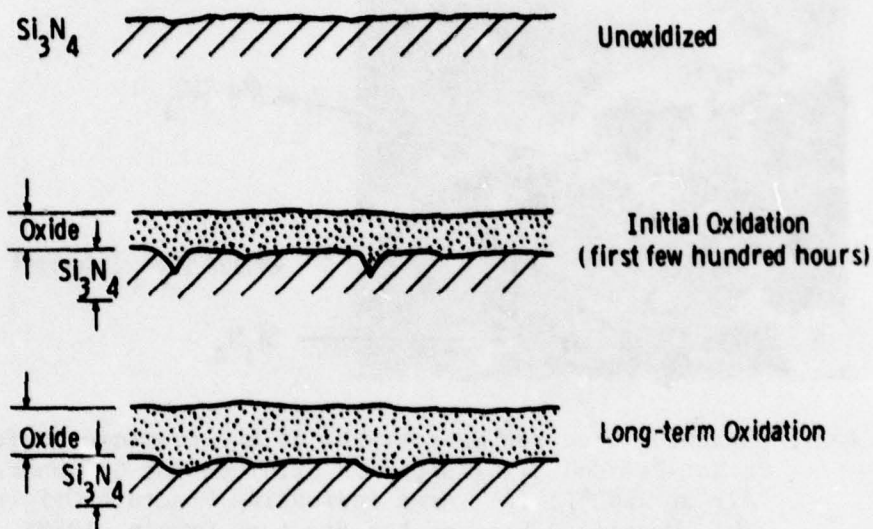
Figure 4-23.   Schematic Representation of Surface
Oxidation of Hot-Pressed Si_3N_4

4.2.3 SILICON CARBIDE (NORTON NC203) - RESULTS

As SiC oxidized to SiO_2, the difference in the molecular weights of SiC (40 g/mole) and SiO_2 (60 g/mole) was reflected as weight gain during oxidation. These weight gain data for oxidation of SiC in 1 atm dry oxygen at different temperatures are summarized in Figure 4-24. The weight gained at and below 2200°F was insignificant. The weight gain versus time curves at all temperatures approximate the classical parabolic behavior after about 1 to 2 hours from the start of oxidation.[3] The parabolic rate constants (K_p), obtained from the slopes of the straight lines in the parabolic plot (Figure 4-25), are shown as a function of reciprocal temperature in Figure 4-26. An activation energy of 481 kJ/mole was obtained for the oxidation of hot-pressed SiC in 1 atm dry oxygen.
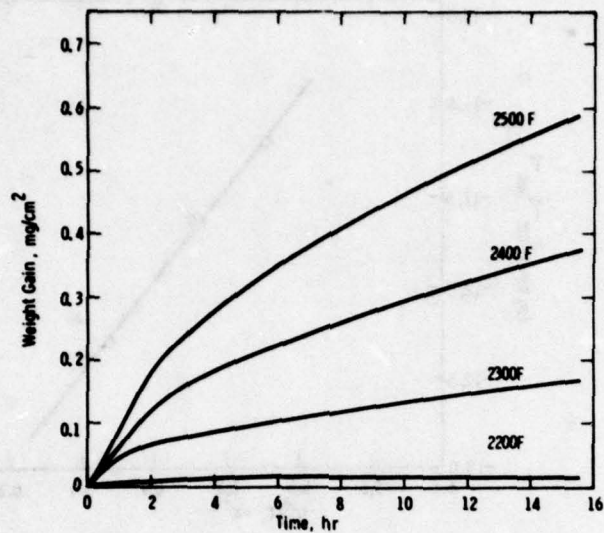
Figure 4-24. Oxidation Behavior of Norton's Hot-Pressed
SiC in Oxygen in 1 Atm Pressure
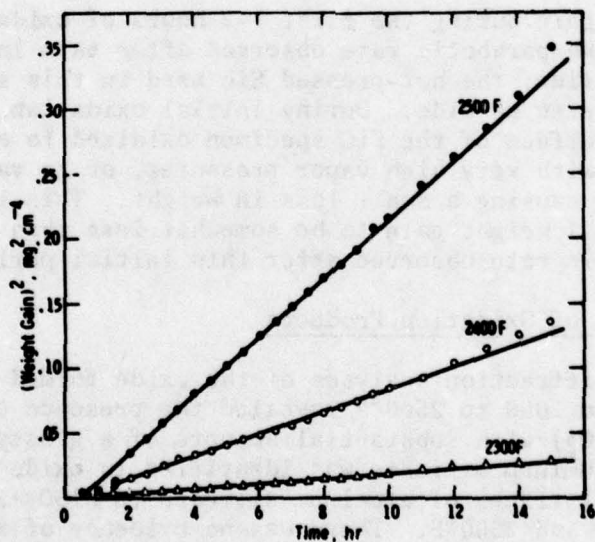
Figure 4-25. Parabolic Plot of Oxidation of
SiC in Oxygen at 1 Atm Pressure
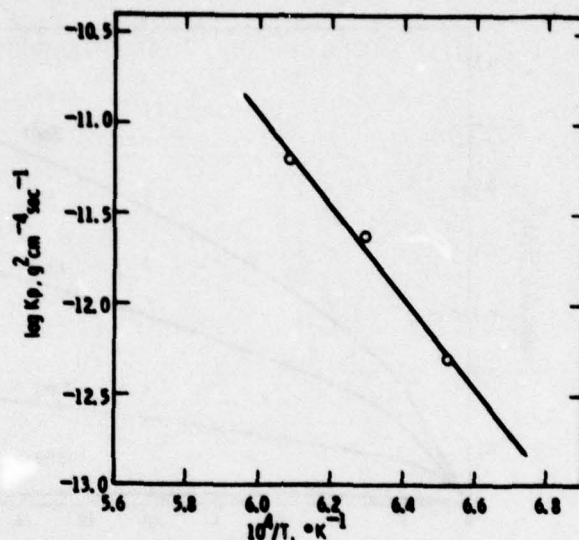
Figure 4-26. Arrhenius Type Plot Showing Parabolic Rate
Constant for Oxidation of SiC in 1 Atm
Oxygen as a Function of Temperature

The weight gain during the first ½-2 hours of oxidation was some-
what less than the parabolic rate observed after this initial oxidation.
As mentioned earlier, the hot-pressed SiC used in this study contained
about 4 w/o tungsten carbide. During initial oxidation, the tungsten
carbide on the surface of the SiC specimen oxidized to either solid
tungsten oxides with very high vapor pressures, or to various volatile
tungsten oxides, causing a small loss in weight. This loss in weight
caused the initial weight gain to be somewhat less than that expected
from the parabolic rate observed after this initial period.[3]

Characterization of Oxidation Products

The X-ray diffraction analyses of the oxide formed on SiC at
temperatures from 2000 to 2500°F revealed the presence of mostly
cristobalite (SiO_2) with substantial amounts of a glassy phase.[3]
No alumina or aluminum silicate was identified in oxide formed up to
2300°F, but small traces of aluminum silicate ($3\ Al_2O_3 \cdot 2\ SiO_2$) were
observed at 2400 and 2500°F. There was no evidence of any tungsten
oxides in the X-ray patterns, indicating that either their concentra-
tion was too low to be detected by X-ray diffraction, or they were
lost in the gaseous state.

The surface morphologies of the oxide films formed on SiC after
oxidation in dry oxygen for 30 hours at various temperatures are shown
in the electron micrographs in Figure 4-27. At 2000°F, very little

202
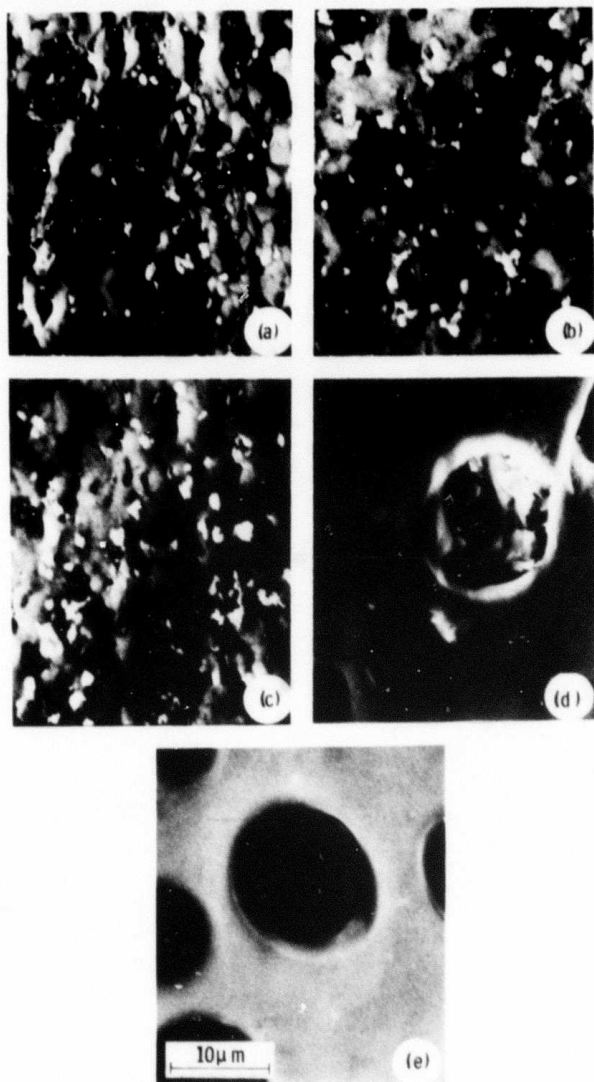
Figure 4-27. Scanning Electron Micrographs of Surfaces of SiC
Specimens Oxidized for 30 Hours: (a) 2000°F,
(b) 2200°F, (c) 2300°F, (d) 2400°F,
(e) 2500°F

oxide was formed. This left the underlying SiC grain structure still
visible after 30 hours of oxidation.(3) At temperatures of 2200°F and
2300°F, the surface was covered with a layer of cristobalite and a
glassy phase with small white particles distributed throughout the

surface. These were inferred to be aluminum silicate by energy disper-
sive X-ray analysis. At temperatures of 2400 and 2500°F, the surface
was uniformly covered with a smooth oxide layer which appeared to have
been liquid at the oxidation temperature. No discrete alumina particles
were observed on that surface. The oxide layers were full of fine pores
which were apparently formed at the oxidation temperature by the escape
of gaseous oxidation products from the SiC/SiO$_2$ interface.[3]

The scanning electron micrograph of a transverse section of an oxi-
dized SiC specimen is shown in Figure 4-28 along with the energy dis-
persive X-ray analysis of both the SiC substrate and the oxide layer
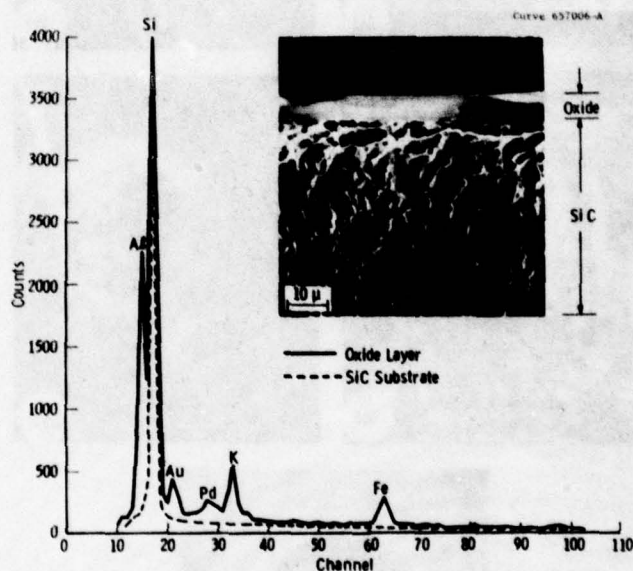
Figure 4-28. Scanning Electron Micrograph of the Transverse Section
of a Silicon Carbide Specimen Oxidized at 2500°F for
1203 Hours with Energy-Dispersive X-ray Analysis in
the Oxide Layer and on the SiC Substrate

thereon. While only the Si peak was detected in the SiC substrate, Al,
K and Fe peaks were found in the oxide film.* These elements must there-
fore, diffuse outward during the oxidation process to concentrate in the
oxide film. Their presence in the oxide was also conf rmed by the elec-
tron microprobe analysis of the oxide film, and also by mass spectrometric
analysis using a Cameca Ion Probe Mass spectrometer.

_____

*The Au and Pd peaks in the scan are from the surface film of an Au-Pd
 alloy deposited on an oxidized SiC specimen to obtain a conducting
 surface.

The existence of cristobalite at a temperature of 2000°F suggested that additive (Al_2O_3) and impurity elements (Fe, K, etc.) affected the devitrification of silica glass and reduced its viscosity.[47] The presence of appreciable amounts of Fe and K in the oxide layer could also explain the formation of a liquid oxide at a temperature as low as 2410°F. A liquid phase should not be formed by the reaction between SiO_2 and Al_2O_3 until ~2700°F.[48] Thus, these additive and impurity elements appeared to control the nature of the surface layer formed as a result of oxidation; this produced a very different oxidation rate for hot-pressed SiC as compared to a pure form (e.g., CVD-SiC). The different concentrations of additives and impurity elements can cause different rates of oxidation by forming oxides of differing viscosities. It is well established that gaseous diffusion is inversely related to the viscosity of the oxide in accordance with Stokes-Einstein relationship. Furthermore, it has been confirmed experimentally that the oxidation rates of SiC materials hot-pressed with different additives (e.g., Al_2O_3 and B), and with varying amounts of the same additive (Al_2O_3) are widely different.[49,50] Therefore, the oxidation behavior of hot-pressed SiC is determined predominantly by the nature and concentration of the hot-pressing additives and the impurity elements rather than by the intrinsic oxidation of SiC to SiO_2.

Discussion

The parabolic nature of the rate curves indicated that the oxidation of hot-pressed SiC was controlled by a diffusional mechanism. Various authors[31-34] suggested that the growth of the oxide layer on SiC occurred by the inward diffusion of oxygen ions or molecules, with an activation energy in the range 65 to 277 kJ/mole. Although there is a wide variation in the literature values of activation energy (presumably due to the formation of silica in either crystalline or amorphous form), oxygen transport as the rate controlling step in the oxidation of hot-pressed SiC seemed unlikely in view of the high value of the activation energy, 481 kJ/mole. However, high activation energy values in the range 405 to 548 kJ/mole have also been reported by Pultz and Hertl[51] for CO(g) desorption from the SiC/SiO_2 interface in the temperature range 2320-2610°F. Pultz[52] also studied the oxidation of particulate SiC in O_2 and O_2-He gas mixtures. He obtained an activation energy of 632 kJ/mole in the temperature range 2435 to 2633°F. In view of these results, it appears that in the oxidation of hot-pressed SiC, the desorption of CO(g) from the SiC/SiO_2 interface is the rate controlling process. The small differences in the values of the activation energy in these investigations may be either due to very high sensitivity of activation energy to temperature ranges, or due to differing viscosities of the oxide layer formed. The evolution of CO(g) causes the formation of a pore network in the oxide layer as observed in the scanning electron micrograph in Figure 4-27.

Effect of Oxidation on the Strength of SiC

The flexural strength of hot-pressed SiC after different periods of oxidation at 2500°F in atmospheric air was measured under conditions of four-point loading using a strain rate of 0.002 inch per minute. The results appear in Figure 4-29. The room temperature strength was reduced somewhat compared to that of unoxidized specimens, due to the cracking of the oxide layer on cooling from the oxidation temperature to room temperature.[9] However, the 2300°F strength remains fairly stable even after 4000 hours of oxidation. The oxide formed on SiC was predominantly SiO_2 which formed a very smooth surface layer. This smooth oxide layer did not cause any surface degradation and the flexural strength, therefore, remained fairly constant.
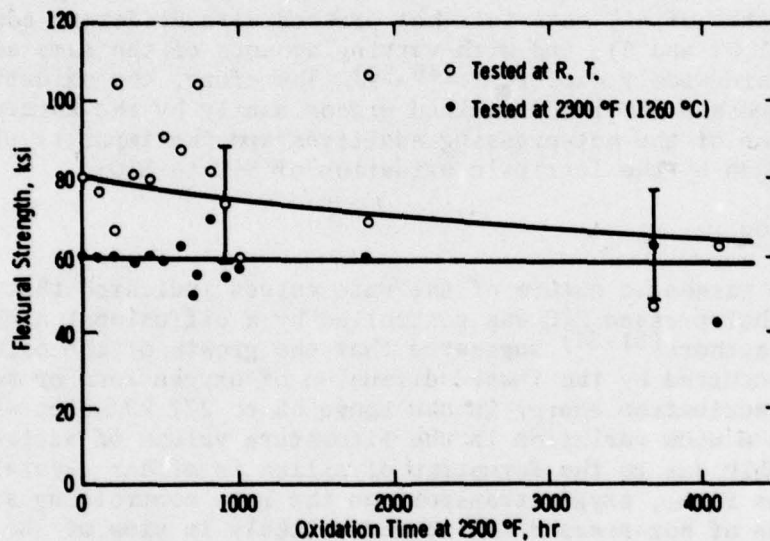
Figure 4-29. Effect of Static Oxidation on Flexural Strength of Norton NC-203 Silicon Carbide

206

4.3 CORROSION-EROSION OF SILICON NITRIDE AND SILICON CARBIDE

4.3.1 PRESSURIZED TURBINE TEST PASSAGE

A test passage that reproduced the operational environment of a large stationary gas turbine was used to determine the corrosion-erosion resistance of Si_3N_4 and SiC specimens.[1] Air compressed to 45 psi in a bank of 30 hp rotary compressors was preheated in an indirectly fired air heater to 600°F and fed into a 6-inch diameter chamber (see Figure 4-30). Fuel was injected into the combustor through a bayonet-mounted nozzle and burned with the compressed air. At the combustor exit, an array of 16 thermocouples were positioned to measure the gas temperature. Downstream of the thermocouple array, a transition section reduced the flow area to a 2 x 3-3/4 inch rectangular cross section and increased the velocity to 500 fps, which is typical of the turbine inlet velocities in stationary gas turbines. At this location, the test specimens were exposed to the hot gas stream. A test section held a pack of eight specimens that were fixtured as shown in Figure 4-31. Downstream of the test section, a damper valve located in the passage maintained typical turbine pressures. The combustion products were cooled by a water spray before passing to a muffler.
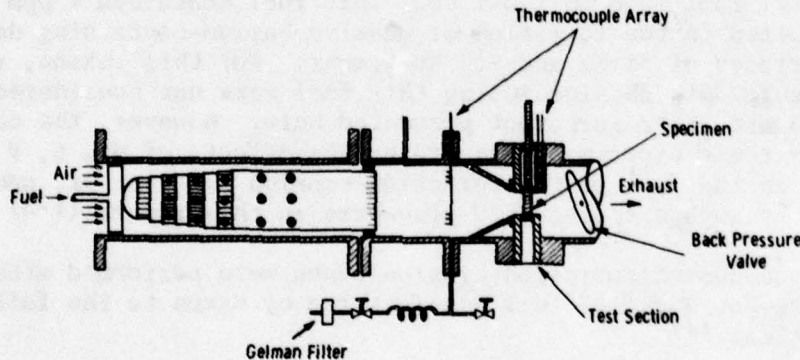
Figure 4-30. Pressure Corrosion Test Passage

The passage, as described above, was used for corrosion-erosion experiments at 2000°F. However, for testing at 2500°F, the passage was completely lined with reaction-sintered Si_3N_4 preforms.[6] Furthermore, the combustor was shortened to approximately 12 inches and made to butt directly against a hot-pressed Si_3N_4 plate of 6-inch diameter with a 2 x 4 inch rectangular hole in the center. The specimen section was installed directly behind the Si_3N_4 plate.
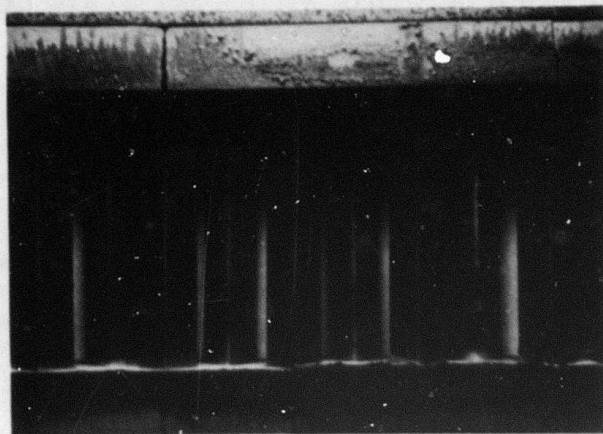
Figure 4-31. Specimens and Holding Fixture

4.3.2 FUEL

The earlier corrosion-erosion experiments were performed with
No. 2 diesel fuel from Gulf Oil Co. This fuel contained 4 ppm barium,
which resulted in the formation of massive barium-containing deposits
on the surfaces of Si_3N_4 and SiC specimens. For this reason, the
weight change data obtained using this fuel were not considered mean-
ingful and are, therefore, not presented here. However, the conclusions
drawn from these experiments regarding the effects of Na, S, V and Mg
additions in the fuel on the corrosion-erosion behavior are considered
valid and as such are discussed elsewhere in this report.[1-3]

All subsequent corrosion-erosion tests were performed with
barium-free No. 2 diesel fuel manufactured by Exxon to the following
specifications.[4]

sulfur	0.35 w/o (max)
ash	0.01 w/o (max)
water and sediment	nil
carbon residue	0.2 w/o (max)

Figure 4-32 shows the front and back surfaces of hot-pressed
Si_3N_4 and SiC specimens which were exposed for 250 hours at 2000°F
and 3 atm pressure to combustion gases at ~500 ft/sec velocity.[4] The
specimens were periodically cooled to room temperature for surface
examination and weight measurements, and underwent thermal cycling
thirteen times during the total period of 250 hours.

208
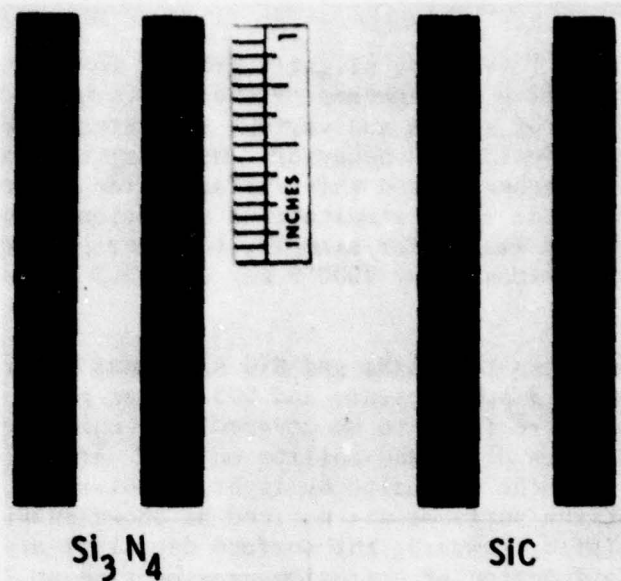
Figure 4-32.   Surface Appearance of Si₃N₄ and SiC Test Specimens after
                250 Hours of Exposure at 2000°F to Combustion Gases
                Obtained by Burning No. 2 Diesel Oil

The surfaces of both silicon nitride and silicon carbide specimens
remained smooth and free of any adherent surface deposits even after
250 hours of exposure. The average weight change (after removing
any surface oxide or superfluous deposits by light sandblast) for both
Si₃N₄ and SiC as a function of corrosion time at 2000°F is shown in
Figure 4-33. All specimens lost weight with time almost linearly, the
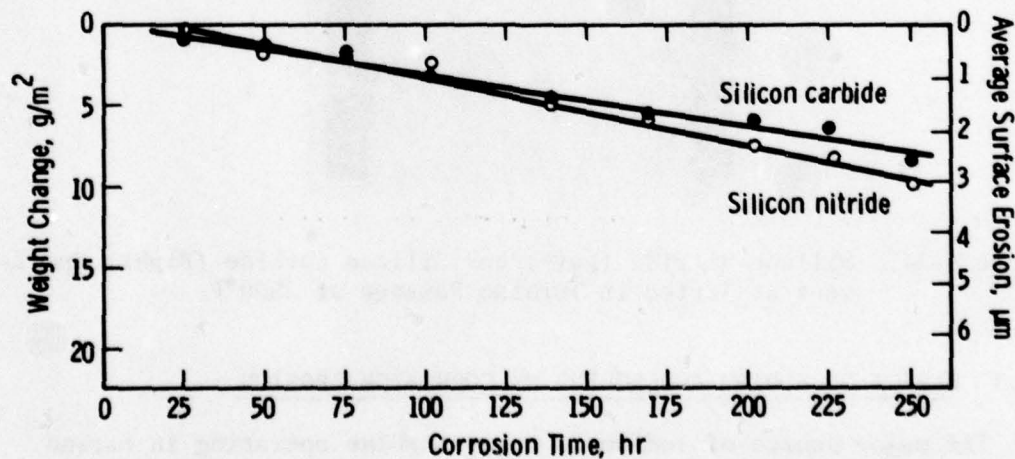
Figure 4-33.   Corrosion-Erosion Behavior of Hot Pressed Silicon Carbide
                and Silicon Nitride in Turbine Passage at 2000°F, 3 Atm
                Pressure and 152 m/s Gas Velocity Using Exxon No. 2
                Diesel Oil

209

magnitude of weight loss being slightly greater for Si_3N_4 than for SiC.[4]
In the highly oxidizing atmospheres of the gas turbine, both Si_3N_4 and SiC
formed a thin layer of silica and various silicates on the surface as
mentioned under the oxidation behavior. However, the impingement of high
velocity combustor gases caused this surface oxide layer to partly erode
away as it was formed. This simultaneous corrosion-erosion attack at
2000°F was extremely small; for example, the average surface erosion
after 250 hours of exposure at 2000°F was only 2.3 µm for SiC and 3 µm
for Si_3N_4.

Figure 4-34 shows the Si_3N_4 and SiC specimens after 43 hours of
exposure at 2500°F, 3 atm pressure and 500 ft/sec gas velocity.[6] The
specimen surfaces were found to be covered with white cristobalite in
addition to $MgSiO_3$ on Si_3N_4 and mullite on SiC. After removing these
surface oxides and other deposits by light sandblasting, some degrada-
tion of the specimen surfaces was noticed as shown in Figure 4-35.
Weight changes (after removing the surface deposits) are shown in
Figure 4-36 as a function of corrosion-erosion time at 2500°F. It
is clear from the data shown in Figure 4-36 that the surface recessions
due to corrosion-erosion at 2500°F are much greater than at 2000°F.
Also, the surface recessions for Si_3N_4 are greater than for SiC.
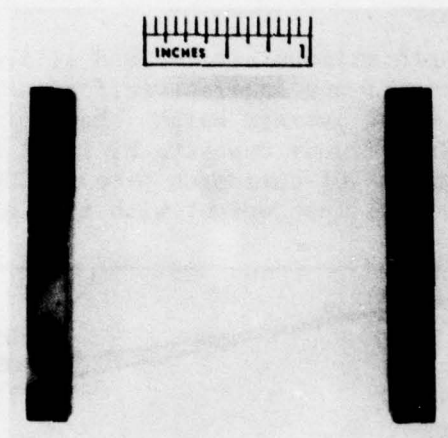
Figure 4-34.   Silicon Nitride (Left) and Silicon Carbide (Right) Speci-
mens as Tested in Turbine Passage at 2500°F

4.3.3 EFFECT OF SODIUM AND SULFUR ON CORROSION-EROSION

The major source of sodium in a gas turbine operating in marine
environment is sea water ingested with intake air. Salt (NaCl) can
also be introduced in a gas turbine as an impurity in the fuel.
DeCrescente and Bornstein[5] have shown that this salt (NaCl), which
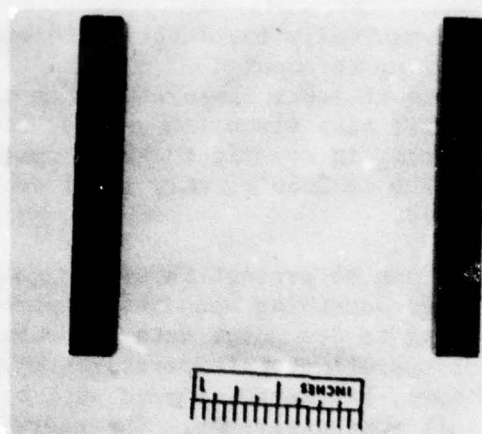
Figure 4-35.   Silicon Nitride (Right) and Silicon Carbide (Left) Speci-
mens from Turbine Passage Test at 2500°F After Sandblast
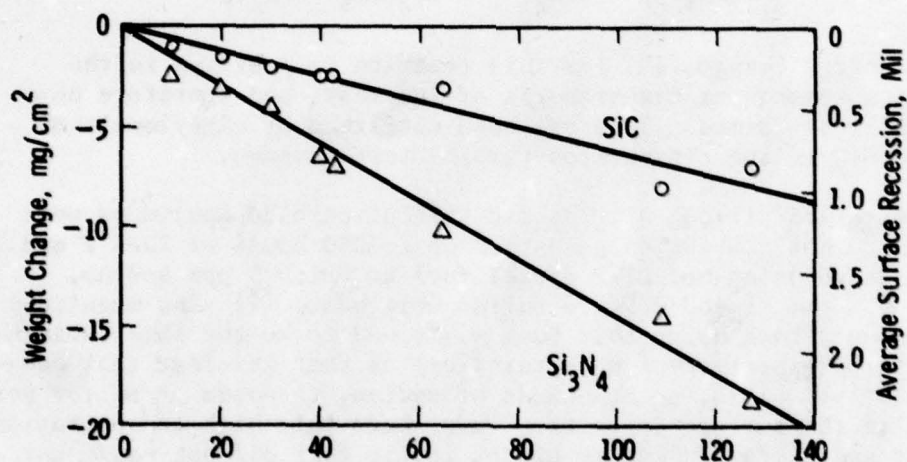
Figure 4-36.   Corrosion-Erosion Behavior of Hot Pressed Silicon-Nitride
in Turbine Passage at 2500°F, 3 Atm Pressure and 500 ft/sec
Gas Velocity Using Exxon GT-2 Oil

is present in gas turbines in the gaseous state, can react with SO_2
and SO_3 gases to form Na_2SO_4 (in condensed or gaseous form) according
to the reactions:

$$2 \, NaCl(g) + SO_2 + 1/2 \, O_2 + H_2O(g) \rightarrow Na_2SO_4 \ (c \ or \ g) + 2 \, HCl(g) \qquad (1)$$

$$2 \, NaCl(g) + SO_3 + H_2O(g) \rightarrow Na_2SO_4 \ (c \ or \ g) + 2 \, HCl(g) \qquad (2)$$

211
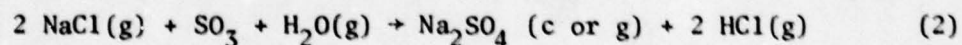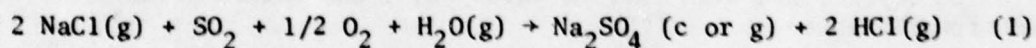
These reactions are thermodynamically favorable (free energy change $\Delta G < 0$) only at temperatures up to about 2550°F. While the conversion of NaCl to Na_2SO_4 is complete at lower temperatures up to about 1832°F, practically no conversion will take place ($\Delta G > 0$) at temperatures above about 2550°F. Therefore, in ceramic turbines operating at temperatures in the range 2000 to 2350°F, only small conversion of NaCl(g) to Na_2SO_4 is expected.

Any Na_2SO_4 thus formed can be present in either gaseous or condensed form in a gas turbine, depending upon the temperature, pressure and concentration. According to dew point data of DeCrescente and Bornstein,[53] in turbines operating at temperatures higher than 1832°F and at 10 atm pressure, all Na_2SO_4 formed will be in the gaseous state even at very high salt concentrations. Therefore Na_2SO_4 should not condense on ceramic parts operating at temperatures above 1832°F.

One could expect the following reaction between Na_2SO_4(g) and SiO_2 formed on the surfaces of Si_3N_4 and SiC:

$$Na_2SO_4(g) + SiO_2(s) \rightarrow Na_2SiO_3 + SO_3(g) \tag{3}$$

The free energy change (ΔG) for this reaction is positive in the turbine atmospheres at temperatures of interest, and therefore no Na_2SiO_3 will be formed. This has been confirmed by experiments on Si_3N_4 and SiC in the pressurized turbine test passage.

Hot-pressed silicon nitride and silicon carbide specimens were subjected to hot combustion gases for up to 250 hours at 2000°F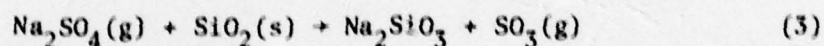 and 3 atm pressure using No. GT-2 diesel fuel to which 5 ppm sodium, 2 ppm V, 0.6 ppm Mg and 0.5 w/o sulfur were added.[3] The magnitude of corrosion attack using this fuel was found to be the same (within the limits of experimental uncertainties) as that in clear fuel containing barium. Also, no compounds of sodium, vanadium or sulfur were detected in the surface deposits. Thus, even this high concentration of sodium and sulfur in intake air or in the fuel did not cause any accelerated corrosion of these ceramic materials.

Some Na_2SO_4 may be expected to condense on ceramic parts at lower temperatures (below about 1832°F) during a final low power cycle or slow cooldown. In such cases, the silica (SiO_2) formed on the surfaces of silicon nitride and silicon carbide parts can react with Na_2SO_4(s) to form sodium silicate (Na_2SiO_3) or even silicon disulfide (SiS_2). The silicon disulfide will be in solid or liquid state, depending upon the temperature. No such compounds, however, were detected in corrosion experiments with fuel to which Na, V and sulfur were intentionally added.
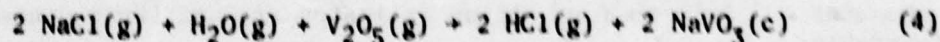
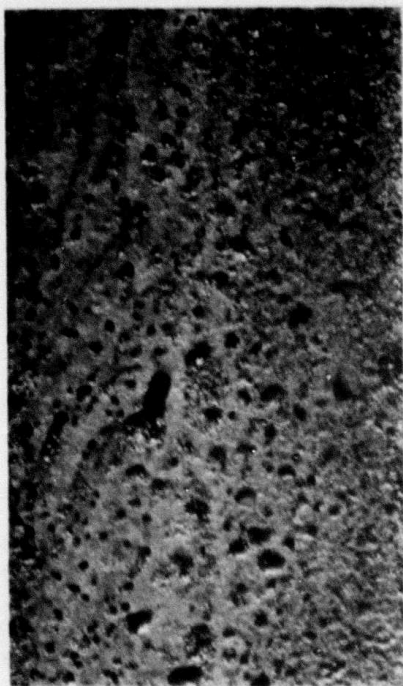## 4.3.4 EFFECT OF VANADIUM ON CORROSION-EROSION

Vanadium is a common impurity in low cost fuels, ranging up to several hundred ppm in some heavy residual fuels. This vanadium is oxidized to vanadium pentoxide (V_2O_5) in the combustion chamber and enters the turbine either in gaseous or in condensed form, depending upon the temperature and concentration. The vapor pressure measurements of Bornstein, et al.,[54] have shown that even at a concentration of 100 ppm vanadium, all V_2O_5 will be present in the gaseous form at temperatures above about 1300°F. However, no compounds between V_2O_5 and SiO_2 (which forms on Si_3N_4 and SiC) have been reported[55] and, therefore, even a very high concentration of vanadium in the fuel by itself will not cause any accelerated corrosion of Si_3N_4 and SiC.

Hot-pressed Si_3N_4 and SiC were exposed to hot combustion gases in the pressurized turbine test passage at 2000°F and 3 atm pressure, using Exxon GT-2 diesel fuel to which 100 ppm vanadium and 0.5 w/o sulfur were added to simulate heavy residual fuels. The surface of a SiC specimen exposed for 44 hours under these conditions is shown in Figure 4-37.[4] The surface had small deposits of magnesium silicate and silica. No compounds of vanadium or sulfur were detected in these surface deposits. After removing the deposits by light sandblasting, the surfaces, shown in Figure 4-37, were found to be smooth and free of any degradation. The magnitude of corrosion attack was also the same as that observed in clean fuel (Figure 4-33). Similar behavior was observed for hot-pressed silicon nitride. One must conclude, therefore, that $V_2O_5(g)$ is innocuous to both Si_3N_4 and SiC and that even heavy residual fuels will not cause any accelerated attack on Si_3N_4 and SiC.

If any $V_2O_5(\ell)$ condenses on the surfaces of Si_3N_4 and SiC at low temperatures, e.g., during cooldown, it could dissolve some SiO_2 from these surfaces. However, the solubility of V_2O_5 and SiO_2 is very small,[3] and therefore a protective layer of SiO_2 will still be maintained on the surfaces of Si_3N_4 and Si_C. In the experiments with very high concentrations of vanadium in the fuel, no V_2O_5 liquid was observed on the specimen surfaces.

During the combustion of fuel which contains vanadium with attendant sea salt ingestion, the NaCl(g) can react with both V_2O_5 and SO_2, forming vanadates of sodium by the following reactions:[56]

$$2 \ NaCl(g) + H_2O(g) + V_2O_5(g) \rightarrow 2 \ HCl(g) + 2 \ NaVO_3(c) \qquad (4)$$

$$6 \ NaCl(g) + 3 \ H_2O(g) + V_2O_5(g) \rightarrow 6 \ HCl(g) + 2 \ Na_3VO_4(c) \qquad (5)$$

Before Surface Cleaning   **After Surface Cleaning**
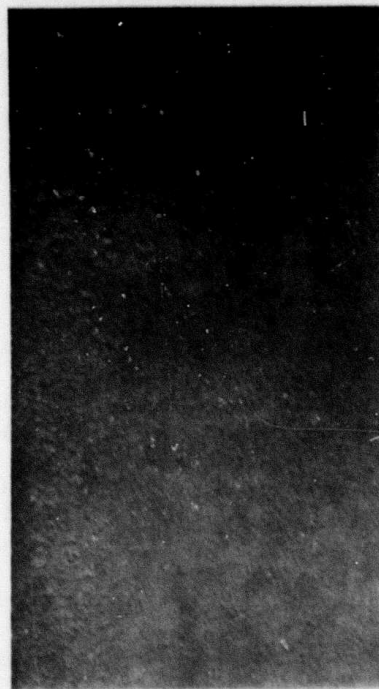
Figure 4-37. Surface Appearance of a Hot-Pressed Silicon Carbide
Specimen After 44 Hours of Exposure to Hot Combustion
Gases at 2000°F, 3 Atm Pressure and 500 ft/sec Velocity
Obtained by Burning GT-2 Diesel Oil Containing 100 ppm
Vanadium and 0.5 w/o Sulfur (10X)

These reactions are thermodynamically favorable at temperatures of
interest (1100-1650°K), and therefore sodium vanadates can form in
the turbine atmosphere in addition to any Na_2SO_4. However, vanadates
of sodium are even more volatile than Na_2SO_4,[54] and if present, will
volatilize away as soon as they are formed from the surfaces of Si_3N_4
and SiC. Furthermore, reactions of the following types between sodium
vanadates and SiO_2 to form sodium silicates are not thermodynamically
favorable:

$$2 \ NaVO_3(c) \ + \ SiO_2 \rightarrow Na_2SiO_3 \ + \ V_2O_5 \tag{6}$$

$$2 \ Na_3VO_4(c) \ + \ 3SiO_2 \rightarrow 3 \ Na_2SiO_3 \ + \ V_2O_5 \tag{7}$$

214
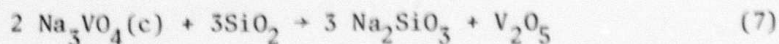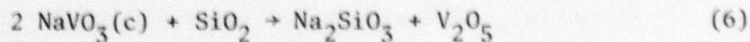
These results were confirmed by the pressurized test passage experiments on Si_3N_4 and SiC at 2000°F using diesel fuel with Na, V and S added, as described under the effects of sodium and sulfur on corrosion behavior.[3] In these experiments, no sodium vanadates or sodium silicates were detected in the surface deposits. Hot-pressed silicon nitride and silicon carbide are, thus, very resistant to attack by commonly found impurities in turbine fuels and intake air.

4.3.5 EFFECT OF CORROSION-EROSION ON FLEXURAL STRENGTH

After surface examination and weight change measurements, flexural strengths of the corroded Si_3N_4 and SiC specimens were measured to determine the effect, if any, of the turbine environment on strength. The flexural strength was measured under conditions of four-point loading (outer span 1.5 inch, inner span 0.5 inch) at 2000°F using a cross-head strain rate of 0.001 per min. The specimen size, as mentioned previously, was 2 x 1/4 x 1/4 inches.

The flexural strength data for Si_3N_4 and SiC specimens corroded at 2000°F using clean Exxon fuel are plotted as a function of corrosion time in Figure 4-38. Unfortunately, the number of specimens available for strength testing was very small. The flexural strength values of uncorroded Si_3N_4 and SiC measured under the same testing conditions are also included in the figure.[2] It appears that flexural strength remains almost unaffected by corrosion-erosion at 2000°F for up to 250 hours. Long-term tests in an alumina lined muffler did show some effect, however.[9] (These data appear as Figure 4-18, page 197.)
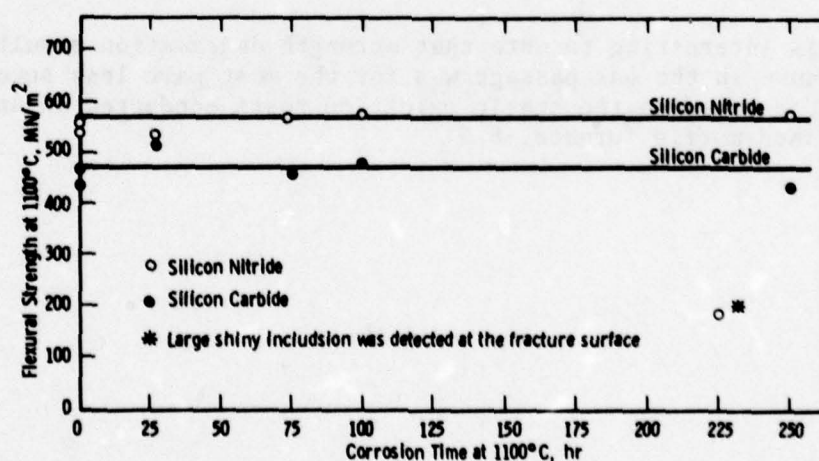

Figure 4-38. Effect of Gas Turbine Environment on the Flexural Strength of Hot Pressed Si_3N_4 and SiC

The flexural strength data for Si_3N_4 and SiC specimens corroded at 2500°F using clean Exxon fuel are shown in Table 4-2 as a function of corrosion time. Again, only one specimen was available for strength testing at each exposure time. However, it is evident that an appreciable degradation in the strength of both Si_3N_4 and SiC is caused by exposure to hot combustion gases at 2500°F.[4]

TABLE 4-2

EFFECT OF CORROSION-EROSION AT 2500°F AND 3 ATM
PRESSURE ON FLEXURAL STRENGTH AT 2000°F

Time (hr)	Si_3N_4 (ksi)	SiC (ksi)
0	80	65
10	65	55
20	65	56
30	63	52
40	63	57
43	60	55
65	54	52
109	57	55
127	51	51
Ref. 4000 hr oxidation at 2500°F - Al_2O_3 muffle[8]	30	60

It is interesting to note that strength degradation resulting from exposure in the gas passage was for the most part less severe than that observed in the static oxidation tests conducted in an alumina-lined muffle furnace.(8,9)

SECTION 5

IMPROVED MATERIAL DEVELOPMENT

5.1 INTRODUCTION

The engineering property requirements for structural ceramic materials, as defined by the DARPA Gas Turbine Program, identified the need for supplemental material development programs. Some of these were sponsored by DARPA directly, while others were funded by various governmental agencies or concerned industrial organizations to meet their own or related objectives. Important materials development work at Westinghouse was supported by the office of Naval Research[57] and the Naval Air Systems Command[58] prior to and in conjunction with the DARPA contract activities.

The more significant efforts to develop an understanding of dense silicon nitride behavior are summarized here because they relate directly to material improvements in many important categories. Developments with the Stationary Ceramic Turbine Project specifically are integrated with other pertinent contributions to relate the critical aspects of materials improvement to advancing turbine technology.

217

5.2 HIGH DENSITY SILICON NITRIDE

5.2.1 BACKGROUND INFORMATION

Powder processes are used almost exclusively to fabricate dense silicon nitride. Deeley[59] was the first to report that pore-free bodies could be made by the hot pressing of Si_3N_4 powder containing a densification aid. Various metal oxides, e.g., MgO, BeO, Al_2O_3, Y_2O_3, CeO_2, etc., have been identified as effective densification aids, with MgO being most prevalently employed.[59-62] Although hot pressing currently produces a more dense and stronger product, the feasibility of pressureless sintering has been demonstrated.[63-65] Again, in the case of pressureless sintering, densification aids play an important role.

The Si_3N_4 powder with metal oxide additives is densified in the presence of a liquid phase at high temperatures according to the general reaction:

$$Si_3N_4 + SiO_2 + \text{metal oxide} + (\text{impurities}) \xrightarrow{\text{Temp}} Si_3N_4 + \text{liquid} \qquad (1)$$
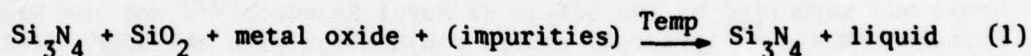
where SiO_2 is unavoidably present at the surface of each Si_3N_4 particle and/or incorporated in the powder in the form of Si_2N_2O. Above the solidus temperature, all four starting constituents of the reaction Eq. (1) react to form a liquid. Neglecting the possible mass losses due to volatilization[63] and dissociation which, incidently, is suppressed by the presence of a liquid phase, the composition of the liquid and the equilibrium fraction of solid Si_3N_4 depend upon 1) the composition of the starting powder, 2) the phase equilibria of the composite system and 3) the densification temperature. The liquid fills the interstices, wets and tends to draw the Si_3N_4 particles into closer approximation and contact by surface tension to permit the solution-reprecipitation of Si_3N_4. This solution-reprecipitation phenomenon appears to be critical to the initiation of the α to β transition in Si_3N_4 and therefore critical to the development of high strength. In the process, voids are eliminated and densification results.

Upon cooling from the densification temperature, the liquid solidifies according to the general reaction:

$$Si_3N_4 + \text{liquid} \xrightarrow{\text{cooling}} Si_3N_4 + \text{secondary phases} \qquad (2)$$
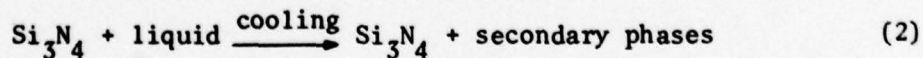
illustrating that Si_3N_4 is truly representative of a polycrystalline, polyphase material.

The number, chemistry and content of the secondary phases depend on the composition of the starting powder and the phase relations in the given composite system. In addition, the crystal structure of Si_3N_4 can

be altered by the concurrent substitution of certain metal cations for silicon and oxygen for nitrogen.[66,67] The starting powders, phase relationships, solid solution alloying, the $\alpha \rightarrow \beta$ phase transformation and the resultant microstructures all influence the mechanical and thermal properties of Si_3N_4 as well as its oxidation resistance. The microstructure of dense Si_3N_4 is governed by the phase relationships of constituents within the starting powder. These same relationships, therefore, control the properties of silicon nitride materials.

5.2.2 FABRICATION

Silicon - the Raw Material

Silicon, the second most abundant terrestrial element but not a natural mineral, is produced commercially in carbon-electrode furnaces by the thermochemical reaction of crushed quartzite rock with high purity coke:[68]

$$SiO_2 + 2C \longrightarrow Si + 2CO$$
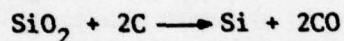
Excess SiO_2 prevents the formation of SiC. The molten Si is tapped, cast, cooled and pulverized to produce a powder of $\sim$98 percent purity. Most of the impurities tend to segregate between the silicon grains as the molten mass solidifies and cools to permit purification to $\sim$99.5 percent Si by acid washing of the pulverized silicon powder.[68] Further purification is accomplished by the synthesis of some volatile silicon compound, and its multiple distillation. The reduction back to silicon occurs by chemical vapor deposition, in hydrogen, usually onto hot silicon filaments to produce polycrystalline rods. The rods are purified further by a flat-zone process. The availability, price and purity differentials between crude silicon powder and powder produced from semiconductor grade silicon is 2 to 3 orders of magnitude. The purity of powder produced by pulverizing semiconductor grade silicon bears little resemblance to that of its polycrystalline or single crystal parent.

Other methods of producing 99.5 percent silicon do not appear to be practical on a commercial scale. The reduction of silicon dioxide with magnesium results in a submicron silicon powder directly,[68] however.

The major cation impurities in unleached silicon powder ($\sim$98 percent purity) are Fe, Al, Ca and Mg. These are present in the starting raw materials. Additional iron contamination is associated with the equipment used in the pulverizing step. Oxygen is the major impurity by far. It is present as SiO_2 at the surface of all Si particles. Part of the oxygen is combined with the major cation impurities as pure oxides or as complex silicates.

Si_3N_4 - the Starting Powder

Silicon nitride exists in two hexagonal structures, α $Si_3N_4(P31C)$[69] and β $Si_3N_4(P6_3/_m)$.[70] The α and β structures were thought originally to be low and high temperature polymorphs, respectively, hence their designation.[71] Jack and coworkers[72] first defined the α structure as an oxynitride with the approximate formula $Si_{11.5}$ N_{15} $O_{0.05}$ based upon X-ray powder pattern data which suggested a refinement in structure due to $\sim$1.5 w/o oxygen which appeared to be incorporated into the lattice.

Marchand, et al,[69] Kohatsu and McCauley,[73] and Kato, et al,[74] used single crystal X-ray data to refine the α structure. All concluded, independently, that the α structure consisted of Si and N atoms only. Various workers[65,75-77] have also shown that α Si_3N_4 powder may have much lower oxygen content than that hypothesized by Jack; e.g., Kato, et al,[74] reported an oxygen content of 0.05 w/o. It is now generally accepted that both the α and β structures can be pure Si_3N_4. Although several suggestions have been made, including Blegen's observation that the α structure is formed by a vapor reaction,[78] leading to the conclusion that α Si_3N_4 is metastable at all temperatures, the thermodynamic interrelation between the two structures remains unknown.

Silicon nitride, whether in the form of powder for subsequent sintering or reaction bonded components, is synthesized from elemental silicon and nitrogen. In the case of reaction bonded silicon nitride, silicon powder is precompacted to the desired shape and nitrided to produce a part of low, but specified, density. Powder for sintered components is prepared by nitridation of loose silicon powder to produce low density "cake" which must be pulverized. Changes in bulk volume are insignificant, essentially nil, even in the case of the reaction bonded products because Si_3N_4 nuclii apparently form by a vapor transport mechanism[79] which permits grain growth to be accommodated within interstitual voids.

In Si_3N_4 powder production, silicon powder of a relatively uniform and small particle size is placed in suitable ceramic (Al_2O_3) containers. In some cases, a desirable nitriding aid, i.e., Fe, is premixed with the Si powder.[80] Nitriding is accomplished in an atmosphere furnace at temperatures between 1200 and 1500°C. A partially reducing atmosphere appears to be desirable, e.g., N_2 + H_2.[81,82] The nitriding cycle is usually divided into low and high temperature steps. The first occurs between 1200-1325°C (below the melting point of silicon 1420°C) for prolonged periods. The second is performed at $\sim$1450°C (above the melting point of silicon) for a short period to fully nitride all remaining free silicon.[79] Since the reaction is exothermic, a thermal gradient can arise in larger powder masses, making the control of temperature difficult in some cases. After cooling, the Si_3N_4 agglomerate is removed from the containers, pulverized, and classified to obtain the desired particle size.

The manufacture of Si_3N_4 powder at Westinghouse (α/β ratio > 9) is consistent with the procedure outlined above. Relatively pure $\overline{Si}$ powder of >325 mesh particle size (Figure 5-1) is premixed (hand blended) with
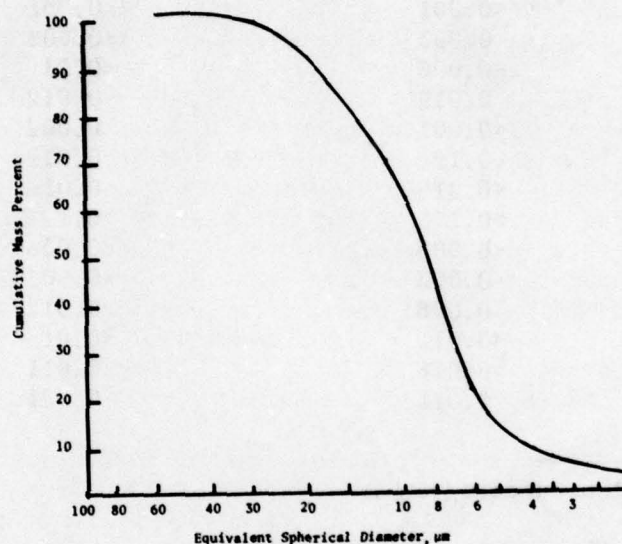

Figure 5-1. Particle Size Distribution in Si Powder

1 w/o metallic Fe powder. The powder mixture is placed in graphite-paper lined alumina containers and nitrided in mullite muffle tubes within a SiC resistance heated furnace at temperatures between 1200° and 1450°C. A forming gas atmosphere consisting of 93 percent N_2 and 7 percent H_2 is used. After nitriding, the Si_3N_4 cake is pulverized, jet milled (Sturdavant Jet Mill) and screened to -100 mesh. Typical cation impurity concentrations are shown in Table 5-1. The oxygen content after processing is 0.5 - 0.7 weight percent.

The mullite muffle tubes were not used initially when the powder processing was scaled up from 1 kg/week to 4 kg/week (single batch charge). Outgassing of H_2O and O_2 from the porous furnace refractories produced oxygen contamination of the powder between 3-5 weight percent. Large amounts of Si_2N_2O were detected in the resultant Si_3N_4 powder. While the furnace modification to install four mullite tubes did decrease the potential furnace capacity, it reduced oxygen contamination to an acceptable level.[9]

221

TABLE 5-1

SPECTROCHEMICAL ANALYSIS* OF CATION IMPURITIES

	Silicon Powder	Silicon Nitride Powder
Al	0.064	0.062
Ag	<0.001	<0.001
B	0.003	<0.003
Bi	<0.003	<0.01
Ca	0.019	0.012
Co	<0.001	0.002
Cr	0.12	0.01
Cu	<0.01	<0.01
Fe	>0.1	>0.1
Mg	<0.003	<0.003
Mo	<0.003	<0.003
Ni	0.008	0.012
Pb	<0.01	<0.01
Ti	0.028	0.011
V	0.011	0.021

*Emission spectrograph.

NOTE: Phases were not determined.

While it is possible to relate the nitriding process to chemical thermodynamics, little was done with this aspect at Westinghouse in the development of a specific nitriding cycle for the production of Si_3N_4 powder. The discussion of the thermodynamic stability of the condensed phases, Si, SiO_2, Si_2N_2O and Si_3N_4, as a function of the oxygen and nitrogen partial pressures at various temperatures from Section 4.0, "Environmental Stability of Silicon Nitride and Silicon Carbide," is applicable. The synthesis of silicon nitride from Si and N_2 apparently is controlled by reaction kinetics since equilibrium conditions are rarely achieved.[83]

The oxygen partial pressure of the system does affect the nitriding kinetics since it governs whether the silicon will exhibit passive or active oxidation. Lin[84] suggests that the direct reaction of N_2 with Si can occur under conditions of active oxidation, but the careful work of Atkinson[87] and coworkers indicates otherwise. Their thermogravimetric experiments and observations of the nitriding of semiconductor grade Si powder and single crystals under conditions of active oxidation show that Si_3N_4 nuclei form on the Si surface and grow by Si transport mechanism. Pores form at the Si surface as the Si_3N_4 scale grows from the initial nuclei. During the initial period, the rate of nitriding is linear. As the pores are closed by the growth of the Si_3N_4 scale,

the rate of nitriding decreases and then effectively ceases. Although the initial rate of nitriding is greater at high N_2 pressures, more Si_3N_4 is eventually formed at lower nitrogen pressures, evidently due to the formation of fewer nuclei and, thus, a slower rate of pore closure.

Since Si is in a state of active oxidation during the nitriding process, the SiO gas can be considered a likely Si transport media.[85] The repetitious, reversible reaction $3Si + 1.5O_{2(g)} \rightarrow 3SiO(g)$ at the Si-gas interface and $3SiO_{(g)} + 2N_{2(g)} \rightarrow Si_3N_4 + 1.5O_{2(g)}$ at the Si_3N_4-gas interface could account for the formation and growth of the Si_3N_4 scale before pore closure. Lin[84] indicates that the standard free energy of $3SiO_{(g)} + 2N_{2(g)} \rightarrow Si_3N_4(s) + 1.5O_{2(g)}$ is positive at nitriding temperatures, but he fails to recognize that neither SiO nor O_2 are in their standard states under nitriding conditions. Assuming reasonable values for the partial pressures of SiO and O_2 in a nitrogen atmosphere, the indicated reaction appears to be feasible. The combined reaction $3Si + 2N_2 \rightarrow Si_3N_4$ has a negative free energy of formation.

Nitriding studies indicate that conditions for active oxidation are necessary and that the reaction involves a vapor phase. Therefore, the nitridation threshold for pure Si should occur at ∿1200°C for a reasonably achieved oxygen partial pressure of ∿10^{-4} atm (Figure 5-2). Ford has managed to accomplish nitridation well below this temperature, however.[86]
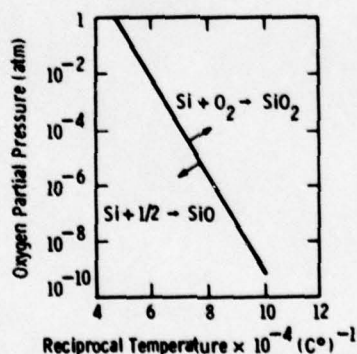
Figure 5-2. Nitridation Threshold for Pure Si Powder

The effect of certain impurities on the nitriding kinetics of silicon is significant. Without impurities, silicon is, at best, difficult to nitride even in low oxygen environments.[88] Of the impurities reported to increase the nitriding kinetics, Fe has received the greatest attention because it is effective and it remains a major impurity in pure Si powder. The actual role played by Fe or other cation impurities has not been identified.

The oxygen content of Si_3N_4 powders ($\alpha/\beta > 8$) has been reported to range between 0.5 - 3.0 w/o, depending on the manufacturer and the particular batch.[65] Assuming that all of the oxygen is present in the form of SiO_2, the SiO_2 molar fractions range between 0.02 and 0.12, with commercial Si_3N_4 powders represented at the high end of this scale. SiO_2, therefore, must be considered an important constituent in the starting powder.

The major cation impurities in Si_3N_4 powder are Fe, Ca and Al. All represent impurities in the starting silicon metal used to manufacture Si_3N_4. Metallic additions used to promote the nitriding of silicon powder increase the level of contamination.[89] The major impurities normally range between 10-5000 ppm.

5.3 EXPERIMENTAL SILICON NITRIDE MATERIALS

5.3.1 PHASE RELATIONS OF Si_3N_4 - SiO_2 - MgO SYSTEMS

The conventional method of preparing Si_3N_4 powder (containing SiO_2 and impurities) for densification consists of mixing in the MgO densification aid and reducing the particle size of the composite powders by wet ball milling. Milling can be accomplished in containers which will not add additional contaminants except volatile hydrocarbons. The WC milling media commonly employed contaminates the powders. However, much of the WC contamination can be removed by subsequent classification.[90] Dry alcohols are used during milling to minimize the hydrolization of Si_3N_4 to SiO_2. Measurements before and after milling have shown a negligible change in oxygen content. Thus, the constituents of the starting Si_3N_4 powder are Si_3N_4 ($\alpha/\beta > 8$), metal oxide and various impurities (Fe, Ca, Al, WC and hydrocarbons).

Phase equilibrium studies of various Si_3N_4-oxide systems do not recognize, SiO_2 as a significant component. As pointed out by Gauckler, et al,[66] one can not consider, apriori, any Si_3N_4-SiO_2-MO system as an ordinary ternary.* If the reciprocal reaction Si_3N_4 + 6/x M_2O_x $\rightleftharpoons$ 3SiO_2 + 4/x M_3N_x (where x = the valence state of the metal ion) is assumed, the system is represented by a square diagram with Si_3N_4, 3SiO_2, 6/x M_2O_x and 4/x M_3N_x located at the four appropriate corners. The composition at each point within the diagram can be represented by an equivalent cation concentration (e.g., $[M^{+4}]$), and an equivalent anion concentration (e.g., $[O^{-2}]$). Such quaternary phase diagrams have been used to illustrate the tie lines for Si_3N_4-Al_2O_3-SiO_2-AlN[66,91] and Si_3N_4-BeO-SiO_2-Be_3N_2[67] systems at 1750°C. They have also been used to illustrate the Si_3N_4-MO solid solutions that exist within these systems at a cation/anion ratio of 3/4.

The important phase diagrams illustrated in Figures 5-3 and 5-4, i.e., the Si_3N_4-MgO-SiO_2[92] and Si_3N_4-Y_2O_3-SiO_2[93] systems, respectively, are represented in the conventional and more convenient manner. For these two systems, a tie line exists between all or most of the Si_3N_4-MgO join. For all practical purposes, this ordinary representation will suffice. The tie lines in both diagrams were obtained (phase identification by X-ray diffraction analysis) for compositions hot pressed at temperatures between 1500-1750°C.** High purity, low oxygen (0.7 w/o) α-Si_3N_4 powder ($\alpha/\beta = 9$) was used to obtain these data. The secondary phases change from one compatibility triangle to another. The type and quantity of each secondary phase is very sensitive to change at low contents when different batches of Si_3N_4 contain different concentrations of SiO_2.

---

*That is, a true binary may not exist along the Si_3N_4-MgO join.
**Each diagram represents an isothermal section without defined regions of liquid. A constant temperature could not be employed since some compositions would exceed their liquidous temperature and destroy the hot-press dies.
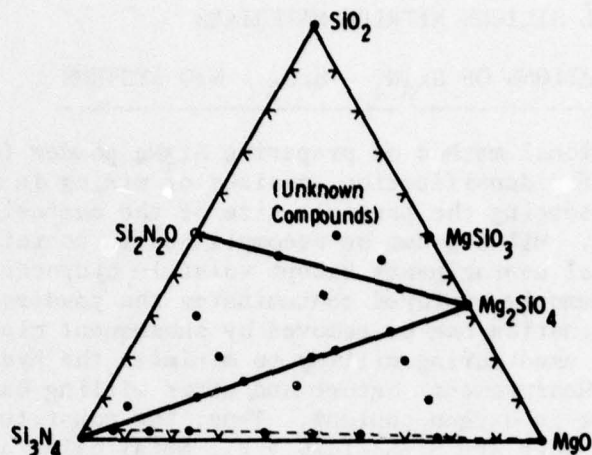
Figure 5-3. Ternary Phase Diagram for the
Si₃N₄·SiO₂·MgO System
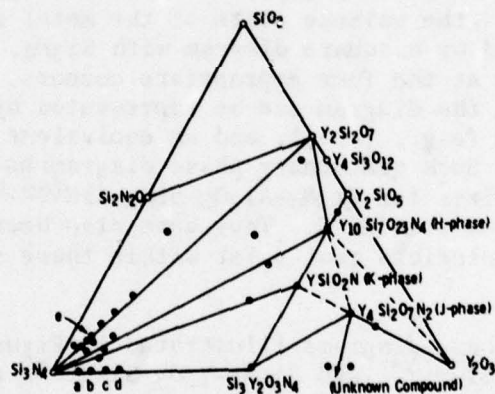
Figure 5-4. Ternary Phase Diagram for the
Si₃N₄·SiO₂·Y₂O₃ System

5.3.2 COMPOSITIONAL EFFECTS: Si_3N_4 - SiO_2 - MgO SYSTEM

Impurities were the first compositional factors known to influence
the high temperature mechanical properties of hot-pressed Si₃N₄.[94,95]
The effect of the major impurities on the strength and creep resistance
of hot-pressed Si₃N₄ (approximate molar composition: Si₃N₄ = 0.79;
MgO = 0.15; SiO₂ = 0.06) at 1400°C is shown in Figure 5-5.[96] To
obtain these data, the impurities were added as oxides (or carbonates)
to relatively pure α-Si₃N₄ powder prior to hot pressing. For the case

226
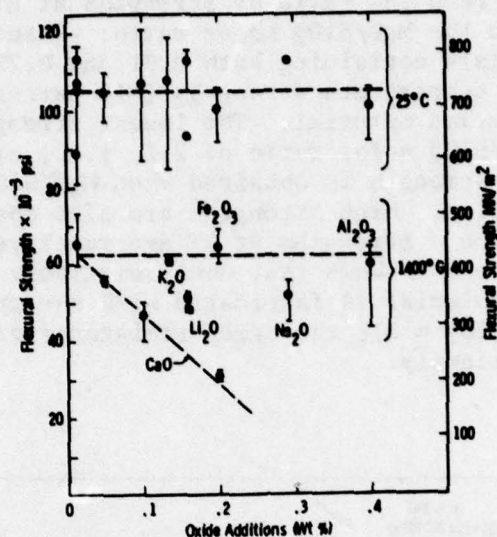
Figure 5-5. Effect of Impurities on the Flexural Strength of Experimental Si_3N_4

where MgO is the densification aid (i.e., material in the Si_3N_4-SiO_2-MgO system), CaO was the most detrimental impurity. Na_2O and K_2O volatilized during fabrication while $\sim 2/3$ of the Li_2O disappeared.

The effect of composition was first reported by Andersson, Lange and Iskoe[97] and more thoroughly studied by Lange.[92] As shown in Figure 5-6 for compositions containing 0.833 mole fraction Si_3N_4, the
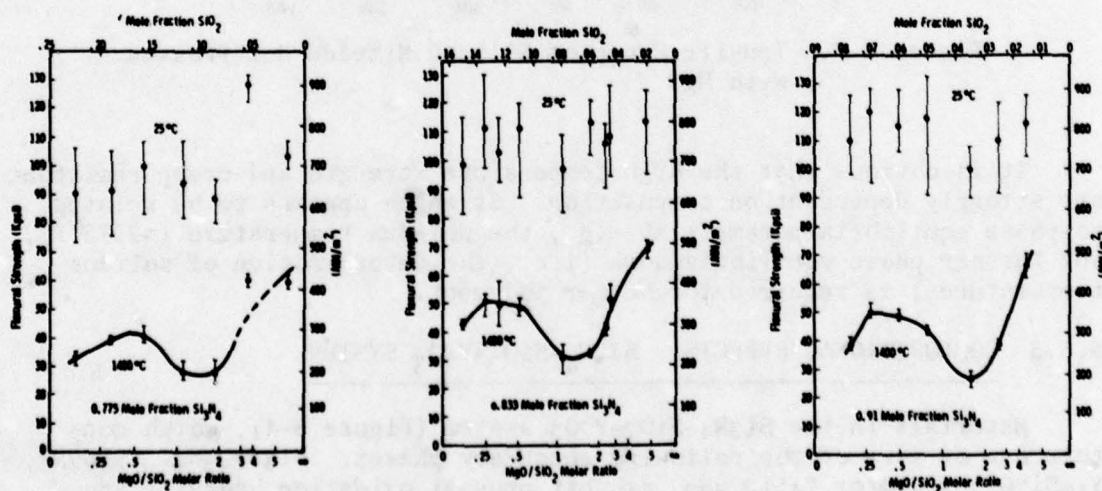
Figure 5-6. Effect of SiO_2 Mole Fraction on the Flexural Strength of Experimental Si_3N_4

227

strength at 2550°C (and the ratio of strengths at RT and 2550°F) are
strongly related to the MgO/SiO$_2$ molar ratio. Exact behavior was also
obtained for materials containing both 0.91 and 0.755 mole fractions of
Si$_3$N$_4$. Lower room temperature strengths ($\sim$15 percent) were obtained for
the 0.955 mole fraction material. The lowest strengths (at 2550°F) were
observed for a MgO/SiO$_2$ molar ratio of 2:1, i.e., along the Si$_3$N$_4$-Mg$_2$SiO$_4$
tie line. Maximum strength is obtained when MgO/SiO$_2$ → ∞, i.e., along
the Si$_3$N$_4$-MgO tie line. High strengths are also observed close to the
Si$_3$N$_4$-Si$_2$N$_2$O tie line. Strengths at RT are relatively independent of
composition. Figure 5-7 shows that when relatively pure Si$_3$N$_4$ powder is
used and when the material is fabricated with the proper MgO/SiO$_2$ ratio
(in this case MgO/SiO$_2$ $\sim$ 3), the creep resistance of hot pressed Si$_3$N$_4$
is improved significantly.
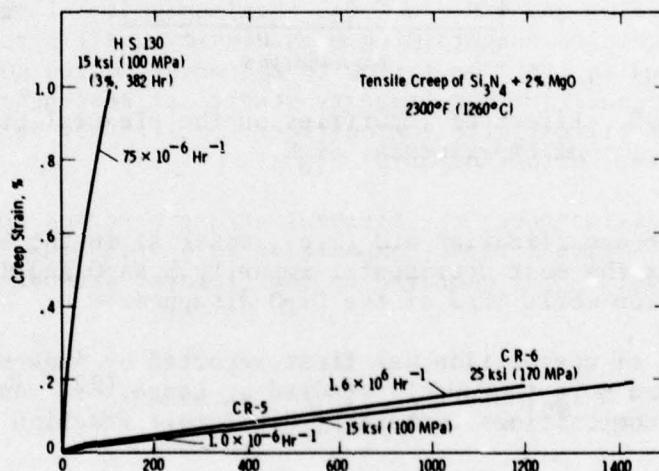
Figure 5-7. Tensile Creep of Silicon Nitride Hot-Pressed
with MgO

It is obvious that the high temperature strength and creep resistance
are strongly dependent on composition. Strength appears to be related
to phase equilibria parameters, e.g., the solidus temperature ($\sim$2372°F),
but further phase equilibria work (i.e., the determination of solidus
temperatures) is required for better judgment.

5.3.3 COMPOSITIONAL EFFECTS: Si$_3$N$_4$-SiO$_2$-Y$_2$O$_3$ SYSTEM

Materials in the Si$_3$N$_4$-SiO$_2$-Y$_2$O$_3$ system (Figure 5-4), which con-
tain one or more of the following secondary phases: Si$_3$Y$_2$O$_3$N$_4$, YSiO$_2$N$_7$,
Y$_{10}$Si$_7$O$_{27}$N$_4$ and/or Y$_4$Si$_2$O$_7$N$_2$, exhibit unusual oxidation behavior and
catastropic strength degradation at elevated temperatures.[93]

228

Detailed oxidation experiments have shown that $Si_3Y_2O_3N_4$ exhibits linear oxidation kinetics, i.e., the oxide surface scale does not protect the $Si_3Y_2O_3N_4$.[93] Preliminary experiments indicate that $YSiO_2N$, $Y_{10}Si_7O_{23}N_4$ and $Y_4Si_2O_7N_2$ also exhibit linear oxidation kinetics. All evidence shows that when these Y-Si-O-N compounds are present as secondary phase, they preferentially oxidize to cause cracks to develop in the polyphase Si_3N_4 material. Thus, the presence of these four compounds is undesirable. The detrimental compounds can be precluded as secondary phases when material in this system is fabricated within the Si_3N_4-Si_2N_2O-$Y_2Si_2O_7$ compatibility triangle.[92]

Large billets (1 x 3.5 x 5.5 inches) of Si_3N_4 were fabricated in the Si_3N_4-Si_2N_2O-$Y_2Si_2O_7$ compatibility triangle at Westinghouse under the DARPA Gas Turbine Program. Previous work, in which smaller billets were fabricated, indicated that both densification and good high temperature properties could be achieved with compositions close to 85.5 w/o Si_3N_4, 10.5 w/o SiO_2 and 4.0 w/o Y_2O_3. Scaleup to the larger billets presented difficulties in obtaining high density until pyrolitic graphite spacers were used to limit heat flow to the water-cooled hot-press rams. Concurrent with densification-property studies at Westinghouse, large (1 x 6 x 6 inch) billets with compositions specified by Westinghouse were purchased from the Norton Company.

Figure 5-8 illustrates the flexural strength versus temperature (in air) of the Norton billet (composition 79.6 w/o Si_3N_4, 15.8 w/o SiO_2 and 4.6 w/o Y_2O_3) as compared to the flexural strength of a large
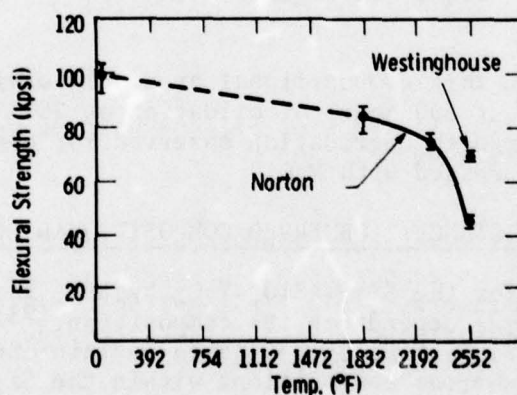
Figure 5-8.   Flexural Strength Comparison of Experimental Si_3N_4 Hot-Pressed with Y_2O_3

billet of Westinghouse material (composition: 85.5 w/o Si_3N_4, 10.5 w/o SiO_2 and 4.0 w/o Y_2O_3).[8] The relative creep resistance of both materials measured in air at 2300°F for three incremental stresses is shown in

Figure 5-9. The reason for the significant difference in mechanical behavior for the two materials appears to be their difference in composition. Norton pressed materials with compositions identical to Westinghouse material did not develop representative strengths due to poor density. Norton's use of Westinghouse powder did not achieve suitable results.
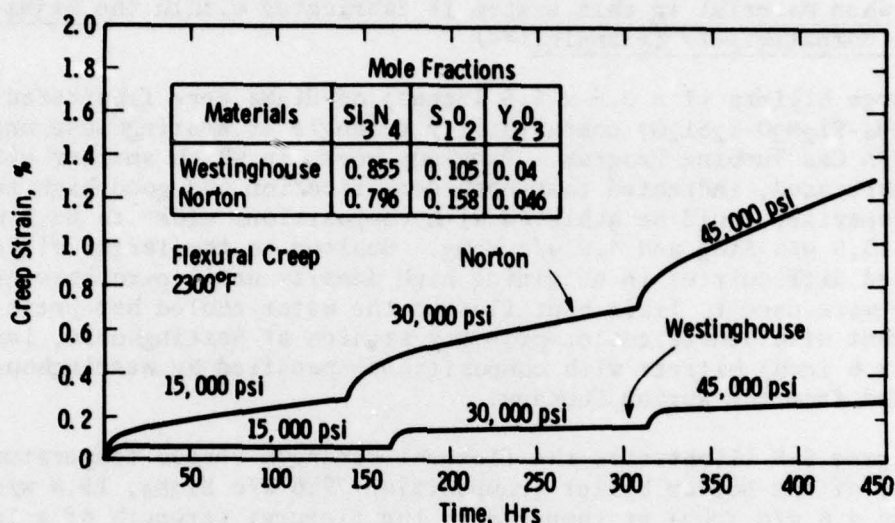

Figure 5-9. Flexural Creep Properties of Experimental
Si_3N_4 Hot Pressed with Y_2O_3

Materials within this compositional area only exhibit ~15 percent strength degradation at 300 hours of oxidation at 2550°F relative to the 40-60 percent strength degradation observed for commercial Si_3N_4 HS130 or NC132 (hot-pressed with MgO).

5.3.4 OXIDATION RESISTANCE: OBSERVED COMPOSITIONAL EFFECTS

As first shown for the Si_3N_4-SiO_2-Y_2O_3 system, the oxidation behavior of dense Si_3N_4 depends on its composition.[93] Compositions that lie within the Si_3N_4-$Y_2Si_2O_7$-Y_2O_3 area contain one or more of the unstable compounds, whereas compositions within the Si_3N_4-$Y_2Si_2O_7$-Si_2N_2O compatibility triangle exhibit unusually good oxidation resistance, apparently due to the compatibility of SiO_2 (the oxidation product of Si_3N_4) with $Y_2Si_2O_7$. Evidently, from an oxidation veiwpoint, the highest metal-silicate is a desirable second phase relative to other second phase silicates.

Materials densified with the aid of MgO do not have the same resistance to oxidation, apparently because of the preclusion of the highest silicate (Mg_2SiO_4) by the phase relations (Figure 5-10). Preliminary observations have shown that materials in the Si_3N_4-SiO_2-MgO system with compositions close to the Si_3N_4-Si_2N_2O tie line have improved oxidation resistance relative to materials fabricated close to the Si_3N_4-MgO tie line. Thus, considering the strength/compositional relationships discussed above, materials in the Si_3N_4-SiO_2-MgO system with both improved strength and oxidation resistance should be fabricated with a MgO/SiO_2 molar ratio of $\sim$0.25.
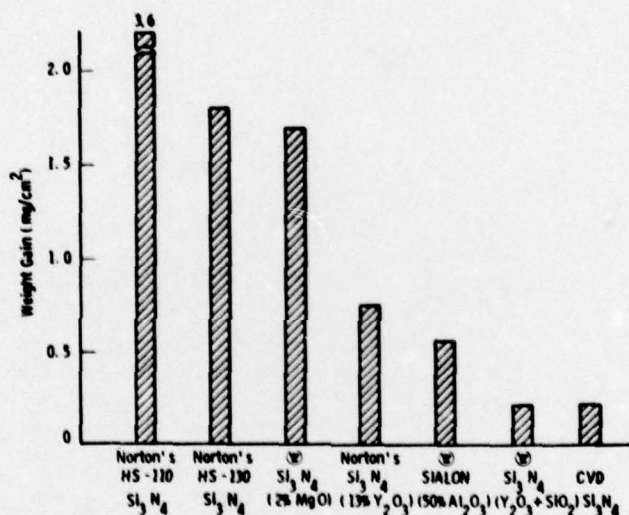
Figure 5-10. Comparative Weight Gains after 400 Hours
Oxidation at 1370°C in Air

Figure 5-10 further illustrates the relative oxidation resistance of the various Si_3N_4 materials. As shown, materials with compositions in the Si_3N_4-$Y_2Si_2O_7$-Si_2N_2O compatibility triangle exhibit resistance to oxidation intrinsic to that of pure Si_3N_4.

5.4   YTTRIA HOT-PRESSED Si_3N_4

The development of yttria hot-pressed silicon nitride by AMMRC (100) provided a new, creep-resistance material with exceptional high temperature strength for turbine vane evaluation. Norton accepted a purchase order to produce 6 x 6 x 1y2 inch billets, two each containing 13.0 percent, 16.5 percent and an optimum composition, for initial property evaluation. Billets containing 13.5 and approximately 12.5 w/o Y_2O_3 were delivered. These exhibited large low density areas which made it impossible to get a realistic estimate of strength potential. Norton was unable to press 16 w/o Y_2O_3 billets successfully.(8)

231

SECTION 6

CONCLUSIONS AND RECOMMENDATIONS

The conclusions and recommendations which follow were extracted from Volume I, "The Program Summary." All pertain specifically to the contents of this volume and are included here to complete the subject matter discussed.

6.1 CONCLUSIONS

1. Major problems remain to be solved before ceramic components are proven useful for practical turbines. The foremost, of course, is the development and characterization of improved materials for extended life in high temperature operation. Present production materials and processes pose a serious problem to design engineers who must provide high reliability for a very conservative power generation business. Improved processing to reduce property variability, better NDE methods and procedures to detect life limiting critical flaws and their distribution, and probabilistic life prediction methodology to assess component reliability, over many thousands of operating hours, are examples of technological areas that must be addressed.

2. The engineering property data base for candidate ceramics should be expanded to include a determination of long-term tensile creep strain, stress rupture and low cycle fatigue. Environmental testing should contain an assessment of the effects of oxidation, hot corrosion and erosion on physical, mechanical and failure properties.

3. The properties of commercial hot-pressed Si_3N_4 and SiC as characterized in this program (state of the art 1973-74) must be be improved for long term use in gas turbines. Stator vane performance was marginal at 2500°F peak gas temperature in the static rig demonstration. Creep behavior is expected to limit silicon nitride as a blade material above 2150°F. However, materials under development show promise of significant improvement, particularly with respect to high temperature strength, creep, and oxidation resistance.

4. Both Si_3N_4 and SiC show superior corrosion/erosion resistance at temperatures to 2000°F where turbine fuel contaminants can be most damaging due to condensation and reaction. The ability of these materials to maintain their strength after this exposure is most encouraging.

5. Detrimental oxidation of hot pressed Si_3N_4 above 2000°F can be prevented through composition control. An example is the use of Y_2O_3 + SiO_2 sintering aids to replace MgO in the production process.

6.2 RECOMMENDATIONS

1. A Base-Line Engine Definition is required to define explicitly the performance objectives of an advanced turbine engine containing ceramic components in order to set specific design goals and materials objectives.

2. Materials and Fabrication Developments are required to improve the properties and reliability of gas turbine ceramics. Through accelerated materials and processing research useful ceramics will evolve and basic information for the continued development of new materials, e.g., composites, coatings, etc. will be provided. Experimental materials from the laboratory should be transferred to commercial facilities where sufficient quantities of consistent-quality material can be reduced to production practice for evaluation in terms of engineering properties and component testing. It is strongly recommended that a comprehensive materials program be organized and managed to insure objectivtiy consistent with the basic engine requirement.

3. Materials Characterization should support the analytical design efforts by providing reliable engineering properties for stress analysis, evaluation of component structural integrity, and lifetime prediction. Failure property characterization, which represents a serious technological gap, should be conducted under combined loading conditions that represent planned rig and engine test conditions. Such a task is difficult. It will require careful planning and critical experiments to be cost effective.

SECTION 7

REFERENCES

1. McLean, A.F., E.A. Fisher and D.E. Harrison, "Brittle Materials Design, High Temperature Gas Turbine," AMMRC-CTR-72-3, Interim Report, March, 1972.

2. McLean, A.F., E.A. Fisher and R.J. Bratton, "Brittle Materials Design, High Temperature Gas Turbine," AMMRC-CTR-72-19, Interim Report, September, 1972.

3. McLean, A.F., E.A. Fisher and R.J. Bratton, "Brittle Materials Design, High Temperature Gas Turbine," AMMRC-CTR-73-9, Interim Report, March, 1973.

4. McLean, A.F., E.A. Fisher and R.J. Bratton, "Brittle Materials Design, High Temperature Gas Turbine," AMMRC-CTR-73-32, Interim Report, September, 1973.

5. McLean, A.F., E.A. Fisher, and R.J. Bratton, "Brittle Materials Design, High Temperature Gas Turbine," AMMRC-CTR-74-26, Interim Report, April, 1974.

6. McLean, A.F., E.A. Fisher and R.J. Bratton, "Brittle Materials Design, High Temperature Gas Turbine, "AMMRC-CTR-74-59, Interim Report, September, 1974.

7. McLean, A.F., E.A. Fisher, R.J. Bratton and D.G. Miller, "Brittle Materials Design, High Temperature Gas Turbine," AMMRC-CTR-75-8, Interim Report, April, 1975.

8. McLean, A.F., E.A. Fisher, R.J. Bratton and D.G. Miller, "Brittle Materials Design, High Temperature Gas Turbine," AMMRC-CTR-75-28, Interim Report, September, 1975.

9. McLean, A.F., R.R. Baker, R.J. Bratton, and D.G. Miller, "Brittle Materials Design, High Temperature Gas Turbine," AMMRC-CTR-76-12, Interim Report, April, 1976.

10. DeSalvo, G.J., "Theory and Structural Design Applications of Weibull Statistics," Westinghouse Astronuclear Laboratory, WANL-TME-2688 May, 1970.

11. Nadai, A., "Theory of Flow and Fracture of Solids," McGraw-Hill Book Co., New York, 1950, pp. 353-359.

12. Davis, E.A., "Creep of Metals at High Temperature in Bending," J. Appl. Mech., March 1938, pp. A29-A31.

13. Popov, E.P., "Bending in Beams with Creep," J. Appl. Phys. 20, 1949, pp. 251-256.

14. Marin, J., Y. Pao and G. Cuff, "Creep Properties of Lucite and Plexiglass for Tension Compression, Bending and Torsion," Trans. ASME, July 1951, pp. 705-719.

15. Findley, W.N. and J. J. Poczatek, "Prediction of Creep-Deflection and Stress Distribution in Beams from Creep in Tension, J. Appl. Mech., June 1955, pp. 165-171.

16. Hu, L.W. and N.H. Triner, "Bending Creep and Its Application to Beam-Column, J. Appl. Mech. March 1956, pp. 35-42.

17. Rosin, R., J. Bersan and G. Urbain, Rev. Hantes, Temper et Retract. 1, 159 (1964).

18. Evans, A.G. and J. V. Sharp, "Transmission Electron Microscopy of Silicon Nitride," Proc. 5th Berkeley Int'l Materials Symposium, Berkeley, CA., September, 1971, p. 1141.

19. Heuer, A., R.F. Fireston, and J.D. Snow, "Non-Basal Slip in Aluminum Oxide, Proc. 2nd Int'l Conference on Strength of Metals and Alloys, (1971), Asilomar, ASTM, p. 1765.

20. Evans, A.G., and J.V. Sharp, "Microstructural Studies on Silicon Nitride," J. Mat. Sci. 6, (1971) p. 1292.

21. Farnsworth, P.L. and R.L. Coble, "Deformation Behavior of Dense Polycrystalline Silicon Carbide," J. Am. Cer. Soc., 49, (1966), p. 264.

22. Hirth, J.P., and J. Lothe, "Theory of Dislocation," McGraw-Hill (1968), p. 498.

23. Hilling, W.B. and R.J. Charles, "Delayed Failure of Polycrystalline and Single Crystal Alumina," J. Wiley and Sons, Inc., New York (1965).

24. Charles, R.J. and R.R. Shaw, General Electric Corp. Report 62-41-3081M, (1962).

25. "Phase Diagrams for Ceramists," American Ceramic Society (1964), p. 210.

26. Pinney, R.W., Subcontract Reports, Battelle Memorial Institute, "Thermophysical Properties of Type A and Type B Silicon Nitride," Sept. 22, 1972 and "Thermophysical Properties of Hot Pressed Silicon Carbide," April 26, 1973.

27. Butler, E., "Observations of Dislocations in β-Silicon Nitride," Philosophical Magazine, Vol. 21 (1970) p. 829.

28. Stull, D.R. and H. Prophet, "JANAF Thermochemical Tables," 2nd Edition, NSRDS-NBS 37, (1971).

29. Blegen, K., Special Ceramics (P. Popper, ed.) British Ceramic Research Assoc., 6, (1975) 223.

30. Wagner, C., J. Appl. Phys. 29, (1958) 1295.

31. Turkdogan, E.T., and P.M. Bills, Amer. Ceram. Soc., Bull. 39, (1960) 682.

32. Horton, R.M., J. Amer. Ceram. Soc. 52, (1969), 121.

33. Gourstat, P., P. Lortholary, D. Tetard and M. Billy, "Proc. 7th Int'l. Symposium on Reactivity of Solids," Bristol, (1972), p. 315.

34. Jorgensen, P.J., M.E. Wadsworth and I.B. Cutler, J. Amer. Ceram. Soc. 42, (1959) 613.

35. Jorgenson, P.J., M.E. Wadsworth and I.B. Cutler, J. Amer. Ceram. Soc., 44, (1961), 258.

36. Adamsky, R.F., J. Phys. Chem., 63 (1959) 305.

37. Ervin, G., J. Amer. Ceram. Soc. 41, (1958) 347.

38. Ainger, F.W., J. Mater. Sci., 1, (1966) 1.

39. Deal, B.E., J. Electrochem. Soc., 110, (1963) 527.

40. Evitts, H.C., H.W. Cooper and S.S. Flaschen, J. Electrochem. Soc. 111, (1964) 699.

41. Sucov, E.W., J. Amer. Ceram. Soc. 46, (1963) 14.

42. Williams, E.L., J. Amer. Ceram. Soc. 48, (1965) 190.

43. Lindner, R. and G. Parfitt, J. Chem. Phys. 26, (1957) 182.

44. Borchardt, G., and H. Schmalzried, Ber. Deut. Keram. Ges. 49 (1972) 5.

45. Majdic, V.A. and H. Henning, Ber. Deut. Keram. Ges. 47 (1970) 53.

46. Volkonskii, B.V. and L.G. Sudakas. Tsement 23 (1957) 17.

47. Turkdogan, E.T., and P.M. Bills, Amer. Ceram. Soc. Bull. 39 (1960) 682.

48. Levin, E.M., C.R. Robbins and H.F. McMurdie, "Phase Diagrams for Ceramists," (M.K. Reser, ed.), The Amer. Ceram. Soc., Columbus, OH (1964).

49. Singhal, S.C. and F.F. Lange, J. Amer. Ceram. Soc., 58 (1975), 433.

50. Kossowsky, R. and S.C. Singhal in "Grain Boundaries in Engineering Materials," (J.L. Walter, J.H. Westbrook and D.A. Woodford, eds.) Claitor's Publishing Division, Baton Rouge, (1975), p. 275.

51. Pultz, W.W., and W. Hertl, Trans. Faraday Soc. 62 (1966) 2499.

52. Pultz, W.W., J. Phys. Chem. 71 (1967) 4556.

53. DeCrescente, M.A. and N.S. Bornstein, "Formation and Reactivity Thermodynamics of Sodium Sulfate with Gas Turbine Alloys," Corrosion, Vol. 24, (1968), 127.

54. Bornstein, N.S., M.A. DeCrescente and H.A. Roth, "Interaction Between Vanadium in Gas Turbine Fuels and Sulfidation Attack," Corrosion, Vol. 28, (1972), 264.

55. Gravette, N.C., D. Barham and L.R. Barrett, "An Investigation of the System $V_2O_5-SiO_2$, Trans. Brit. Ceram. Soc., Vol. 64 (1966), 205.

56. Bessen, I.I. and R.E. Fryxell, "Turbine Corrosion and Protection in Marine Environments," in Gas Turbine Materials Conference Proceedings, Naval Ship Engineering Center and Naval Air Systems Command, (1972), 73.

57. ARPA Continuation of Office of Naval Research Project, Westinghouse Designation-"Powder" Contract No. N0014-74-C-0282.

58. Naval Air Systems Command Project to Understand the Performance of Si Compounds in Si_3N_4 and SiC, Westinghouse Designation "Seram" Contract No. N00019-72-C-0278.

59. Deeley, G.G., Brit. Pat. No. 942,082, Nov. 20, 1963, G.G. Deeley, J.M. Herbert and N.C. Moore, Powder Met., No. 8, 145 (1961).

60. Gazza, G.E., J. Am. Ceram. Soc., 56, 662, (1973).

61. Huseby, I.C. and G. Petzow, Powder Met. Int., 6, 17, 1974.

62. Mazdiyasni, K.S. and C.M. Cooke, J. Am. Ceram. Soc., 57, 563, 1974.

63. Terwilliger, G.R. and F.F. Lange, J. Mat. Sci., 10, 1169, 1975.

64. Jack, K.H. and W.I. Wilson, Nature Phys. Sci. (London) 238, 28, July 10, 1972.

65. Lange, F.F.,"Task I" Fabrication, Microstructure and Selected Properties of SiAlON Compositions," Final Report NAVAIR N00019-73-C-0208, Feb. 26, 1974.

66. Gauckler, L.J., H.L. Lukas, and G. Petzow, J. Am. Ceram. Soc., 53, 346, (1975).

67. Huseby, I.C., H.L. Lukas, and G. Petzow, J. Am. Ceram. Soc., 58, 377, (1975).

68. Rochow, E.G., Comprehensive Inorganic Chemistry, "Silicon" p. 1323, Pergamon Press.

69. Marchand, R., Y. Laurent, J. Lang and M. Th. LeBihan, Acta. Crys. B25, 2157, 1969.

70. Hardie, D. and K.H. Jack, Nature (London) 180, 332, (1957).

71. Turkdogan, E.T., P.M. Bills and V.A. Tippett, J. Appl. Chem. 8, 296, (1958).

72. Wild, S., P. Grieveson and K.H. Jack, Special Ceramics, 5, 385, Ed. by P. Popper, B.C.R.A., Stoke-on-Trent, (1972).

73. Kohatsu, I. and J.W. McCauley, Mat. Res. Bull. 9, 917 (1974).

74. Kato, K., Z. Inque, K. Kijima, I. Kawada, H. Tanaka, and T. Yamane, J. Amer. Ceram. Soc., 58, 90 (1975).

75. Priest, H.F., F.C. Burns, G.L. Priest and E.C. Skaar, J. Amer. Ceram. Soc., 56, 395 (1973).

76. Edwards, A.J., D.P. Elias, M.W. Lindley, A. Atkinson and A.J. Moulson, J. Mat. Sci., 9, 516, 1974.

77. Campos-Loriz, D. and F.L. Riley, J. Mat. Sci., 11, 195, (1976).

78. Blegen, K., Special Ceramics, 6, 223 (See Ref. 13).

79. Parr, N.L., G.F. Martin, and E.R.W. May, Special Ceramics, p. 102, Ed. by P. Popper, Academic Press (1960).

80. Yamuchi, T. and H. Suzuki, U.S. Patent 3,206,318, Sept. 14, 1965.

81. Lumbey, R.J., Brit. Patent, 1,206,468, September 23, 1970.

82. Brennan, A.C. and J.G.R. Phillips, Brit. Patent 1,335,842, October 31, 1973.

83. Singhal, S.C., Ceramurgia Internat. In Press 1976.

84. Sin-Shong Lin, J. Amer. Ceram. Soc., 58, 271, 1975.

85. Huettinger, K.J., High Temperature, High Pressures 2, 89, 1970.

86. Mangles, J., Current Work at Ford on ARPA DAAG 46-71-C-0162

87. Atkinson, A., A.J. Moulson, and E.W. Roberts, J. Mat. Sci. 10, 1242, (1975).

88. Messier, D.R., P. Wong and A.E. Ingram, J. Amer. Ceram. Soc., 56, 171 (1973).

89. Yamauchi, T. and H. Suzuki, U.S. Patent 3,206,318, Sept. 14, 1965.

90. Baumgartner, H.R. and D.W. Richerson, Fracture Mechanics of Ceramics, 1, p. 367, Ed. by R.C. Bradt, D.P.H. Hasselman and F.F. Lange, Plenum, (1974).

91. Jack, K.H., J. Mat. Sci., 11, 1135 (1976).

92. Lange, F.F., "Phase Relations in the Si_3N_4-SiO_2-MgO System: Compositional Effects on Strength and Oxidation Resistance," ONR Tech. Report. No. 9, Contract No. N00014-74-C-0284.

93. Lange, F.F., S.C. Singhal and R.C. Kuznicki, "Phase Relations and Stability Studies in the Si_3N_4-$SiO_2Y_2O_3$ Pseudo-Ternary System," Tech. Rept. No. 6, ONR N00014-74-C-0284, April 1, 1976.

94. Kossowsky, R., Ceramics for High Peformance Applications, p. 665, Ed. by J.J. Burke, A.E. Gorum and R.N. Katz, Brook Hill, 1974.

95. Evans, A.G. and S.M. Wiederhorn, J. Mat. Sci. 9, 270, 1974; A.G. Evans, L.R. Russell and D.W. Richerson, Met. Trans. 6A, 707, (1975).

96. Richerson, D.W., Bul. Amer. Ceram. Soc., 52, 560 (1973).

97. Iskoe, J.L, F.F. Lange and E.S. Diaz, J. Mat. Sci., 11, 908, (1976).

98. Andersson, C.A., F.F. Lange and J.L. Iskoe, "Effect of MgO/SiO_2 Molar Ratio on High Temperature Strength of Hot-Pressed Si_3N_4," ONR Tech. Rept. No. 3, Contract No. N00014-74-C-0284, October 15, 1975.

99. Lange, F.F., H.J. Siebeneck and D.P.H Hasselman, J. Amer. Ceram. Soc., (In Press).

100. Gazza, G.E., Hot Pressed, High Strength Silicon Nitride, U.S. Patent 3,830,652, August 20, 1974.

Abstract

In 1971 Norton obtained an exclusive license to produce Lucas hot pressed silicon nitride in the United States. That process made a high-density, high strength ceramic material with excellent potential for high temperature application, i.e., industrial gas turbine components, available commercially. Project funds were used to develop an engineering property data base to describe Norton HS130/Noralide NC132 silicon nitride and Noralide NC203 silicon carbide. The list includes tensile, flexure , shear, and compressive strengths from room temperature to 2550°F for appropriate directions in anisotropic materials along with elastic/shear moduli and Poisson's ratio. Creep resistance is defined in terms of creep strain and stress rupture life as a function of temperature, time, and environment. Thermal properties were also considered, i.e., thermal expansion, conductivity, and specific heat. Equipment and test procedures are discussed.

No material characterization study is complete without a thorough examination of microstructure. Morphology, grain boundaries, and the effects of compositional variations are considered with respect to silicon nitride and silicon carbide.

The microstructural characterization led to process and product improvements in the commercial materials and eventually revealed paths for the development of improved varieties of silicon nitride and silicon carbide. Westinghouse activity in the area of material development involving magnesia and/or yttria silicon nitride systems is reviewed to put the entire question of materials and their critical part in component design and development into proper perspective.

REPORT DOCUMENTATION PAGE		READ INSTRUCTIONS BEFORE COMPLETING FORM
1. REPORT NUMBER AMMRC CTR 76-32 Volume IV	2. GOVT ACCESSION NO.	3. RECIPIENT'S CATALOG NUMBER
4. TITLE (and Subtitle) BRITTLE MATERIALS DESIGN, HIGH TEMPERATURE GAS TURBINE - MATERIAL TECHNOLOGY		5. TYPE OF REPORT & PERIOD COVERED Final Report
		6. PERFORMING ORG. REPORT NUMBER
7. AUTHOR(s) D.G. Miller, C.A. Andersson, S.C. Singhal, F.F. Lange, E.S. Diaz, R. Kossowsky Westinghouse Electric Corporation		8. CONTRACT OR GRANT NUMBER(s) DAAG 46-71 C-0162
9. PERFORMING ORGANIZATION NAME AND ADDRESS Westinghouse Electric Corporation Pittsburgh, Pennsylvania 15235		10. PROGRAM ELEMENT, PROJECT, TASK AREA & WORK UNIT NUMBERS D/A Project: ARPA Order 1849 AMCMS Code: Agency Accession DA OD4733
11. CONTROLLING OFFICE NAME AND ADDRESS Army Materials and Mechanics Research Center Watertown, Massachusetts 02172		12. REPORT DATE December 1976
		13. NUMBER OF PAGES
14. MONITORING AGENCY NAME & ADDRESS(if different from Controlling Office)		15. SECURITY CLASS. (of this report) Unclassified
		15a. DECLASSIFICATION/DOWNGRADING SCHEDULE

16. DISTRIBUTION STATEMENT (of this Report)

Approved for public release; distribution unlimited.

17. DISTRIBUTION STATEMENT (of the abstract entered in Block 20, if different from Report)

18. SUPPLEMENTARY NOTES

19. KEY WORDS (Continue on reverse side if necessary and identify by block number)

20. ABSTRACT (Continue on reverse side if necessary and identify by block number)

ABSTRACT

In 1971 Norton obtained an exclusive license to produce silicon nitride in the United States. That industrial gas turbine material, high strength ceramic material with excellent potential for high temperature application, is here to describe Norton HS130/Norelide NC132 silicon nitride and Norelide NC203 silicon carbide. Project funds were used to develop properties data flexure, shear and compressive strength from room temperature to 2500°F for appropriate directions in anisotropic materials along with elastic modulus and Poisson's ratio. Creep resistance is defined in terms of creep strain and stress rupture life as a function of temperature, stress, and environment. Thermal expansion, thermal conductivity, and specific heat. Equipment and test procedures are discussed.

No material characterization study is complete without a thorough evaluation of microstructure. Morphology, grain boundaries, and the effects of compositional variations are considered with respect to silicon nitride and silicon carbide.

The microstructural characterization led to process and product improvement in the commercial materials and eventually revealed paths for the development of improved varieties of silicon nitride and silicon carbide. Westinghouse activity in the area of material development involving magnesia and/or yttria-silicon nitride system is reviewed to put the entire question of materials and their critical part in component design and development into proper perspective.